CORA Cork Open Research Archive
Cartlann Taighde Oscailte Chorcaí

| | |
|---|---|
| Title | Statistical modeling strategies for estimation of the arterial input function in dynamic positron emission tomography data analysis |
| Authors | Xiu, Zhaoyan |
| Publication date | 2023-03 |
| Original Citation | Xiu, Z. 2023. Statistical modeling strategies for estimation of the arterial input function in dynamic positron emission tomography data analysis. PhD Thesis, University College Cork. |
| Type of publication | Doctoral thesis |
| Rights | © 2023, Zhaoyan Xiu. - https://creativecommons.org/licenses/by-nc-nd/4.0/ |
| Download date | 2026-10-31 11:44:30 |
| Item downloaded from | https://hdl.handle.net/10468/14535 |

UCC
University College Cork, Ireland
Coláiste na hOllscoile Corcaigh

# Statistical Modeling Strategies for Estimation of the Arterial Input Function in Dynamic Positron Emission Tomography Data Analysis

Zhaoyan Xiu

NATIONAL UNIVERSITY OF IRELAND, CORK

DEPARTMENT OF STATISTICS

**Thesis submitted for the degree of Doctor of Philosophy**

March 2023

Head of Department: Dr Michael Cronin

Supervisors: Dr Jian Huang
Dr Eric Wolsztynski

Research supported by Science Foundation Ireland in part under grant numbers 11/PI/1027 and 12/RC/2289-P2, co-funded under the European Regional Development Fund, in part by ACRIN-6688, in part by the National Cancer Institute (CA-42045), and in part the National Institute of Aging (031485). No conflict of interest to report. This work complies with Ethical Standards.

# Contents

List of Figures . . . . . v
List of Tables . . . . . xi
List of Nomenclatures . . . . . xii
Acknowledgements . . . . . xvi
Abstract . . . . . xvii

**1 Introduction** **1**
1.1 Motivation . . . . . 1
1.2 Main Objectives . . . . . 2
1.3 Outline and Contribution . . . . . 3

**2 Background to the Problem** **4**
2.1 Positron Emission Tomography . . . . . 4
2.1.1 Introduction . . . . . 4
2.1.2 Physics in PET . . . . . 5
2.1.3 Clinical Applications . . . . . 7
2.1.4 Steps in PET Imaging . . . . . 8
2.2 Basic PET Data Analysis Techniques . . . . . 9
2.2.1 Static PET data . . . . . 10
2.2.1.1 Standardized Uptake Value . . . . . 12
2.2.1.2 Equilibrium Analysis . . . . . 13
2.2.2 Tracer Kinetics . . . . . 15
2.2.2.1 Compartmental Models . . . . . 15
2.2.2.2 Graphical Methods . . . . . 17
2.2.2.3 Spectral Analysis . . . . . 21

**3 AIF Estimation Methods** **24**
3.1 Image-derived Input Function Estimation . . . . . 24
3.1.1 Segmentation Methods . . . . . 26
3.1.1.1 Cluster Analysis . . . . . 27
3.1.1.2 Factor Analysis of Dynamic Structures . . . . . 28
3.1.1.3 Independent Component Analysis . . . . . 28
3.1.2 Simultaneous Estimation . . . . . 29
3.2 Population-based Input Function Estimation . . . . . 31
3.3 Common AIF models . . . . . 32
3.3.1 Feng's Model . . . . . 33
3.3.2 Tri-exponential Model . . . . . 33
3.3.3 Convoluted Models . . . . . 34
3.4 Approximation from Venous Blood Information . . . . . 35
3.4.1 Arterialised Venous Blood . . . . . 35
3.4.2 Venous Input Function . . . . . 35
3.5 Whole Body Blood Circulation Model . . . . . 36

**4 Tracer Travel Rate Projection Model** **41**
4.1 Introduction . . . . . 41

4.2 Modelling Approach . . . 42
4.2.1 Theory . . . 42
4.2.2 The Fast Curve . . . 43
4.2.3 The Intermediate-fast curve . . . 45
4.2.4 The Intermediate-slow Curve . . . 46
4.2.5 The Slow Curve . . . 46
4.2.6 The Loss Curve . . . 47
4.3 TRPM Specification and Optimization . . . 48
4.3.1 Gamma Distribution . . . 49
4.3.2 Component Curves . . . 50
4.3.3 Quadratic Programing Problem . . . 50
4.3.4 Gauss-Newton Method . . . 52
4.3.5 Bayesian Penalty . . . 55
4.3.6 Leave-one-out Cross Validation . . . 55
4.3.7 Generalized Cross Validation . . . 56
4.3.8 Optimization . . . 56
4.4 Results . . . 58
4.4.1 Data . . . 58
4.4.1.1 Directly Sampled Arterial Data . . . 58
4.4.1.2 PET Imaging Data . . . 59
4.4.2 Penalized TRPM . . . 61
4.4.2.1 FDG Studies . . . 62
4.4.2.2 Water Studies . . . 64
4.4.3 Assessment of TRPM with Penalty on Imaging Data . . . 66
4.4.3.1 FDG Studies . . . 66
4.4.3.2 Water Studies . . . 69
4.5 Discussion . . . 73
4.5.1 Computational Complexity . . . 74
4.5.2 Interpretation of the Components . . . 74
4.5.3 Interpretation of the Linear Parameters . . . 75
4.5.4 Weights . . . 76
4.5.5 Scale Factor Estimation . . . 77
4.5.6 Comparison with Existing Models . . . 77
4.5.7 Estimation of Tracer Kinetic Parameters in Tracer Kinetics 78
4.5.8 Application to Other Tracers . . . 78

**5 Population-based Projection Modelling of AIFs 80**
5.1 Introduction . . . 80
5.2 Model Specification . . . 83
5.2.1 AIF Model Specification . . . 83
5.2.2 Model Fitting . . . 84
5.2.2.1 Estimation of $\pi_k$ given $\Delta_k$ and $\theta$ . . . 85
5.2.2.2 Estimation of Delay $\Delta_k$ given $\theta$ . . . 86
5.2.2.3 Estimation of Population Parameter $\theta$ . . . 86
5.2.2.4 Fitting Individual Curves . . . 87
5.2.2.5 Model Regularization . . . 87

5.2.3 Model Selection . . . 88
5.2.4 Scale Factor Estimation . . . 89
5.3 Evaluation . . . 90
5.3.1 Data . . . 90
5.3.2 Model Selection . . . 91
5.3.3 Model Fitting . . . 93
5.3.4 Scale Factor Estimation . . . 93
5.4 Simulation Studies . . . 94
5.4.1 Validation Study on Model-derived Template . . . 95
5.4.1.1 Model-based Simulation Template . . . 95
5.4.1.2 Model Validation and Assessment . . . 97
5.4.2 Sensitivity to Training Population Size . . . 97
5.4.3 Effect of Using a Training Population . . . 99
5.4.4 Benchmark on Bootstrapped Data . . . 100
5.4.4.1 sAIF-based Simulation Template . . . 100
5.4.4.2 Benchmarking . . . 100
5.4.4.3 Reduced SAIF-based Simulation Template . . . 101
5.4.5 Simulated FDG-PET Kinetic Study . . . 102
5.4.5.1 Simulation Design . . . 102
5.4.5.2 Validation of the 2C Model . . . 103
5.4.5.3 Re-parameterization . . . 104
5.5 Results . . . 104
5.5.1 Comparative Analysis . . . 104
5.5.2 Gain from a Population-based Approach . . . 106
5.5.3 Impact on Kinetic Modelling . . . 106
5.6 Discussion . . . 108
5.7 Conclusion . . . 110

**6 Discussion and Conclusions** **121**
6.1 Summary of Contributions . . . 121
6.2 Opportunities for Future Research . . . 123
6.2.1 Application to Other Tracers . . . 123
6.2.2 Estimating the AIF from Imaging Data . . . 123
6.2.3 Reduced Scanning Times . . . 124
6.2.4 Assessment of Spillover in PET Imaging Data . . . 127
6.2.5 Improvement of TRPM . . . 128
6.2.6 Normalizing by Area Under the Curve . . . 129
6.3 Conclusion . . . 129

**A List of Publications and Presentations by the Author** **A1**
A.1 Journal Paper . . . A1
A.2 Peer-reviewed Conferences . . . A1

**B Assessment of Tracer Concentration at Injection** **B3**

**C Convolution between Injection Function and Gamma Distribution** **C7**

**D Historical Information from Arterially Sampled Data for TRPM D9**
D.1 FDG Analysis . . . . . D10
D.2 Water Analysis . . . . . D11
D.3 Principal Component Analysis of Parameter Estimates . . . . . D15

# List of Figures


2.1 Exterior of a PET/CT scanner from Siemens Biograph series. . . 5
2.2 PET (left) and PET/CT (right) 3D images acquired on the GE Advance scanner at University of Washington from a sarcoma patient (Dunnwald et al. 2008) in transverse, coronal and sagittal views from AMIDE (Loening & Gambhir 2003). The tumor is marked by the ellipse ROI (region of interest) function in the software. . . . . 5
2.3 Physics in PET (JROGEL 2012). . . . . 7
2.4 Steps in PET imaging (adapted from Turku BioImaging team 2018). . . . . 9
2.5 a, c, e, and g show the input functions that produce the tissue responses in b, d, f, and h, respectively (Bailey et al. 2005). . . 11
2.6 Points and solid triangles are measured values in the putamen and cerebellum in a healthy subject, respectively. Concentration in the reference region is estimated by the difference between two measured values and fitted to a solid line by a set of three exponentials. Equilibrium is defined to happen at the maximum of the fitted curve (Farde et al. 1989). . . . . 14
2.7 Three most commonly used compartmental models and macroparameters of interest (Bertoldo et al. 2014a). . . . . 18
2.8 An example of a Patlak plot (A) and a Logan plot (B), with an irreversible ([$^{18}$F]FDG) and a reversible ([$^{11}$C](R)-rolipram) tracer, respectively. The data appear to reach a straight line after time $t^*$. The slope of each line is an approximation of $K$ and $V_T$, respectively (Bertoldo et al. 2014a). . . . . 20
2.9 Example of spectral analysis quantification. (a) Kinetic spectrum indicates three components are reported including one with $\beta = 0$ (in red). (b) Corresponding curves of concentration are presented in dashed lines, and summation of the curves is performed (solid line) to obtain the final fit (Veronese et al. 2016). 23

3.1 Block diagram of one free quantification tool for AIF (adapted from Bertran et al. 2016). . . . . 26
3.2 Flowchart of the ICA procedure for generating IDIF and MRGlc (Chen et al. 2007). . . . . 29
3.3 TACs from multiple regions in FDG PET study are estimated by convolution between AIF and IRFs. (Feng et al. 1997) . . . . . 30
3.4 A example of AIF for water (left) and FDG (right) study. Concentration is normalized to peak and time is in the unit of minute. Experimental data are from directly sampled AIF acquired in University of Washington (Huang & O'Sullivan 2014). Sampling is at discrete time points, and adjacent points are linked by straight lines. . . . . 33

3.5 Markovian model based on whole body blood circulation. Graphic representation (left) and probability transition matrix (right) (Huang & O'Sullivan 2014). . . . . 37
3.6 Fitting imaging data from one ROI using the extended BCM (Xiu et al. 2016). Considering one pool is contaminated by signals from the other pools, and assuming time-invariance, a signal from one ROI is fitted by linear combination of arterial, venous, and body vascular time courses. The image is from a water and FDG dynamic PET study at University of Washington (Dunnwald et al. 2008), and ROIs are drawn by experts for different blood pools. . . . . 39

4.1 Graphic representation of tracer kinetics in blood circulation system (left) and compartments setting for AIF modelling (right). Note that while heart and lungs are playing other roles instead of pumping blood and supplying oxygen, they are regarded as compartments of organs and tissues. . . . . 44
4.2 PDF (left) and CDF (right) of gamma distribution with different parameters (Wikipedia contributors 2018b). . . . . 50
4.3 Plot of logit(x) in the domain of 0 to 1, where the base of logarithm is e (Wikipedia contributors 2018d). . . . . 52
4.4 Diagram of steps in TRPM optimization. . . . . 57
4.5 FDG-PET and $H_2O$-PET data acquired at the university of Washington (Graham et al. 2002, Muzi et al. 2009, Eyal et al. 2010, O'Sullivan et al. 2009, Huang & O'Sullivan 2014). FDG-PET data with 1-minute injection (left), FDG-PET data with 2-minute injection (mid) and $H_2O$-PET data with bolus injection (right). . . 59
4.6 Exampled of manually drawn ROI on left ventricle of heart from PET imaging using AMIDE (Loening & Gambhir 2003). Small red circles with 6 mm diameter inside of big yellow markers in transverse (left), coronal (mid) and sagittal (right) views together as ROI for left ventricles. . . . . 60
4.7 An example fit using TRPM with penalty: sum of squared error (left), effective degree of freedom (mid) and GCV score (right) against the weight of penalty. . . . . 61
4.8 Scatter plot (left) and distributions (right) of mean squared errors of TRPM on 91 FDG studies. . . . . 62
4.9 Left: Residuals of 2465 AIF data points against square root of time (minute); Right: Scatter plot of Residuals from TRPM with and without penalty. . . . . 63
4.10 Distributions of parameter estimates (logit transformed) from TRPM with and without penalty on FDG study. . . . . 63
4.11 Scatter plot (left) and distributions (right) of mean squared errors of TRPM on 39 water studies. . . . . 64

4.12 Left: Residuals of 1117 AIF data points against square root of time (minute); Right: Scatter plot of Residuals from TRPM with and without penalty. . . . . 64
4.13 Distributions of parameter estimates (logit transformed) from TRPM with and without penalty on the water study. . . . . 65
4.14 Left: 53 AIFs from FDG imaging data (grey) and one example (black); Right: Performance of TRPM on that example. . . . . 66
4.15 Nine example fits using TRPM on imaging FDG AIFs. . . . . 67
4.16 Scatter plot (left) and distributions (right) of mean squared errors of TRPM on 53 FDG studies from imaging data set using TRPM with and without penalty. . . . . 68
4.17 Comparison of residuals for 1273 individual points in FDG studies from imaging data set using TRPM with and without penalty. 68
4.18 Distributions of parameter estimates from 53 FDG studies using TRPM without the penalty term ($Without$) and with the penalty term ($With$), and distributions of the penalty for model parameter estimation ($Penalty$). . . . . 69
4.19 Left: 52 AIFs from water imaging data (grey) and one example (black); Right: Performance of TRPM on that example. See Appendix D for the definition of Fast, Inter and Slow curves of TRPM in the water study. . . . . 70
4.20 Nine example fits using TRPM on water AIFs. . . . . 71
4.21 Scatter plot (left) and distributions (right) of mean squared errors of TRPM on 52 water studies from imaging data set using TRPM with and without penalty. . . . . 72
4.22 Comparison of residuals for 2912 individual points in water studies from imaging data using TRPM with and without penalty. . 72
4.23 Distributions of parameter estimates from 52 water studies using TRPM without the penalty term ($Without$) and with the penalty term ($With$), and distributions of the penalty for model parameter estimation ($Penalty$). . . . . 73

5.1 Flowchart of typical PBIF and IDIF strategies, along with the proposed PBPM methodology. Red and green blocks indicate use of individual subject and population data respectively. Step 3 of each method is an AIF model fitting step. Blood sampling for step 6A is not used in some IDIF approaches (hence the dashed line); when used, fewer points are typically required compared to blood sampling used in step 6B. Using individual image-derived data (1A) at step 3B(ii) of the PBPM approach (instead of arterial sampling data) would require an extra step in order to scale the output to a physiological level, as in step 5 of an IDIF method. . . . . 81

5.2 Normalized kinetic PET time activity curves acquired at the University of Washington (Graham et al. 2002, Muzi et al. 2009, Eyal et al. 2010, O'Sullivan et al. 2009, Huang & O'Sullivan 2014): 78 FDG-PET curves with 1-minute injection duration (A), 27 FDG-PET curves with 2-minute injection duration (B); 39 $H_2O$-PET curves with bolus injection (C); 32 FLT-PET curves with 1-minute injection (D). . . . . 91
5.3 Left: model selection for $H_2O$ (top) and FDG (center for one-minute injections; bottom for two-minute injections) studies on the basis of the leave-one-out cross-validated error defined in Section 5.2.3. Right: corresponding basis component fits. . . . 92
5.4 Examples of individual PBPM fits to FDG (left), $H_2O$ (middle) and FLT (right) arterial data, where the population-fitting components $f_j$ shown in each plot, defined as the convolutions between the exponential components $e_j$ with the population gamma profile $G$ in (5.1), are scaled by individual mixing weights $\pi_j$ (with $j = 1, 2, 3$ for FDG and FLT data and $j = 1, 2$ for $H_2O$ data). 94
5.5 Scatterplot of estimated scale factors (Eq. 5.4) against actual values obtained directly from arterial sampling data from 91 FDG AIF studies, showing a significant association between the two samples (Pearson correlation $\rho = 0.83$, two-sided paired t-test $p = 0.9999$. . . . . 95
5.6 Examples of PBPM fits on a simulated curve for each noise level. 97
5.7 Top-left: root mean square error (RMSE) distributions for the 400 AIF fits obtained from PBPM at each noise level. Top-right and bottom: distributions of estimation errors $\Pi_i - \hat{\Pi}_i, i = 1, 2, 3$. Blue boxplots represent the distributions of parameter estimates obtained using estimated nonlinear parameters for $\theta = (\alpha, \beta, \phi_1, \phi_2, \phi_3)$, whilst the orange shadow boxplots indicate those same distributions when the true values for the nonlinear parameters were used. . . . . 98
5.8 Distribution of 3-fold cross-validated AIF PBPM fit errors for varying training population sizes $n$. . . . . 99
5.9 Top: distribution of PBPM and individual leave-one-out cross-validated fit errors (respectively darker and lighter colored) at varying noise levels. Bottom: percentage difference between 'individual' and PBPM at medium noise level. . . . . 111
5.10 Top: Boxplot of 58 shifted arterially sampled AIFs. Bottom: Median of AIFs at each time point (empty circle) and P-spline smoothing of the medians with different values of smoothing parameter colored with red and violet blue. . . . . 112
5.11 Performance of fit on 500 simulation FDG- and $H_2O$-PET studies using BCM, TE, CTE and PBPM. . . . . 113

5.12 Model performance comparison for PBPM, TE, CTE and BCM on FDG (left) and $H_2O$ (right) PET simulation studies. Distributions of RMSE (5.10) for the two clinical cohorts (bottom) depict the relative fitting performance of the four models. . . . . 114
5.13 Top left: One example of clinical AIF; Top right: Simulated data and true data; Bottom left: Residuals of estimated curve to simulated one (black) and true one (red); Bottom right: Simulated data and fitted curve. . . . . 115
5.14 Top left: Example of a clinical AIF. Top right: Simulated data and true data. Bottom left: Residuals of estimated curve to simulated one (black) and true one (red). Bottom right: Simulated data and fitted curve. . . . . 116
5.15 Distribution of percentage errors in estimating parameters using BCM, CTE, TE, PBPM estimated AIF and the true clinical AIF. . 116
5.16 3D (top) and 2D (bottom) scatter plot of the fit MSE for simulated data at noise level 0.04 against $K_1$ and $k_2$. . . . . 117
5.17 Surface plot of the criterion $(z)$ with respect to re-parameterized parameters $P_1$ $(x)$ and $P_2$ $(y)$. . . . . 118
5.18 Model performance comparison for BCM, TE, CTE and PBPM on the FDG- (A), $H_2O$- (B) and FLT- (C) PET studies. Distributions of cross-validated errors (5.12) depict the relative fitting performance of the four models, and indicate that PBPM remains competitive for different tracers. . . . . 118
5.19 Comparison of cross-validated errors obtained when using a training population strategy to estimate the nonlinear parameters $\theta$ that determine the structure of the PBPM basis components (left), over a fully individual approach where the parametric vector $\theta$ is estimated directly from the same individual sampling data (right), showing a lower error tends to be achieved from a population-based strategy ($p < 0.0001$, one-sided paired Wilcoxon test). . . 119
5.20 Distributions of percentage errors in estimates of flow $K_1$ (top left) and $k_2$ (bottom left) parameters from 1C modelling of simulated $H_2O$ uptake data, and flux $K_i$ (centre top), distribution volume $V_D$ (centre bottom), $K_1$ (top right), and $k_2$ (bottom right) parameters from 2C modelling of simulated FDG uptake data, using respectively BCM, TE, CTE, PBPM AIF estimates, or the true AIF used in simulating the template curves. . . . . 120

6.1 Example of ROI-LV drawing on PET imaging data of LABCa patients from University of Washington (top) (Mankoff et al. 2002, 2003, Tseng et al. 2004, Dunnwald et al. 2008, 2011, O'Sullivan et al. 2017). Imaging data are processed in AMIDE (Loening & Gambhir 2003). Example of PBPM fit on ROI-LV FDG data (bottom left) and $H_2O$ data (bottom right). . . . . 124
6.2 Paired scatter plot of estimated linear coefficients from PBPM applying to arterially direct sampled data. . . . . 125

6.3 Distributions of PBPM fit errors (left), and of fit errors relative to the reference 62.5-minute fit (right), from the 58 FDG-PET SAIFs for varying scanning times. . . . . 126
6.4 Left: 91 FDG-PET directly-sampled AIFs (Green) and 53 image-extracted ROI-LVs (Pruple); Mid: Mean and 95% confidence interval of the data; Right: Distribution of estimated linear coefficients for third components. . . . . 127
6.5 One example fit of the extended PBPM. Spillover is the estimated linear coefficient for the extended term. . . . . 128

B.1 Manually drawn ROI from PET imaging data from AMIDE (Loening & Gambhir 2003), located in the patient's arm. . . . . B4
B.2 Mean and 95% confidence interval of TACs from ROIs at the injection, arm and right ventricle for 50 FDG-PET studies and a convolution between gamma and square wave with different widths (blue). . . . . B4
B.3 Mean of TACs from ROIs at the injection, arm and right ventricle 51 $H_2O$-PET studies and a convolution between gamma and square wave with different widths (blue). . . . . B6

D.1 Left: 91 arterially sampled FDG AIFs in grey dots, and one example in black; Right: TRPM fit on one example from that set. Black dots and line indicate sample and fit, respectively. . . . . D9
D.2 Performance of TRPM without penalty on 91 arterially sampled AIFs from FDG studies. . . . . D10
D.3 Distribution of estimated parameters from 91 FDG studies. . . . D12
D.4 Left: 39 arterially sampled AIFs from water studies in grey, and one example in black; Right: TRPM fit on one example from that set. Black dots and line indicate sample and fit, respectively. . . D13
D.5 Performance of TRPM without penalty on 39 Arterially sampled AIFs from water studies. . . . . D14
D.6 Distribution of estimated parameters from 39 water population data. . . . . D14
D.7 Principal components of scaled TRPM parameter estimates from directly sampled AIFs from FDG (left) and water (right) studies and their cumulative proportion of variance. . . . . D16

# List of Tables

2.1 Some commonly used radioisotopes in PET. . . . . 8

4.1 Mean (standard deviation) of estimated parameters using different methods (TRPM without the penalty term (Without), TRPM with the penalty term (With), and TRPM penalty for model parameter estimation (Penalty)) in water studies. . . . . 73

5.1 Top section: patient information in mean (sd) of 105 FDG, 39 $H_2O$ and 32 FLT studies (only 101 Weight and Height for FDG studies). Bottom section: median sampling durations and numbers of time points per tracer. . . . . 91
5.2 Fixed gamma and exponential parameters estimated from the FDG-PET cohort and used for simulation. . . . . 96
5.3 One-sided paired Wilcoxon test p-values for the cross-validated BCM, TE, CTE and PBPM MSEs of Fig. 5.18. The alternative hypotheses $H_A$ for these tests are provided to assist in interpreting the test outputs. Here $H_A$ is accepted at the 1% significance level for p-values lower than 0.01 (significant results in bold). . . . . 106

6.1 Mean and standard error of percentage errors ($i.e.\ 100\times\frac{actual-predict}{actual}\%$) fitting 58 SAIFs using reduced scanning times. . . . . 126

D.1 Principal component loadings for the FDG analysis. . . . . D15
D.2 Principal component loadings for the water analysis. . . . . D15

# List of Nomenclatures

$iid$ Independent and Identically Distributed

3D Three Dimension/Dimensional

AIF Arterial Input Function

AUC Area Under Curve

AVB Arterialised Venous Blood

B/I Bolus plus Continuous Infusion

BCM Whole Body Blood (Tracer) Circulation Model

BF Blood Flow

BP Binding Potential

BSA Body Surface Area

CAD Coronary Artery Disease

CLT Central Limit Theorem

CTE Convolved Tri-exponential Model

DoF Degree of Freedom

DUR Differential/Dose Uptake Ratio

FADS Factor Analysis of Dynamic Structures

FDG Fluorodeoxyglucose

FLT Fluorothymidine

FOV Field of View

GCV Generalized Cross Validation

ICA Independent Component Analysis

IDIF Image-derived Input Function

IRF Impulse Response Function

LABCa Locally Advanced Breast Cancer

LBM Lean Body Mass

LC Lumped Constant

LOOCV Leave-one-out Cross Validation

LOR Line of Response

MRGlc Metabolic Rate of Glucose

MSE Mean Squared Errors

MTT Mean Transit Time

nAIF Normalized Arterial Input Function

NBV Nalder Blood Volume

NF Normalized Factor

NLS Nonlinear Least Squares

PBIF Population-based Input Function

PBPM Population-Based Projection Model

PCA Principal Component Analysis

PDF Probability Density Function

PET Positron Emission Tomography

PVE Partial Volume Effect

QPP Quadratic Programing Problem

RC Recovery Coefficient

sAIF Sampled Arterial Input Function

SF Scale Factor

SP Spill-over Coefficient

SUR Standardized Uptake Ratio

SUV Standardized Uptake Value

TAC Time Active Curve

TE Tri-exponential Model

TRPM Travel-Rate Projection Model

VIF Venous Input Function

I, Zhaoyan Xiu, certify that this thesis is my own work and I have not obtained a degree in this university or elsewhere on the basis of the work submitted in this thesis.

*Zhaoyan Xiu*

To everyone

# Acknowledgements

I would like to express my sincerely gratitude to all those who helped me during the writing of this thesis.

My deepest gratitude goes first and foremost to Drs Jian Huang and Eric Wolsztynski, my supervisors, for their constant encouragement and guidance. They walked me through all the stages of the writing of this thesis. Without their consistent and illuminating instructions, this thesis could not have reached its present form.

Secondly, I wish to acknowledge Finbarr O'Sullivan's invaluable contribution in the early stages of this work. Finbarr provided critical insight about this topic and helped steer the initial phase of this project, especially for the work presented in Chapter 4. I also want to acknowledge the key importance of our collaboration with Mark Muzi at University of Washington, Seattle, especially in the later phase of this project. As a co-author of our paper on the Population-Based Projection Model developed in Chapter 5, Mark brought a wealth of clinical experience and expert knowledge to this work, along with a unique opportunity to develop and experiment our model on rich clinical datasets. These collaborations were key in bringing this work to its current standards.

Thirdly, I thank my peers Dr. Tian Mou, Fengyun Gu, Ran Ren, Qi Wu, Yuankun Hu, Tao Lan and Xiangyu Meng. We studied together. We worked together. And we helped each other work out problems.

Last but not the least, my thanks would go to my beloved family for their loving considerations and great confidence in me all through these years.

# Abstract

Kinetic modelling of dynamic PET data requires knowledge of tracer concentration in blood plasma, described by the arterial input function (AIF). Arterial blood sampling is the gold standard for AIF measurement, but is invasive and labour intensive. A number of methods have been proposed to accurately estimate the AIF directly from blood sampling and/or imaging data. In this work, we review some of the main methodologies for AIF estimation, and present two alternatives that aim at addressing some of their major limitations. We developed a tracer travel rate projection model as an early AIF modelling attempt based on tracer travel history in the circulatory system. A penalty was considered for model parameter estimation and we used arterially sampled data for evaluation. To improve on this first model, we developed a population-based projection model that exploits historical data to estimate individual AIFs. We represent the history of a tracer atom at a sampling site by its travel time, modeled as a sum of the time for the atom to initially progress from the injection site to the right ventricle of the heart, and the time it spends in circulation before being sampled. The former is modeled as a realization from a gamma distribution, whose parameters are common to all subjects in the population, and estimated from a collection of arterial sampling data for the given tracer. The latter is represented by a subject-specific linear mixture of these population profiles. This approach can be seen as a projection of individual AIF characteristics onto a basis of population profile components. It also incorporates knowledge of injection duration into the model fit, allowing for varying injection protocols. Analyses of arterial sampling data from $^{18}$F-FDG, $^{15}$O-$H_2O$ and $^{18}$F-FLT clinical studies show that the proposed model can outperform reference techniques. The statistically significant gain offered by using population data to train the basis components, as opposed to fitting these from the single individual sampling data, is measured on the FDG cohort. Kinetic analyses demonstrate the reliability and potential benefit of this approach in estimating physiological parameters. These results are further supported by numerical simulations that demonstrate convergence of the proposed technique with decreasing noise levels, and stable levels of performance under varying training population sizes and noise levels.

# Chapter 1

# Introduction

## 1.1 Motivation

Positron emission tomography (PET) is one of the main medical imaging modalities used for assessment and management of cancer and other complex diseases. Different from some commonly known imaging techniques such as computerized tomography (CT) and magnetic resonance imaging (MRI), PET allows monitoring of functional reactions to a specified tracer injected into a subject. Isotope labeled molecules of a specific substance, such as glucose, water, or another metabolic agent, quickly become absorbed in tissue. During this process, a pair of (gamma) photons are emitted in roughly opposite directions and captured by the detection ring of the scanner, to make a four-dimensional image as metabolization of the injected dose takes place. The output PET image thus renders the concentration of tracer in a particular region that can reflect the functional condition of the subject in terms of the type of tracer used. The concentration of tracer measured in data extracted from a particular region of interest (ROI) in the image can be used to derive physiological and physical parameters of the subject. PET imaging is a sophisticated modality that proposes significant technical and mathematical challenges, not only in creating the image from noisy signals, but also in analyzing the relationship between imaging data and disease characteristics.

PET can provide either 3-dimensional data in space or 4-dimensional data in space and time. For 4D data, dynamic studies of the tracer kinetics are possible. A variety of methods are developed to model tracer kinetics in the body. These usually require (approximate) knowledge of the concentration of tracer

in arterial blood over time, also called arterial input function (AIF), as it provides information of tracer availability in tissues and organs. In other words, when output, $i.e.$, the tracer's concentration in a region of interest is given, tracer input in that region is needed to estimate the parameters involved in the functional process related to the tracer in that particular region.

Given the AIF, kinetic modelling of the dynamic imaging data can be used to measure physiologic parameters, such as blood flow and glucose metabolic rate (Huang & Phelps 1986, Herscovitch et al. 1983, Raichle et al. 1983, Sokoloff et al. 1977). There exist techniques for estimating physiological parameters that do not require the AIF, such as reference region approaches for receptor-radioligand studies (Zanderigo et al. 2014). To be valid, these techniques require the existence of a measurable, reliable reference region that is devoid of the target receptor, and for comparisons to be appropriate, the reference region properties must be independent of treatment effects and groups (Zanderigo et al. 2014). A region meeting these criteria has not yet been identified, or might not exist, for many radioligands. AIF estimation therefore constitutes a realistic, intermediate objective for many applications of dynamic data analysis for the determination of metabolic processes.

Determination of the AIF is a challenging task. The gold standard and most accurate approach is to use direct arterial blood sampling, but this requires multiple arterial blood samples over the whole scanning period, and presents several drawbacks including patient discomfort, additional costs, and potential risk due to its invasive nature.

## 1.2 Main Objectives

Our group have access to sets of PET data from the University of Washington. These data include arterially sampled AIF and PET images that the AIF can be extracted from, but where no arterially sampled AIF and images are from a same subject. This work aims to identify and develop methods that can accurately and effectively estimate AIF in a statistical and noninvasive way. Its main objectives are to compare and test popular PET kinetic methods, develop a novel approach for AIF estimation that can accurately describe the AIF and improves upon existing techniques, and provide a proof of concept on typical clinical data. We also aim to create an open-source implementation of the suc-

cessful technique for other groups to avail of.

## 1.3 Outline and Contribution

Chapters 2 and 3 introduce the background to the problem and some existing solutions. Chapter 4 proposes a first modelling approach that is based on physical and physiological compartments inside the blood circulation system. Further work on this concept led to an alternative population-based projection model which is developed in Chapter 5. Results from numerical experiments and analyses on clinical data are also presented and discussed in that section. Chapter 6 closes this thesis with a summary of our contributions, and a discussion of opportunities for future work.

The contributions of this thesis are as follows:

1. A travel-rate projection model (TRPM) for AIF estimation is developed in Chapter 4. This model was presented at the Royal Statistics Society's Annual Meeting (2018). Despite a number of limitations when it comes to its application, this model provides a solid conceptual basis and theoretical support for a stronger model introduced in Chapter 5. The TRPM still has value for future research, since it can yield reasonable AIF estimates, leverages a representation of the blood circulation system within a human body, and is parameterized in a way to hold physical and physiological interpretation.

2. A population-based projection model (PBPM) for AIF estimation is developed in Chapter 5. This is the main contribution of this thesis, providing improved accuracy and flexibility over the TRPM. This contribution includes evaluation of the methodology with three different tracers. Our results demonstrate validity of this novel approach against existing models. A journal paper introducing this approach is under review at the time of writing. A pre-print also available on the IEEE TechRxiv (2022).

3. The PBPM is implemented in the open software R (R Core Team 2016), and published on Github (2020). Everyone is welcome to use and comment on it.

# Chapter 2

# Background to the Problem

## 2.1 Positron Emission Tomography

### 2.1.1 Introduction

Positron emission tomography (PET) is a nuclear medicine imaging modality that was developed in the mid-twentieth century. Over the past few decades, PET has become one of the most effective and powerful tools in the management of many diseases.

Compared to PET, computerized tomography (CT) and magnetic resonance imaging (MRI) may be better known by the general public as they are also routinely used in the treatment of physical injuries and many common conditions. Unlike PET, CT and MRI produce anatomical images at high resolutions, whereas PET is used to quantify functional and metabolic information. One of the limitations of PET is that it cannot locate the signals from the patient's body as accurately as CT and MR. Therefore, a PET image normally needs to be combined with CT or MR image for registration of signal location, and for attenuation correction during the PET image reconstruction. This can be achieved by PET/CT (see Fig.2.1 and Fig.2.2) or PET/MRI scans. Another significant aspect of PET imaging is that patients are exposed to radiation during and after a scan, potentially introducing the risk of triggering unnecessary side effects, and limiting achievable quality of the output image. Notwithstanding, PET has been proven effective in the treatment of certain diseases (Maisey 2005). Although CT and MR are widely used for many clinical purposes, PET has become key in diagnosing, treating and analyzing many types of cancer, especially.

Figure 2.1: Exterior of a PET/CT scanner from Siemens Biograph series.

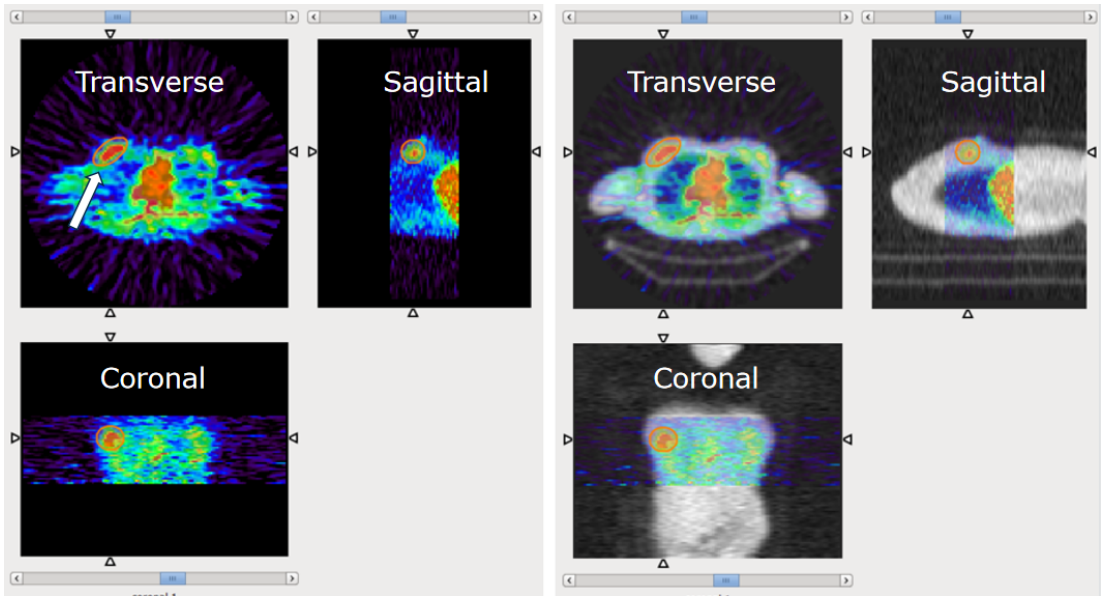


Figure 2.2: PET (left) and PET/CT (right) 3D images acquired on the GE Advance scanner at University of Washington from a sarcoma patient (Dunnwald et al. 2008) in transverse, coronal and sagittal views from AMIDE (Loening & Gambhir 2003). The tumor is marked by the ellipse ROI (region of interest) function in the software.

### 2.1.2 Physics in PET

The term *positron* was introduced by Carl D. Anderson (Wikipedia contributors 2018a) in 1932 when he first observed these subatomic particles, and this experimental observation proved the postulation about this unknown particle proposed by Paul A.M. Dirac (Wikipedia contributors 2018f) in 1928. This discovery won Nobel Prizes in Physics for each of these scientists in 1933 and 1936, respectively. A positron has the same mass as an electron, but it has a positive charge instead.

Depending on the aim of the study, the type of radioactive tracer to be used must be selected in the first place, and a tiny dose of this tracer will be introduced to the subject. Positrons are emitted inside the subject as radioactive tracer atoms decay triggering a reaction described by Eq. ((2.1)) where a proton ($p$) in a nucleus is transformed to a neutron ($n$), a positron ($\beta^+$) and a neutrino ($v$) (Bailey et al. 2005). The rate of decay of a given radionuclide is characterized by a parameter called half-life ($t_{\frac{1}{2}}$). For example, $^{18}$F-labeled fluorodeoxyglucose (FDG), the most common tracer for PET imaging of cancers, has a half-life of 109.7 minutes, which means that half of the total radionuclides are expected to decay in 109.7 minutes after they are produced. The synthesis of FDG for PET therefore needs to take place near enough to the scanning site. Radioactivity $A(t)$ left after time $t$ is a function of initial activity $A(0)$ and $t$ (see Eq. (2.2)). The decay constant $\lambda$ is inversely proportional to the half-life of the isotope (see Eq. (2.3)) (Bailey et al. 2005). The two common units of radioactivity are Becquerels ($Bq$) (1 decay per second), named after Henri Becquerel (Wikipedia contributors 2018c) and Curie ($Ci$) ($1nCi = 37Bq$) named after Marie Curie (Wikipedia contributors 2018e).

$$p \xrightarrow{\text{transforms}} n + \beta^+ + v \tag{2.1}$$

$$A(t) = A(0)e^{-\lambda t} \tag{2.2}$$

$$\lambda = \frac{ln(2)}{t_{\frac{1}{2}}} \tag{2.3}$$

After a positron is emitted, it will not travel far before hitting an electron, at which point mutual annihilation happens to the positron and the electron, and two gamma rays, also called photons, are produced with the same energy (511keV) and traveling in opposite directions (see Figure 2.3). The gamma rays have very high frequency which enables them to penetrate through the tissues. Detector rings are designed to collect the signals of these photons. A mathematical algorithm in the scanner is used to select and handle paired signals, and distinguish true events from random and scattered events. Random events are collected paired signals that are not emitted by the collision of a positron and an electron, and scattered events are paired signals produced by one collision, but where the direction of the gamma rays has been scattered due to particle

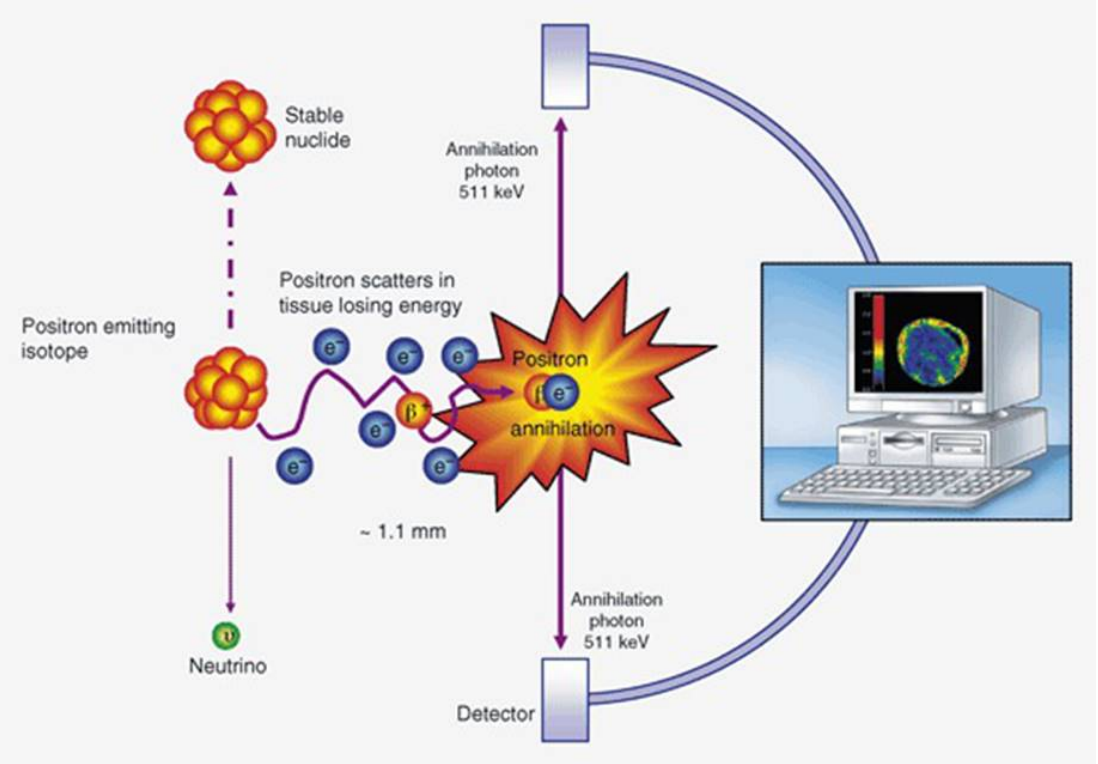


Figure 2.3: Physics in PET (JROGEL 2012).

collisions. The paired signals of interest are those signals coincidently collected by the detector whose trails are in a line, called line of response (LOR). The filtered signals will be saved as a sinogram and transformed into images that can reflect the concentration of tracer in the subject. A series of reconstruction and correction schemes must then take place to produce the output scan (Bailey et al. 2005).

### 2.1.3 Clinical Applications

PET imaging is used in various clinical applications. Three main areas are oncology, cardiology and neurology, although the primary use of PET is in oncology. Shortly after the $^{18}$F-FDG is introduced to the patient, glucose molecules arrive to cancer cells, gathering in the tumor, and their signals will be detected and imaged. Among all PET tracers, FDG is the most commonly used (over 90% of PET scans use FDG), and plays a crucial role in cancer diagnosis and management. Some examples of applications of PET in oncology are: staging and restaging, identifying a tumor site, differentiating malignant nodules from benign ones, *etc.*.

PET is also used to diagnose and study some heart diseases and brain disorders, *e.g.*, coronary artery disease (CAD) and dementia, by evaluating the glucose utilization, blood flow (BF), receptor binding, $etc.$ (Maisey 2005). Depending on the physiological parameters of interest for a disease, an increasing number of new radiotracers have been developed based on existing ligands. Some popular radioisotopes with their half-life are presented in Table 2.1. Taking brain studies into consideration, more than 100 radiotracers have been developed to target aggregated proteins, channels, enzymes, neuroreceptors and transporters (NIMH 2018).

Table 2.1: Some commonly used radioisotopes in PET.

| Radioisotope | Half-life (min) |
|---|---|
| $^{18}$F | 109.7 |
| $^{11}$C | 20.4 |
| $^{13}$N | 9.96 |
| $^{15}$O | 2.07 |
| $^{123}$I | 793.2 |

### 2.1.4 Steps in PET Imaging

Generally, PET imaging requires several steps, shown in Fig. 2.4. Firstly, the isotope ($e.g.$, $^{18}$F) is produced in a cyclotron by accelerating some previously defined particles (Sabbatini, R. M.E. 1997). The half-life of these isotopes is relatively short, less than two hours for $^{18}$F, which means these isotopes can not be stored for PET scanning. Radioactivity of isotopes will keep dropping after they are produced. Therefore, this isotope production process needs to take place just before the PET scan. The waiting time until isotope being injected into the patient needs to take the isotope's half-life into consideration. Also, this waiting time must be recorded as reference for calculation of remaining radioactivity. The isotope is then labeled on some biological molecule, say $^{18}$F on glucose molecules. The tracer then gets introduced into the patient mostly via intravenous injection, or for some tracers by gas inhalation or orally as a pill.

The patient is placed in the PET scanner where the target ROI should be in the field of view (FOV) of the detector ring. Patients are required not to move during scanning. A scan can be as short as minutes or last over one hour, mostly depending on the isotope half-life. A longer half-time usually allows for a longer

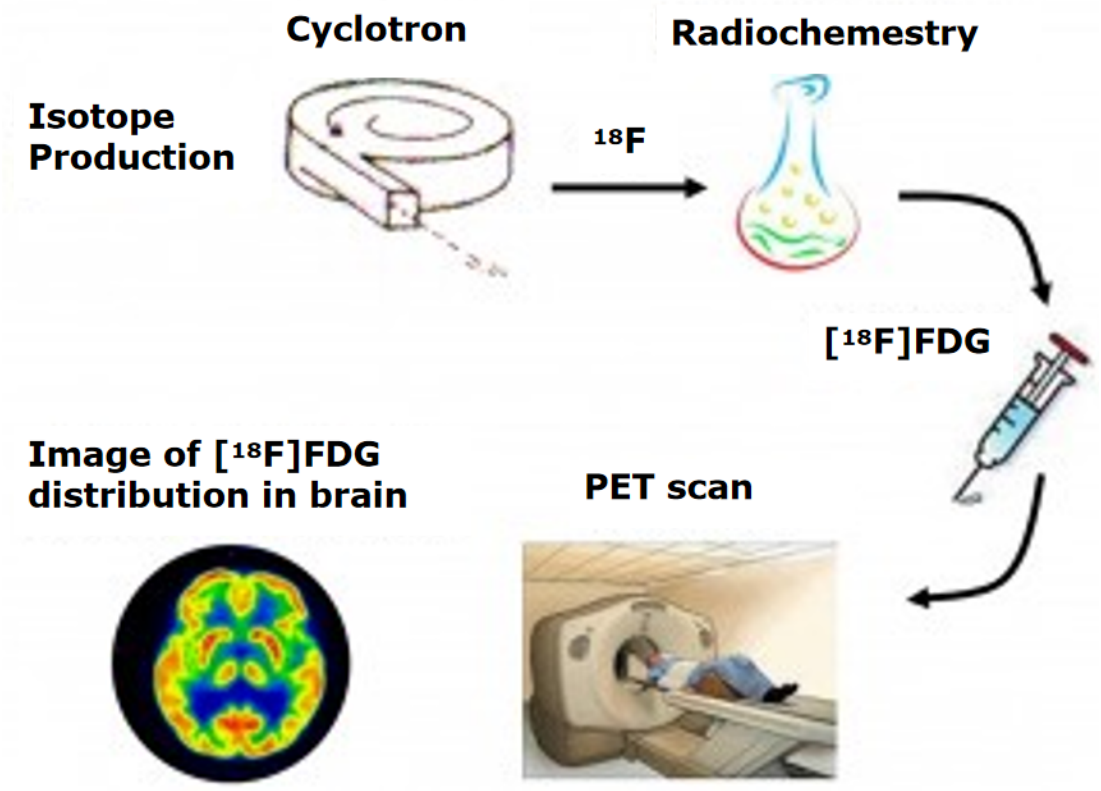


Figure 2.4: Steps in PET imaging (adapted from Turku BioImaging team 2018).

scanning time. A sampling time protocol is necessary for dynamic PET imaging, based on the decay time of the isotope and past experience of the time course of tracer concentration, also called time active curve (TAC), in target regions. More frequently sampling will take place during the period where the shape of the TAC changes comparatively faster (typically, early in the scanning time frame). Signals collected from the subject can be organized as sinograms, which are then reconstructed into images. Two common methods for reconstruction are filtered back-projection (FBP) and iterative reconstruction (detail in (Bailey et al. 2005)). In dynamic PET studies, 3-dimensional spatial time course data are produced. Information in the user-defined ROI can be extracted for further analysis. Both static and dynamic imaging can be performed. In this study we concern ourselves with the analysis of dynamic PET data.

## 2.2 Basic PET Data Analysis Techniques

Physical and physiological parameters can be derived from a dynamic PET scan to quantify characteristics of interest related to the condition of a patient at

the molecular level. To define these parameters, the connection between occurrence and development of the disease and any changes that it brings to the body of a patient need to be identified. In this section, some basic PET data analysis techniques developed to this end are introduced.

### 2.2.1 Static PET data

The TACs of a region or a volume of interest account for two factors: the physiological and biochemical parameters of the local tissue of the subject, and plasma concentration of the injected tracer. After injection, the tracer will travel in the blood throughout the body. Depending on the tracer used, PET may provide information on specific material exchange with local tissues and metabolism. These exchanges between blood and tissue can help characterize a patient's body condition. The plasma concentration of tracer over time, called the arterial input function (AIF) quantifies the availability of tracer concentration in a target tissue at a given time $t$. Assuming the AIF is given, the time courses in the ROI will only depend on the retention characteristics of tissue for the tracer. For example, in brain studies, FDG can be used to derive the cerebral metabolic rate of glucose (MRGlc) over time and $^{15}$O-water can be used for estimation of cerebral blood flow. There are a variety of models developed for description of the relationship between plasma and local tissue tracer concentration for different tracers.

In dynamic PET studies for most radiotracers, tracer concentration at an observation site is assumed to have a linear time-variance biological response to the injected dose, so that the TAC in a tissue region $C_T(t)$ can be expressed as a convolution between the AIF $C_P(t)$ and the tissue impulse response function (IRF) $R(t)$, also known as residue function (see Eq. (2.4) where $\circledast$ is defined to be a convolution symbol here and after)(Hawe et al. 2012, O'Sullivan et al. 2014), where $C_T(t)$ is measured as activity per unit of tissue volume ($cm^3$), $C_P(t)$ is measured as activity per unit blood volume ($ml$), and $R(t)$ is the normalized tissue residue function whose area under the curve (AUC) over the height-of-tail value (residue function at the end of the study) gives the mean transit time (MTT) of the tracer in tissue.

$$\begin{aligned} C_T(t) &= C_P(t) \circledast R(t) \\ C_T(t) &= \int_0^t R(t-s) C_P(s) ds \end{aligned} \tag{2.4}$$

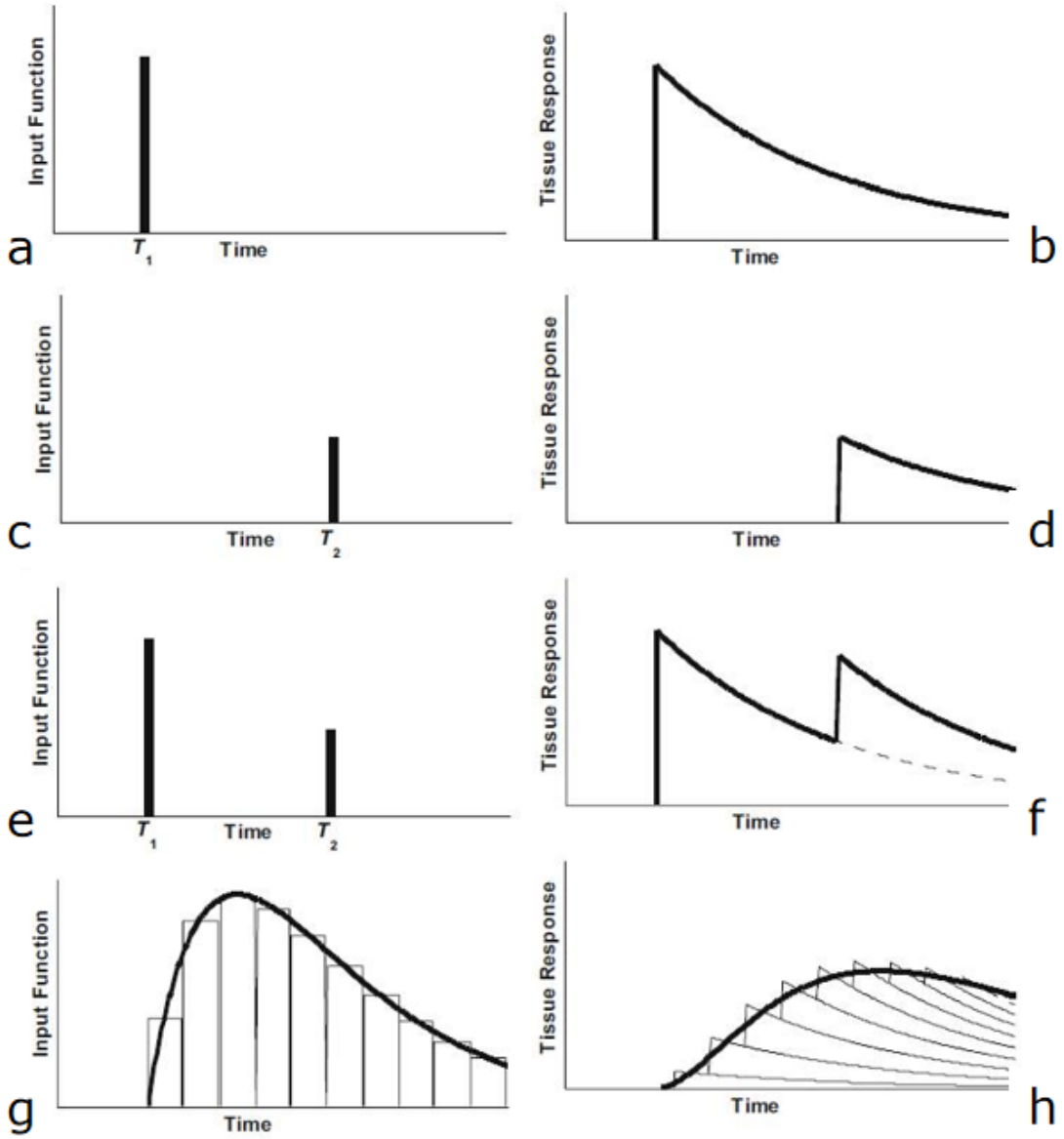


Figure 2.5: a, c, e, and g show the input functions that produce the tissue responses in b, d, f, and h, respectively (Bailey et al. 2005).

Fig. 2.5 gives a graphical interpretation of the convolution. When the input is an ideal bolus input, the corresponding tissue response is a function of a rapid rise followed by a exponential decrease. The tissue response is the summation of responses when there are multiple injections, and it is the integral when injection is a continuous input function. The measured data can not only be ROI data, but also voxel-level data (Tomasi et al. 2009, O'Sullivan et al. 2014). Our focus in this section will be set on ROI-based analysis.

In a target ROI, the measured activity contains signal from not only tissue, but also capillaries (see Eq. (2.5) where $C_I(t)$ is the TAC of radiotracer in ROI, and

$V_B$ is the unit of blood per unit volume of tissue):

$$C_I(t) = V_B C_P(t) + (1 - V_B) C_T(t) \tag{2.5}$$

This implies that physiological parameters, such as the distribution volume and local blood flow can be derived only if we have a thorough model or method to describe the physiological and physical exchange between capillarities and tissue. In other words, if we can define the residue function by the knowledge of the underlying physiological process that happens to a certain radiotracer in the target tissue, with the knowledge of time course data from the measured ROI and plasma supply of the tracer, the physiological parameter involved in the process can be estimated. Simple methods can provide some macro parameters. Here we introduce two semi-quantitative indices that can be easily calculated for routine clinical use.

#### 2.2.1.1 Standardized Uptake Value

Standardized uptake value (SUV), also called differential (or dose) uptake ratio (DUR) and standardized uptake ratio (SUR) in some literature, has been introduced to PET as a semi-quantitative index in oncology since the 1980s (Thie 2004). The SUV is a ratio of radiotracer concentration ($e.g.$ in $KBq/ml$) in a particular ROI to injection dose ($e.g.$ in $MBq$), and to a normalized factor (NF) which is based on some noninvasive characteristic information of the subject, $e.g.$, body weight (in $kg$), body surface area (BSA) (in $m^2$ (Bois & Bois 1916)) and lean body mass (LBM) (in $kg$ (Zasadny & Wahl 1993)) (Bertoldo et al. 2014a).

$$SUV = \frac{radiotracer\ concentration}{\frac{injection\ dose}{NF}} \tag{2.6}$$

The SUV can be simply, quickly and noninvasively acquired and applied for a wide range of radiotracers (Joseph A. Thie & Smith 2000). Generally, a higher SUV corresponds to a more tracer accumulative area. SUV calculation can be affected by factors ranging from the PET imaging techniques to evaluation time of SUV to characteristics of the subjects (Boellaard et al. 2004, Boellaard 2009). Thus, validation prior to the use of SUV is necessary. Also, since the SUV is a simple statistical summary, it can provide only limited information for estima-

tion of physiological parameters of the subject (Hamberg et al. 1994).

#### 2.2.1.2 Equilibrium Analysis

Equilibrium analysis is another single-scan method. It is used mostly for reversible ligand-receptor studies. In a ligand-receptor study, when the radioactive ligand reaches the target tissue, it has potential to bind with the receptor. A physiological parameter of interest called binding potential ($BP$) is used to describe the exchange between ligand and receptor in this reversible process. $BP$ can be derived from 3-compartmental modelling (Mintun et al. 1984) (introduced in the next subsection), but equilibrium methods for estimating $BP$ are preferred in routine use since they do not require knowledge of the AIF, which is not always feasible, and they also have considerable accuracy (Ito et al. 1998). Here we should note that $BP$ is actually $BP_{ND}$, where $ND$ is short for “non-displaceable". After ligands pass from the capillarities into tissue, they are called non-displaceable before specific binding.

Transient equilibrium is a moment where the binding reaches its maximum rate. To define the time of this moment, another tissue without receptor is chosen in the first place (see Fig. 2.6). The putamen is a target tissue, and the cerebellum is a receptor-free tissue. Then the difference between radioactivity in the two regions is the radioactivity of reference tissue or the specific binding concentration of tracers. $BP_{ND}$ is estimated by the ratio between concentration of tracer in target region and in the reference tissue (Ito et al. 1998):

$$BP_{ND} = \frac{C_T(t_{equil})}{C_{ref}(t_{equil})} \tag{2.7}$$

The true equilibrium can be produced using continuous infusion (Carson et al. 1993, Laruelle 2000). To hasten the steady state, tracer can be administered as a combination of bolus plus continuous infusion (B/I) (Kao et al. 1996). The total volume of distribution ($V_T$) can be estimated at true equilibrium by the ratio between tracer concentration in tissue and in plasma (2.8)) (Lassen 1992):

$$V_T = \frac{C_T(t_{equil})}{C_P(t_{equil})} \tag{2.8}$$

When the reference tissue is not available, $V_T$ is an alternative for $BP_{ND}$ as an

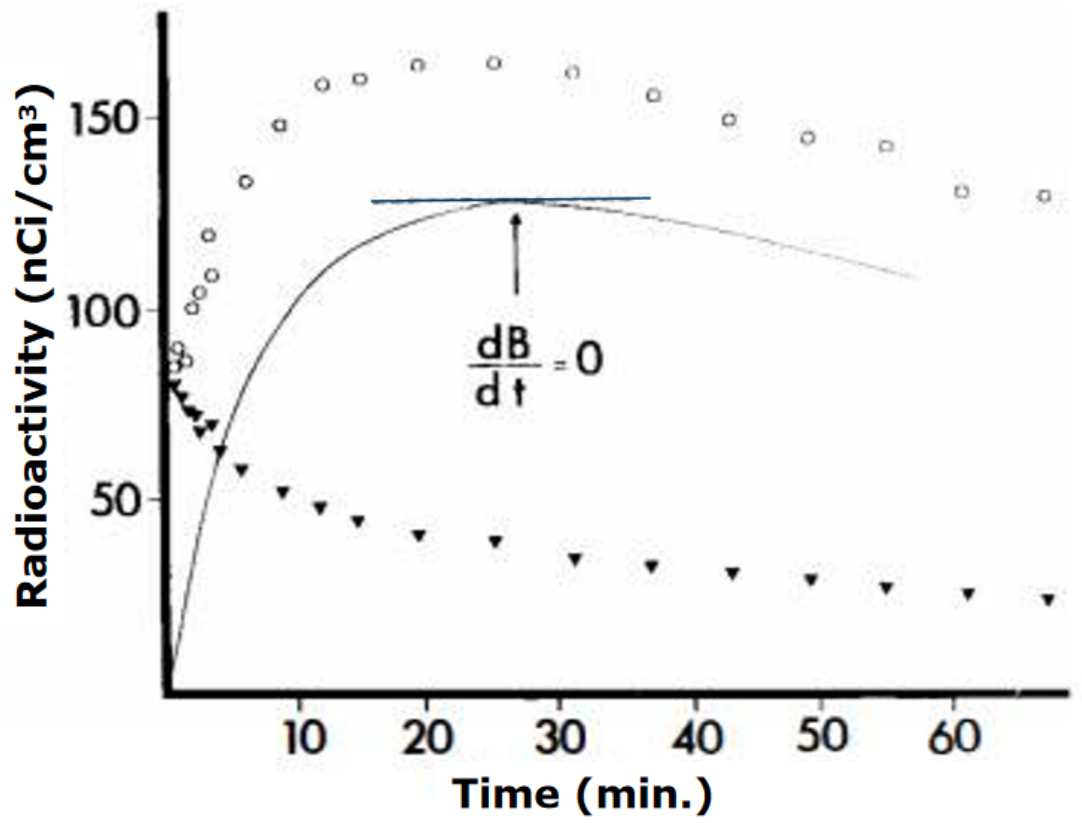


Figure 2.6: Points and solid triangles are measured values in the putamen and cerebellum in a healthy subject, respectively. Concentration in the reference region is estimated by the difference between two measured values and fitted to a solid line by a set of three exponentials. Equilibrium is defined to happen at the maximum of the fitted curve (Farde et al. 1989).

interpretive ratio. $V_T$ indicates the capacity of local tissue for tracer uptake, but it is more robust than SUV, since the calculation does not need injection dose and information of the patients. B/I can also be used to evaluate pre- and post-intervention binding levels by administering a stimulus during the infusion (Carson et al. 1997). A limitation is that a standard protocol for B/I may not be optimal under all circumstances which can cause bias for certain individuals (Endres & Carson 1998).

Although it is easier and quicker to analyze static PET data, the information they contain restricts the analysis to spatial and structural characterization. To make the best use of four dimensional PET data, a variety of mathematical models were built for tracer kinetics in the ROI. These methods broaden the range of statistical parameters.

## 2.2.2 Tracer Kinetics

### 2.2.2.1 Compartmental Models

Among all tracer kinetic methods for dynamic PET, compartmental modelling is the most commonly used method for analyzing physiological and biochemical exchanges of radiotracer in blood and tissues (Anderson 1983, Huang & Phelps 1986). The most popular compartment models are one-tissue compartmental models developed for quantifying blood perfusion using $^{15}$O-water (Kety & Schmidt 1948), and two-tissue compartmental models first developed for the measurement of local cerebral glucose utilization using $^{14}$C-deoxyglucose (Sokoloff et al. 1977) and $^{18}$F-FDG (Phelps et al. 1979). Two-tissue compartmental models are also widely used for ligand-receptor assessment (Mintun et al. 1984) (see Fig. 2.7). The principle of compartmental models is to define the compartments as distinct states that the radiotracer can stay in. The states can be set either in terms of physical locations ($i.e.$ intra- and extra- vascular space, intra- and extra- cellular space, $etc.$) or biochemical forms of the tracer ($i.e.$ before and after metabolism, before and after binding to the receptor, $etc.$).

Since the AIF is normally assumed to be known, intra-vascular space is always set as one compartment. In Fig. 2.7, the rate constants between different states have units of $ml/cm^3/min$ for $K_1$ and $min^{-1}$ for $k_2$, $k_3$ and $k_4$. $K_1$ is the perfusion rate of tracer passing trough the capillarity to tissue, and the others are percentage rates of tracer transforming from one compartment to another. For model A, $C_1(t)$ is the concentration of radiotracer in the form of FDG staying in tissue, and $C_2(t)$ is the concentration of radiotracer in the form of FDG-6-$PO_4$, which is the metabolite of FDG under enzyme action (hexokinase). The reverse of this metabolic process needs phosphatase, which is absent in many regions of the body; therefore, the minimal reverse rate is negligible. The rate of FDG-6-$PO_4$ to be dephosphorylated cannot be ignored when it is considerable in some regions (Phelps et al. 1979). Model B is a simple one-compartmental model that suits the PET water ($i.e.$ $H_2O$) studies, since water will not be involved in any tissue metabolism or functioning. Thus, water is valuable for $in-vivo$ estimation of local blood flow (Frackowiak et al. 1980). Model C is mostly for ligand-receptor analysis. $C_1(t)$ here is the concentration of radiotracer that is nondisplaceable in tissue, and $C_2(t)$ is the concentration of tracer that has specific binding to the receptor. Some important parameters that can be expressed as combinations of microparameters are presented in Fig.

2.7 as well.

Taking a two-tissue compartmental model with four rates for FDG PET as an example (Model A in Fig. 2.7 with reversible metabolism), the first order derivative of the concentration of radiotracer in tissue compartments can be defined by the rate constants and the concentrations of radiotracer in other compartments:

$$\begin{aligned} \frac{dC_1(t)}{dt} &= K_1 C_P(t) - (k_2 + k_3) C_1(t) + k_4 C_2(t) \\ \frac{dC_2(t)}{dt} &= K_3 C_1(t) - k_4 C_2(t) \end{aligned} \tag{2.9}$$

Then the regional MRGlc can be estimated as:

$$MRGlc = \frac{C_{glc}}{LC} K \tag{2.10}$$

$$K = \frac{K_1 k_3}{k_2 + k_3} \tag{2.11}$$

where $C_{glc}$ is the concentration of glucose in plasma, LC (lumped constant) is a ratio that is used to transform the FDG uptake rate to glucose uptake rate, and K is the uptake rate of FDG (Phelps et al. 1979).

$C_{glc}$ and LC are considered to be constant in a single PET experiment. Having the AIF and TAC of radiotracer extracted from ROI, if only $C_T(t)$ in Eq. (2.5) is considered here ($i.e.\ C_I(t) = C_T(t)$), we have the following expression of TAC in a target tissue:

$$C_I(t) = C_1(t) + C_2(t) \tag{2.12}$$

By solving Eq. (2.9), the microparameters ($k_i$'s) can be estimated, and hence likewise the macroparameters. The estimating process involves Laplace transform techniques and least squares approach (Zaidi 2006). Then the residue function can be derived from these estimations (Hawe et al. 2012). Here, we omit the calculation part, since it is computationally elaborate (Zeng et al. 2012) and not of interest for now. According to the derivation in (Phelps et al. 1979), $C_1(t)$ and $C_2(t)$ can be expressed as

$$\begin{aligned} C_1(t) &= \frac{K_1}{A_1 - A_2}[(k_4 - A_1)e^{-A_1 t} + (A_2 - k_4)e^{-A_2 t}] \circledast C_P(t) \\ C_2(t) &= \frac{K_1 k_3}{A_2 - A_1}(e^{-A_1 t} - e^{-A_2 t}) \circledast C_P(t) \end{aligned} \tag{2.13}$$

where

$$\begin{aligned} A_1 &= [k_2 + k_3 + k_4 - \sqrt{(k_2 + k_3 + k_4)^2 - 4k_2 k_4}]/2 \\ A_2 &= [k_2 + k_3 + k_4 + \sqrt{(k_2 + k_3 + k_4)^2 - 4k_2 k_4}]/2 \end{aligned} \tag{2.14}$$

Thus $C_I(t)$ can be estimated by

$$C_I(t) = \frac{K_1}{A_2 - A_1}[(k_3 + k_4 - A_1)e^{-A_1 t} + (A_2 - k_3 - k_4)e^{A_2 t}] \circledast C_P(t) \tag{2.15}$$

In the irreversible situation ($i.e.\ k_4 = 0$), Eq. (2.14) becomes

$$A_1 = 0,\ A_2 = k_2 + k_3 \tag{2.16}$$

and $C_I(t)$ can be simplified into

$$C_I(t) = \frac{K_1}{k_2 + k_3}[k_3 + k_2 e^{-(k_2 + k_3)t}] \circledast C_P(t) \tag{2.17}$$

An extended use of compartmental modelling is to directly apply it to imaging data (Feng et al. 1997) or a sinogram (Yetik & Qi 2006) for estimation of physiological parameters without information of AIF. Generally, the AIF is needed for compartmental approaches. The development of compartmental models not only provides us with a special way to interpret a residue function, but also leads us to a series of simple graphical methods for dynamic PET quantification.

#### 2.2.2.2 Graphical Methods

Graphical methods use transformed data to provide a new relationship ($i.e.$ linear) between them and TACs of interest in the ROI, and estimate physiological parameters of interest. These parameters can be estimated by the slope or intercept of a fitted line or curve at or after a certain time. Two popular methods

Figure 2.7: Three most commonly used compartmental models and macro-parameters of interest (Bertoldo et al. 2014a).

are the Patlak plot (Patlak et al. 1983) and Logan plot (Logan et al. 1990) (see Figure 2.8).

**2.2.2.2.1 The Patlak plot** was developed to approximate uptake rates of FDG (K) in Eq. (2.11) for irreversible tracers ($i.e.\ k_4 = 0$) (Patlak et al. 1983). With this approach, Eq. (2.17) can be written as

$$C_I(t) = \frac{K_1 k_3}{k_2 + k_3} \int_0^t C_P(s)ds + \frac{K_1 k_2}{k_2 + k_3} \int_0^t C_P(s) e^{-(k_2+k_3)(t-s)} ds \tag{2.18}$$

As $(k_2 + k_3)t$ increases with $t$, the exponential term in Eq. (2.18) will fade as study continues, and the convolution term approaches to $C_P(t)$. Then Eq. (2.18) can be written as

$$C_I(t) \approx K \int_0^t C_P(s)ds + W C_P(t) \tag{2.19}$$

where

$$W = \frac{K_1 k_2}{(k_2 + k_3)^2} \tag{2.20}$$

Dividing $C_P(t)$ on both sides of Eq. (2.19), yields

$$\frac{C_I(t)}{C_P(t)} = K \frac{\int_0^t C_P(s)ds}{C_P(t)} + W \tag{2.21}$$

Eq. (2.21) defines the Patlak method. As shown in Fig. 2.8 A, only two sampling points after time $t^*$ are sufficient for estimation of the slope ($i.e.$ the FDG uptake rate) (Patlak et al. 1983).

**2.2.2.2.2 The Logan plot** is used to estimate the total volume of distribution ($V_T$) for reversible tracers (Logan et al. 1990). It can be derived from a one-tissue compartmental model as shown in Fig. 2.7 Model B, $i.e.$

$$\begin{aligned} \frac{dC_I(t)}{dt} &= K_1 C_P(t) - k_2 C_I(t) \\ C_I(t) &= K_1 \int_0^t C_P(s)ds - k_2 \int_0^t C_I(s)ds \end{aligned} \tag{2.22}$$

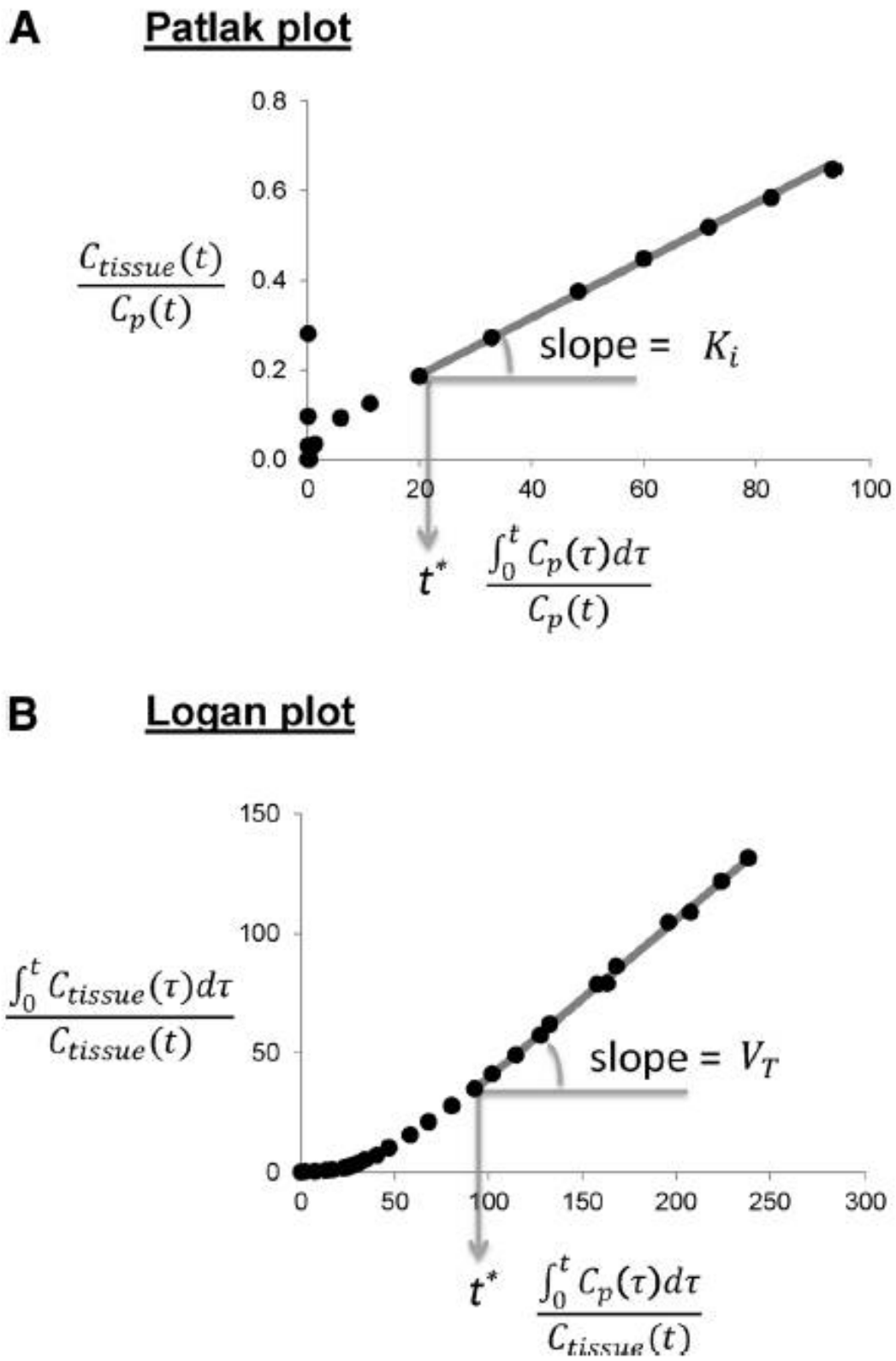


Figure 2.8: An example of a Patlak plot (A) and a Logan plot (B), with an irreversible ([$^{18}$F]FDG) and a reversible ([$^{11}$C](R)-rolipram) tracer, respectively. The data appear to reach a straight line after time $t^*$. The slope of each line is an approximation of $K$ and $V_T$, respectively (Bertoldo et al. 2014a).

Dividing $k_2$ and $C_I(t)$ on both sides of the integrated equation in Eq. (2.22) and rearranging, we get

$$\frac{\int_0^t C_I(s)ds}{C_I(t)} = V_T \frac{\int_0^t C_P(s)ds}{C_I(t)} - \frac{1}{k_2} \tag{2.23}$$

This is the equation used in the Logan plot. As shown in Fig. 2.8 B, the slope is an approximation of $V_T$. The time at which equilibrium is achieved ($t^*$) needs to be predefined for different regions and radiotracers. Similarly to the Patlak method, only two sampling points are need for estimation of the slope of the straight line (Logan et al. 1990).

The simplicity of graphical methods has promoted their use as routine clinical tools. However, the definition of $t^*$, the optimal data acquisition protocol, and a full understanding of the data are essential for their application (Choi et al. 1991, Logan et al. 2001, Kimura et al. 2007).

#### 2.2.2.3 Spectral Analysis

Spectral analysis was introduced to dynamic PET as a non-parametric technique for describing the tissue response given the AIF and ROI data without any prior assumptions on the number of compartments or components (Cunningham & Jones 1993). The measured concentration of radiotracer in the ROI is modelled as a convolution between the AIF and a sum of $k$ exponential terms as follow:

$$C_T(t) = \sum_{j=1}^{k} C_P(t) \circledast \alpha_j \cdot e^{-\beta_j t} \tag{2.24}$$

where the $\alpha_j$'s and $\beta_j$'s ($\beta_1 < \beta_2 < \cdots < \beta_k$) are assumed to be real-valued and nonnegative, and $k$ is the maximum number of components, and typically set to be large (say $k > 100$). The $\beta_j$'s are predefined based on past experience. And the $\alpha_j$'s are estimated by a nonnegative least squares approach (Lawson & Hanson 1974). The example of Fig. 2.9 provides an interpretation of a spectral analysis, where each component corresponds to one point in the kinetic spectrum and one time course curve as the convolution between the AIF and component ($i.e.\ C_P(t) \circledast \alpha_j \cdot e^{-\beta_j t}$). The estimated parameters also correspond to rate constants in compartmental models and physiological parameters of local tissue (Veronese et al. 2016). Development and limitations of spectral methods

are also introduced in the review paper (Veronese et al. 2016). Main limitations can be categorized as the problem caused by nonnegative constraints on the parameters in the model, computational complexity of the estimation procedure, and the necessity of a given AIF. AIF estimation methodologies are discussed in the next chapter.

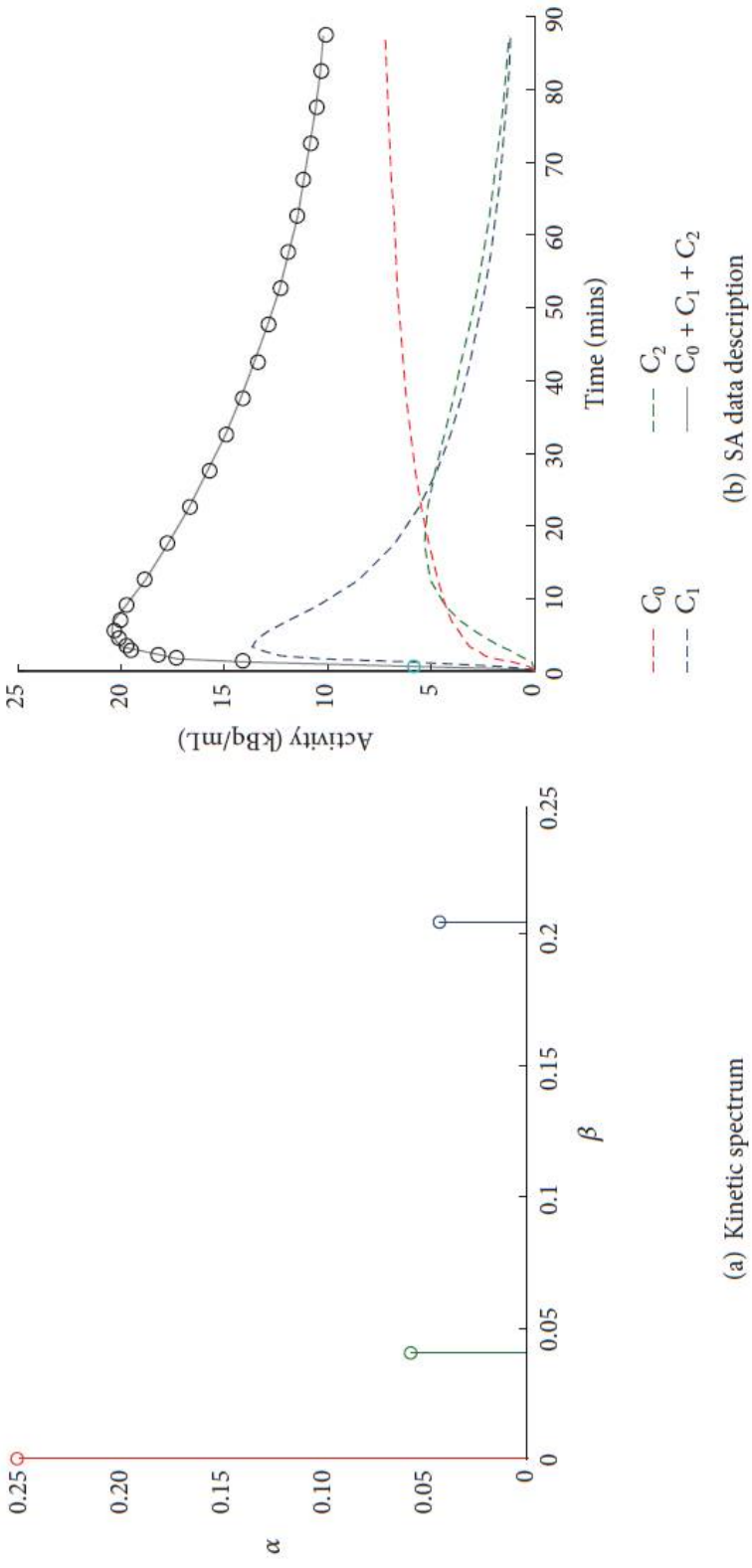


Figure 2.9: Example of spectral analysis quantification. (a) Kinetic spectrum indicates three components are reported including one with $\beta = 0$ (in red). (b) Corresponding curves of concentration are presented in dashed lines, and summation of the curves is performed (solid line) to obtain the final fit (Veronese et al. 2016).

# Chapter 3

# AIF Estimation Methods

AIF estimation plays a fundamental role in most kinetic methodologies, as dynamic PET studies require knowledge of the AIF (Sokoloff et al. 1977, Patlak et al. 1983, Kato et al. 1984, Logan et al. 1990, Cunningham & Jones 1993, Bailey et al. 2005). Directly sampled AIF is the gold standard as it can provide the concentration of radiotracer in plasma by direct calculation. However it needs intra-arterial cannulation during the PET scan (Spence et al. 1998, Syvanen et al. 2006a) and protocols for blood sampling and handling (Graham & Lewellen 1993). This makes the sampling process not only invasive for the subject, but also laborious and costly to the hospital or research center (Clark & Kruse 1992). Thus, directly sampled AIF is not always feasible in many PET centers (Eberl et al. 1997). Although the amount of blood sampling can be reduced, noninvasive alternatives need to be developed to avoid arterial cannulation (Kato et al. 1984). Some popular methods are introduced in this section.

## 3.1 Image-derived Input Function Estimation

Image-derived input functions (IDIF)(Chen et al. 1998, Laforest et al. 2005, Kim et al. 2006, O'Sullivan et al. 2009, Croteau et al. 2010, Zanotti-Fregonara et al. 2011, Fung & Carson 2013, Sari et al. 2017) are obtained by fitting an AIF model to arterial blood pool tracer activity extracted from PET image data, rather than obtained from arterial sampling. Such data are usually extracted from a region of interest (ROI) within a dynamic PET image (see Fig. 3.1) that requires either a large blood vessel or the left cardiac ventricle in the field of

view (FOV) that the time active curve (TAC) of concentration of radiotracer in arterial blood can be easily extracted (Choi et al. 1991), and therefore tend to be noisier. However, for brain studies, no such big pools are available. Carotid arteries are intracranial arterial blood pools that are frequently used in the literature (Chen et al. 1998, Zanotti-Fregonara et al. 2011, 2012, Bertran et al. 2016, Sari et al. 2017). This method usually requires three main steps: locating the carotid artery, correcting the partial volume effect (PVE) and spillover, and separating radioligand from radiometabolites (Zanotti-Fregonara et al. 2011).

Usually, the average or the highest signals in the ROI are extracted to obtain a time course to characterize the concentration of tracer in arterial blood. IDIF approaches may also require at least one physical blood sample to scale the image-derived AIF curve, and may include tracer uptake information both before and after tracer metabolism. Alternatively, PET signals from multiple regions (not necessarily arterial blood pools) may be leveraged to recover AIF and thereby kinetic parameters, via simultaneous estimation of the input function (Ogden et al. 2010).

The first step can be easily achieved by collecting all the voxel values within the ROI of carotid arteries, and locating voxels that have a relatively high concentration of radiotracer (Chen et al. 1998, Croteau et al. 2010). For the second step, PVE is due to the contamination of tracer signals from surrounding tissue, and spill-out from blood to tissue. The relationship between TAC measured from ROI and spillover-free AIF is

$$C_{carotid}(t) = RC \cdot C_P(t) + SP \cdot C_T(t) \tag{3.1}$$

where the $C_{carotid}(t)$ is the measured TAC, $C_P(t)$ and $C_T(t)$ are the true concentrations of radiotracer in blood and surrounding tissue, respectively, and RC and SP are recovery and spillover coefficients that are both nonnegative and independent of time. TACs in Eq. (3.1) at a given time protocol can be obtainable from blood free multiple ROI image extracting and analyzing techniques (Croteau et al. 2010). Then a linear least squares approach can be used to derive the coefficients. Step three involves biochemical information depending on the selected radiotracer and the subject which cannot be acquired from the image. This means that IDIF techniques normally require several blood samples to estimate the rate of metabolites within blood (Sanabria-Bohórquez et al. 2003). To conclude, IDIF cannot avoid blood sampling, despite the need for blood sam-

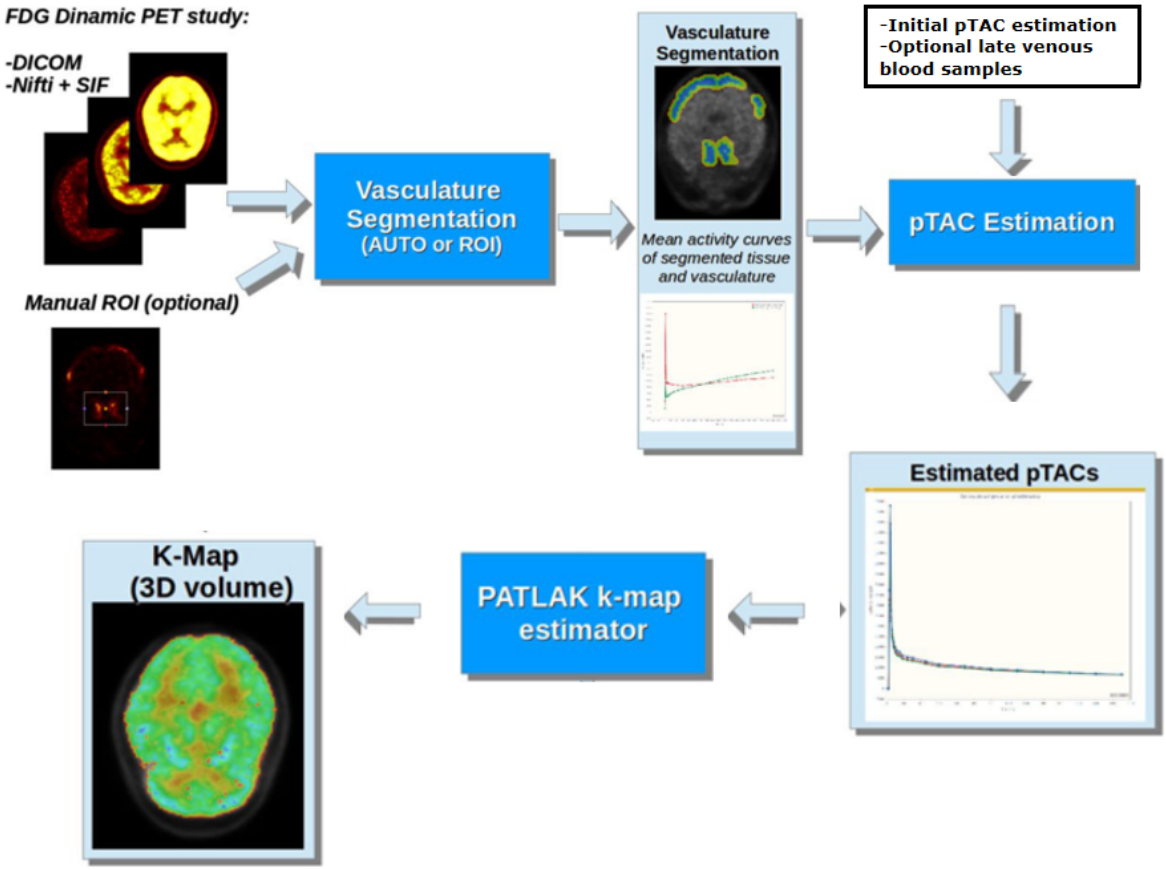


Figure 3.1: Block diagram of one free quantification tool for AIF (adapted from Bertran et al. 2016).

ples in step three, and the correction in step two without the information of true blood samples can be sensitive to the technique (Zanotti-Fregonara et al. 2011, Zhou et al. 2012).

### 3.1.1 Segmentation Methods

Although an ROI can be easily drawn for IDIF modelling, its accuracy and reliability need to be further validated. Segmentation is an automatic way to create ROIs based on voxel level in high dimensional data (O'Sullivan 1993, Wong et al. 2002, O'Sullivan 2005, O'Sullivan et al. 2010). For a brain study, where an ROI for the carotid artery is hard to define, segmentation methods are especially useful for AIF extraction. Even with large blood pools like the left ventricle in the FOV, the signals can be contaminated by the adjacent tissue ($i.e.$ myocardium). The overlapped signals may cause bias in AIF estimation when appropriate correction is not applied. Segmentation methods can be used to

separate the signals of tracers in blood from the ones in other structures.

The signal measured in each voxel is defined as $z_x(t)$, where $x$ represents the coordinate of each voxel and $t$ is the time of sampling. Then the signals can be categorized into different components, each with its own characteristics. The total signal can be calculated by summation of weighted TACs from a number J of such components (O'Sullivan 2005)

$$z_x(t) = \sum_{j=1}^{J} w_{x,j} C_j(t) + \epsilon_x(t) \tag{3.2}$$

where the $C_j(t)$ is the TAC for the $j$th characterized component, $w_{x,j}$ is the weight for each TAC at each location, and $\epsilon_x(t)$ is the deviation for each estimate, which is assumed to be random and with mean zero.

Hereafter we introduce some popular methods for estimation of these components.

#### 3.1.1.1 Cluster Analysis

Cluster analysis is a method consisting in dividing the signals into clusters. It is generally used to represent a series of points in the Euclidean space by some cluster centroids. One simple candidate for clustering is K-means (Bottou & Bengio 1995). Assuming TACs in each pixel ($i.e.$ $z_x(t)$) are represented as one point in Euclidean space, for each given $L$ ($i.e.$ $L = 1, 2, \ldots, 10$), $L$ cluster centroids can be easily calculated by iteratively attributing all points to their nearest cluster and redefining the new centres by averaging the points assigned to the cluster. Initially, $L$ clusters are randomly selected. Noting that each point is actually a vector, then a new centre is calculated by

$$\kappa_l^{h+1}(t) = \frac{1}{N(\kappa_l)} \sum_{x \in \kappa_l} z_x(t) \tag{3.3}$$

where $\kappa_l^{h+1}(t)$ is the centre of the $l$th cluster at the $h+1$th iteration, $\kappa_l$ is defined as the $l$th cluster, which includes all points nearest to $\kappa_l^h(t)$, and $N(\kappa_l)$ is the number of such points at the $i$th iteration. With the within-clusters variance converging, we will finally obtain $L$ cluster centroids. One of them is an estimation of normalized plasma TAC (Liptrot et al. 2004).

#### 3.1.1.2 Factor Analysis of Dynamic Structures

Factor analysis of dynamic structures (FADS) is one of the most widely used segmentation methods. It uses principal component analysis (PCA) (Barber 1980) to find the components which components that capture the most information in the data, and applies an iterative algorithm to rotate the components to constrain the weights and TACs in Eq. 3.2 to be nonnegative (physiologically meaningful factors cannot be negative) (Wu et al. 1995). Since the AIF will have distinct characteristics from the TAC in tissue or venous blood, it can be distinguished as one of the components. In a canine $^{13}$N-ammonia PET dynamic study, TACs in left and right ventricular blood pools and in the myocardium were found to account for 95% of the total variance of the data (Wu et al. 1995).

The oblique transformation for rotating the components is argued to result in non-unique estimates of nonnegative components (Houston 1984). To resolve this issue, prior assumptions of the anatomical structure are necessary (Naganawa et al. 2005).

#### 3.1.1.3 Independent Component Analysis

Independent component analysis (ICA) does not require any anatomical assumptions, but it requires at most one Gaussian distributed component (Hyvarinen & Oja 1997). ICA searches for components representing spatial distribution of TACS ($i.e.$ tissue blood volume) that are independent. In this framework, Eq. (3.4) represents tracer signals over time in each voxel ($i.e.\ z_x(t)$):

$$z_x(t) = w_P(x)C_P(t) + w_T(x)C_T(t) \tag{3.4}$$

where $w_P(x)$ and $w_T(x)$ are independent components at location $x$, and $C_P(t)$ and $C_T(t)$ are TAC in plasma and tissue, respectively (Naganawa et al. 2005). Fig. 3.2 presents a general ICA procedure. FastICA (Hyvarinen & Oja 1997), EPICA (Naganawa et al. 2005) are methods for performing ICA, and MAX-ICA and VEN-ICA (Chen et al. 2007) are for correction of PVE and spillover.

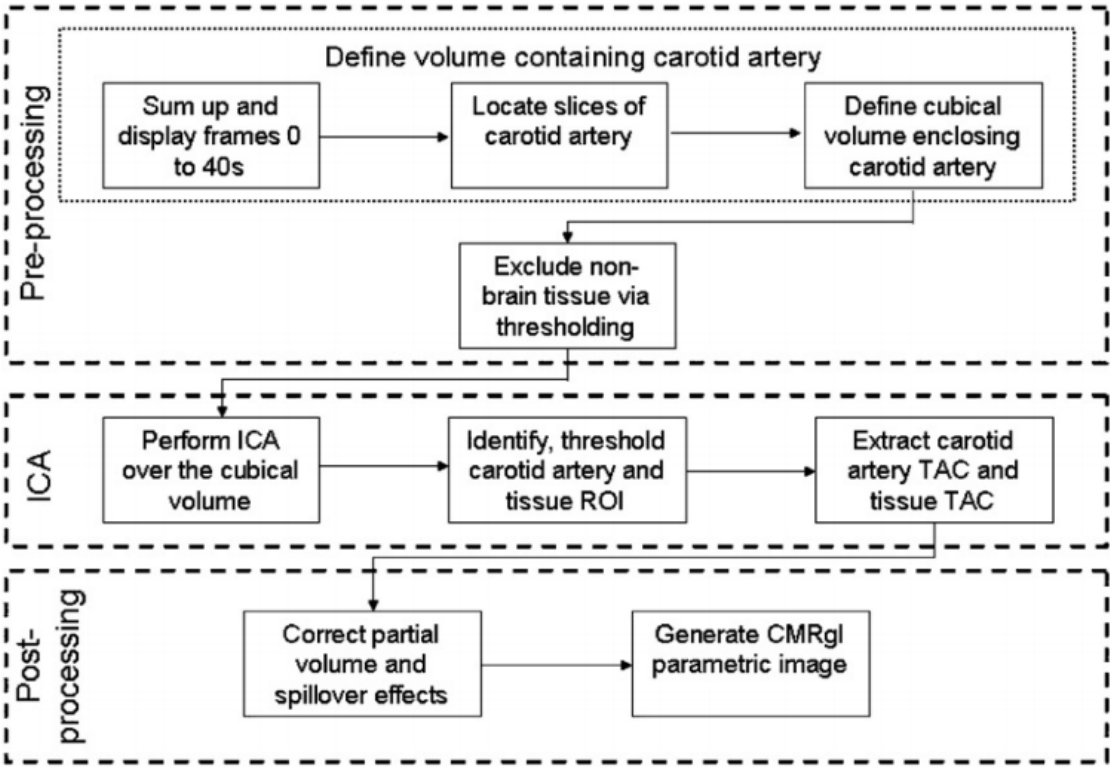


Figure 3.2: Flowchart of the ICA procedure for generating IDIF and MRGlc (Chen et al. 2007).

### 3.1.2 Simultaneous Estimation

Simultaneous Estimation of input function (SIME) is another potential noninvasive alternative for deriving AIF (Zanotti-Fregonara et al. 2011). TACs in one ROI can be modelled as a convolution between the AIF and IRF (recall Eq. (2.4) and Eq. (2.5)). For FDG PET studies, considering a four-parameter two-tissue compartmental model, TACs from different ROIs in the PET image can be modelled as convolutions between the AIF (Feng's model Eq. (3.6)) and a function of $K_1$, $k_2$, $k_3$ and $k_4$ (see Fig. 3.3 and Eq. (2.13)). In a given region, the AIF and IRF can not be determined simultaneously, and one of the two functions at least needs to be defined. However, with the information from multiples regions, AIF and IRF can be estimated at the same time (Feng et al. 1997). A nonlinear least squares approach is used to optimize the cost function with high dimensional parameters (Levenberg 1944).

Two or more regions are needed for the SIME approach (Koon-Pong Wong; Feng 2001), and at least one venous blood sample is needed as an alternative to arterial blood (Guo et al. 2007).

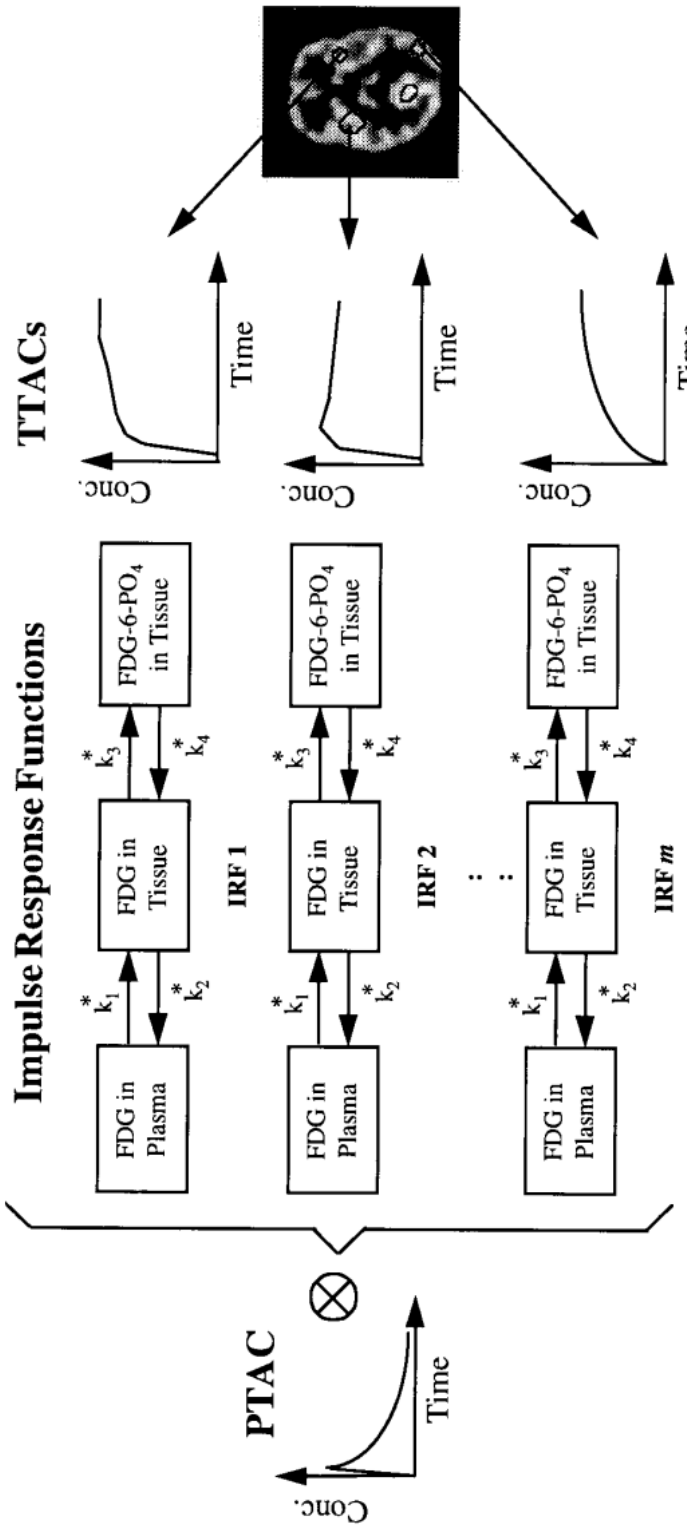


Figure 3.3: TACs from multiple regions in FDG PET study are estimated by convolution between AIF and IRFs. (Feng et al. 1997)

## 3.2 Population-based Input Function Estimation

Population-based input functions (PBIF) (Takikawa et al. 1993, Eberl et al. 1997, Shiozaki et al. 2000, Philipp et al. 2006, Zanotti-Fregonara et al. 2012, O'Sullivan et al. 2009) are obtained by estimating a patient's AIF by scaling an overall population arterial input pattern (obtained from historical information on the patient's population or by averaging fits from the overall cohort) based on individual subject information (depending on availability, historical cohorts have 10-30 blood samples through 60-90 minutes of data, and have a combination of patient weight, body surface area, lean body mass or cerebellar FDG activity) (Zanderigo et al. 2013, Bentourkia 2006). The choice of time points at which this information is extracted is a likely contributor to variability in estimation of the signal scale. With this approach, the individual is assumed to have the same tracer injection protocol and physiological characteristics as the population. For a PBIF, the AIF $C_P(t)$ is modelled as

$$C_P(t) = s \cdot C_P^{pop}(t) \tag{3.5}$$

where $C_P^{pop}(t)$ is a standard AIF averaged from a set of population AIFs, and $s$ is a scale factor based on individual subject information. PBIF have potential to be used as blood free AIF. However, standard AIF estimates from two distinct groups may differ greatly, which hinders estimation for an individual that shares different physiological characteristics from the population. Estimation from an individual with a distinct AIF structure is impossible (Zanotti-Fregonara et al. 2012). Also, PBIF estimates using a specific radiotracer need to be calculated based on arterial sampled TACs from a population using same radiotracer. Further validation of PBIF estimators is needed for new radiotracers.

Other shape-driven models are also developed $e.g.$ representing the AIF by a convolution between a population AIF and a kernel function that allows shape parameters to be specified for a subject (Olshen & O'Sullivan 1997) or modelling AIF by a parametric model with four parameters that are able to directly switch the shape of a template AIF ($i.e.$ peak location, rise and fall behaviors, and tail height) (O'Sullivan et al. 2010). Both can be used as alternative AIF representations.

## 3.3 Common AIF models

The complexity of AIF structures makes representation of their shape a challenging task (see Fig. 3.4). The shape of an AIF can be distinguished into three parts: a constant zero at the beginning up to tracer delivery, a rapid increase when the injected tracer initially progresses to the sampling site, and a slow exponential decrease corresponding to clearance of the tracer. Various mathematical constructions such as Feng's model (Feng et al. 1993), tri-exponential models (Parsey et al. 2000) and convoluted models (Tonietto et al. 2015) have been developed to provide a continuous and noise-free description of the AIF obtained from either clinically sampled (as in typical PBIF strategies) or image-derived (as in typical IDIF strategies) signals.

The tri-exponential construction and its convolved alternative rely on a linear mixture of exponential density functions fitted to sample arterial data. The tri-exponential model (TE) fits the AIF shape in two parts: a first linearly increasing piece from the time the AIF starts rising at to its peak, and a second piece modelling the AIF from its peak to the end of study using a linear combination of the three exponential curve. In comparison to Feng's model, the TE model provides more flexibility to describe the AIF. However, neither model accounts for the length of the tracer injection and could lead to poor fit of the initial part of the AIF curve.

An adaptation of the TE model was proposed (Tonietto et al. 2015) that includes the information of injection duration by convolving the injection profile and linear combination of three exponential curves. This convolved tri-exponential (CTE) model addresses some of the issues of the original TE model, but relies on a boxcar function of duration to describe the injection profile, which used on its own may not represent the pattern of tracer arrival into plasma realistically. This particular limitation has been addressed in some works (Holt et al. 2012, Poulin et al. 2013, Sari et al. 2014, Huang & O'Sullivan 2014), by using a convolution of a double Butterworth function with the TE function (Sari et al. 2014), or of a square wave with a gamma function (Huang & O'Sullivan 2014). Final individual AIF estimates are obtained by scaling the estimated AIF pattern to the individual physiological level commonly using either image-derived blood level estimates from a reference region (after partial volume correction) or blood sampling data.

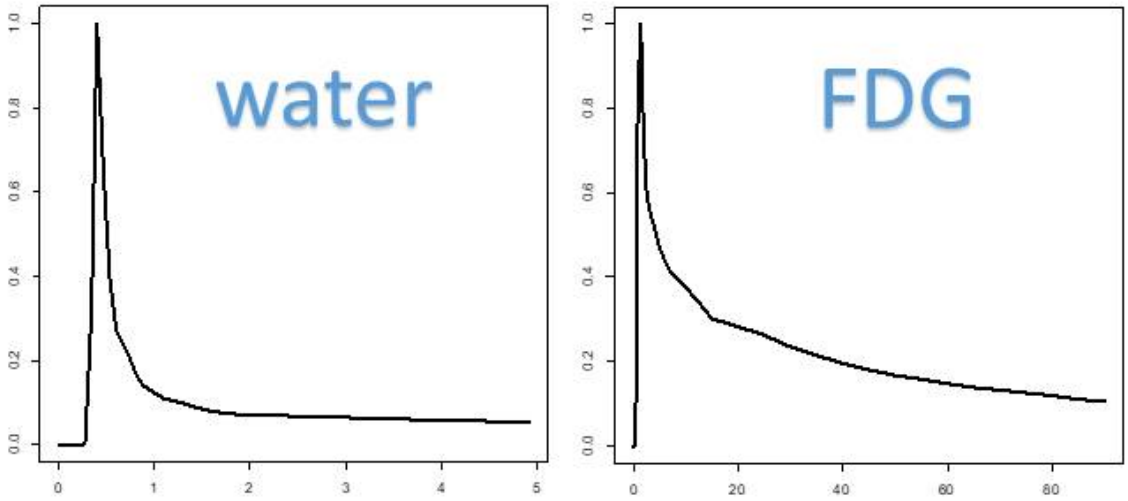


Figure 3.4: A example of AIF for water (left) and FDG (right) study. Concentration is normalized to peak and time is in the unit of minute. Experimental data are from directly sampled AIF acquired in University of Washington (Huang & O'Sullivan 2014). Sampling is at discrete time points, and adjacent points are linked by straight lines.

### 3.3.1 Feng's Model

Feng's model is an optimal model of the blood circulatory based on bolus injection under compartmental assumptions. The model is defined as

$$C_P^{feng}(t) = \begin{cases} 0 & \text{if } t < t_o \\ [A_1(t-t_o) - A_2 - A_3]e^{\lambda_1(t-t_o)} & \\ +A_2 e^{\lambda_2(t-t_o)} + A_3 e^{\lambda_3(t-t_o)} & \text{if } t \geq t_o \end{cases} \tag{3.6}$$

where $t_o$ is the time delay constant and $A_i$s and $\lambda_i$s ($i = 1, 2, 3$) are coefficients and eigenvalues of the model (Feng et al. 1993). The Feng's model fits the AIF by a vertical rise at given time $t_o$ when signals appear, and followed by an exponential decay. However, model performance is impacted when injection is not a bolus.

### 3.3.2 Tri-exponential Model

The tri-exponential model adds one time knot ($t_p$) when the AIF reaches its peak. It models the AIF as a straight line for the rapid rise and a mixture of

three exponentials to represent slow decay

$$C_P^{tri-exp}(t) = \begin{cases} 0 & \text{if } t < t_o \\ \sum_{i=1}^{3} A_i(t - t_o) & \text{if } t_o \leq t < t_p \\ \sum_{i=1}^{3} A_i e^{-\lambda_i(t-t_p)} & \text{if } t \geq t_p \end{cases} \tag{3.7}$$

This model tends to provide a better description of AIF compared to Feng's approach, and favored in the community (Tonietto et al. 2015). Although the TE model has taken the injection time into consideration, the segment line between $t_o$ and $t_p$ cannot reflect the increase with radian.

### 3.3.3 Convoluted Models

A technical modelling improvement consists in introducing an injection profile into the previous two models (Tonietto et al. 2015). For Feng's model, the convoluted form is simply

$$C_P^{con-feng} = C_P^{feng}(t) \circledast I(t) \tag{3.8}$$

where I(t) is the indicator function, a square wave rising over time $T$

$$I(t) = \begin{cases} 0 & \text{if } t < 0 \\ 1/T & \text{if } 0 \leq t < T \\ 0 & \text{if } t \geq T \end{cases} \tag{3.9}$$

for the tri-exponential model, the convoluted form omits the straight line part, since the injection profile can be estimated by the term $I(t)$, $i.e.$

$$C_P^{con-tri} = C_P^{t-tri}(t) \circledast I(t) \tag{3.10}$$

where

$$C_P^{t-tri}(t) = \begin{cases} 0 & \text{if } t < t_o \\ \sum_{i=1}^{3} A_i e^{-\lambda_i(t-t_p)} & \text{if } t \geq t_o \end{cases} \tag{3.11}$$

These convoluted models include injection information for description of the AIF, which makes them more accurate and flexible. Since injection time ($T$) is normally known prior to the calculation, the computational complexity of these techniques does not increase much (Tonietto et al. 2015).

## 3.4 Approximation from Venous Blood Information

In dynamic PET imaging, the concentration of radiotracer in arterial blood is consider as an input function, since it brings radiotracer from heart to tissues and organs, and supplys oxygen and nutriments. As venous blood flows back to the heart, the concentration of radiotracer will be distinct from that in arterial blood. Although venous blood has different characteristics from arterial blood, it is an attractive alternative for arterial blood since venous cannulation is less invasive to the patient and easier to operate.

### 3.4.1 Arterialised Venous Blood

Arterialised venous blood (AVB) can be used as an alternative for arterial blood for AIF extraction (Brooks et al. 1989, Choi et al. 1991, Copeland et al. 1992). It is achieved by measuring the concentration of tracer in venous blood by placing a catheter in a antecubital or dorsal hand vein that has been heated (van der Weerdt et al. 2002). The heating results in a dilatation of blood vessels, which increases the blood flow without affecting the metabolism. Nevertheless, this process is likewise not favored by neither patients nor clinicians (Vriens et al. 2009).

### 3.4.2 Venous Input Function

The venous input function (VIF) approach applies an arterio-venous transform scheme to estimate AIF from VIF (Syvanen et al. 2006a). It assumes that

$$C_V(t) = C_P(t) \circledast T_{a-v} \tag{3.12}$$

where $C_T(t)$ and $C_P(t)$ are the concentrations of radiotracer in venous and arterial plasma, respectively, and $T_{a-v}$ is the arterio-venous transform. Several

attempts of arterio-venous transforms were reported. Among them, a biexponential function (Syvanen et al. 2006a) of the forms.

$$T_{a-v} = A_1 e^{-a_1 t} + A_2 e^{-a_2 t} \tag{3.13}$$

where $A_1$, $A_2$, $a_1$ and $a_2$ are free model parameters to be optimized, leads to the AIF being represented by

$$C_P(t) = C_V(t) \circledast T_{a-v}^{-1} \tag{3.14}$$

The method yielded promising results and requires further validation for different tracers, and greater sample sizes.

## 3.5 Whole Body Blood Circulation Model

An alternative, compartment model based technique was developed by our group to estimate the AIF from a whole-body tracer circulation model (BCM) (Huang & O'Sullivan 2014, O'Sullivan et al. 2017). Fig. 3.5 provides an illustration of it. In this representation, the fate of each tracer atom is represented by an eight-state Markov chain process discrete by heart beats, where each state represents one important location in the blood circulation system. They are left and right heart ventricles, vascular and extra-vascular tissues in the lungs and other organs, venous blood pool and body loss that tracers may stuck in. Each pool is defined as a state in which the radiotracer can stay (note that body loss is an absorbing state). To use the BCM, theoretically, time course of the tracer concentration from one of the eight states is required. Since the left ventricle is one of those states represented in the stochastic process, the AIF signal can be approximated by the tracer concentration in the left ventricle observed from PET imaging over time. Otherwise clinically sampled arterial data can be used for evaluation of one of these Markov states. Although high dimensionality of the parameters involved in the model constitutes a computational challenge, this physiologically meaningful representation can yield an accurate AIF estimation.

The initial probability distribution of the tracer is $\pi^0 = (1, 0, 0, 0, 0, 0, 0, 0)$, where the entire radiotracer concentration is assumed to be in right ventricle at

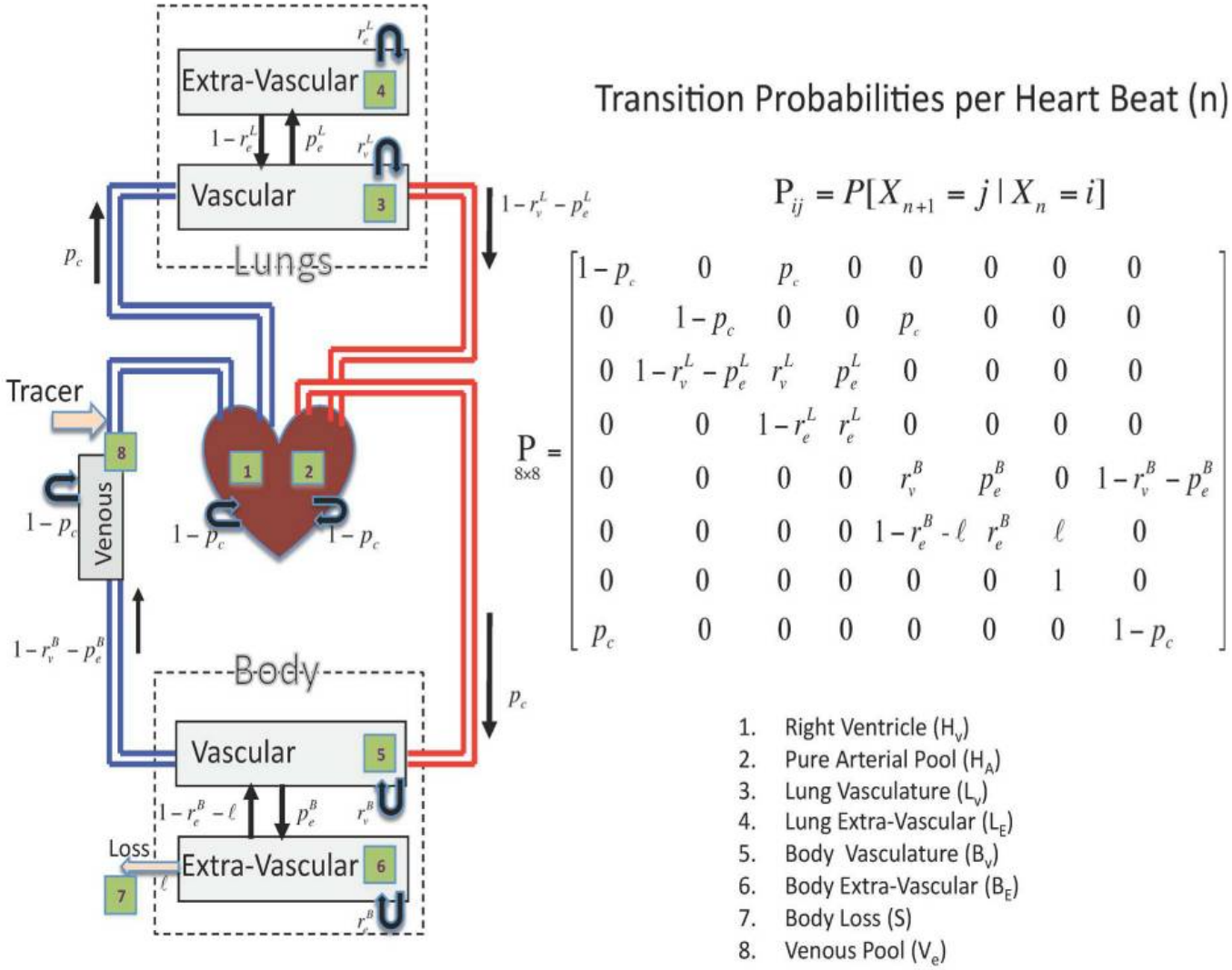


Figure 3.5: Markovian model based on whole body blood circulation. Graphic representation (left) and probability transition matrix (right) (Huang & O'Sullivan 2014).

the beginning of the study. Considering each transition happens at each heart beat, the probability distribution after the $k$th heart beat is

$$\pi^k = \pi^0 P^k \tag{3.15}$$

where $P$ is the transition matrix in Fig. 3.5. With the knowledge of the input curve at the initial state, the concentration of tracer at time $t$ in each pool can then be derived as

$$C_j(t) = C_I(t) \circledast \{\pi^{B(t)}\}_j \tag{3.16}$$

where $j = 1, 2, \cdots, 8$. $C_I(t)$ is the input curve at the right heart ventricle, and $B(t)$ is the total number of heart beats up to time $t$. Since $\{\pi^{B(t)}\}$ is discrete in time, assuming $\tau$ is the average number of heart beats per unit time, we have

$$C_j(t) = \sum_{k=0}^{[\tau t]} C_I(t) \cdot \pi_j^{[\tau t]-k} \tag{3.17}$$

where $C_I(t)$ is assumed to be the convolution of injection profile ($I_d$) and a gamma dispersion from the injection site to the right ventricle ($gamma(\alpha, \beta)$). Assuming injection takes place at a constant rate, $I_d$ is set to be an indicator function rising over injection duration $d$. From this, $C_I(t)$ can be written as

$$\begin{aligned} C_I(t) &= I_d(t) \circledast gamma(t|\alpha, \beta) \\ &= \int_0^{t-\Delta} I_d(t - \Delta - s) g(s) ds \end{aligned} \tag{3.18}$$

where $\Delta$ is a time shift parameter (either positive or negative) describing the possible delay between time of injection and measurement. After a series of transformations and parameterizations, a weighted nonlinear least squares approach is used to optimize the parameters (including eight parameters in the transition matrix in Fig. 3.5, $\alpha$, $\beta$ and $\Delta$ in Eq. (3.18), assuming $\tau$ and $d$ are given). Similar to the other AIF models, a scale factor $A$ is estimated separately from Nadler blood volume (NBV) (Nadler et al. 1962) and injection dose (Huang & O'Sullivan 2014). Output of the BCM consists of eight time course curves specific to eight blood pools. The left ventricle is considered as a pure arterial pool in BCM, and the AIF is estimated as

$$C_P(t) = \hat{C}_2(t) \tag{3.19}$$

where $\hat{C}_2(t)$ is the curve of the fitted BCM model corresponding to the left heart ventricle.

The BCM has been evaluated on a set of clinical water and FDG-PET studies, and proven reliable and reproducible for AIF extraction (O'Sullivan et al. 2017). Also, BCM offers the opportunity to estimate PVE and spillover, since it allows to distinguish time courses of radiotracers in multiple blood pools, simultaneously (see Fig. 3.6).

Nevertheless, the computational complexity and great time consumption for

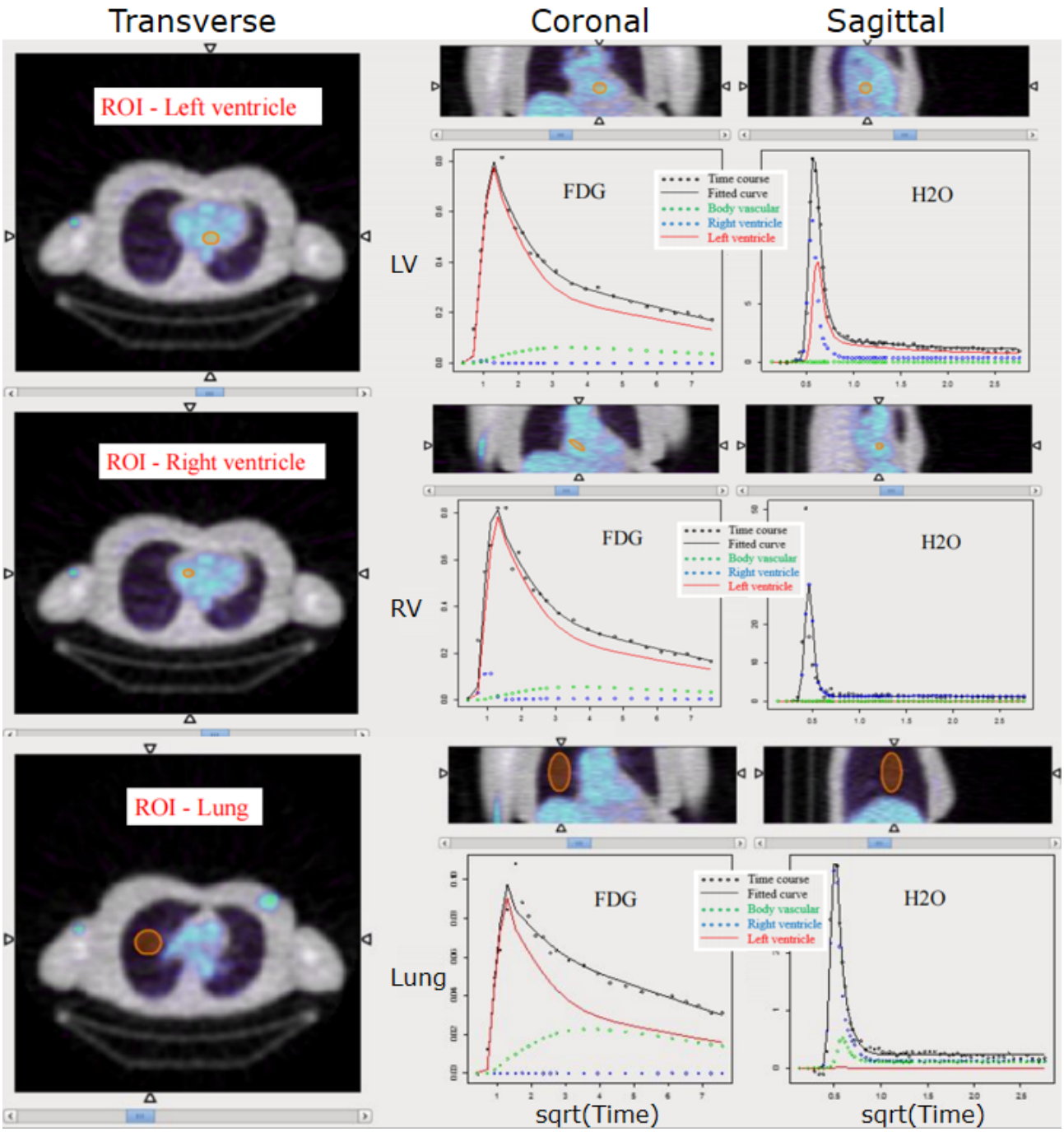


Figure 3.6: Fitting imaging data from one ROI using the extended BCM (Xiu et al. 2016). Considering one pool is contaminated by signals from the other pools, and assuming time-invariance, a signal from one ROI is fitted by linear combination of arterial, venous, and body vascular time courses. The image is from a water and FDG dynamic PET study at University of Washington (Dunnwald et al. 2008), and ROIs are drawn by experts for different blood pools.

optimization may limit the use of BCM. Noninvasive alternatives for AIF extraction are developed in the following chapters, that are somehow inspired by the BCM.

# Chapter 4

# Tracer Travel Rate Projection Model

## 4.1 Introduction

The whole body blood circulation model (BCM) for noninvasive extraction of AIF has shown promising results. The idea of BCM is to model the tracer activity in circulatory blood by separating some blood pools that correspond to their physical states (Huang & O'Sullivan 2014, O'Sullivan et al. 2017). Compartmental models provide an effective aspect of tracer kinetics in blood circulation by dividing different physiologically defined compartments (Sokoloff et al. 1977, Phelps et al. 1979). The two techniques are used in solving two distinct problems. One is for tracers traveling in whole body circulation and the other is for transform among local compartments. But both of them take the circulatory system into consideration, and divide the body into parts, either physiologically or physically. Inspired by the idea from BCM and compartmental models, some simplified modelling methods to BCM for AIF extraction are developed, $e.g.$ the Population-based Projection Model PBPM. In this chapter, one of the modelling methods is presented. Although this model may not be ideally used in practical use, it provides some explanation and support for the core concept used in PBPM.

In Section 4.2 we describe the theoretical construction of the TRPM. In Section 4.3 we indicate how we specify the model in terms of the choice of distributions and functions used as basis components, as well as the numerical techniques used to fit the model. Section 4.4 provides results if experiments carried out on this modelling methodology.

## 4.2 Modelling Approach

### 4.2.1 Theory

PET imaging requires radio-active tracer molecules to be introduced into the subject before scanning. Usually, tracer labeled molecules ($e.g.$ $^{18}$F-FDG) are injected into the vein, blood will directly bring them back to heart. Then as the heart beats, the blood circulation system will carry the tracer molecules to organs and tissues that need nutrition and oxygen. The fate of the tracer generally depends on the characteristics of the molecule which the tracer molecules are labeled on. For example, if it is FDG, the tracer tends to be accumulated in organs and tissues that can metabolize glucose, or cancer cells for patients with cancers. However, when the tracer molecules are labeled on water molecules, then they will be accumulated in anywhere of the circulatory system that blood can possibly reach. As scanning continues, the accumulation of tracer molecules in different regions of the body will provide the information of subject that doctors and researchers want. Since blood brings the tracer molecules to those regions, the information of their input from the blood is key piece of jigsaw in the whole puzzle. AIF is the dynamic concentration of radiotracer in plasma which represents the availability of tracer to the tissues and organs that blood can reach. The availability is of our great interest, which leads us to this new approach for AIF representation in both physical and physiological ways.

When it comes to the analysis of blood circulation in PET dynamic study, the information is mainly from extraction of blood during the scanning. The extracted data start from the introduction of the tracer to the body, and the tracers have distinct fates before being sampled. Direct sampling for AIF usually needs to be operated at an artery site (sometimes a venous site as alternative), since arterial blood is directly supplying for the rest of body with nutrition and oxygen (see Fig. 4.1). In our model setting, at one sampling site, the radiotracers that have been sampled will be categorized into groups by their own history. For example, for those tracer molecules that have never passed through the vascular membrane, which means that they are always traveling in blood, the expected travel time is comparatively short. At the very beginning of the study, most sampled tracer molecules will be in this category. However, at time of sampling, the tracer molecules which have no experience outside the vasculature are categorized into another group. This does not imply that at the beginning of study, there is no possibility that the sampled tracer molecules are from the

other groups. At each time of sampling, the proportion of tracer molecules in each group is always changing.

As study continues, an increasing number of tracer molecules will have extra-vascular history, $e.g.$ they can be reversed from metabolism or receptor binding. Also, an increasing number of tracer molecules are expected to leave the study when they are brought to an irreversible place like the bladder where they are physically or physiologically stuck. The expected travel time for those tracer molecules to be sampled that have extra-vascular experience is considerably longer, even infinity. Then it is reasonable to say that in the late time of study, there are almost no tracer molecules sampled from the first group where tracer molecules have no extra-vascular experience in that group. Based on this theory, the AIF ($C_P(t)$) at a specific time is the summation of concentration of tracer from different groups at the sampling site at that time. If we can model the shape of TAC of each group, the AIF is only a linear combination of all the TACs. Then this assumption leads to questions about how many characteristic groups are existing, and how they can be defined.

### 4.2.2 The Fast Curve

The fast curve is defined as a TAC for those tracer molecules at a sampling site that have no extra-vascular experience. To model the fast curve, the injection profile and dispersion are considered. Injection profile is the availability of radiotracer to the body. It is normally assumed to be an indicator function, since the injection is usually at a constant rate, $i.e.$

$$I_d(t) = \begin{cases} 1 & \text{if } t_o \leq t \leq t_o + d \\ 0 & \text{else} \end{cases} \tag{4.1}$$

where $I_d(t)$ is the injection profile, $d$ is the duration of injection, and $t_o$ is the time that injection starts. The shape looks like a square wave rising over the injection time. Here we only consider the shape of the AIF ($i.e.$ normalized AIF), since the scale factor for AIF involves variables of characteristics from the individual subject, $e.g.$ body surface area (BSA), lean body mass (LBM) (Shiozaki et al. 2000). Estimation method for scale factor will be developed in next chapter.

The dispersion is modelled as a two-parameter gamma density $g(\cdot|\alpha, \beta)$, since

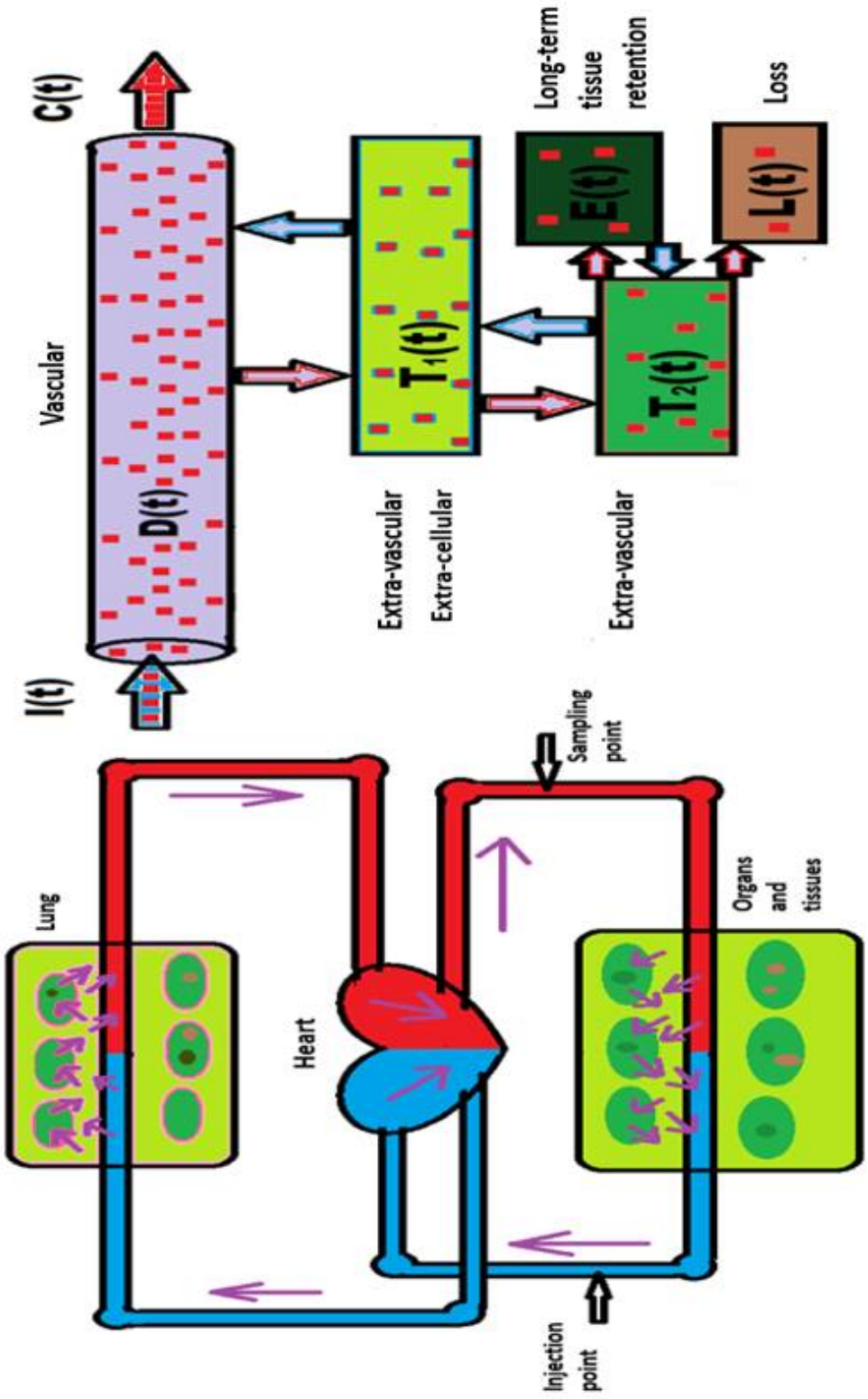


Figure 4.1: Graphic representation of tracer kinetics in blood circulation system (left) and compartments setting for AIF modelling (right). Note that while heart and lungs are playing other roles instead of pumping blood and supplying oxygen, they are regarded as compartments of organs and tissues.

the shape of the probability density function (PDF) of gamma fits the feature of tracer's arrival at the sampling site, considering that the radiotracers travel in a catheter (See Appendix B). The shape of the gamma density is skewed to the right when $\alpha$ is small ($i.e. < 3$), which matches the expected transit time of tracer molecules that have never been outside the blood vessel from injection site to sampling site. Another consideration about the time delay arises due to the fact that measured data may not temporally coincide with injection. The time delay $\Delta$ to shift the curve is needed (note that $\Delta$ can be either positive or negative). Then the fast curve can be modelled as a shifted convolution between $I_d(t)$ and $g(t|\alpha, \beta)$

$$C_{fast}(t) = \int_0^t g(t-s|\alpha,\beta) I_d(s-\Delta) ds \tag{4.2}$$

In Figure 4.1, the compartments setting is presented. $I(t)$ is the input of tracer to the body, and $C(t)$ is the sampled AIF. The fast group has a TAC which is a proportion of $C(t)$ that estimates the tracer activity of tracer molecules that have never reached outside of the vasculature. The dispersion of arrival of tracer molecules at the sampling point is $D(t)$. $D(t)$ in this case is $g(\cdot|\alpha, \beta)$ in Eq. (4.2).

### 4.2.3 The Intermediate-fast curve

The intermediate-fast (inter-fast) curve models the tracer molecules at the sampling site that have extra-vascular experience, but have no experiences of entering cells or long-term stay in tissue. The expected transit time is considerably longer than that of tracer molecules from the fast group. An exponential density $e(\cdot|\lambda_f)$ is used to describe the dispersion of transit time for the inter-fast and fast groups where $\lambda$ is the rate parameter. The inter-fast curve is represented by a convolution between $C_{fast}(t)$ and $e(t|\lambda_f)$

$$C_{inter-fast}(t) = \int_0^t e(t-s|\lambda_f)[g(\alpha,\beta) * I_d](s-\Delta) ds \tag{4.3}$$

In Figure 4.1, the tracer molecules in intermediate-fast group have reached the compartment with $T_1(t)$, but they have never been to the box with $T_2(t)$. The travel time for the tracer molecules in this group is modelled as a convolution between $D(t)$ and $T_1(t)$. $T_1(t)$ in this case is $e(t|\lambda_f)$ in Eq. (4.3).

### 4.2.4 The Intermediate-slow Curve

The intermediate-slow (inter-slow) curve is similar to the inter-fast curve. They model the tracer molecules that have extra-vascular and cellular experience before they arrive at the sampling site. The expected transit time is slightly longer than that of tracer molecules from the inter-fast group. Instead of using another exponential density to convolve with the inter-fast curve, here we simply use the form from Eq. (4.3), but using exponential density $e(\cdot|\lambda_s)$ with a smaller rate parameter ($i.e.\ \lambda_s < \lambda_f$). Then the inter-slow curve can be expressed as

$$C_{inter-slow}(t) = \int_0^t e(t-s|\lambda_s)[g(\alpha,\beta) * I_d](s-\Delta)ds \tag{4.4}$$

In Figure 4.1, the tracer molecules in intermediate-slow group have a history of reaching the box with $T_2(t)$, but no experience of further boxes. $T_2(t)$ is modelled as an exponential density. Since convolution between exponential densities is an exponential density, the travel time for tracer molecules in intermediate-slow group is modelled as convolution between $D(t)$, $T_1(t)$ and $T_2(t)$. In this case, $T_1(t) \circledast T_2(t)$ is $e(\cdot|\lambda_s)$ in Eq. (4.4).

### 4.2.5 The Slow Curve

The slow curve models the tracer molecules that have long-term tissue retention. The tracer can be reversed from time consuming activity, such as metabolism or receptor-binding. Usually it depends on the number of tracer molecules from inter-slow curve, since they need to reach a particular spatial location to accomplish the complicated procedure. Reasonably, if there are no tracer molecules in the inter-slow group, potentially no tracer molecules can enter the slow group. As long as $C_{int-slow}(t)$ at the time points that are greater than 0, potential of tracer molecules from slow group can be detected at sampling site are increasing. The slow curve then can be modelled as an integral of the inter-slow curve, which also can be deemed as a convolution between $C_{int-slow}$ and $1$. The expression for the slow curve is

$$C_{slow}(t) = \int_0^t \int_0^s e(s-u|\lambda_s)[g(\alpha,\beta) * I_d](u-\Delta)duds \tag{4.5}$$

In Figure 4.1, the tracer molecules in the slow group have reached compartment

with $E(t)$, and returned and sampled after they are back from the compartment. In this case, $E(t)$ is $1$, and convolution between a function and 1 is the integral of the function.

### 4.2.6 The Loss Curve

The loss curve models the potential loss of the tracer in a study. As the study continues, an increasing number of tracer molecules will leave the study due to some unpredictable factors. That will cause an additional drop of the AIF, especially at the late period of study. Without taking the loss of tracer into consideration, the estimated curve may be biased at the tail ($i.e.$ higher than the true value). Assuming that the loss of tracer happens when tracer molecules remain for a long time in tissues or organs ($i.e.$ related to inter-slow group). Theoretically, a convolution between $C_{int-slow}(t)$ and a triangle shape curve $(1 - \frac{t}{T_{max}})$ ($T_{max}$ is the total time of the study) would work. However, if the shape of loss curve is all we need, removing the constant in that triangle curve, the time $t$ carries all the features of loss group. Then the loss curve can be represented by a convolution between $C_{int-slow}(t)$ and $t$ (note that coefficient for loss curve is non-positive).

$$C_{loss}(t) = \int_0^t s \int_0^{t-s} e(s-u|\lambda_s)[g(\alpha,\beta) * I_d](u-\Delta)duds \tag{4.6}$$

In Figure 4.1, the tracer molecules in the loss group have reached compartment with $L(t)$. Since this compartment is irreversible, they will not be sampled. The proportion of TAC that represents tracer molecules in this group need to be removed from the estimated AIF. $L(t)$ in this case is $t$ in Eq. (4.6). Since without considering some constant that can be covered and included by other parameters, $L(t)$ only has the feature of time $t$.

There is actually another interpretation of the loss group. Along with the slow group, they represent those tracer molecules that have comparatively long travel time. The difference between slow and loss groups is that the latter never come back. Then after the linear parameter $\pi_4$ and $\pi_5$ in Eq. (4.7) are estimated, setting $\pi_4$ to positive and $\pi_5$ to negative, $\pi_4 \cdot C_{slow}(t) + \pi_5 \cdot C_{loss}(t)$ models the TACs of all the tracer molecules that have further experience of the box with $T_2(t)$ in Figure 4.1. This combined curve can be regarded as a slow curve that represents the tracer molecules which have long-time tissue retention.

Then the full model for normalized AIF (nAIF) is

$$\begin{aligned} {}_nC_P(t) = \pi_1 \cdot C_{fast}(t) + \pi_2 \cdot C_{int-fast}(t) + \pi_3 \cdot C_{int-slow}(t) \\ + \pi_4 \cdot C_{slow}(t) + \pi_5 \cdot C_{loss}(t) + error \end{aligned} \tag{4.7}$$

where $\pi_j$s ($j = 1, 2, \ldots 5$) are linear coefficients for five component curves with constraint that $\pi_1$, $\pi_2$, $\pi_3$ and $\pi_4$ are non-negative and $\pi_5$ is non-positive. For simplicity, this model for normalized AIF is named Travel-rate Projection Model (TRPM). Since the complexity of tracer activity in whole body circulation system depends on potential functional process of the tracer labeled molecule and half-life of the isotope, the number of compartments involved in the study may differ.

## 4.3 TRPM Specification and Optimization

In this section, we introduce some of the predominant methodologies for parameter optimization and algorithmic implementation of the TRPM.

Let the time-course data be given by $\{z_i, t_i, w_i\}$ for $i = 1, 2, \cdots, m$, where $t_i$s and $z_i$s are sampling time and normalized concentration of tracer in plasma at the corresponding sampling time for subject $i$, respectively, and $m$ is the total number of subjects. The normalized concentration means that the given TACs need to be scaled by its maximum concentration. Then we can apply our TRPM on each curve. $w_i$ is a weight that is given to indicate the reliability of that measurement. The weights are set to be uniform when no supplementary information is given. Then data can be modeled as

$$z_i = \eta(t_i|\theta, \pi, \Delta) + w_i^{-1/2}\epsilon_i \tag{4.8}$$

where $\eta(t|\theta, \pi, \Delta) = {}_nC_P(t)$ in Eq. (4.7), $\theta$ is a parameter vector that specifies the gamma and exponential densities in each component curve, *i.e.* $\alpha$, $\beta$, $\lambda_f$ and $\lambda_s$, $\pi$ is another parameter vector of the linear parameters $a_j$s in Eq. (4.7), $\Delta$ is a time adjustment for individual subject (recall Eq. (4.2)), and $\epsilon_i$s are the errors. Then objective function can be written as

$$f(\theta, \pi, \Delta) = \sum_{i=1}^{m} w_i(z_i - \eta(t_i|\theta, \pi, \Delta))^2 \tag{4.9}$$

Methods have been developed to optimize the parameters and applied in an open programing tool R (R Core Team 2016) (3.2.4 Revised).

### 4.3.1 Gamma Distribution

The dispersion is modeled using the gamma and exponential distributions. The exponential distribution is a special case of the gamma distribution when the shape parameter $k$ equals to $1$ (see Fig. 4.2 for the PDF and CDF of the gamma distribution). The expression of the PDF and CDF are as follow

$$\begin{aligned} \text{PDF}: \quad & g(x) = \frac{1}{\Gamma(k)\theta^k} x^{k-1} e^{-x/\theta} \\ \text{CDF}: \quad & G(x) = \frac{\gamma(k, x/\theta)}{\Gamma(k)} \end{aligned} \tag{4.10}$$

where

$$\begin{aligned} \Gamma(k) &= \int_0^\infty t^{k-1} e^{-t} dt \\ \gamma(k, x/\theta) &= \int_0^{x/\theta} t^{k-1} e^{-t} dt \end{aligned} \tag{4.11}$$

As $k$ increases, the $gamma(k, \theta)$ will converge to a Gaussian distribution $N(\mu, \sigma^2)$ according to central limit theorem (CLT) where $\mu = k\theta$ and $\sigma^2 = k\theta^2$. Therefore, in our case, the shape parameter of gamma is set to be small ($i.e.\ 1 < k < 2.2$). This setting ensures that the gamma PDF is right-skewed which coincides with the fact that arrival of tracer molecules to a sampling point appears to have a right-skewed density waiting time feature. The scale parameter $\theta$ decides the tail of the PDF. A greater $\theta$ indicates a long tail that it allows the dispersion for those tracers' arrival to have a longer expected travel time before they are sampled.

The role of the gamma distribution is to create a component as each curve introduced in the last section, $i.e.$ fast curve from Eq. (4.2) can be expressed as

$$\begin{aligned} C_{fast}(t) &= \int_0^t g(t - s|\alpha, \beta) I_d(s - \Delta) ds \\ &= G(\alpha, \frac{t - \Delta}{\beta}) - G(\alpha, \frac{min(t - \Delta - d, 0)}{\beta}) \end{aligned} \tag{4.12}$$

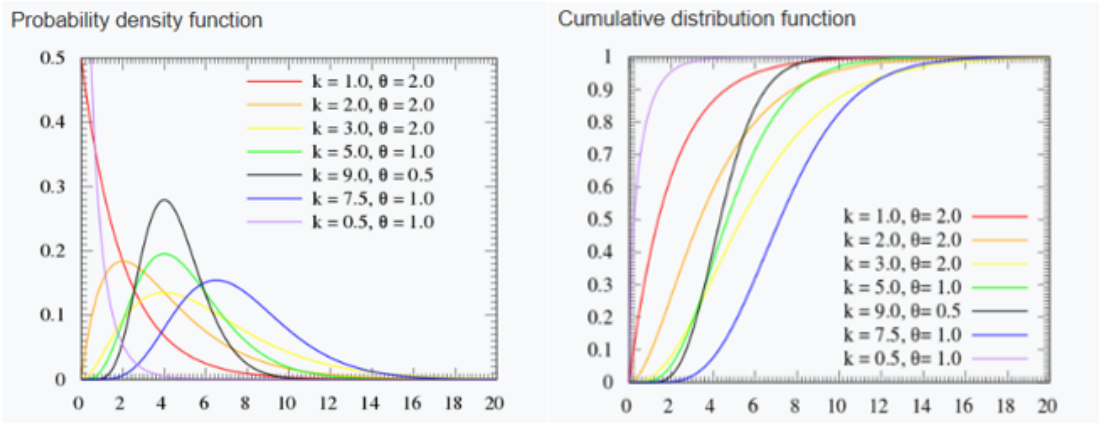


Figure 4.2: PDF (left) and CDF (right) of gamma distribution with different parameters (Wikipedia contributors 2018b).

where $\alpha$ and $\beta$ are the shape and scale parameter in $gamma(k, \theta)$, respectively. $G(\cdot)$ is the gamma CDF in Eq. (4.10). $d$ is the injection duration, and $\Delta$ is the shift parameter.

See Appendix C for calculation of the convolution applied in the program.

### 4.3.2 Component Curves

The first procedure involved in programing is to enable calculation of each curve given sampling time $t_i$s (where $i = 1, 2, \ldots, m$ specifies the $i$th sampling for one subject with $m$ samplings), density parameters $\theta$ and time shift $\Delta$. Taking the fast curve into consideration, given the information before, the $C_{fast}(t_i)$ can be calculated based on Eq. (4.2). Like wise, $C_{int-fast}(t_i)$, $C_{int-slow}(t_i)$, $C_{slow}(t_i)$ and $C_{loss}(t_i)$ can be defined. For simplicity, these curves can be loaded into a $m \times J$ matrix $A$, where $m$ and $J$ are the number of sampling times and components, respectively. If it is the full model, $J$ should be equal to five, and each of $j$th columns of $A$ ($j = 1, 2, \cdots, 5$) is corresponding to one of the components ($i.e.$ fast, inter-fast, inter-slow, slow and loss, respectively). Then for each individual of items $a_{i,j}$ in matrix $A(t_i, \theta, \Delta)$

$$a_{i,j} = C_j(t_i|\theta, \Delta) \tag{4.13}$$

### 4.3.3 Quadratic Programing Problem

Having matrix $A$ for the component curves, the normalized AIF is

$$z_i = \sum_{j=1}^{J} \pi_j a_{i,j} + w_i^{-1/2} \varepsilon_i \quad i = 1, 2, \ldots, m \tag{4.14}$$

where $a_{i,j}$ is calculated in Eq. (4.13), and $\pi_j$s are linear parameters in Eq. (4.7). We optimize the $\pi_j$s with constraint $\pi_j \geq 0$ for $j = 1, 2, \ldots, 4$ and $\pi_5 \leq 0$

$$\hat{\pi}(\theta, \Delta) = \arg\min\{\frac{1}{2} \sum_{i=1}^{m} w_i [z_i - \sum_{j=1}^{J} \pi_j a_{i,j}]^2\} \tag{4.15}$$

Expanding the quadratic function, we have

$$\hat{\pi}(\theta, \Delta) = \arg\min\{\frac{1}{2} \sum_{i=1}^{m} [w_i z_i^2 - 2\sqrt{w_i} z_i \sum_{j=1}^{J} \sqrt{w_i} a_{i,j} \pi_j + (\sum_{j=1}^{J} \sqrt{w_i} a_{i,j} \pi_j)^2]\} \tag{4.16}$$

Let $W = diag(w_1, w_2, \ldots, w_m)$, remove the constant $w_i z_i^2$ from the bracket, and reorganize the linear and quadratic terms of $\pi$

$$\hat{\pi}(\theta, \Delta) = \arg\min\{-(A^T(\sqrt{W}\mathbf{z}))^T \pi + \frac{1}{2} \pi^T (A^T W A) \pi\} \tag{4.17}$$

where $A$ stands for matrix $A(t_i, \theta, \Delta)$ with item $a_{i,j}$, and $A^T$ is the transpose of $A$.

An existing program of the Goldfarb-Idnami Method (original by Berwin A. Turlach 2019) developed in R is aiming at solving quadratic programming problems with constraint in the form of

$$\begin{aligned} &\underset{x}{minimize} \quad f(x) = -V^T \mathbf{x} + \frac{1}{2} x^T M x \\ &\text{subject to} \quad C^T x \geq x_0 \end{aligned} \tag{4.18}$$

where $V$ and $M$ are the vector and matrix in quadratic function to be minimized, respectively, $C$ is the matrix that defines the constraint of $x$ with a vector $x_0$. With proper input, $\hat{\pi}(\theta, \Delta)$ is able to be acquired.

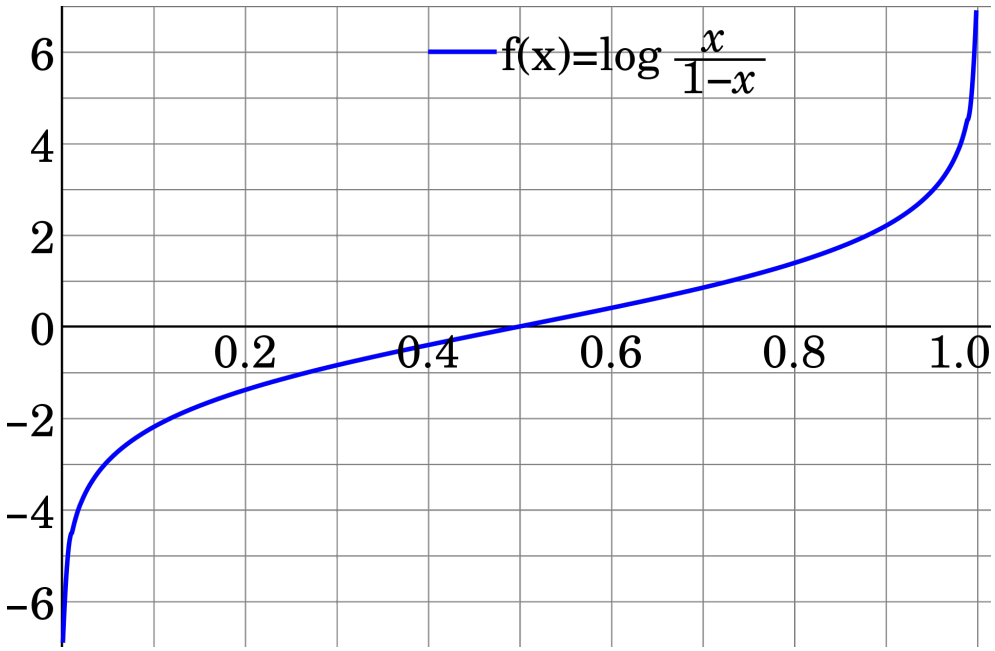


Figure 4.3: Plot of logit(x) in the domain of 0 to 1, where the base of logarithm is e (Wikipedia contributors 2018d).

### 4.3.4 Gauss-Newton Method

Then we deem $\pi$ a function of $\theta$, given $\Delta$, the optimization will end up with only a nonlinear least squares (NLS) problem. We apply a Gauss-Newton type method (Hartley 1961) to optimize the parameters. With one initial guess

$$\theta^0 = (\alpha^0, \beta^0, \lambda_f^0, \lambda_s^0) \tag{4.19}$$

is approximated from past experience, the boundaries are set to be

$$\theta^H = (\alpha^H, \beta^H, \lambda_f^H, \lambda_s^H) \tag{4.20}$$

as the high boundary, and lower boundary

$$\theta^L = (\alpha^L, \beta^L, \lambda_f^L, \lambda_s^L) \tag{4.21}$$

Since the scales of the parameters differ considerably, we apply a logit transform to the proportion ($p$) of $\theta$ located between the boundaries. Fig. 4.3 presents the plot of logit transform, and in our program, $\varsigma$ is set to be within (-4,4), which already includes over 99.99% of the values of $\theta$ within the boundaries.

$$\varsigma = \log \frac{p}{1-p} \tag{4.22}$$

where $p = \frac{\theta - \theta^L}{\theta^H - \theta^L}$. Then we can also write $\varsigma$ a function of $\theta$

$$\varsigma(\theta) = \log \frac{\theta - \theta^L}{\theta^H - \theta} \tag{4.23}$$

Inversely, $\theta$ can be written as a function of $\varsigma$

$$\theta(\varsigma) = \theta^L + (\theta^H - \theta^L)\frac{e^{\varsigma}}{1+e^{\varsigma}} \tag{4.24}$$

Since $\theta$ and $\pi$ are both corresponding to a given $\varsigma$, then given $\Delta$ we are able to rewrite the objective function as a function of $\varsigma$ as follows:

$$l_{\Delta}(\varsigma) = \sum_{i=1}^{m} w_i (z_i - \eta_{\Delta}(t_i; \theta, \pi|\varsigma))^2 \tag{4.25}$$

Here we apply a Gauss-Newton Method to optimize $l(\varsigma)$. Using Taylor expansion, at the $(h+1)^{th}$ iteration,

$$\eta_{\Delta}(\varsigma^{h+1}) \approx \eta_{\Delta}(\varsigma^h) + J_l^h d^h \tag{4.26}$$

where $d$ is the increment of $\varsigma$, and also expected to be a descent direction to reduce $l_{\Delta}(\varsigma)$, $i.e.$

$$d^h = \varsigma^{h+1} - \varsigma^h \tag{4.27}$$

and $J$ is the Jacobian matrix of $l_{\Delta}(\varsigma)$, which is a $m \times S$ matrix filled with the first derivative of $\eta_{\Delta}(\varsigma)$ at each direction of $\varsigma$ by column, where $S$ is the number of parameters in $\varsigma$:

$$J_l^h = \frac{\partial l_{\Delta}(t_i, \varsigma^h)}{\partial \varsigma_s} \quad s = 1, 2, \ldots, S \tag{4.28}$$

This can be approximated by the difference quotient

$$J_l^h \approx \frac{l_\Delta(t_i, \varsigma|\varsigma_s = \varsigma_s^h + 0.01) - l_\Delta(t_i, \varsigma^h)}{0.01} \tag{4.29}$$

Then we find the gradient of $l_\Delta(\varsigma)$. In order to minimize $l_\Delta(\varsigma)$, the gradient is set to $0$, $i.e.$

$$\frac{\partial l_\Delta(\varsigma)}{\partial \varsigma_s} = -2J_l^T W(\mathbf{z} - \eta_\Delta(\varsigma)) = 0 \tag{4.30}$$

As iterations continue, $\eta_\Delta(\varsigma^{h+1})$ is expected to be increasingly closer to the observed $\mathbf{z}$ in terms of a decreasing $l_\Delta(\varsigma)$ in the direction of the gradient. Plugging Eq. (4.26) into it, we get

$$-2J_l^T W(\mathbf{z} - \eta_\Delta(\varsigma^h) - J_l^h d^h) = 0 \tag{4.31}$$

Let $\Psi$ to be short for the Jacobian matrix and $\Psi^T$ to be the transpose, we can calculate the descent direction by

$$d^h = (\Psi^T W \Psi)^{-1} W(\mathbf{z} - \eta_\Delta(\varsigma^h)) \tag{4.32}$$

However, $l_\Delta(\varsigma)$ is only guaranteed to be decreasing when the parameter moves in the descent direction with a small enough distance. The step size $\tau$ is introduced to prevent an inappropriate approximation at the iteration. The step size $\tau$ can be optimized simply by a line search. Then the iteration is

$$\varsigma^{h+1} = \varsigma^h + \tau d^h \tag{4.33}$$

We search for $\varsigma^*$ that $l_\Delta(\varsigma^*) \leq l_\Delta(\varsigma^h)$ for $|\varsigma^* - \varsigma^h| < \delta$ where $\delta$ is a preset tolerance. The iterative process will also cease if $h$ reaches the maximum tolerated times of iteration.

The range of $\Delta$ depends on the injection duration, which varies according to the type of radiotracer injected. For example, the injection duration for FDG typically ranges from one to two minutes, thus, the range of $\Delta$ will be set as $[-1, 1]$ (based on past experience), and the values to be chosen from are 21 values identically segmented from $-1$ to $1$. Similarly, for a H2O study, the range of $\Delta$ will be set from $-5$ to $5$ seconds.

### 4.3.5 Bayesian Penalty

As the number of sampling points $m$ is usually somewhere between 20 and 50 (based on sampling and scanning protocols in PET studies, $e.g.$ see Table 5.1), which is somewhat small given the number of parameters ($i.e.$ four nonlinear and five linear parameters), a penalized weighted NLS criterion is also applied to improve overall estimation of the nonlinear parameters. The objective function is

$$L_\lambda(\theta) = \sum_{i=1}^{m} w_i(z_i - \eta_\Delta(t_i|\theta))^2 + \lambda(\theta - \mu)^T \Sigma^{-1}(\theta - \mu) \tag{4.34}$$

where $\mu$ and $\Sigma$ are the mean and covariance matrix of estimated $\hat{\theta}$ from a population, respectively, and $\lambda$ is the weight of the penalty. When $\lambda = 0$, the objective function only depends on the data. As $\lambda$ increases, the estimation increasingly accounts for historical information. This methodology adopts generalized cross validation (GCV) that takes the effective degree of freedom (DoF) of the penalized NLS into consideration when optimizing $\lambda$, since the value of $\lambda$ introduces bias to the optimization (O'Sullivan & Wahba 1985).

### 4.3.6 Leave-one-out Cross Validation

Before applying generalized cross validation (GCV), another validation scheme named leave-one-out cross validation (LOOCV) is used. It is similar to GCV in essence, and can be used to derive a formula of GCV score and to check the outcome from GCV. The LOOCV calculates the true error at each point from the curve produced by the model by estimating the value without information of said value (Cawley 2006). In other words, each time point is removed when estimating the value of that point, in order to calculate the mean cross validation error of all points from the curve. However, in our case, not all time points can be used. The starting and ending values would not be used for cross validation, since this may artificially increase the error by removing important information about the curve. Likewise, the peak time point cannot be used, since it sets the location of the curve. Then LOOCV is expressed as follow

$$LOOCV(\lambda) = \sum_{i=2, i\neq p}^{m-1} w_i[z_i - \hat{z}_i(\lambda)]^2 \tag{4.35}$$

where $p$ indexes peak time $t_p$. $\hat{z}_i(\lambda)$ is the estimated value at $t_i$ from the curve with $z_i$ omitted. By minimizing $LOOCV(\lambda)$, we optimize the weight of the penalty $\lambda$.

### 4.3.7 Generalized Cross Validation

Similarly to LOOCV, GCV estimates the true error of each fitted point, but it considers all time points (Golub et al. 1979). The GCV score is calculated by a weighted mean squared errors (MSE) divided by the effective degree of freedom.

$$GCV(\lambda) = \frac{1}{m}\sum_{i=1}^{m} w_i[z_i - \eta(t_i|\hat{\theta}_\lambda)]^2/[\frac{1}{m}trace(I - M(\lambda))]^2 \tag{4.36}$$

where $\hat{\theta}_\lambda$ is the estimated $\hat{\theta}$ based on given $\lambda$. $trace(\cdot)$ of a matrix is the summation of all elements on the main diagonal, $i.e.$ for an $m\times m$ matrix $S$,

$$trace(S) = \sum(s_{11} + s_{22} + \cdots + s_{mm}) \tag{4.37}$$

where $s_{ij}$ is the element of S at the $i$th row and $j$th column. $I$ denotes the identity matrix, also called unit matrix that has $m$ rows and columns

$$I = diag(1, 1, \cdots, 1) \tag{4.38}$$

and $M(\lambda)$ is also an $m\times m$ matrix defined as

$$M(\lambda) = A(A^TA + m\lambda I)^{-1}A^T \tag{4.39}$$

where $A$ is the component matrix (see Eq. (4.13)) given $\theta$ and $\Delta$.

### 4.3.8 Optimization

Figure 4.4 provides the optimizing steps for TRPM. An open source implementation of the software in R (R Core Team 2016) is made available (Xiu et al. 2020). For each given $\lambda$, and a given initial guess of the nonlinear parameters $\theta^0$ (see Eq. (4.19)), the corresponding $GCV(\lambda)$ and estimated $\hat{\theta}(\lambda)$ are

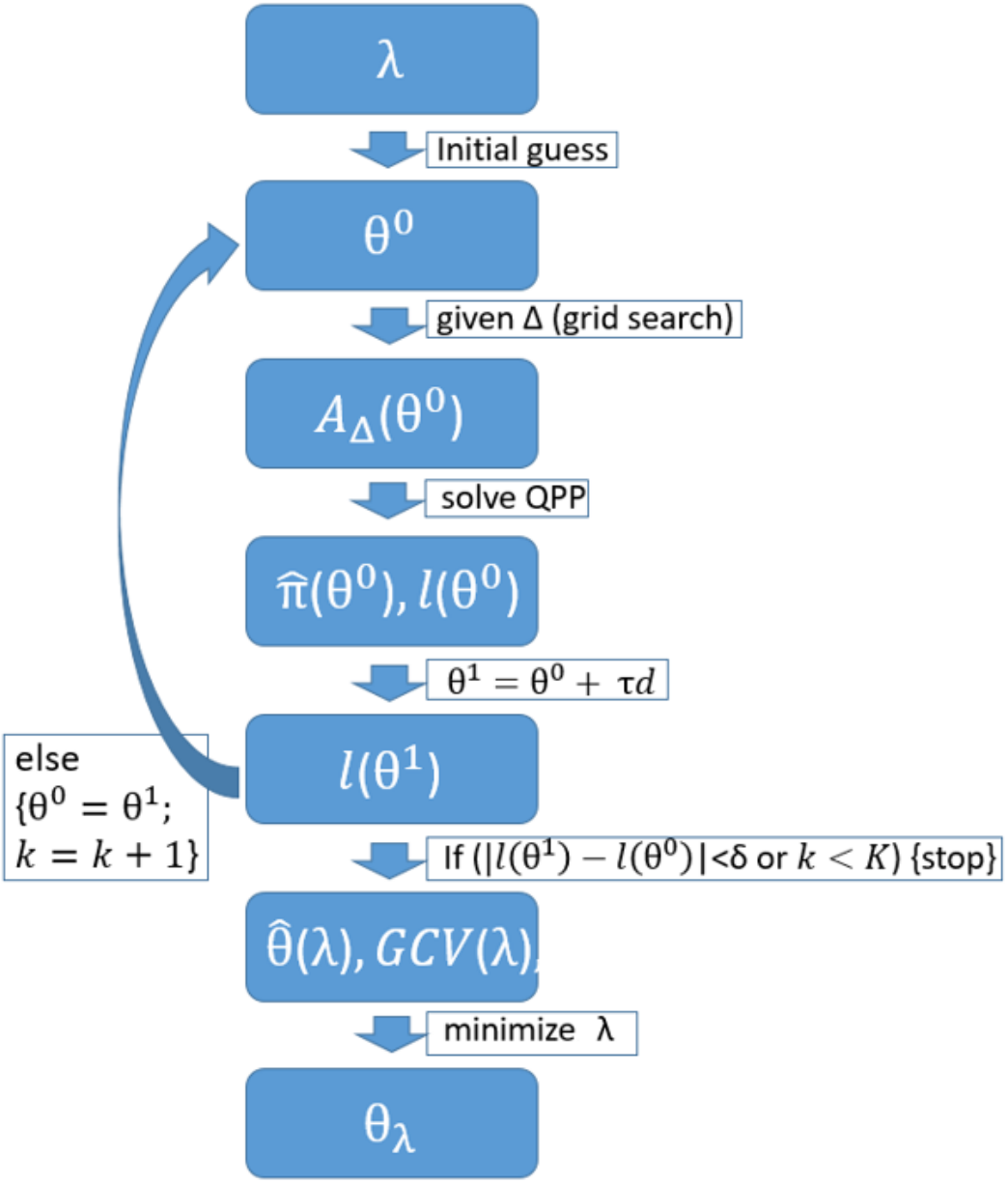


Figure 4.4: Diagram of steps in TRPM optimization.

produced. This step involves building component curves, using QPP and the Gauss-Newton method introduced previously in this chapter. Historical estimation of the exponential and gamma parameters in the model with Bayesian penalty (see Eq. (4.34)) for GCV calculation requires $\theta$ to be optimized for each arterially sampled AIF when $\lambda = 0$. By minimizing $GCV(\lambda)$, we are able to receive optimized $\hat{\theta}_\lambda$ for each individual AIF, as well as linear parameters $\hat{\pi}(\theta_\lambda)$ and optimized $\Delta$. Then, estimated AIF can be represented by plugging the estimated parameters into TRPM (see Eq. (4.7)).

## 4.4 Results

### 4.4.1 Data

In order to examine and evaluate the model, two datasets acquired from University of Washington are considered. Data include a set of directly sampled AIFs (sAIF) and a set of PET images along with patients' corresponding noninvasive information, $i.e.$ weight, height, gender and injection dose of the tracer. sAIF is considered the gold standard for AIF extraction. The shape and scale of sAIF both play significant roles in dynamic PET quantitative analysis in terms of the information that they carry. In that sense, sAIF can be not only used to evaluate the model of Eq. (4.7), but is also valuable for scale factor estimation. The peak of sAIF can be considered as the scale factor when the shape of AIF ($i.e.$ nAIF) has been estimated. For the imaging data, an ROI is drawn on site of arterial blood pool. When the left ventricle of the heart is in the PET FOV, it can be a good candidate, since the size of left ventricle is comparatively large as an arterial blood pool, and the location of left ventricle can be easily defined. The average concentration of tracer in the left ventricle region of interest (LV-ROI) is extracted as an alternative to sAIF. However, the LV-ROI contains limited information of the scale for true concentration of tracer in blood, thus it can only be used for shape estimation purpose.

#### 4.4.1.1 Directly Sampled Arterial Data

Directly sampled arterial data involve two separate datasets, one comprising of 91 FDG-PET studies and another of 39 $H_2O$-PET studies, all acquired at the University of Washington (Graham et al. 2002, Muzi et al. 2009, Eyal et al. 2010, O'Sullivan et al. 2009, Huang & O'Sullivan 2014). The data were from both healthy subjects and patients with cancer conditions. FDG studies included 36 females and 55 males with mean weight of 79.81 (sd=17.23) kg and height of 1.74 (0.10) m, mean injection dose of 9.26 (1.41) mCi, and peak activity of 1.74 (0.54) mCi. The $H_2O$ studies included 15 females and 24 males with mean weight of 76.13 (14.44) kg and height of 1.76 (0.08) m. The injection dose for $H_2O$ studies averaged to 22.72 (20.92) mCi and mean peak value was 13.57 (15.03) mCi. Durations of FDG injections are either 1 or 2 minutes (58 and 33 cases respectively), and bolus injection for $H_2O$ was assumed to be 5 seconds. After injection, water and FDG study will last around 5 and

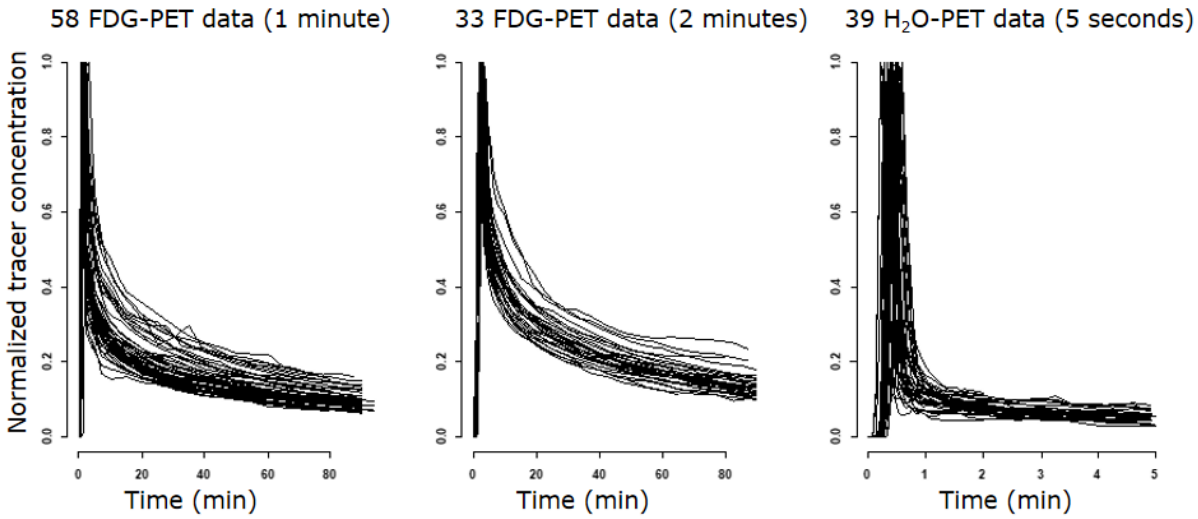


Figure 4.5: FDG-PET and $H_2O$-PET data acquired at the university of Washington (Graham et al. 2002, Muzi et al. 2009, Eyal et al. 2010, O'Sullivan et al. 2009, Huang & O'Sullivan 2014). FDG-PET data with 1-minute injection (left), FDG-PET data with 2-minute injection (mid) and $H_2O$-PET data with bolus injection (right).

90 minutes, respectively. The data included SAIFs of the subjects along with gender, weight (WT), height (HT) and injection dose (ID). The normalized AIFs are presented in Figure 4.5. Each curve typically includes three parts: a plateau of 0 concentration at the beginning, followed by a rapid increase after injection, and an exponential decay (see Fig. 3.4 for one example of each).

#### 4.4.1.2 PET Imaging Data

PET imaging data are from a study of PET imaging in locally advanced breast cancer (LABCa) patients whose protocols were approved by the institutional review board at University of Washington (Mankoff et al. 2003, Dunnwald et al. 2008, 2011, O'Sullivan et al. 2017). Fifty three selected patients were from the Breast Cancer Specialty Center in the university. They were historically confirmed breast carcinoma, and scheduled for chemotherapy prior to surgery. Patients underwent multiple PET scans before, during and after neoadjuvant chemotherapy, and the baseline imaging is of our interest. The imaging data involve PET images on an Advance Tomography (General Electric Medical Systems) from water and FDG studies for each patient. The injection was a 1- to 4-mL volume bolus of 725-1902 MBq for water studies, and a 7- to 10-mL volume infusion of 218-396 MBq over 2 minutes for FDG studies. Dynamic images

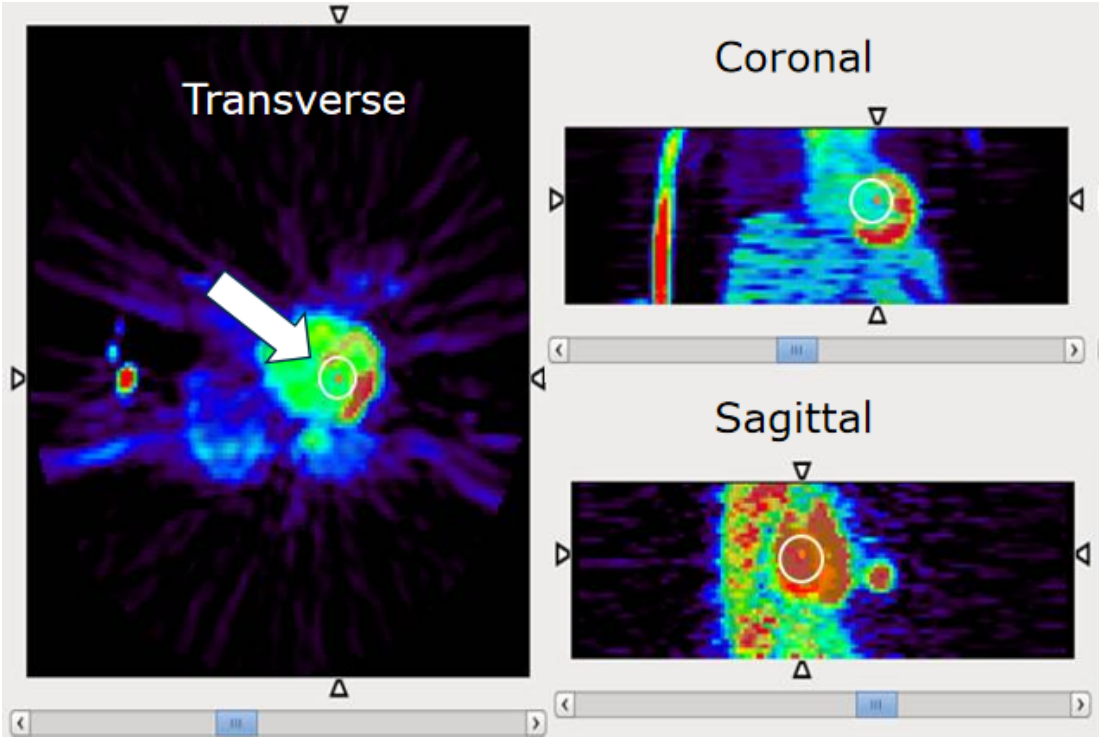


Figure 4.6: Exampled of manually drawn ROI on left ventricle of heart from PET imaging using AMIDE (Loening & Gambhir 2003). Small red circles with 6 mm diameter inside of big yellow markers in transverse (left), coronal (mid) and sagittal (right) views together as ROI for left ventricles.

were acquired over 7.75 and 60 minutes after the start of infusion for water and FDG study, respectively. Fifty seven and twenty five time points are considered for each water and FDG study, respectively.

ROI was a manually drawn sphere with diameter of 6 mm on the site of left ventricles of the heart for each image. The location can be easily found from the overlapped images, since the heart muscle around the left ventricle has visibly higher intensity than the inside and surrounding areas. The average of tracer concentration in ROI at each time point is extracted. The data may contain negative values at the beginning of the study, depending on the choice of image reconstruction settings, and they are set to be zero. No further smoothing is performed on the data, therefore, LV-ROI curves are noisier than sAIFs.

The full TRPM is applied for the FDG study due to the involvement of glucose in metabolic system. However, reduced models are also considered, since they may reduce parameters that are not effective. For the water study, a reduced TRPM is sufficient in theory, thus, we need to design experiments for choosing the correct components for the model. Erroneous design of the model may

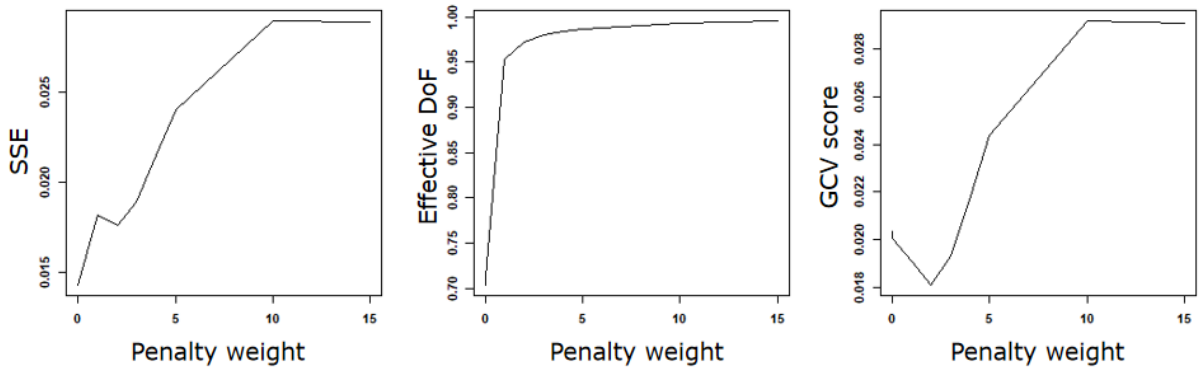


Figure 4.7: An example fit using TRPM with penalty: sum of squared error (left), effective degree of freedom (mid) and GCV score (right) against the weight of penalty.

cause reduced accuracy in cross validation of the prediction and unnecessary calculations.

### 4.4.2 Penalized TRPM

We present the performance of TRPM on arterially sampled AIFs without penalty in Appendix D. Then, using the estimated parameters as historical information, we fit all arterially sampled and imaging data by TRPM with penalty. For the FDG study, we use the full TRPM that includes all five components. We only use three components for water study since water will not be involved in as much complicated processes as FDG will. The relationship between the scale factor $A$ and estimated parameters is also analyzed in the end of this section.

The estimated parameters are used as a Bayesian penalty in TRPM. By applying this method, we can reduce potential greater fit error when we are fitting some particular individuals with high noise AIFs, especially for the imaging data which are usually noisier than sampled data. It can also enhance the ability of our model in the situation when information given is limited, $e.g.$ data with fewer time points or with only early period. As it is mentioned in Section 3.3.5, the $\lambda$ in Eq. (4.34) plays a role of weight for the penalty. When $\lambda = 0$, the optimization will only depend on the data. As $\lambda$ increases, the penalty takes more and more proportion in the optimization process. It means that the estimated parameters will be more likely to have a distribution that has the same parameters we estimated as the penalty.

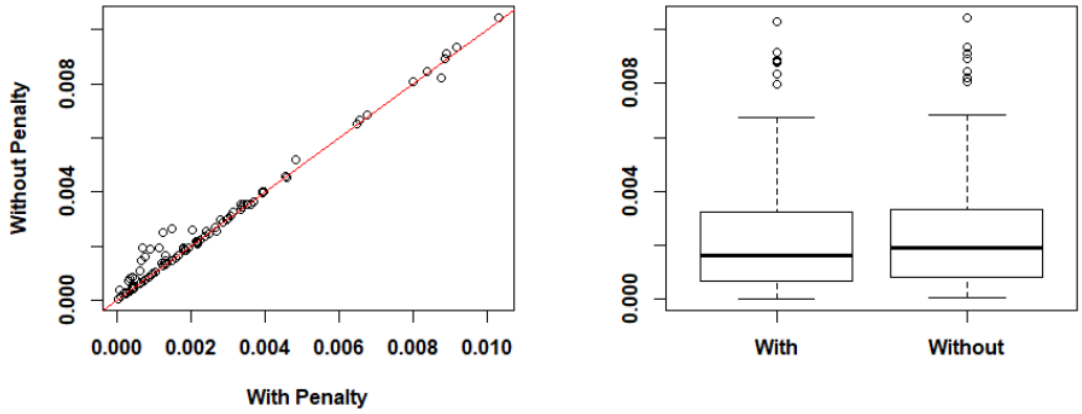


Figure 4.8: Scatter plot (left) and distributions (right) of mean squared errors of TRPM on 91 FDG studies.

Figure 4.7 presents an example of errors that we obtained from applying TRPM with penalty on one AIF from FDG study. The x-axis for three plots are the penalty weight, $i.e.\ \lambda$. We first set a vector of weights as the grid. And our algorithm searches for the $\hat{\lambda}$ that minimizes GCV score

$$GCV(\lambda) = \frac{\sum_{i=1}^{m} w_i[z_i - \eta(t_i|(\hat{\theta_\lambda}))]^2}{effective\ degree\ of\ freedom} \tag{4.40}$$

which is a different form of Eq. (4.36) in Section 3.3.7. For individual fit, the sum of squared error and the effective degree of freedom are increased as the penalty weight increases. But the GCV score is a convex function, which we seek to minimize.

We apply penalized TRPM on arterially sample data here, and run some comparisons between the parameters we estimated from this section.

#### 4.4.2.1 FDG Studies

Figure 4.8 gives a visual interpretation of the benefit of penalization in our TRPM. From the scatter plot, the points on the left of the unit line (red) indicate instance for this fit where penalized TRPM outperforms TRPM.

Then we look at the performance of TRPM on individual time points in Figure 4.9. We can see that both provide similar results. The total sum of squared residuals from estimations using TRPM with and without penalty are 5.78 and 6.13, respectively. Adding a penalty reduces the overall fit error by 5.7%, compared to a fit obtained without penalty.

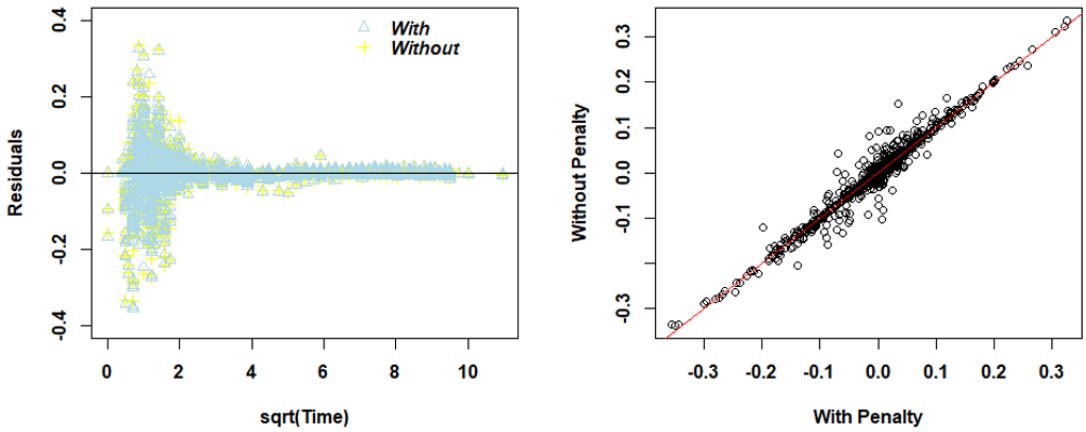


Figure 4.9: Left: Residuals of 2465 AIF data points against square root of time (minute); Right: Scatter plot of Residuals from TRPM with and without penalty.

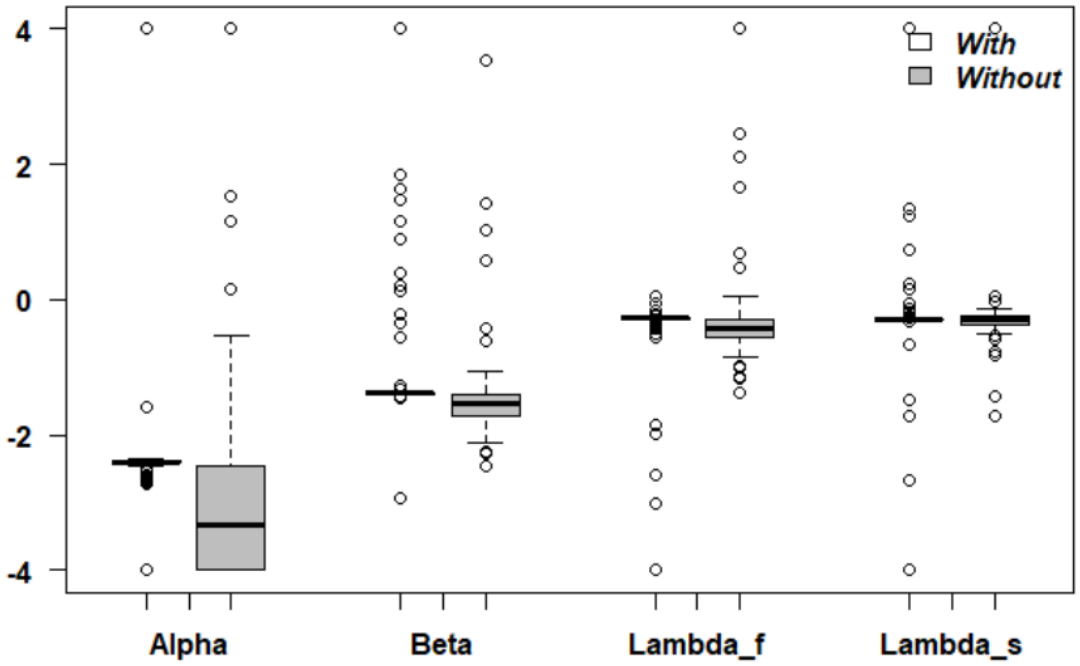


Figure 4.10: Distributions of parameter estimates (logit transformed) from TRPM with and without penalty on FDG study.

Figure 4.10 compares estimated parameters and the penalty. Since all the non-linear parameters except shift are parameterized by a logit transform (see Section 3.3.4) before they are optimized, we present transformed parameters. The penalty reduces the variance of estimated parameters dramatically. Depending on the scale and variation of those parameters, the estimations can be deemed matching the penalty.

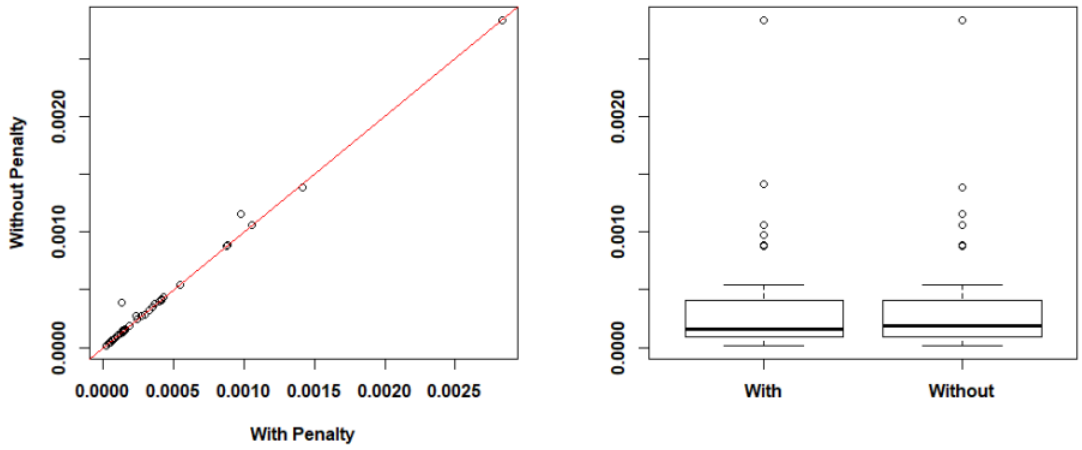


Figure 4.11: Scatter plot (left) and distributions (right) of mean squared errors of TRPM on 39 water studies.

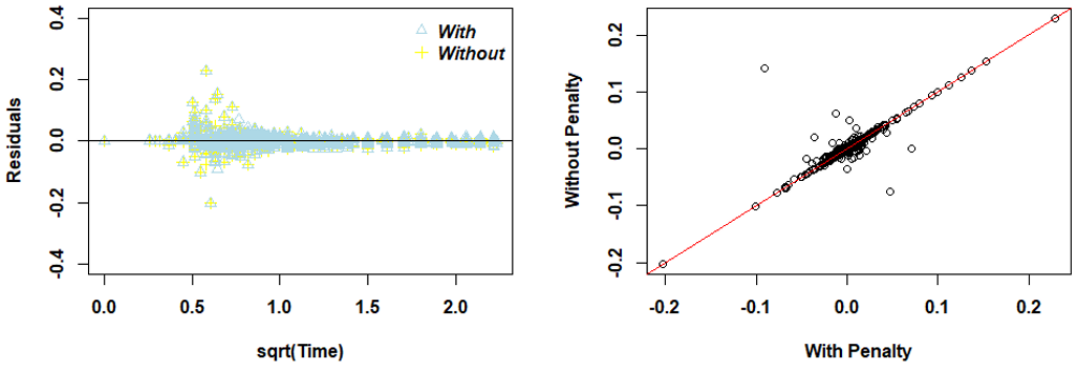


Figure 4.12: Left: Residuals of 1117 AIF data points against square root of time (minute); Right: Scatter plot of Residuals from TRPM with and without penalty.

#### 4.4.2.2 Water Studies

Then we look at the performance of TRPM with penalty on the water study. Figure 4.11 presents the MSE of 39 fit on AIFs from the water study. The median of MSE for TRPM with penalty is smaller than it without penalty. The mean and standard deviation (in brackets) is 3.68(5.19) $\cdot 10^{-4}$ and 3.80(5.22) $\cdot 10^{-4}$ for TRPM with and without penalty, respectively. Then mean of MSE for TRPM with penalty is 3.2% smaller. It coincides with the plot that the difference between the two measures is small.

Then we assess the fit on each individual. There are 1117 time points for the water study. The overall performance for both measurements looks similar in Figure 4.12. Sum squared error of 1117 points for TRPM with and without penalty is 0.408 and 0.418, respectively. The model with penalty reduces the SSE by only 2.4%.

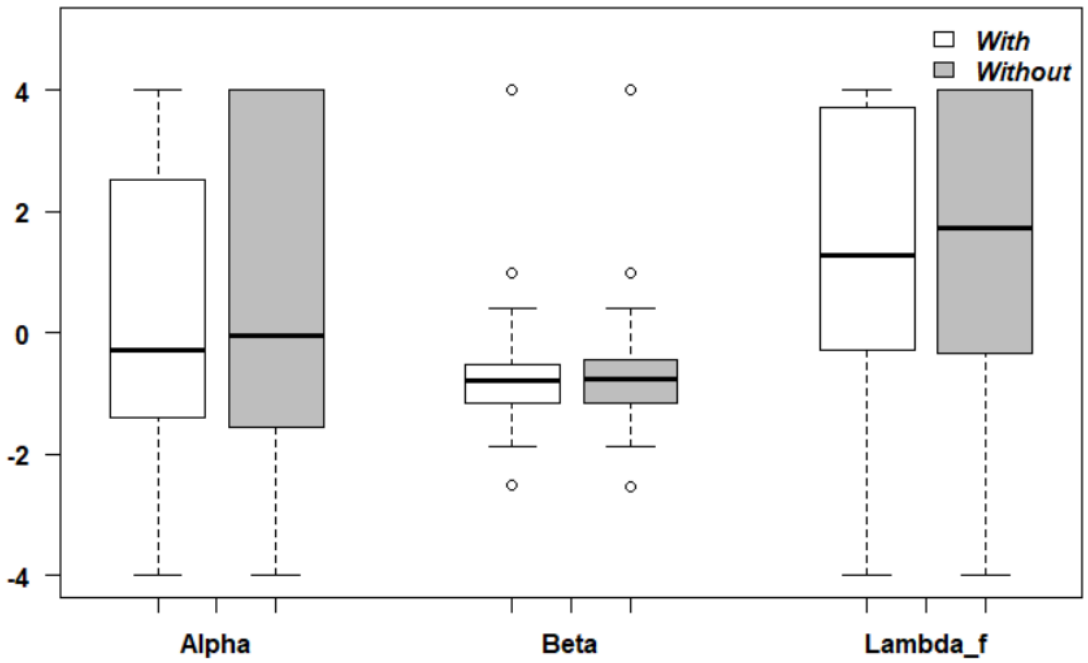


Figure 4.13: Distributions of parameter estimates (logit transformed) from TRPM with and without penalty on the water study.

Figure 4.13 presents the distribution of transformed parameters. It is clear that the estimated parameter using TRPM with penalty has smaller range and similar median to the penalty itself. This is reasonable since the application of penalty makes the estimations have similar distribution to penalty itself.

Taking the above into consideration, TRPM works well even without penalty in terms of the errors in absolute value and percentage. However, the use of penalty in TRPM increases the accuracy of model. In the future application of TRPM, when facing problems without enough information, $i.e.$ lack of data or very noisy data, the TRPM with penalty will bring more benefit in the optimization process. Nevertheless, the disadvantage of adding a penalty is that it dramatically increases the calculation time of optimization. It can take over 10 times of the calculation comparing to the TRPM without penalty for each individual fit. Also, it needs historical information to be analyzed before we can apply them, which may bring some unnecessary work. At this stage, we still believe that the advantage of using a penalty outweighs its disadvantage. The Bayesian penalty in future updates may enable automatic model training via machine learning techniques. With other information of the patients, distribution of parameters may be more specific if we can find the correlation between the patients' information and the model parameters. Here we will conduct more

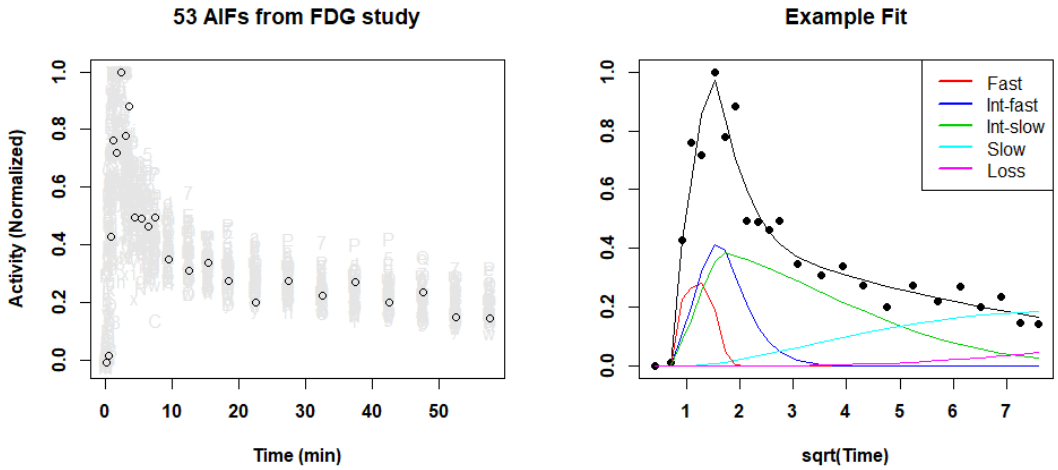


Figure 4.14: Left: 53 AIFs from FDG imaging data (grey) and one example (black); Right: Performance of TRPM on that example.

assessments of the model in imaging data.

### 4.4.3 Assessment of TRPM with Penalty on Imaging Data

The imaging data is introduced in Section 3.2.2. The difference between two sets of data is that the imaging data is very noisy. The curve from the image dataset is not as smooth as it from the directly sampled dataset. In this sense, a more comprehensive assessment of the performance of estimation is suggested. We will compare the estimated parameters with the penalty and check how the distribution of estimations performs. Since the two data sets have some distinct features, the results can be interesting in two ways. Would the parameters estimated from the directly sampled data match the ones from the imaging data, and how is the performance of TRPM on noisy data set?

#### 4.4.3.1 FDG Studies

Figure 4.14 presents the 53 AIFs from the FDG imaging data and one example fit. The sampling frame follows a same protocol which can be observed in the left plot. Then we look at the example fit. It is easy see that the curve is not smooth, but the fit is reasonable. To give a visual intuition about the performance, we present more examples in Figure 4.15. The fits catch most of the pattern to AIFs from imaging data. There are points off the fitted curves, but the trend of the curves are reasonably fitted for each example.

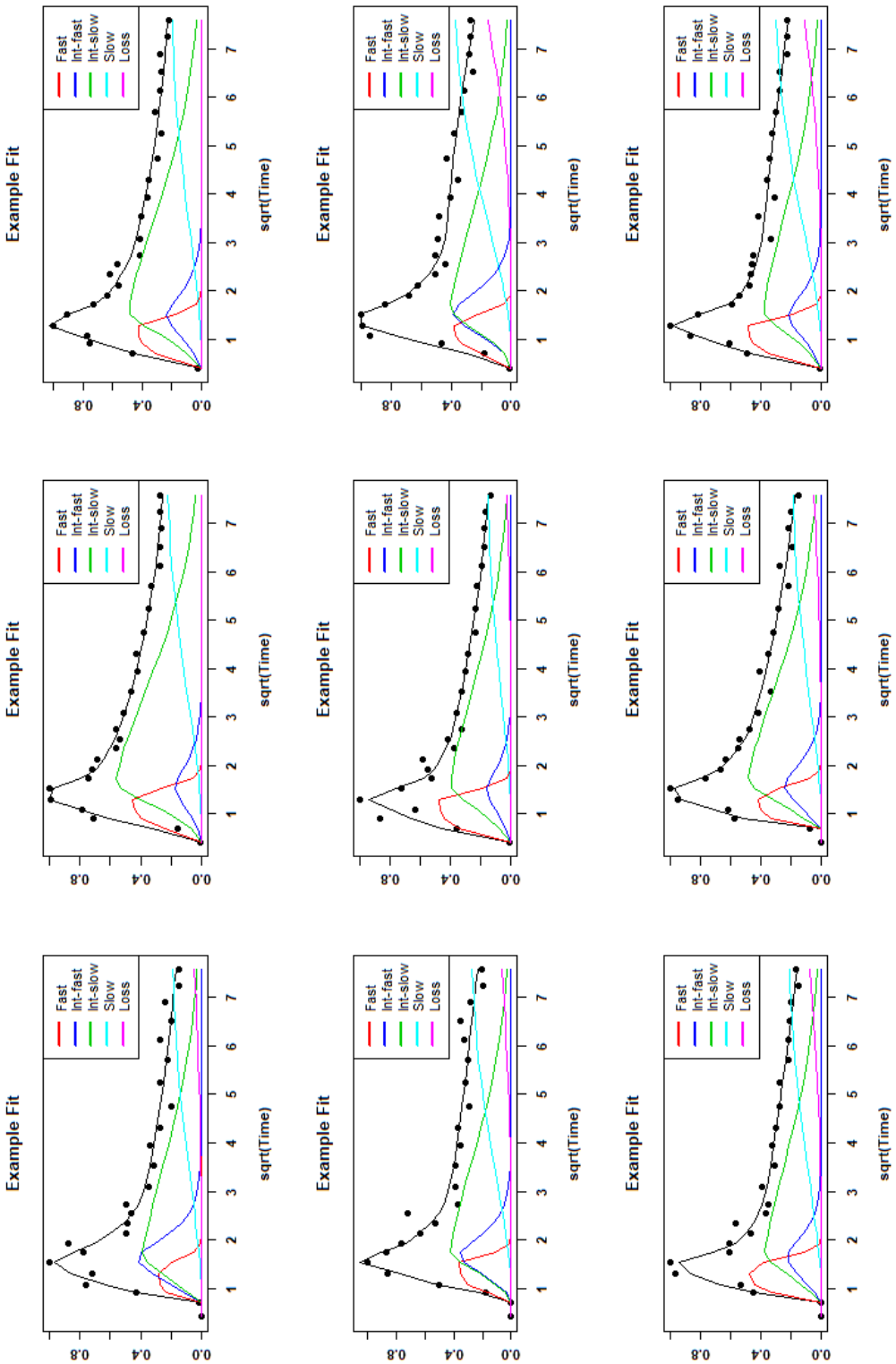


Figure 4.15: Nine example fits using TRPM on imaging FDG AIFs.

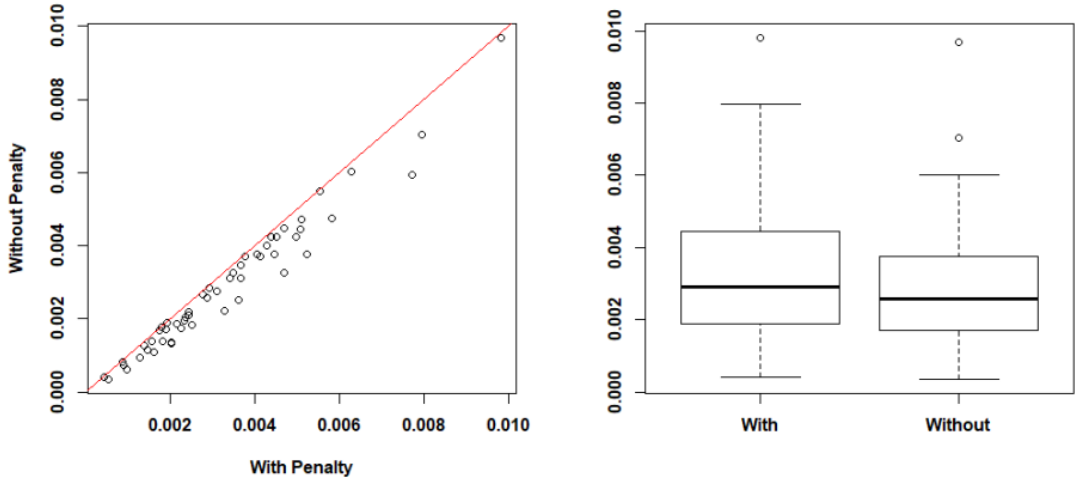


Figure 4.16: Scatter plot (left) and distributions (right) of mean squared errors of TRPM on 53 FDG studies from imaging data set using TRPM with and without penalty.

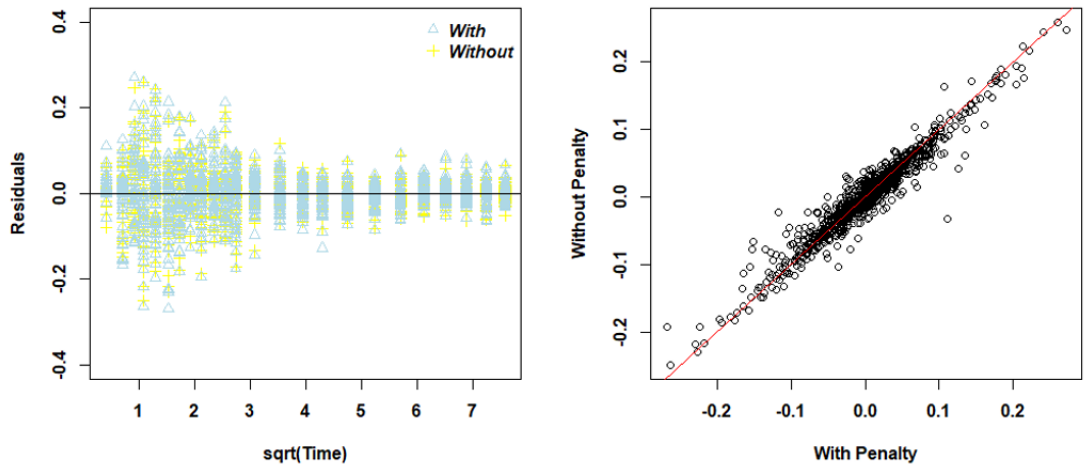


Figure 4.17: Comparison of residuals for 1273 individual points in FDG studies from imaging data set using TRPM with and without penalty.

Figure 4.16 and 4.17 provide a reference of the errors produced in the optimization process. TRPM without penalty outperforms TRPM with penalty. But in terms of GCV score, the TRPM with penalty is definitely better, since $\lambda = 0$ is one of the options in the selection of the penalty weight. Behaviors of the curves from two sets of data are different, thus, the difference between sum of squared errors (0.176 vs 0.154) is acceptable. Also, the noise of imaging data is comparatively great. The greater error may not imply a worse fit. From the example fits, we can see that those estimated curves are reasonably good and the consistency of estimations is also good.

Figure 4.18 indicates the fact that the penalty strongly effects the estimation.

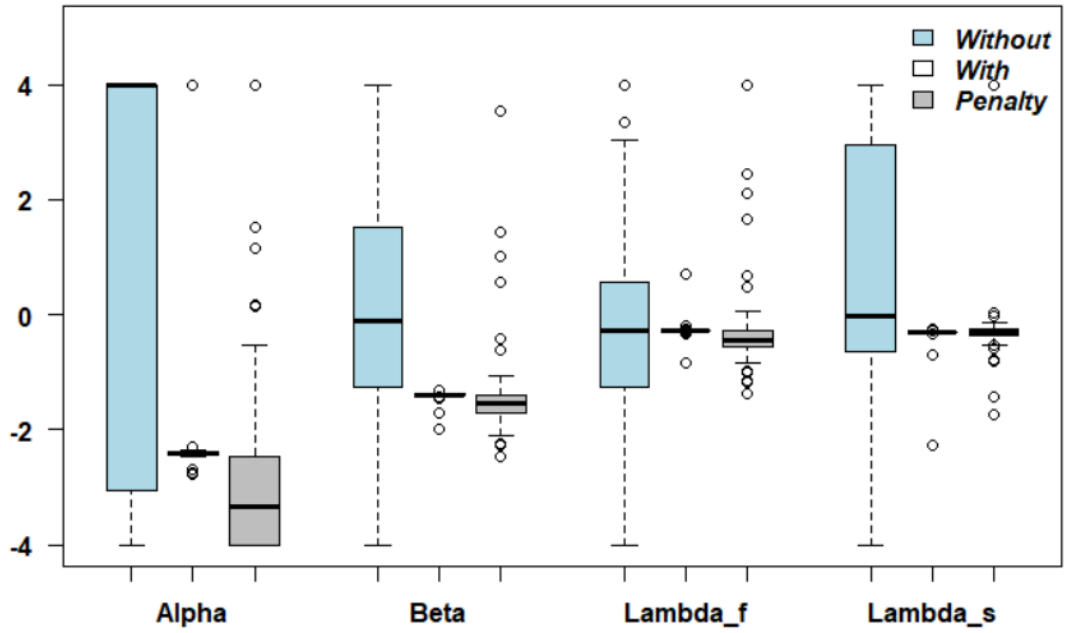


Figure 4.18: Distributions of parameter estimates from 53 FDG studies using TRPM without the penalty term ($Without$) and with the penalty term ($With$), and distributions of the penalty for model parameter estimation ($Penalty$).

Without penalty, we can see the estimated parameters spread over the whole domain. The variation of parameters brings a better MSE result, but it reduces the constancy of model. That is why in terms of a cross validation error, the TRPM with penalty performs better. In Figure 4.18, the estimated parameters from TRPM with penalty have very small variation. This virtue can be potentially used in future for fixing those parameters or locating them in a given interval of estimates more accurately. If the non-linear parameters in TRPM can be fixed or even predicted easily, the TRPM will be only a problem of solving a quadratic function. The numerical and computational complexity involved in the calculation process will be dramatically reduced.

#### 4.4.3.2 Water Studies

Figure 4.19 gives the AIFs from the water studies. Along with Figure 4.20, we can visually assess examples of performance on TRPM for water studies. At the early time, when the AIF is rapidly increasing and decreasing, the fit catches that pattern well. Also the model could fit most of the peak points with reasonable accuracy. However, from these examples, we can see that the fitted peak values are always smaller than the actual ones. Especially for the mid-right of the plot in Figure 4.20, the estimated peak is quite off.

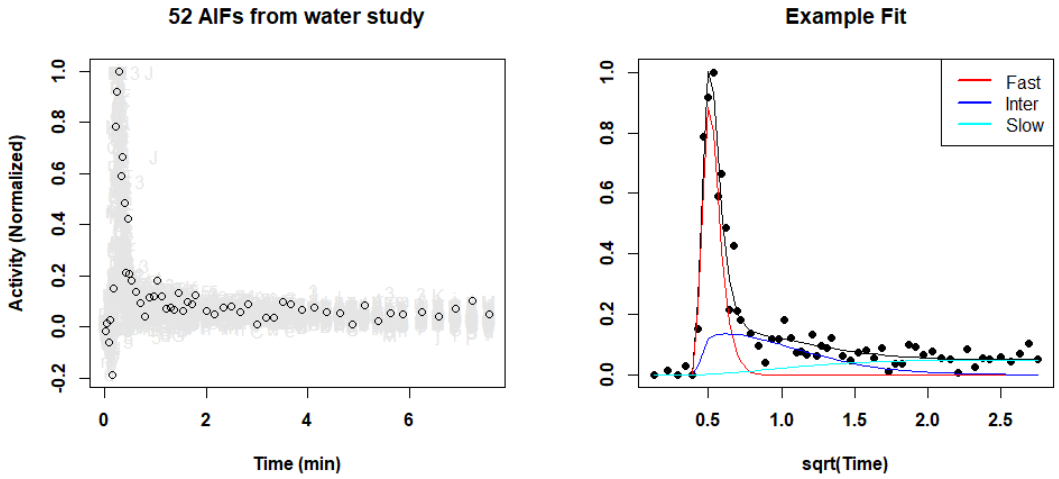


Figure 4.19: Left: 52 AIFs from water imaging data (grey) and one example (black); Right: Performance of TRPM on that example. See Appendix D for the definition of Fast, Inter and Slow curves of TRPM in the water study.

Considering all fits, 31 out of 52 peak values are underestimated, and only 13 are overestimated. The model tends to underestimated the peak, which may effect the estimation of contrast (a peak to tail ratio), then the other parameters derived from or depending on it. One of the reasons why TRPM fails to fit the peak is that variation of AIFs at the beginning of study is greater than late study. However, we do not add enough weights to them, then the fit error depending on those points contributes less than they should do. Another reason could be that TRPM cannot distinguish the peak time from the other ones. We do not have an auto system to set the actual peak time to be peak time in our model. The estimated curve is actually shifted. These two reasons could be the main cause of the underestimation to peak values. From my perspective, overestimation is better than underestimation, since if the value is already detected, the true peak value should greater or equal to the detected peak value. This need to be reconsidered. Since the imaging data is noisy, we cannot jump to the conclusion before we can prove it. Anyway, we can see that although the estimated peak is not always the actual peak, the difference between two values is comparatively small.

The tails of AIFs from the water studies are very noisy, but the trend of slow decay is clear, and the pattern is well captured by our model. Taking the above into consideration, the overall performance of fit using TRPM on 52 AIFs from imaging data of water studies seems reasonable.

Then we do some comparisons between TRPM on the same dataset with and

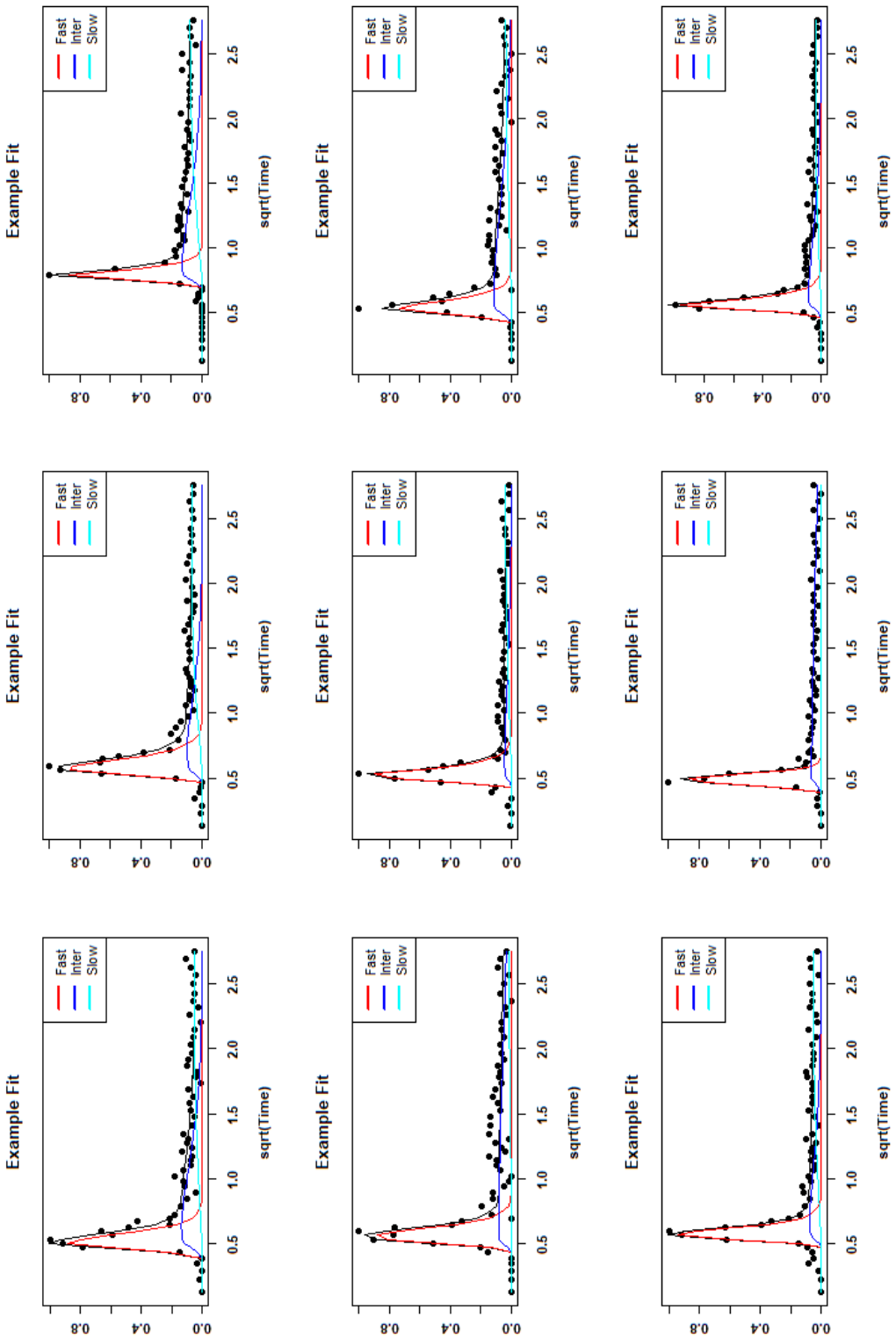


Figure 4.20: Nine example fits using TRPM on water AIFs.

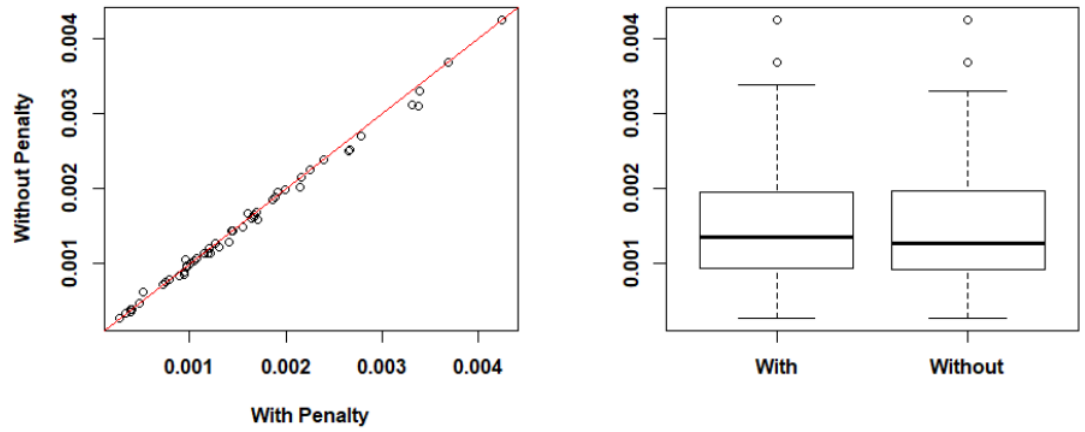


Figure 4.21: Scatter plot (left) and distributions (right) of mean squared errors of TRPM on 52 water studies from imaging data set using TRPM with and without penalty.

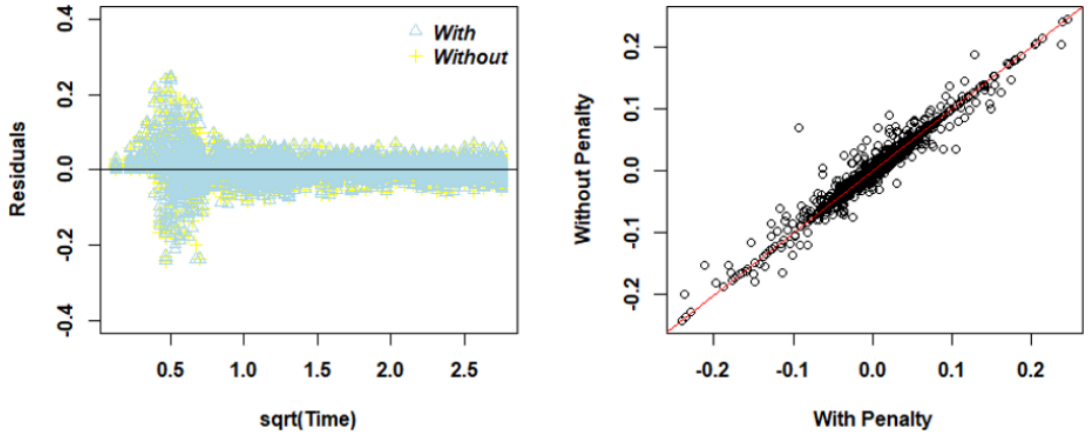


Figure 4.22: Comparison of residuals for 2912 individual points in water studies from imaging data using TRPM with and without penalty.

without penalty like we do for the FDG study. Figures 4.21 and 4.22 present errors that TRPM produces for each subject and individual sampling point. The results show that the difference between the two methods is negligible. For a fewer number of parameters, $i.e.$, 3 nonlinear parameters for TRPM for the water study, the advantage of adding a penalty is not as important as for models with a greater number of parameters. Figure 4.23 shows that the effect of penalty for water studies is less than that for FDG studies. The estimated parameters using TRPM with penalty tend to have similar distributions to those from TRPM without penalty. Estimation remains highly dependent on the data itself.

Table 4.1 shows that the standard deviation of the estimation is reduced by adding a penalty to our model. The mean estimates for each parameter con-

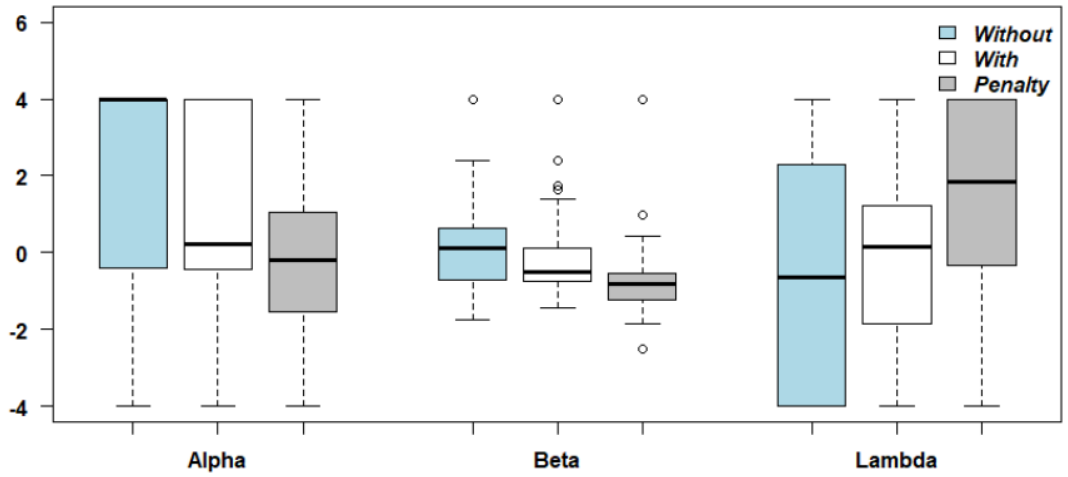


Figure 4.23: Distributions of parameter estimates from 52 water studies using TRPM without the penalty term ($Without$) and with the penalty term ($With$), and distributions of the penalty for model parameter estimation ($Penalty$).

verges to the theoretical mean of the penalty, which coincides with our expectation. This indicates that the penalty may not greatly improve on the typical error produced in TRPM. However, it mitigates the magnitude of estimation error, and thus reduce the variation in estimations at the individual subject level.

Table 4.1: Mean (standard deviation) of estimated parameters using different methods (TRPM without the penalty term (Without), TRPM with the penalty term (With), and TRPM penalty for model parameter estimation (Penalty)) in water studies.

| | $\alpha$ | $\beta$ | $\lambda$ |
|---|---|---|---|
| Without | 1.77 (2.80) | 0.12 (1.32) | -0.56 (3.09) |
| With | 1.19 (2.42) | -0.02 (1.29) | -0.13 (2.43) |
| Penalty | 0.13 (2.91) | -0.67 (1.03) | 1.19 (2.84) |

## 4.5 Discussion

Taking the above results into consideration, the TRPM has been proven a good model for AIF prediction in Dynamic PET FDG and water studies. The fitted curves consistently capture the main patterns in the data. Estimation performance when using penalization is reasonable and consistent with our expectation.

### 4.5.1 Computational Complexity

TRPM involves more or less nonlinear components. The expression of these components needs a good understanding of the relationship between shape of each component and the parameter involved in it. Gamma density as the input pattern is the core in our model. In order to accurately create these nonlinear curves, we need to add linear interpolation to the curves multiple times. For this reason, we take more time points into consideration during the optimization process. One shift parameter in the model is found by grid search. This parameter is about the time delay that adjusts the sampling time. Introducing this parameter is important to improve the accuracy of TRPM when fitting to different patients with different sampling times. This parameter is necessary unless we have a precise and detailed injection protocol to estimate it.

The estimation procedure involves the Gauss-Newton iteration method, which can end up being a bottleneck in R. Moreover, GCV brings massive calculation complexity in not only programing, but also computing in R. Each grid search for the penalty weight increases calculation time. We have sacrificed a great deal of time consumption for the accuracy and consistency of TRPM, but the code could be optimized. Other free software such as C could be considered in that sense, since C can be faster when dealing with large numbers of iterations.

### 4.5.2 Interpretation of the Components

In Section 3.2.1, the components in TRPM are introduced in detail. The question here is that do we need more evidence to prove that the components are what we expected. For example, as we apply the gamma density, the AUC represents expected travel time of the tracer. This can be true for all the basis curves. With knowledge of the body functioning to the tracer, some of the travel time may be able to estimated from other studies. If this travel time is not what we expect, other interpretations should be prepared. Even more components could be added to the model if we have more information about the behavior of the tracer. Under this condition, some components could turn to be fixed by specifying the parameters from the population. Then the nonlinear least squares can be removed from the model optimization procedure. As a result, the components will be more meaningful and useful for further analysis of model parameters and physiological parameters of the patients.

Also, there are some remaining questions about the loss curve. Although in practice, the loss curve will be regarded as part of curve that represents the long term retention of the tracer molecules along with the slow curve, the concept of this curve is abstract. In fact, the loss curve is derived from a more complicated curve in Section 3.2.1. The slow curve and loss curve have interaction with each other. Proportion of the slow curve and the loss curve can construct a positive curve. This curve actually represents a group of tracer molecules that are unlikely to come back from the tissue. Then I believe that this is even harder to interpret the reason why a positive curve represents a group of tracer molecules being sampled that never come to sampling point. Introducing the loss curve to TRPM is for a better understanding of the destination for all the tracer molecules introduced to the subject. Loss and slow curves together can provide a positive curve that can be accepted easier. The interpretation of loss curve still needs more exploration.

Finally, the nonlinear parameters except the shift are all from some distribution densities. They either represent the shape or scale of the distribution. With estimated parameters, the mean and variance of the distribution can be calculated. If any of these parameters can be connected to existing physiological parameters of body circulation system or dynamic PET studies, even physical parameters $e.g.$ BSA of the subject, that could improve model relevance to specific cohorts and therefore increase its performance.

### 4.5.3 Interpretation of the Linear Parameters

Linear parameters of TRPM represent the proportion of each component over time. At a particular time, the product of the component value and its linear coefficient is the concentration of tracer in the same group. However, interpretation of the linear coefficients is not easy. From past experience, we know the linear coefficient of the fast curve is normally the greatest. This is because the absolute value of AIF at the beginning of study is greater than at the late times. Linear coefficients of fast and intermediate curves interact with each other. A greater coefficient of the fast curve usually results in a smaller coefficient of the intermediate curve. Linear coefficients of the slow curve tend to be close in value to the tail height of the AIF.

The reason for this is that each component of the model gets normalized when optimizing the linear parameters, which results in removal of information on

the scale factors of these components. Without normalizing, the linear parameters in TRPM could have carried more practical information. Thus, the actual values of these parameters may not be of interest, but a value that is either too large or too small should be taken into consideration as it may flag issues, especially in view of the ambiguity between the linear and non-linear parameters present in the model. This further hinders their physiological interpretation.

### 4.5.4 Weights

In the optimization process, assigning each value of AIF a weight seems to be a reasonable thing to do. We know that the variation of AIF at the beginning of study is greater. As the study continues, the concentration of tracer in body tends to reach the equilibrium. Usually, the weight given to each point can account for the variance of the value at that point. We give a greater weight to a point that has a greater variation or to a point whose value is more important. In our study, the greatest weight should be given to the peak of AIF. The tail of AIF can be given a smaller weight. The weights can either be constants that depend on the difference between variance of peak and tail value, or be directly derived from the inverse of the variance.

In our study, the weights are set to be 1 for each point. It means that we have not introduced any special weight to any point for our model. Actually, several attempts have been performed using different settings of weights. However, none of them improve the prediction of AIF, not only in terms of the overall performance, but also for the fit to the peak value itself. This does not mean that the weights are not working. If we check the performance of our model in the last section, we know that there are fewer points at the beginning of the AIF and the fits on them are not as good as fits to the tail in terms of the fit errors. Absolute values of AIF at the beginning as so much greater that at the tail, as well as the noise. Then part of the fit error is caused by the data. In this sense, we allow greater fit error at the early study. However, the performance of TRPM fitting an AIF at the early study is important since those values are essential for deriving some parameters in PET dynamic study, $e.g.$ the peak to tail ratio and the AUC. Here, we may still need to find a way to distinguish the random error from the systematic error.

### 4.5.5 Scale Factor Estimation

TRPM can be used to fit normalized AIFs. However, determination of the AIF requires the scale factor or the true peak value to be estimated. The scale factor has a close relationship with the injection dose of the tracer and physical parameters of the subject (Zanderigo et al. 2014). We attempted to connect some of our estimated parameters to the patients' physical information by applying regression analysis, but these attempts did not prove effective. Then we also conducted a regression analysis of the scale factor with respect to the parameter estimates, with comparably disappointing results. Further improvement of the model in future work, with improved interpretation of the model parameter estimates, may help establish a suitable relationship between the latter and the scale factor.

### 4.5.6 Comparison with Existing Models

Some mathematical models like Feng's model (Feng et al. 1993), tri-exponential models (Parsey et al. 2000) and convoluted models (Tonietto et al. 2015) have been introduced in Section 3.5. Model that based on physical and physiological change in blood circulation system of body like BCM (Huang & O'Sullivan 2014, O'Sullivan et al. 2017) is also introduced in Section 3.7. We so far have done comparison between our TRPM and BCM. TRPM is faster in calculation time and more accurate in terms of fit error produced in fitting AIFs. Cross validation will be implemented for model assessment and benchmarking in future works aiming at developing the TRPM. BCM has a comprehensive and detailed interpretation of the tracer kinetic in blood circulation system whereas TRPM provides a simpler concept applying the knowledge of compartmental models and blood circulation system. Each has potential to explore the relationship between parameters in models and subjects. The calculation time for TRPM is definitely longer than these mathematical models since TRPM involves more complicated formulas and optimization procedures. However, the accuracy of TRPM need to be compared with those models. On one hand, we can check the gain when we sacrifice the calculation time. On the other hand, the TRPM is built under a physiological background. If the it can outperform the other models, the application of TRPM can extend more in the clinical use.

### 4.5.7 Estimation of Tracer Kinetic Parameters in Tracer Kinetics

In Section 2.2, some analytical methods for tracer kinetics are mentioned. Those parameters involved are of our great interest, $i.e.$ AUC, volume of distribution. Using AIF estimated from TRPM to derive these parameters is the goal. If we have more comprehensive data that include information of both PET image data and corresponding blood samples that we can check the estimation, we are able to validate and understand TRPM in a more comprehensive way.

In Section 2.3.6, SIME is introduced as a alternative method for AIF extraction (2011). This method involves interaction between AIF models and compartmental models. The idea from it has potential to improve TRPM since TRPM also has a relationship with compartmental models. If the connection can be quantified, $i.e.$ the parameters in TRPM can be transformed to parameters in compartmental models, the simultaneous estimation may be possible. However, this method needs more than one region to work on (Koon-Pong Wong; Feng 2001). Parameter setting before optimization in TRPM requires past experience of applying the model on one region. If the target is arterial blood pool, the setting will be the same as what we obtained from previous fitting on arterially sampled data. If the target is a venous blood pool or mixed blood pool, the parameters involved in TRPM are different. We have not tested the performance of TRPM in fitting other regions that include not only arterial blood. The model is expected to work for it, but the interpretation of parameters estimated from fitting those blood curves need to be redefined. The relationship between parameters of arterial and venous blood is our interest.

### 4.5.8 Application to Other Tracers

So far, TRPM has been only applied in FDG and water studies. We know that the settings for TRPM in fitting different tracers differ. For each new tracer, a thorough analysis needs to be conducted based on a set of directly sampled data. This involves choosing components, finding the best initial guess and range of parameters, optimizing historical estimations, $etc.$. Further exploration should be done for other commonly used tracers.

We introduced in Section 2.1.3 that there is a group of tracers involved in receptor binding in the nervous system. Also from Section 2.2.2, we know how

the compartmental models work for these tracers. It would be interesting to apply TRPM to such data. The model selection should be similar to that of FDG studies.

# Chapter 5

# Population-based Projection Modelling of AIFs

## 5.1 Introduction

The TRPM can accurately estimate and describe the AIF. However, the limitations of the TRPM (see Section 4.5) would outweigh its merit, $e.g.$ the ambiguity of the model parameters and the computational complexity, which leads us to develop a more efficient and adaptive method. Firstly, we want to simplify the computational process in individual AIF fitting, and at the same time, the model still contains the tracer's characteristics of its travel rate in blood circulation system. Secondly, we deploy the relationship between the components and the linear parameters within TRPM, and find the pattern of how they interact in the fitting process. Thirdly, a novel method for prediction of the scale factor can be developed based on the parameters within the proposed model. Then, the method should statistically outperform or at least have a similar accuracy in fitting AIFs with existing methods. Besides, the estimated AIF from the model should be applicable in deriving the parameters within PET kinetic models ($e.g.$ two-compartmental model for FDG study). Finally, the proposed model should be applicable to different tracers in a easy way.

Here we consider a modified PBIF-type approach by adjusting a population AIF profile to individual characteristics extracted from either arterial sampling or image-derived data, to achieve reliable patient-adaptive AIF estimation throughout the whole time course. In a sense the proposed population-based projection model (PBPM) combines population profiling (as in a PBIF approach) with in-

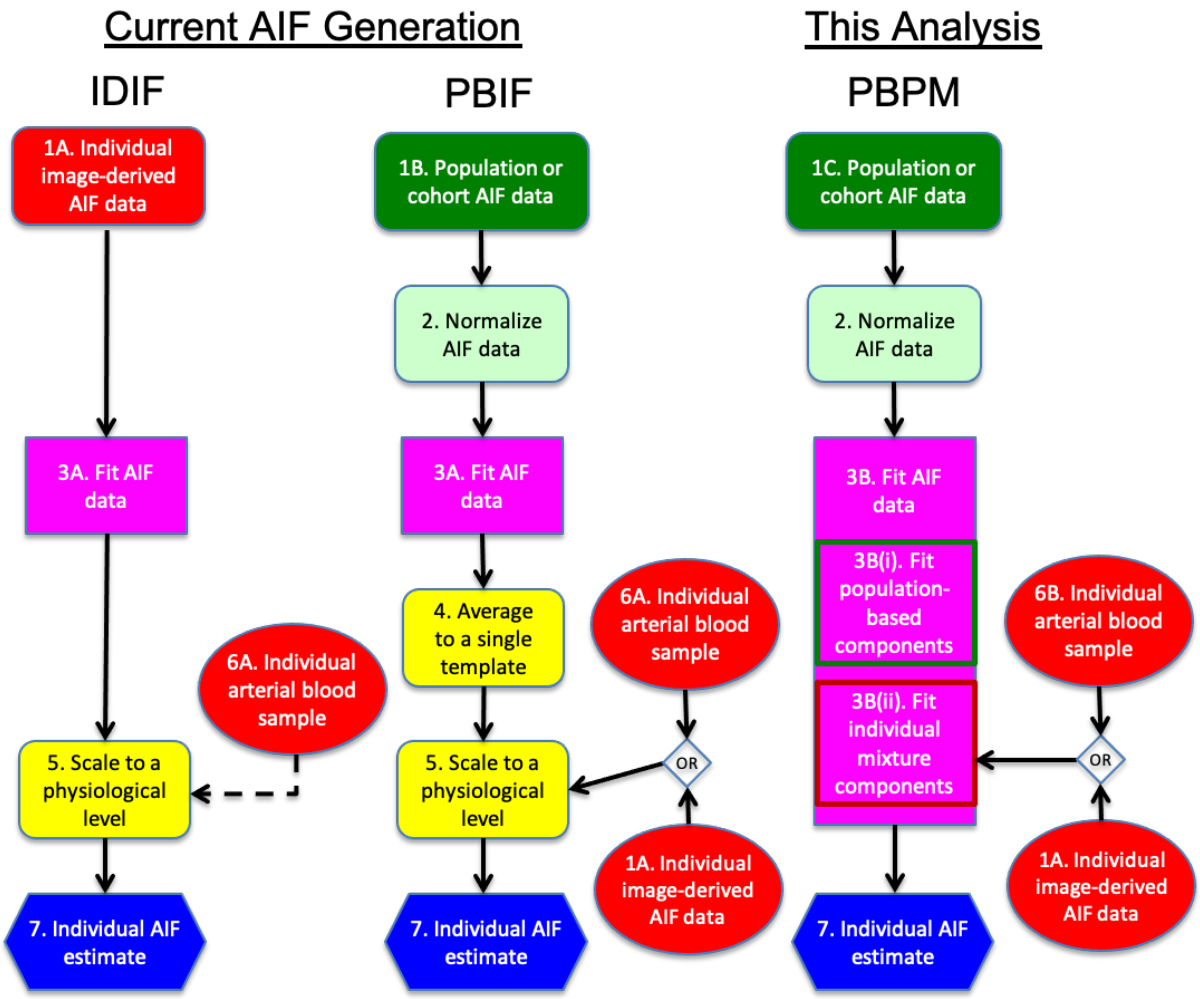


Figure 5.1: Flowchart of typical PBIF and IDIF strategies, along with the proposed PBPM methodology. Red and green blocks indicate use of individual subject and population data respectively. Step 3 of each method is an AIF model fitting step. Blood sampling for step 6A is not used in some IDIF approaches (hence the dashed line); when used, fewer points are typically required compared to blood sampling used in step 6B. Using individual image-derived data (1A) at step 3B(ii) of the PBPM approach (instead of arterial sampling data) would require an extra step in order to scale the output to a physiological level, as in step 5 of an IDIF method.

dividual arterial input data modelling (as in an IDIF approach). As such, it differs from both these strategies, in a number of ways. Unlike IDIF strategies, the PBPM leverages population information, and does not depend on the availability of imaging data (although it can also be applied using such data). Unlike PBIF strategies, it does not average population components into a single individual template pattern, but instead produces a different pattern for each individual, by fitting a linear mixture of population profile components

to subject-specific arterial sampling data. Fig. 5.1 describes the overall process and illustrates how it differs from typical PBIF and IDIF processes. To produce individual fits, the PBPM mixture components are fitted to population data, and a combination of these fits is adapted to each subject, unlike with Tri-exponential-type (TE-type) methods. The latter could also be adapted for use in step 3B in the flowchart, but no such report was found in the literature. The proposed PBPM allows the use of functions other than exponentials, should a particular tracer require it, and can operate with a different number of components depending on the PET tracer used. This number can be automatically selected; two or three such population components are typically sufficient for individual AIF estimation. The proposed PBPM also provides more flexibility with respect to temporal characteristics of the data. It allows for injection duration to be included in the modelling, which makes it applicable to PET studies with different injection durations. Unlike TE-type constructions, it does not require specification of two key time points (signal start and peak time), and can adapt to different peak times thanks to its parametrization. An adequate model fitting procedure is also proposed hereafter. A penalized positive constrained least squares method is developed and implemented in R (R Core Team 2016) for estimation of individual mixing weights. Statistical regularization is built in to adapt relative weight placed on the individual and population information according to the noise level in a given dataset of each individual, to facilitate patient-adaptive fitting of cohort characteristics.

This paper focuses on describing aspects related to the PBPM (step 3B in the flowchart), and benchmarking this model against reference methods typically used in step 3A of PBIF and IDIF frameworks. Section 5.2 develops the proposed model, and provides details on the methodological developments for fitting the model to clinically sampled arterial data, including regularization and cross-validation for selection of the number of components. Section 5.5 illustrates the model on three separate arterial sampling datasets of respectively FDG-, $H_2O$-, and FLT-PET imaging studies. The potential of the model is demonstrated in a comparative analysis against another three methods of reference, namely the TE, CTE and BCM models. An open source implementation of the software in R (R Core Team 2016) is made available (Xiu et al. 2020), which is further validated and benchmarked against the three reference methods via statistical resampling analyses. Finally, the impact of the proposed AIF representation on kinetic analysis is evaluated via resampling of uptake templates in one- and two-compartment models.

## 5.2 Model Specification

This section presents the modelling strategy used for patient-specific AIF representation based on PET tracer concentration profiling, including aspects of model fitting and calibration.

### 5.2.1 AIF Model Specification

To specify the proposed PBPM, let the travel time $T$ of a specific atom at a specific arterial sampling site be modelled as the sum of the time ($T_{ir}$) for the atom to initially progress from the injection site to the right ventricle (RV) of the heart, and the time ($T_c$) it spends in circulation, before being sampled at the site:

$$T = T_{ir} + T_c$$

$T_{ir}$ is modeled as a realization from a gamma distribution ($G$) with shape and rate parameters $\alpha$ and $\beta$, respectively. The circulation time is modelled as a shifted excess circulation time ($\xi$) with the value of the shift ($\Delta$) being specific to the location of sampled blood-site within the circulatory system

$$T_c = \Delta + \xi$$

If the probability density ($f$) of $\xi$ is known, it is possible to combine this distribution with the injected dose profile in the right ventricle to evaluate the tracer concentration at any particular time. Under the conventional assumptions of time invariance and linearity of tracer kinetics, a bolus injection at time $t = 0$ will produce a temporal concentration of tracer atoms in the RV proportional to the distribution $G$. A more complex temporal injection profile, $e.g.$ specified by an indicator function $I(\cdot)$, would yield an RV concentration profile $C_{RV}$ characterized by an accumulation over the whole injection time, such that

$$C_{RV}(t) = G \otimes I(t) = \int_0^t G(t-s)I(s)ds$$

The evolution of this profile to the concentration profile at the blood site of interest, $C_P$, is governed by the circulation time distribution. This is given by a shifted convolution with the excess circulation travel time density

$$C_P(t) = f \otimes C_{RV}(\cdot - \Delta)(t) = \int_0^t f(t-s)G \otimes I(s-\Delta)ds$$

We approximate the distribution $f$ of excess circulation travel time $\xi$ by a linear mixture of $J$ components to obtain an estimate

$$\hat{f}(\xi) = \pi_1 e_1(\xi) + \pi_2 e_2(\xi) + \cdots + \pi_J e_J(\xi)$$

where the $\pi_1$, $\pi_2$,..., $\pi_J$ are mixing fractions of the component densities $e_1$, $e_2$,..., $e_J$, with constraint $\pi_j > 0, \forall j = 1, \ldots, J$. With this representation, an estimate of the concentration profile becomes

$$\hat{C}_P^J(t) = \sum_{j=1}^{J} \pi_j \int_0^t e_j(t-s) G \otimes I(s-\Delta) ds \tag{5.1}$$

In this expression, the convolution ($\otimes$) of the square wave $I()$ with the gamma distribution $G$ describes a population injection profile, adjusted to individual subjects by a patient-specific delay $\Delta$. In this approach the population component densities $e_1$, $e_2$,..., $e_J$ are assumed to be standard exponentials with characteristic rates $\phi_1 > \phi_2 > \cdots > \phi_J > 0$. While many other possibilities could be considered ($e.g.$ gamma, Weibull, etc.), a mixture of exponential distributions makes for a simple and flexible model. We presume the mixing components are representative of the entire circulatory system, and functional components $e_1$, $e_2$,..., $e_J$ and $G$ are held fixed across subjects in the population of study.

Ambiguity may arise in the estimation of the linear coefficients $\hat{\pi}_1$ and $\hat{\pi}_2$, in cases where the corresponding distribution ranges overlap. To remove this ambiguity, a constraint $\pi_1 > \pi_2$ can be imposed when estimating these linear parameters. This constraint ensures that at early time points, the first component contributes mostly to the peak of AIF representation. A similar constraint may be applied to further mixing coefficients, although in our experience on the data of Section 5.5, it was not necessary as there was no practical ambiguity between $\pi_2$ and $\pi_3$ in a three-component mixture applied to dynamic FDG-PET data.

### 5.2.2 Model Fitting

Suppose blood time course data from a training population of $n$ subjects

$$\{(t_{ik}, z_{ik}, w_{ik}),\ i = 1, 2, \ldots, m_k,\ k = 1, 2, \ldots, n\}$$

are available, where $z_{ik}$ is the concentration of the $i$th measurement of the $k$th subject, measured at time $t_{ik}$ with measurement reliability $w_{ik}$ and $m_k$ is the number of time points used in clinical sampling for the $k$th subject. Here, $t_{ik}$ and $z_{ik}$ are given, and $w_{ik}$ can be set based on past experiences. Each time course $z_{ik}$ is modeled for $i = 1, 2, \ldots, m_k$, $k = 1, 2, \ldots, n$ as

$$z_{ik} = \hat{C}_P(t_{ik}|\Delta_k, \pi_k, \theta) + w_{ik}^{-1/2}\varepsilon_{ik},$$

where $\hat{C}_P(t|\Delta_k, \pi_k, \theta)$ is defined in the previous subsection with the subject-dependent linear parameter vector $\pi_k = c(\pi_{1k}, \pi_{2k}, \ldots, \pi_{Jk})$ (estimated from each individual subject), and subject-independent non-linear parameter vector $\theta = c(\alpha, \beta, \phi_1, \ldots, \phi_J)$ (estimated from population AIFs). The $\varepsilon_{ik}$'s are assumed to be i.i.d. realizations of Gaussian random variables modelling additive noise. We propose to estimate $\theta$ by minimizing the objective function defined by

$$l(\theta) = \sum_{k=1}^{n} \min_{\Delta_k, \pi_k} \sum_{i=1}^{m_k} w_{ik}(z_{ik} - \hat{C}_P(t_{ik}|\Delta_k, \pi_k, \theta))^2$$

An algorithm for this optimization is implemented in R(R Core Team 2016). Minimization of $l(\theta)$ requires a preliminary two-step estimation of $\pi_k$ and $\Delta_k$, which is described in the following two subsections, respectively.

#### 5.2.2.1 Estimation of $\pi_k$ given $\Delta_k$ and $\theta$

We first consider the objective function of estimation of $\pi_k$ given $\Delta_k$ and $\theta$. The linear mixture is fitted by minimizing, for $k = 0, 1, \ldots, n$, criterion

$$\begin{aligned} l_1(\pi_k|\Delta_k, \theta) &= \sum_{i=1}^{m_k} w_{ik}(z_{ik} - \hat{C}_P(t_{ik}|\Delta_k, \pi_k, \theta))^2 \\ &= \sum_{i=1}^{m_k} w_{ik}\left(z_{ik} - \sum_{j=1}^{J} \pi_{jk} A_{ijk}\right)^2 \end{aligned}$$

with respect to $\pi_k$ given $\Delta_k$ and $\theta$, where the $j$th component of the linear mixture for the $k$th patient, hereafter denoted by $A_{ijk}$ for convenience, can be calculated as

$$A_{ijk} = A_j(t_{ik}|\Delta_k, \theta) = \int_0^{t_{ik}} e_j(t_{ik} - s)G \otimes I(s - \Delta_k)ds$$

for $i = 1, \ldots, m_k, j = 1, \ldots, J$, where the mixing parameters $\{\pi_{jk}\}_{j=1}^{J}$ are constrained positive. An R implementation of the Goldfarb-Idnami method (original by Berwin A. Turlach 2019) is employed to solve this positivity-constrained least-squares problem. We denote the resulting minimizer of $l_1(\pi_k|\Delta_k, \theta)$ as $\hat{\pi}_k = \hat{\pi}(\Delta_k, \theta)$.

#### 5.2.2.2 Estimation of Delay $\Delta_k$ given $\theta$

Then we consider the estimation of delay $\Delta_k$ given $\theta$. Inserting $\hat{\pi}_k(\Delta_k, \theta)$ in the objective function $l_1$, we have the reduced objective function

$$l_2(\Delta_k|\theta) = l_1(\hat{\pi}_k(\Delta_k, \theta)|\theta)$$

Given population characteristics $\theta$, a grid search may be carried out to minimize $l_2(\Delta_k|\theta)$ with respect to $\Delta_k$. The measured data may not be coincident with the timing of the injection, and a parameter $\Delta_k$, positive or negative, is introduced to account for this. In this study, 21 evenly distributed grid points in the range of [-60 s, +60 s] were used. The resulting minimizer of $l_2$ is denoted as $\hat{\Delta}_k$.

#### 5.2.2.3 Estimation of Population Parameter $\theta$

Finally, the population-specific parameters $\theta = (\alpha, \beta, \phi_1, \ldots, \phi_J)$ are estimated by minimizing

$$l(\theta) = \sum_{k=1}^{n} \sum_{i=1}^{m_k} w_{ik}(z_{ik} - \hat{C}_P(t_{ik}|\hat{\Delta}_k, \hat{\pi}_k, \theta))^2$$

using the algorithm in Fig 4.4, where function $l_1$ and $l_2$ are applied to deal with the optimization problem with estimation of $\pi_k$ and $\Delta_k$ in $l$, respectively.

Initial values for $\theta^0 = (\alpha^0, \beta^0, \phi_1^0, \ldots, \phi_J^0)$ may be selected based on experience from previous experiments and some physiological reasoning about the average travel time of each type of tracer in the blood circulation system. Lower and upper bounds $\theta^L = (\alpha^L, \beta^L, \phi_1^L, \ldots, \phi_J^L)$ and $\theta^H = (\alpha^H, \beta^H, \phi_1^H, \ldots, \phi_J^H)$, respectively, can be set based on experience from the population of patients receiving the same tracer injection, and physiological reasoning. Since the scales of the parameters differ considerably, and also to avoid the complexity of constrained minimization, the following parameter transformation may be performed. Let

$p = \frac{\theta - \theta^L}{\theta^H - \theta^L}$ be transformed via a logit transform into

$$\varsigma = \log \frac{p}{1-p}$$

Inversely,

$$\theta = \theta^L + (\theta^H - \theta^L)\frac{e^\varsigma}{1+e^\varsigma}$$

Thus, the constrained minimization with respect to $\theta$ can be performed as unconstrained minimization of $l(\varsigma)$ with respect to $\varsigma$. A Gauss-Newton type method was implemented in R to optimize $l(\varsigma)$.

#### 5.2.2.4 Fitting Individual Curves

The population parameter estimates $\hat{\theta} = \arg\min_\theta l(\theta)$ defined in Step (5.2.2.3) can be used instead of being re-evaluated when fitting time activity curves for "new" patients ($i.e.$ patients outside of the training population of $n$ studies used to obtain $\hat{\theta}$), thus reducing the number of parameters required to obtain an individual fit. In such cases, simultaneous estimation of $\pi_k$ and $\Delta_k$ can be achieved by grid search over $G$ values $\{\hat{\Delta}_k^1, \ldots, \hat{\Delta}_k^G\}$, corresponding estimates $\{\hat{\pi}_k^1, \ldots, \hat{\pi}_k^G\}$ being obtained instantaneously via linear regression.

#### 5.2.2.5 Model Regularization

In cases of high signal-to-noise ratio[1], regularization of the patient-specific mixing weights $\pi$ can be applied to control variability of these estimates. Once the number ($J$) and parameters of the population components have been determined, a penalized nonlinear least squares approach using the historical linear parameters as a Bayesian penalty for individual fit (O'Sullivan & Wahba 1985) is used for this approach. Regularization on $\pi = \pi_k$ parameters for the $k$th patient is achieved using the following individual objective function:

$$\begin{aligned} f_\lambda(\pi|\Delta,\theta) =& W(\mathbf{z}^T - \pi^T {A_\Delta}^T)^2 \\ &+ \lambda(\pi^T - {\pi_0}^T)\Omega^{-1}(\pi^T - {\pi_0}^T)^T \\ =& -[({A_\Delta}^T(\sqrt{W}\mathbf{z}))^T + \lambda {\pi_0}^T\Omega^{-1}]\pi \\ &+ \pi^T({A_\Delta}^T W A_\Delta + \lambda\Omega^{-1})\pi \end{aligned} \tag{5.2}$$

[1] e.g. if using small and/or noisy PET imaging data for AIF estimation

where $\mathbf{z} = \{z_{ik}\}_{i=1}^{m_k}$, $A_\Delta = [A_{ijk}]_{i,j}$ is a matrix of dimension $m_k \times J$, and $W = W_k$ is a vector of $w_{ik}$s defined in Section 5.2.2.1. All components in the vectorized mixing weights $\pi$ are constrained to be nonnegative, and $\pi_0$ and $\Omega$ respectively denote the mean and covariance matrix of the linear parameters obtained from population-based estimation. The regularization parameter $\lambda$ controls the trade-off between individual and population data contributions, larger values of $\lambda$ constraining individual estimates to be closer to the population profile $\pi_0$, which suits higher-noise scenarios. The optimization is a quadratic problem for which we used the Goldfarb-Idnami method(original by Berwin A. Turlach 2019).

Parameter $\lambda$ is set by minimizing the generalized cross-validation (GCV) score which is defined as the MSE adjusted by the effective degree of freedom:

$$GCV(\lambda) = \frac{\frac{1}{m}\sum_{i=1}^{m}(z_{ik} - \hat{z}_{ik}(\lambda))^2}{\left(\frac{1}{m}\text{Trace}(I - A_\Delta({A_\Delta}^T A_\Delta + m\lambda I)^{-1}A_\Delta^T)\right)^2},$$

where $\hat{z}_{ik}(\lambda)$ is $\hat{C}_P(t_{ik}|\Delta_k, \pi_k, \theta)$ based on minimization of the objective function (5.2), for a given $\lambda$.

### 5.2.3 Model Selection

Similarly to compartmental analysis of dynamic PET data, the number of components needed in the linear mixture (5.1) may depend on the tracer used in the studies. More components may be included if the tracer molecules can participate in metabolic activity. For example, in water studies, tracers do not participate in any metabolic activity, and a one-compartmental model is normally used for water dynamic studies. Models using more than one compartment are applied to studies involving other tracers for more complicated circulatory or metabolic systems (Sokoloff et al. 1977).

Here a leave-one-out approach is developed for selection of the number of components to be used in the proposed linear mixture (5.1) so as to minimize model complexity defined as

$$Err(J) = \sum_{k=1}^{n} \min_{\Delta_k, \pi_k} \sum_{i=1}^{m_k} \frac{w_{ik}}{m_k}(z_{ik} - C_P^J(t_{ik}, \Delta_k, \pi_k, \hat{\theta}_k))^2, \tag{5.3}$$

where $J = 2, 3 \ldots$ is the number of components, $C_P^J(\cdot)$ defines the predicted AIF

based on PBPM with $J$ components given linear and non-linear parameters, and

$$\hat{\theta}_k = \arg\min_{\theta_k} \sum_{j \neq k}^{n} \min_{\Delta_k, \pi_k} \sum_{i=1}^{m_k} \frac{w_{i,k}}{m_k} \left( z_{i,k} - C_P^J(t_{i,k}, \Delta_k, \pi_k, \theta_k) \right)^2$$

A cross-validated error ($\hat{Err}$) may not necessarily be the minimum model complexity $Err$ for the chosen $J$, but should be reasonably small for all values $Err(J)$ in the range of $J$.

### 5.2.4 Scale Factor Estimation

An overarching objective of AIF estimation is to design methods that can rely on image-derived input data instead of invasive sampling. In this context, scaling of PBPM estimates of the AIF obtained from image-derived arterial signals is required to obtain final parametric imaging estimates. This evaluation typically requires at least one blood sample point (from either arterial or venous blood) (Takikawa et al. 1993, Brock et al. 2005, Tonietto et al. 2019), or an adequately calibrated image-derived measurement from reference tissue (e.g. cerebral tissue) (Bentourkia & M'hamed 2005, Bentourkia 2006), which is not always feasible. Routine individual subject information may alternatively be used to this end. In (Bentourkia & M'hamed 2005) the authors use FDG uptake measured in cerebellum ROI from a single scan acquisition to normalize a PBIF estimate. In (Rissanen et al. 2015) the authors show that body surface area can be used as an alternative to blood sampling in PBIF normalization in brain $C^{11}$-TMSX PET studies. In (Akerele et al. 2021), the authors use injection dose and weight information to scale PBIF estimates in $C^{11}$-DPA-713 PET studies. Here we propose a regression model for the scale factor that does not require arterial blood sampling or a large blood-pool in the field of view. This model uses injection dose $X_{ID}$, blood volume $X_{BV}$ (estimated from non-invasive patient information on body weight, height and gender(March et al. 2013)) and tail height of the AIF curve ($\hat{\pi}_3$, the linear coefficient for the third component in the PBPM) as independent variables:

$$log(S) = \beta_0 + \beta_1 X_{ID} + \beta_2 X_{BV} + \beta_3 \hat{\pi}_3 + \text{noise} \tag{5.4}$$

## 5.3 Evaluation

This section introduces the three clinical datasets used for evaluation of the potential of the proposed PBPM model, and illustrates typical PBPM fits for these data.

### 5.3.1 Data

The proposed PBPM was applied to three separate datasets which partially overlapped with the data introduced in Section 4.4.1, comprising of blood sampling data obtained during the acquisition of respectively 105 FDG-PET studies, 39 $H_2O$-PET studies, and 32 FLT-PET studies, all acquired at the University of Washington (Graham et al. 2002, Muzi et al. 2006, 2009, Eyal et al. 2010, O'Sullivan et al. 2009, Huang & O'Sullivan 2014). Ten randomly selected studies from each of these 3 sets were used for PBPM fitting of the population components $\theta$. The rest of the data were used to obtain individual fits from each of the models used in the following comparative analyses. The data were from both healthy subjects and patients with cancer conditions. Durations of FDG injections were either 1 or 2 minutes (78 and 27 cases respectively), bolus injection for $H_2O$ was assumed to be 5 seconds, and duration of FLT injection was 1 minute. The datasets are summarised in Table 5.1. The data included sample AIFs of the subjects along with gender, weight, height and injection dose. Median sampling durations and numbers of sampling time points per tracer are also summarised in that table. The most common sampling frame for FDG was as follows (min): 0, 0.25, 0.5, 0.75, 1, 1.5, 2, 2.5, 3, 4, 5, 6, 7, 10, 13, 15, 20, 25, 30, 35, 40, 50, 60, 70, 80, 90. For $H_2O$, it was 0, 0.067, 0.13, 0.20, 0.27, 0.33, 0.40, 0.47, 0.53, 0.60, 0.67, 0.73, 0.80, 0.87, 0.93, 1.08, 1.27, 1.42, 1.58, 1.75, 1.92, 2.25, 2.58, 2.92, 3.25, 3.58, 3.92, 4.25, 4.58, 4.92. For FLT, it was 0, 0.25, 0.5, 0.75, 1.00, 1.25, 1.5, 1.75, 2, 2.5, 3, 4, 5, 6, 7, 8, 10, 15, 20, 30, 40, 50, 60, 90, 110. Injections were performed either manually or automatically. A saline flush was used after every injection. A single study for each patient was used in the analyses. The normalized AIFs are presented in Fig. 5.2. Each curve typically includes three parts: a plateau of 0 concentration at the beginning, followed by a rapid increase after injection, and an exponential decay. No imaging data were used in the following analyses.

Table 5.1: Top section: patient information in mean (sd) of 105 FDG, 39 $H_2O$ and 32 FLT studies (only 101 Weight and Height for FDG studies). Bottom section: median sampling durations and numbers of time points per tracer.

| Tracer | FDG | $H_2O$ | FLT |
|---|---|---|---|
| Injection Dose (mCi) | 8.92 (1.48) | 22.72 (20.92) | 4.43 (0.59) |
| Gender | 37F; 68M | 15F; 24M | 7F; 25M |
| Weight (kg) | 79.1 (15.6) | 76.1 (14.4) | 82.4 (17.3) |
| Height (cm) | 174.7 (9.6) | 175.8 (8.3) | 175.6 (9.5) |
| Peak (mCi) | 1.87 (0.57) | 13.57 (15.03) | 0.77 (0.47) |
| Number of points | 26 | 30 | 27 |
| Sampling duration (min) | 90 | 4.917 | 110 |

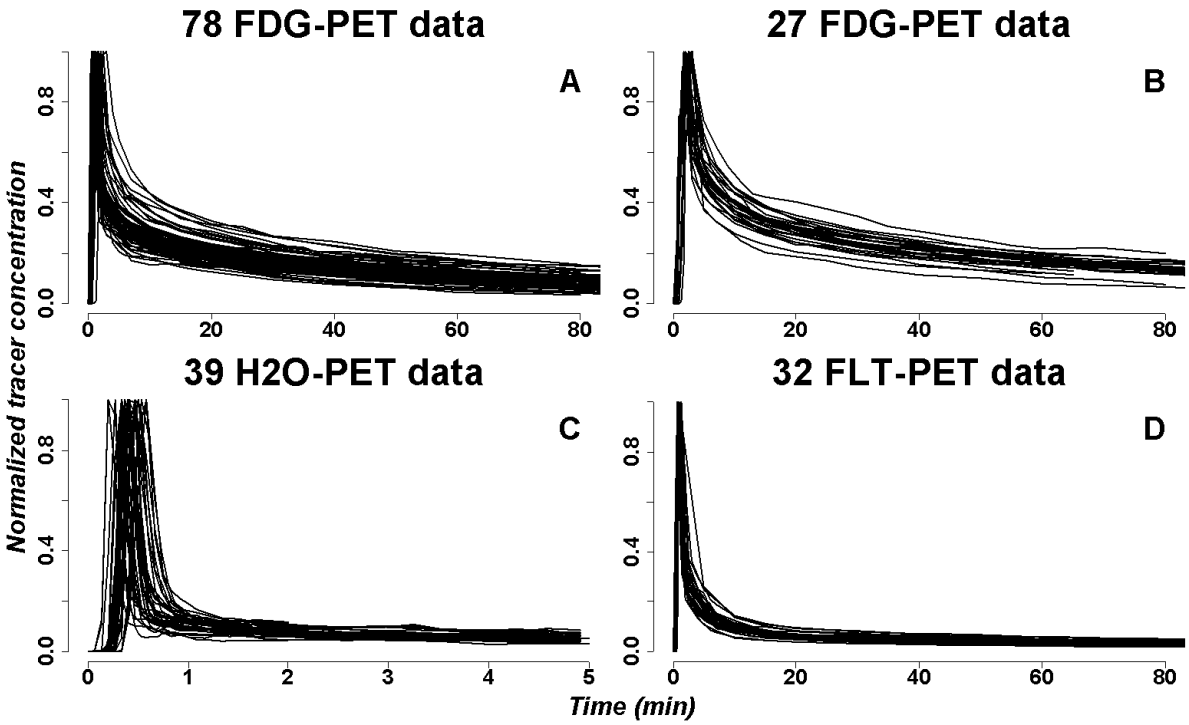


Figure 5.2: Normalized kinetic PET time activity curves acquired at the University of Washington (Graham et al. 2002, Muzi et al. 2009, Eyal et al. 2010, O'Sullivan et al. 2009, Huang & O'Sullivan 2014): 78 FDG-PET curves with 1-minute injection duration (A), 27 FDG-PET curves with 2-minute injection duration (B); 39 $H_2O$-PET curves with bolus injection (C); 32 FLT-PET curves with 1-minute injection (D).

### 5.3.2 Model Selection

The clinical datasets were used to estimate the population-based parameters in the proposed PBPM model for varying numbers of components. Figure 5.3 depicts the cross-validated error $\hat{Err}$ defined from $Err(J)$, for the FDG- and

$H_2O$-PET cohorts respectively, after carrying out the model selection procedure described in Section 5.2.3. For the FDG set an elbow was clearly identified at 3 components, indicating a 3-component mixture to be optimal in the sense of loss $Err(J)$. Three exponentials with different rates convolved with a gamma distribution were thus estimated from the population data to approximate the travel time distribution of the FDG and FLT tracers, yielding a reasonable representation in PBPM (which aligns with the traditional two-tissue compartment modelling of FDG molecules in the blood circulation system). For the $H_2O$ set, there was no clear elbow and a 2-component mixture seemed the optimal choice according to this selection method. Note that this model selection rule is only indicative, and using an over-specified mixture ($i.e.$ using more components) may also mechanically impact the bias-variance tradeoff achieved by the model.

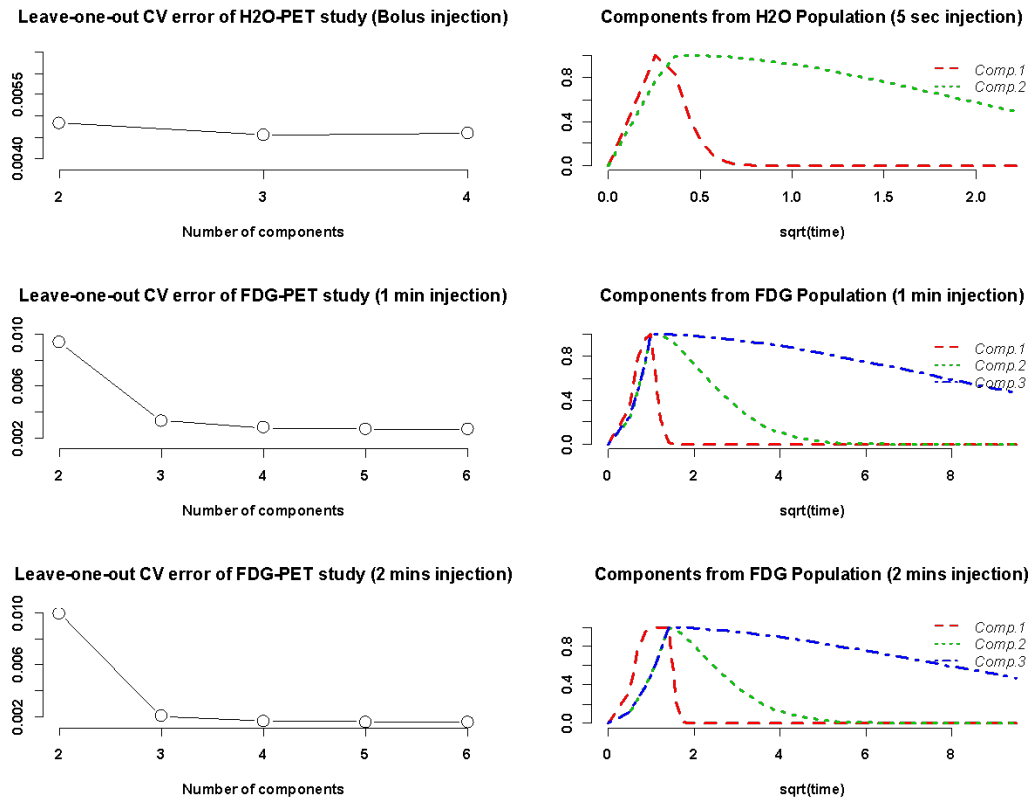


Figure 5.3: Left: model selection for $H_2O$ (top) and FDG (center for one-minute injections; bottom for two-minute injections) studies on the basis of the leave-one-out cross-validated error defined in Section 5.2.3. Right: corresponding basis component fits.

### 5.3.3 Model Fitting

Arterial sampled data were used to estimate the population-based parameters in the proposed PBPM model as described in Sections 5.2.2 and 5.2.3. For the set of FDG studies, the model selection procedure described in Section 5.2.3, suggests that three components would yield an appropriate representation in PBPM (which aligns with the traditional two-tisue compartment modelling of FDG molecules in the blood circulation system). Three exponentials with different rates convolved with a gamma distribution were estimated from the population data to approximate the travel time distribution of the FDG and FLT tracers. Following the same approach, it was determined that two exponential components, again fitted from the population data, should be used to approximate the travel time distribution of the $H_2O$ tracer. Since, unlike FDG, $H_2O$ is not involved in the metabolic process, it seems reasonable that the number of components used to describe the $H_2O$ AIF might be one less than FDG. Figure 5.4 shows examples of AIF fits obtained from PBPM for both FDG- and $H_2O$-PET studies. It illustrates the appropriateness of a two-component mixture for the latter.

Examples of individual PBPM fits shown in Fig. 5.4 illustrate how the third component in the FDG and FLT PBPM fits, and the second component in the $H_2O$ PBPM fit, could adequately represent the sample AIF tail patterns.

As for the training population size required to fit the mixture components, behaviour of the PBPM model may vary with the PET tracer used. Results from a numerical investigation on the FDG cohort presented in Section 5.4.2 indicated that model fitting was relatively insensitive to this parameter, with comparable cross-validated model fit error distributions obtained when using population parameter estimates obtained from population sizes ranging from 5 to 60 studies in the FDG setting.

### 5.3.4 Scale Factor Estimation

Results on 91 FDG AIF studies from the scale factor estimation procedure described in Section 5.2.4 are depicted in Fig. 5.5 (4 patients were removed from the set of 95 curves used in other analyses, due to missing information on patient heights and weights). They show significant alignment between estimated scale factors (Eq. 5.4) and actual scale factor values obtained directly from ar-

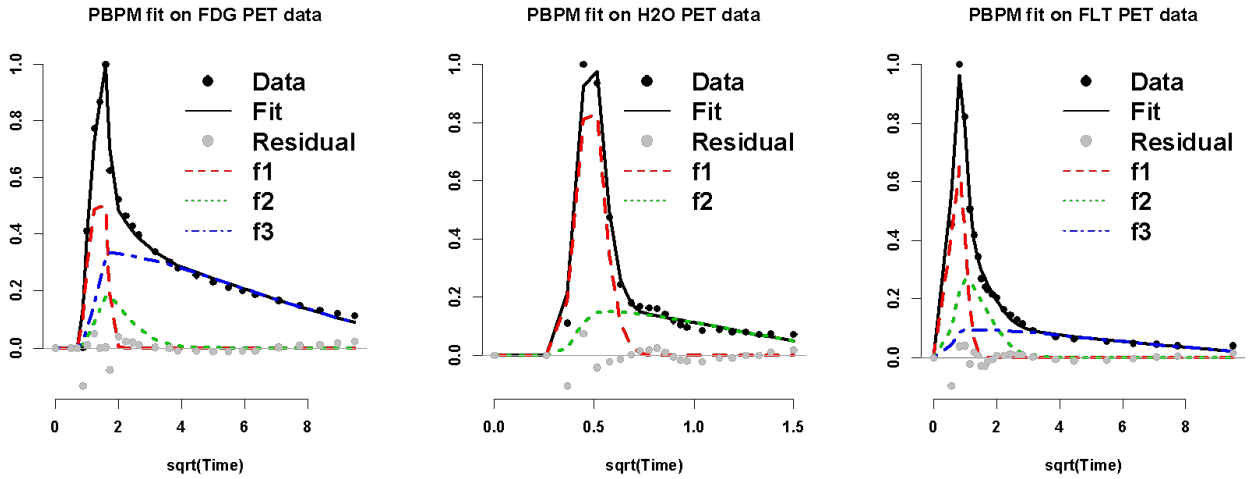


Figure 5.4: Examples of individual PBPM fits to FDG (left), $H_2O$ (middle) and FLT (right) arterial data, where the population-fitting components $f_j$ shown in each plot, defined as the convolutions between the exponential components $e_j$ with the population gamma profile $G$ in (5.1), are scaled by individual mixing weights $\pi_j$ (with $j = 1, 2, 3$ for FDG and FLT data and $j = 1, 2$ for $H_2O$ data).

terial sampling data (Pearson correlation $\rho = 0.83$, two-sided paired t-test with $p = 0.9999$ under the null hypothesis $H_0$: True difference in means is equal to $0$).

## 5.4 Simulation Studies

Five simulation-based analyses were conducted to validate the model and its implementation. The first analysis was carried out on an AIF template generated from the PBPM model (with additive random noise), to validate the implementation and evaluate model performance at varying noise levels. The second simulation study analyses the sensitivity of the PBPM model to training population size. The third study tests the effect of using a training population instead of fitting individual data without historical information. The forth analysis was carried out a bootstrapped resampling of a single clinically sampled AIF to benchmark the different models on model-independent data. The fifth method generates simulated curves and applies them on two-compartmental model. Performance is benchmarked to existing models.

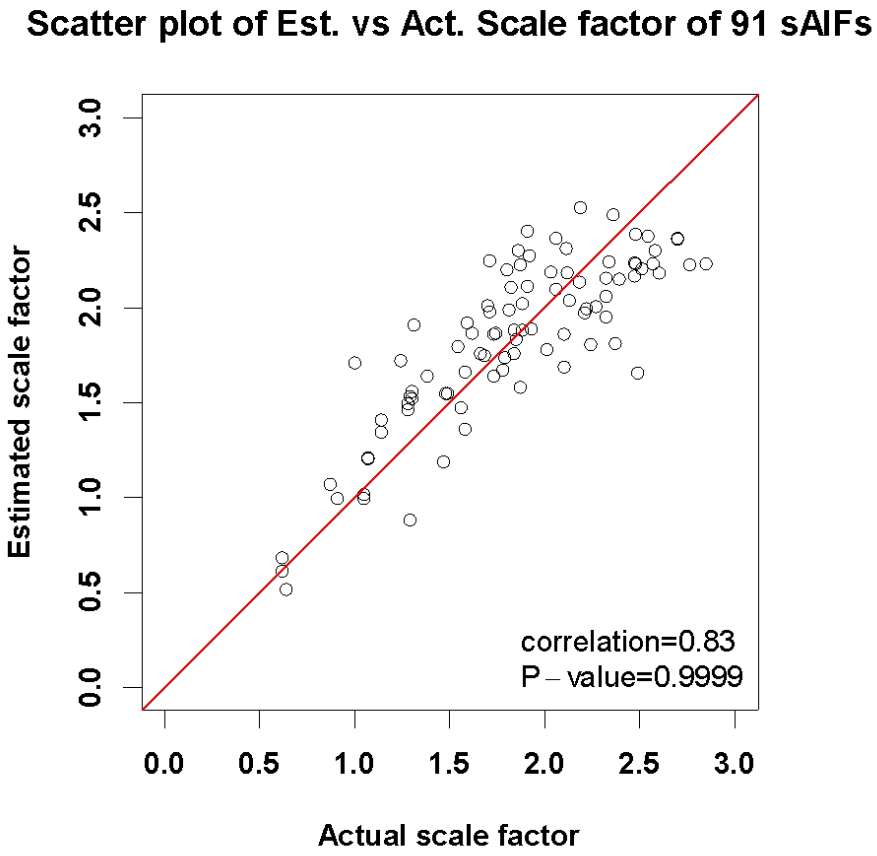


Figure 5.5: Scatterplot of estimated scale factors (Eq. 5.4) against actual values obtained directly from arterial sampling data from 91 FDG AIF studies, showing a significant association between the two samples (Pearson correlation $\rho = 0.83$, two-sided paired t-test $p = 0.9999$.

## 5.4.1 Validation Study on Model-derived Template

### 5.4.1.1 Model-based Simulation Template

We start with creating simulated AIFs with noises added to linear coefficients in PBPM and sum of the component curves. Three mixture components were fitted to the FDG-PET imaging cohort to obtain estimates of the gamma and exponential parameters (See Table 5.2). To simulate individual AIF curves, the (linear) mixing parameters were generated randomly via an acceptance-rejection algorithm, drawing values from a Normal distribution so that $\Pi_j \sim N(\bar{\pi}_j, \sigma(\pi_j))$, $j = 1, 2, \ldots, m$, where $m$ is the number of observation times, and enforcing some *ad hoc* constraints. A value for $\Pi_3$ was then set given $\Pi_1$ and $\Pi_2$ to ensure that $\sum_{i=1}^{3} \Pi_j \geq 1$ (since the peaks of the components are misaligned,

and the component curves are all normalized by their peaks), and the simulated time courses were defined as

$$C_p^{sim}(t_i) = \Pi_1 C_1(t_i|\theta) + \Pi_2 C_2(t_i|\theta) + \Pi_3 C_3(t_i|\theta) \tag{5.5}$$

In detail, the following steps were taken to simulate the AIF curves (model settings are based on mean and standard deviation of the estimates from historical experiences):

Step 1 - Generate random component curves $C_1(t_i|\theta)$, $C_2(t_i|\theta)$ and $C_3(t_i|\theta)$ using the nonlinear parameter values of Table 5.2 and given observation protocol $t_i$s

Step 2 - Generate $0.4 < \Pi_1 < 0.8$ and $0.08 < \Pi_2 < 0.35$ via acceptance-rejection

Step 3 - Generate $\Pi_3 = \frac{1-max\{\Pi_1 C_1(t_i|\theta)+\Pi_2 C_2(t_i|\theta)\}}{max\{C_3(t_i|\theta)\}}$

Step 4 - Test that $\Pi_3$ satisfies

$$0.17 < \Pi_3 < 0.37 \tag{5.6}$$

$$0.99 < \Pi_1 + \Pi_2 + \Pi_3 < 1.15 \tag{5.7}$$

and repeat Steps 2–4 if necessary until the above constraints are satisfied, to ensure adequate values for the mixing coefficients.

Table 5.2: Fixed gamma and exponential parameters estimated from the FDG-PET cohort and used for simulation.

| | |
|---|---|
| $\hat{\alpha}$ | 2.1784 |
| $\hat{\beta}$ | 7.8741 |
| $\hat{\phi}_1$ | 88.3992 |
| $\hat{\phi}_2$ | 0.1488 |
| $\hat{\phi}_3$ | 0.0088 |

We first calculated $C_p^{sim}(t_i|\theta, \Pi_1, \Pi_2, \Pi_3)$ by 5.5 given 400 sets of parameter simulations. Then sets of 400 simulated curves were generated by 5.8 at varying noise levels termed *high*, *mid-high*, *medium*, *mid-low* and *low*

$$C_P^{sim}(t_i) = C_p^{sim}(t_i) + \epsilon(\cdot) \tag{5.8}$$

where $\epsilon(medium) \sim N(0, .05)$ when $t_i < 1.5(min)$ and $\epsilon(medium) \sim N(0, .01)$

when $t_i \geq 1.5(min)$ for level *medium*. $\epsilon(high)$, $\epsilon$(*mid-high*), $\epsilon$(*mid-low*) and $\epsilon(low)$ are 3, $\frac{3}{2}$, $\frac{2}{3}$ and $\frac{1}{3}$ times of $\epsilon(medium)$, respectively. Figure 5.6 presents one example simulated curve and its fit for each noise level.

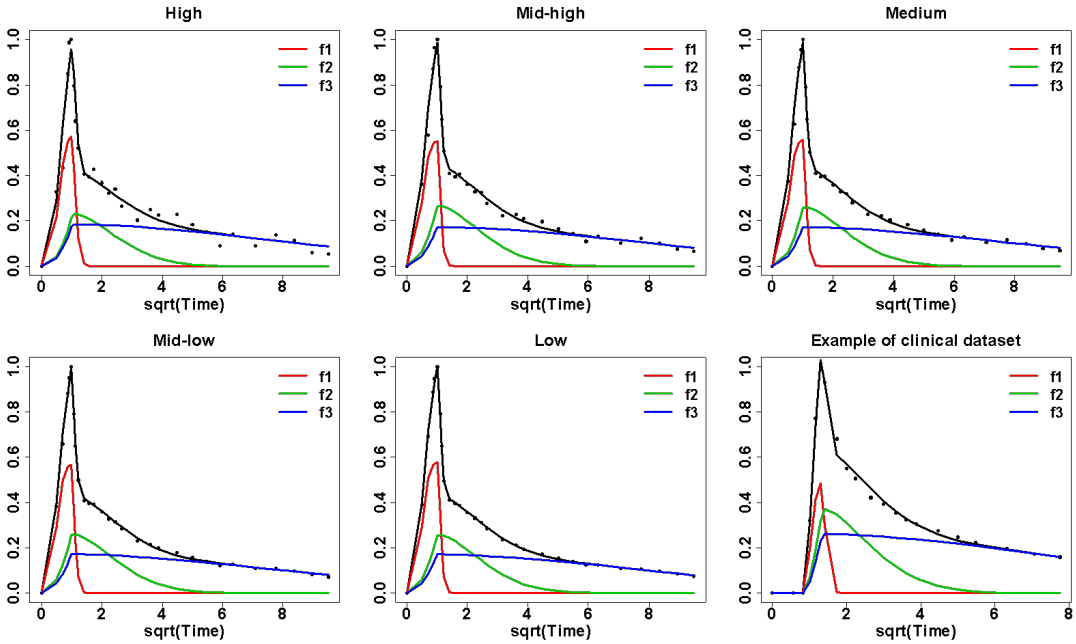


Figure 5.6: Examples of PBPM fits on a simulated curve for each noise level.

### 5.4.1.2 Model Validation and Assessment

Figure 5.7 presents the performance of PBPM on 400 simulated AIFs where medium noise level is as above when the noise pattern is set to be similar to the fit residual of the directly sampled AIFs. The RMSE distributions show overall improvement in model fit as noise level decreases, as expected. Note that the regularization term introduced in the objective function (5.2) described in Section 5.2.2.5 is likely to constrain the limit RMSE value to be strictly positive. The parameter estimation error distributions in Figure 5.7 show an increase in estimation efficiency as noise level decreases. These results demonstrate that the PBPM modelling approach is consistent with different noise levels and accurate, and validates its implementation (Xiu et al. 2020).

## 5.4.2 Sensitivity to Training Population Size

As for the training population size required to fit the mixture components, behavior of the PBPM model may vary with the PET tracer used. An experiment

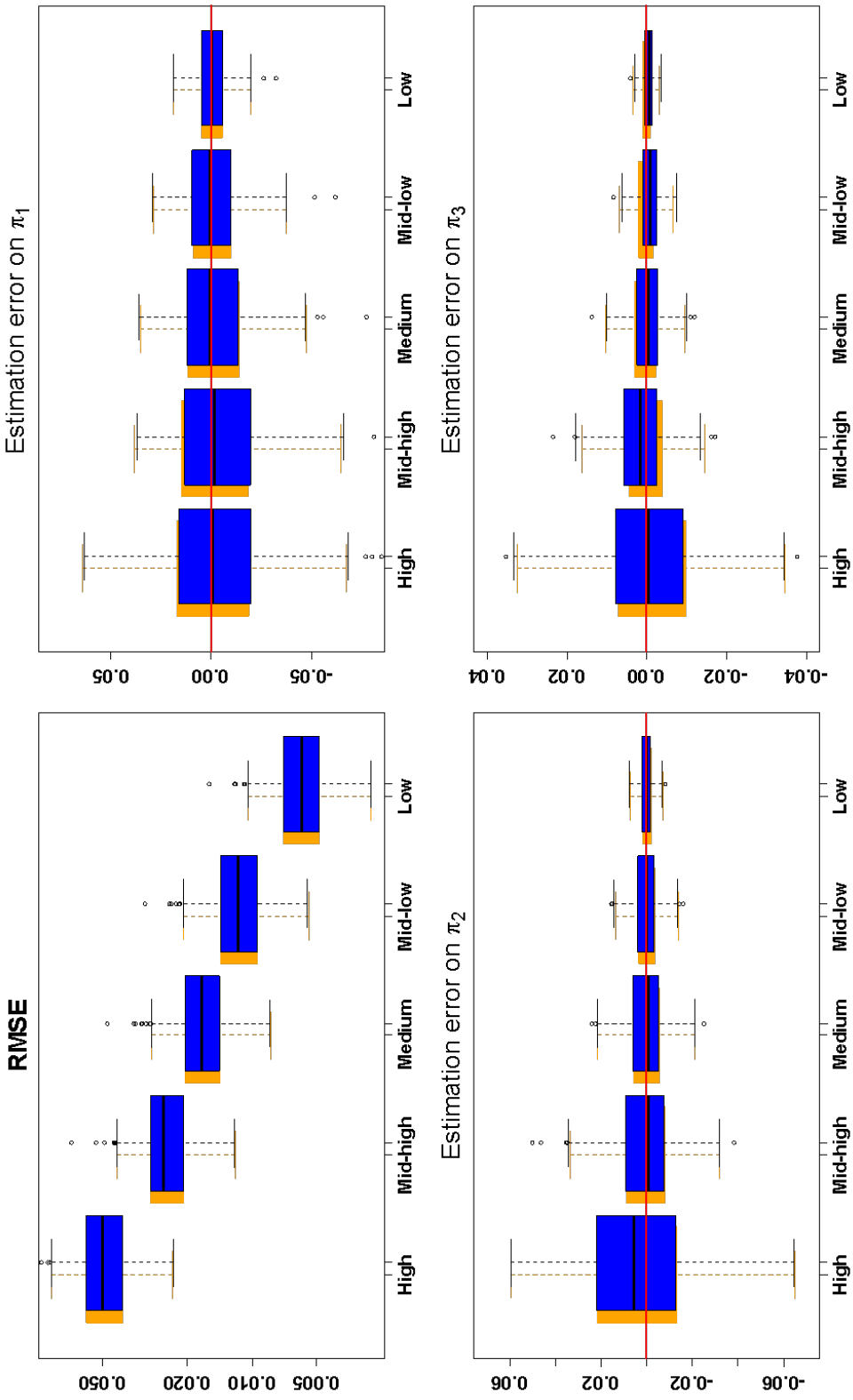


Figure 5.7: Top-left: root mean square error (RMSE) distributions for the 400 AIF fits obtained from PBPM at each noise level. Top-right and bottom: distributions of estimation errors $\Pi_i - \hat{\Pi}_i, i = 1, 2, 3$. Blue boxplots represent the distributions of parameter estimates obtained using estimated nonlinear parameters for $\theta = (\alpha, \beta, \phi_1, \phi_2, \phi_3)$, whilst the orange shadow boxplots indicate those same distributions when the true values for the nonlinear parameters were used.

on the FDG cohort was carried out, using random subsets ranging from $n = 5$ to $n = 60$ studies taken from the overall set as training population studies, and monitoring cross-validated model fit errors. The results from this analysis, shown in Figure 5.8, indicated that model fitting was relatively insensitive to this parameter, with comparable error distributions across the range of population sizes.

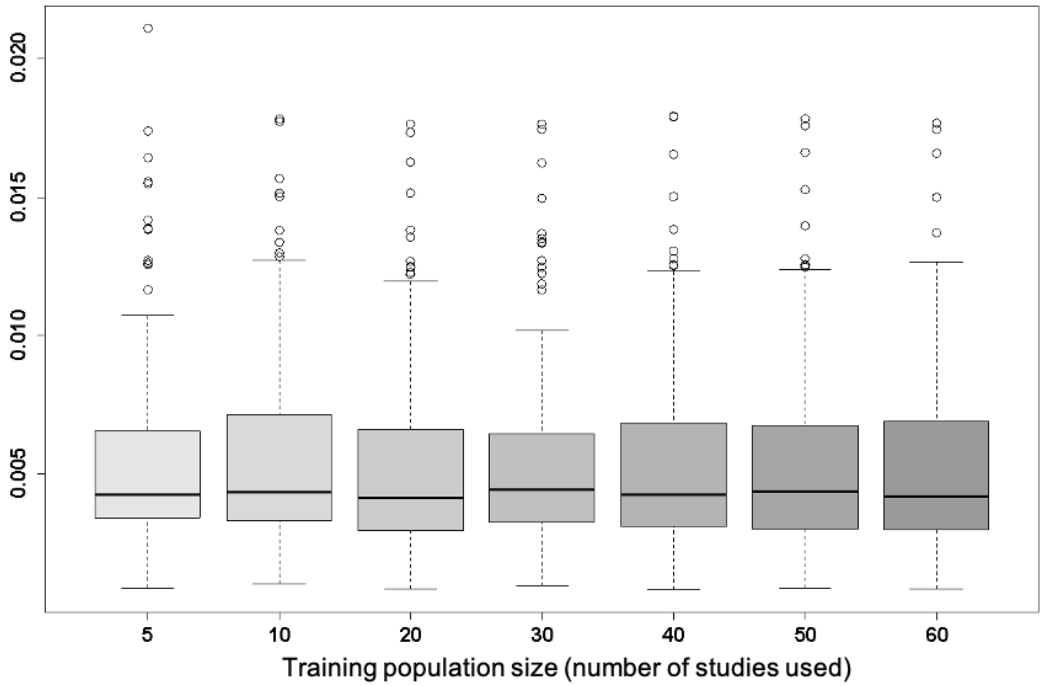


Figure 5.8: Distribution of 3-fold cross-validated AIF PBPM fit errors for varying training population sizes $n$.

### 5.4.3 Effect of Using a Training Population

An experiment was carried out to assess the potential gain offered by employing a population-based strategy over a fully individual approach to estimate the basis components when fitting the PBPM to sampling data. The same simulation process defined by (Eq. 5.8) was applied to generate 210 simulated curves from the PBPM templates. A random set of 10 of these curves were used as a training population to obtain estimates $\hat{\theta}$ of the nonlinear parameters $\theta$. The remaining 200 curves were fitted once following the proposed methodology (using this estimated $\hat{\theta}$ to generate PBPM fit), and independently a second time by re-estimating the nonlinear parameters $\theta$ individually ($i.e.$ without using the estimate derived from the training population). We refer to the former AIF esti-

mate as the PBPM fit, and the latter AIF estimate as the individual fit. Fit errors were calculated for each of the 200 curves and cross-validated using leave-one-out cross-validation. Figure 5.9 shows the distribution of cross-validated fit errors obtained from each of the PBPM and individual fits, at varying noise levels. The results show a clear gain resulting from the population-based methodology.

### 5.4.4 Benchmark on Bootstrapped Data

#### 5.4.4.1 sAIF-based Simulation Template

The set of 58 SAIFs associated with the FDG-PET studies described in Section 4.4.1.1 were used to generate a template AIF curve. First, all SAIF curves were scaled by their maximum, so that all peaks were equal to one. The curves were assumed to have constant zero activity before injection time. All sample time course peaks were then aligned at 1.5 minute, as the majority of non-shifted SAIF peaks originally aligned around this reasonable value. Following these realignments, the pre-processed dataset formed a set of SAIFs with 200 distinct time points, and the median and standard deviation of the AIFs at each of these time points were calculated, as depicted in Figure 5.10 (top). These median SAIF values were used to make up the template. Two smoothing schemes were applied independently to early and later time points (before and after 5 minutes) of the medians, since the variability in median values varies over time, as shown in Figure 5.10 (bottom). This smoothing was achieved by applying P-splines with different smoothing parameters to the early and later time sets of medians. Additive noise was generated at each time point of the smooth AIF templates as a normal realization with mean zero and standard deviation equal to that of shifted AIFs at that time.

For $H_2O$-PET studies, a similar simulation approach is applied. Since in practice, there would typically be less than 100 time points in FDG and $H_2O$ studies, we used 30 and 40 random time points from FDG- and $H_2O$-PET studies, respectively.

#### 5.4.4.2 Benchmarking

Here we consider another three models from Chapter 3 for benchmarking purposes. They are a former whole-body blood circulation model (BCM) (Huang &

O'Sullivan 2014, O'Sullivan et al. 2017) proposed by our group, a straightforward tri-exponential model (TE) (Feng et al. 1993, Zanderigo et al. 2014), and a convolved tri-exponential model (CTE) (Tonietto et al. 2015). Figure 5.11 suggests that PBPM has significant improvement in accuracy in FDG studies and comparable accuracy in $H_2O$ simulations. Considering the other models all need nonlinear least squares (NLS) in their fitting, PBPM has clear advantage in computational speed and at the same time, would not drop significantly in terms of accuracy. Taking above into consideration, the PBPM has overall better performance in capturing the mathematical shape of the AIF in FDG-PET studies compared to the other three models and about average accuracy in fitting the AIF in $H_2O$-PET.

#### 5.4.4.3 Reduced SAIF-based Simulation Template

The set of 58 and 39 SAIFs associated with the FDG- and $H_2O$- PET studies described in Section 4.4.1.1 were used to generate template AIF curves $C_p^{tem}(t_i)$. Each template curve has the same time points as the SAIF that it is from. A series of normal realizations $\epsilon(t_i)$ are added to the template to create simulations as follows:

$$C_P^{sim}(t_i) = C_p^{tem}(t_i) + \epsilon(t_i) \tag{5.9}$$

Let $\hat{C}_P(t_i)$ be the predicted curve to the simulated AIF. We define the root mean square error as

$$RMSE = \sqrt{\frac{1}{m_v}\sum_i (C_p^{tem}(t_i) - \hat{C}_P(t_i))^2} \tag{5.10}$$

where $m_v$ is the number of observations in the validation set.

The BCM, TE and CTE models were also used for benchmarking purposes. Figure 5.12 suggests that true errors calculated from the models in the simulation studies support the results in Section 5.5.1.

### 5.4.5 Simulated FDG-PET Kinetic Study

In Section 2.2, we introduced some of the main methods for quantitative analysis in PET tracer kinetic studies. Compartmental models are commonly used for derivation of physiological parameters of interest, such as flow in $H_2O$ and metabolic rate of glucose (MRglu) in FDG. Eq. (2.10) gives the formula for calculation of $MRglu$. Except for $flux\ K$, the other two parameters in the formula can be obtained in a physical way. Then they are always considered as constants. Therefore, in our simulation study, we should demonstrate that PBPM has capacity to retrieve $k$s from simulated FDG-PET data and a given AIF. The clinical data are from Section 4.4.1.1.

#### 5.4.5.1 Simulation Design

According to Section 2.2.2.1, for FDG-PET studies, if we apply two-compartmental model (2C model), the true concentration of tracers in the ROI can be regarded as

$$\begin{aligned} C_I^{true}(t,K) &= VBC_P^{sampling}(t-\Delta) + [R * C_P^{sampling}(.-\Delta)](t,K) \\ &= VBC_P^{sampling}(t-\Delta) + \sum_{i=1}^{2} \phi_i(K) \int_0^t e^{-\theta_i(K)(t-s)} C_P^{sampling}(s-\delta)ds \end{aligned}$$

where $K = (K_1, k_2, k_3, k_4)$, $\Delta$ is a delay parameter, and $R$ is the tissue impulse response function (residue function) in 4-K two-compartmental model. and

$$\theta_1(K) = \frac{k_2 + k_3 + k_4 + \tau}{2}$$

$$\theta_2(K) = \frac{k_2 + k_3 + k_4 - \tau}{2}$$

$$\phi_1(K) = K_1 \frac{\theta_1 - k_2 - k_4}{\tau}$$

$$\phi_2(K) = -K_1 \frac{\theta_1 - k_2 - k_4}{\tau}$$

where

$$\tau = \sqrt{(k_2 + k_3 + k_4)^2 - 4k_2k_4}$$

Noises are added to the true data as

$$C_I^{sim}(t) = C_I^{tem}(t, K) + \lambda\epsilon(t) \tag{5.11}$$

where $\lambda$ is the noise level and $\epsilon$ is a Gaussian realization varying over time and follows $N(0, \sigma(t))$ and $\sigma(t) = [C_I^{tem}(t, K)]^{\frac{1}{2}}$.

Thus $z_i = C_I^{sim}(t_i)$ where $i = 1, 2, ..., m$.

Then we optimize the objective function

$$f(K) = \sum_{i=1}^{m} \frac{w_i}{m}[z_i - C_I^{true}(t_i, K)]^2$$

where $w_i = \frac{1}{|z_i|}$

and get estimation of $K$ that

$$\hat{K} = arg\min_K f(K)$$

In Section 5.5.3, we compare the performance in estimating $K$ using different AIF models.

#### 5.4.5.2 Validation of the 2C Model

Fig. 5.13 provides an example of the simulation process. The AIF used to generate simulated data is the same as the AIF used in the optimization process, and we fix parameters $k_3$ and $k_4$ to reduce the variability in the simulation study. Fig. 5.14 shows that percentage errors of estimated parameters are centered around 0 and not biased when the noise level is set to be small (0.001) and the delay parameter is set to be a constant (.26667). The results show that the 2C model works well in this simulation study.

Fig. 5.15 shows that in fitting the individual parameters of $K_1$ and $k_2$, the PBPM yields reasonable performance in terms of the distribution of fit errors compared

to other existing models. However, when it comes to the macro parameters, the results do not align with the individual parameters. One possible problem that leads to this situation could be the ambiguity in model parameterization, which impacts the optimization process when estimating the parameters within the 2C model itself.

The criterion surface, depicted in Fig. 5.16, has limited convexity in the P2 direction. When $K_1$ and $k_2$ vary in the same direction (monotonically), the fit MSE remains in the valley.

#### 5.4.5.3 Re-parameterization

To eliminate the effect of ambiguity of parameters in the 2C model, a re-parameterization method was applied. Here we let

$$P_1 = flux = \frac{K_1 k_3}{k_2 + k_3}$$
$$P_2 = k_2 + k_3$$

and

$$P_3 = K_3$$

Also we use a grid search instead of NLS for optimization to reduce complexity. Fig. 5.17 presents a surface plot of the new criterion for re-parameterized parameters. It shows that the surface has reasonable convexity and could be a good criterion for estimating the flux.

## 5.5 Results

This section provides output of comparative analyses between the proposed PBPM and reference approaches, using the three clinical datasets introduced in Section 5.3.1.

### 5.5.1 Comparative Analysis

PBPM-derived AIF estimates were compared to alternatives obtained from another three models described in Section 3, namely a whole-body blood circula-

tion model (BCM) (Huang & O'Sullivan 2014, O'Sullivan et al. 2017), a straightforward tri-exponential model (TE) (Feng et al. 1993, Zanderigo et al. 2014), and a convolved tri-exponential model (CTE) (Tonietto et al. 2015). For each tracer, the PBPM was fitted using a random sample of 10 arterial blood sampling curves for estimation of the population parameters $\theta = (\alpha, \beta, \phi_1, \ldots, \phi_J)$ (and not for any other step), and the rest of the data for estimation of individual AIF signals, $i.e.$ of $\{(\pi_k, \Delta_k), k = 1, \ldots, n\}$ (and not for any other step). In other words, the 10 randomly selected "population curves" were used as "historical data" in this framework. These were only used for the purpose of fitting the PBPM, and not the BCM, TE and CTE models. A comparative analysis between these four models was carried out in terms of the sum of MSEs obtained for each of the $n$ scaled AIF fits $\{\hat{z}_{i,k} = \hat{C}_P(t_{i,k}|\hat{\pi}_k)\}_{k=1}^n$, defined by

$$E = \sum_{k=1}^{n} \left( \frac{\sum_{i=1}^{m_k} (z_{i,k} - \hat{z}_{i,k})^2}{m_k} \right)$$

This fit error was cross-validated in the comparative analysis, using

$$\hat{E} = \sum_{k=1}^{n} \left( \frac{\sum_{i=2}^{m_k - 1} (z_{i,k} - \hat{z}^*_{i,k})^2}{m_k - 2} \right) \tag{5.12}$$

for comparison, where $\hat{z}^*_{i,k} = \eta^*(t_{i,k}|\hat{\pi}^*_k)$ and $\eta^*(t_{i,k}|\hat{\pi}^*_k)$ is the set of optimal parameter estimates for the data $\{(t_{j,k}, z_{j,k})\}_{j=1, j\neq i}^m$.

The boxplots of the cross-validated error distributions of Fig. 5.18 (bottom) illustrate that PBPM is competitive for both tracers. For the FDG set, the PBPM model yields comparable performance and improved accuracy over TE, and outperforms BCM both in terms of median error and standard error. For the $H_2O$ set, the BCM and PBPM models show greater flexibility in fitting the AIF data compared to the tri-exponential alternatives, and PBPM also yields a lower median error compared to BCM. Nonparametric, one-sided paired (Wilcoxon) tests under the null hypothesis that PBPM model fit errors that are greater than or equal to those obtained from the other model (Table 5.3) indicated a significantly lower PBPM error compared to TE and CTE for both the FDG and $H_2O$ sets at the 1% significance level. And no model statistically outperform PBPM in terms of the MSE if we apply same test on the other side.

Table 5.3: One-sided paired Wilcoxon test p-values for the cross-validated BCM, TE, CTE and PBPM MSEs of Fig. 5.18. The alternative hypotheses $H_A$ for these tests are provided to assist in interpreting the test outputs. Here $H_A$ is accepted at the 1% significance level for p-values lower than 0.01 (significant results in bold).

| Model Reference | FDG | $H_2O$ | FLT |
|---|---|---|---|
| MSE: mean (sd) | | | |
| BCM | 0.0116 (0.0094) | 0.0086 (0.0069) | 0.0127 (0.0072) |
| TE | 0.0073 (0.0047) | 0.0099 (0.0040) | 0.0066 (0.0035) |
| CTE | 0.0073 (0.0047) | 0.0169 (0.0080) | 0.0112 (0.0055) |
| PBPM | 0.0063 (0.0045) | 0.0073 (0.0039) | 0.0070 (0.0041) |
| Wilcoxon p-value | | | |
| $H_A$: $MSE_{BCM} > MSE_{PBPM}$ | $\mathbf{< 0.001}$ | 0.312 | **0.002** |
| $H_A$: $MSE_{TE} > MSE_{PBPM}$ | **0.002** | **0.004** | 0.512 |
| $H_A$: $MSE_{CTE} > MSE_{PBPM}$ | $\mathbf{< 0.001}$ | $\mathbf{< 0.001}$ | **0.010** |

### 5.5.2 Gain from a Population-based Approach

Figure 5.19 illustrates the gain obtained by using a population-based strategy to estimate the nonlinear parameters $\theta$ for the PBPM basis component profiles, over a fully individual fitting process where all model parameters $(\pi, \Delta, \theta)$ would be estimated from the single patient sampling data. A one-sided paired Wilcoxon test, under the null hypothesis that the average cross-validated PBPM error is not less than the average cross-validated individual fit error, confirmed the gain achieved when using estimates $\hat{\theta}$ obtained from a separate training population ($p < 0.0001$).

### 5.5.3 Impact on Kinetic Modelling

AIF estimation is of interest in the context of calculation of kinetic parameters. Impact of the proposed PBPM approach on parametric imaging was evaluated in that sense via Monte Carlo simulation of $H_2O$- and FDG-PET time activity curves generated from one-compartment (1C) and two-compartment (2C) models respectively(Sokoloff et al. 1977, Morris et al. 2004, Hawe et al. 2012, Bertoldo et al. 2014b, Dimitrakopoulou-Strauss et al. 2021), where

$$\frac{dC_1(t)}{dt} = K_1 C_p(t) - (k_2 + k_3) C_1(t) + k_4 C_2(t) \tag{5.13}$$

$$\frac{dC_2(t)}{dt} = k_3 C_1(t) - k_4 C_2(t) \tag{5.14}$$

(with $k_3 = k_4 = 0$ in the 1C model) describe exchanges between arterial plasma $C_p$ and the first and second tissue compartments $C_1$ and $C_2$. A set of template $H_2O$ time activity curves $\{z_{t,true}\}_{i=1}^{N}$ were created by evaluating the 1C model with each of the $N = 39$ clinical arterial samples from the $H_2O$ dataset described in Section 5.3.1 and with true parameter values $K_1 = 0.2$, $k_2 = 0.8$, $V_B = 0.05$, $\Delta = 0.25$ (found relevant in other studies (Watabe et al. 2001) in modelling tissue activity around the aorta in tumor blood flow studies). Similarly, a set of template FDG time activity curves $\{z_{t,true}\}_{i=1}^{N}$ were obtained by evaluating the 2C model with each of the $N = 91$ clinical arterial samples from the FDG dataset of Section 5.3.1 and with true parameter values $K1 = 0.102; k2 = 0.13; k3 = 0.062; k4 = 0.0068; V_B = 0.04; \Delta = 0.2667$ (found relevant in other studies (Feng et al. 1995) for modelling of grey matter activity in cerebral MRglu studies). This process yielded a set of respectively 39 and 91 unique template uptake curves. These templates were normalized to 1 so estimation of a scale factor was not required in this experiment. Finally, simulated uptake curves were obtained for each scenario by adding Gaussian noise with standard deviation $\sigma = \phi\sqrt{z_{t,true}}$ with $\phi = 0.001$ for $H_2O$ and $\phi = 0.04$ for FDG[2] to 10 replicates of each of these template curves. This yielded respectively 390 and 910 simulated time activity curves for these two settings.

Estimates of flow ($K_1$) and $k_2$ for the $H_2O$ scenario, and of flux ($K_i = K_1k_3/(k_2 + k_3)$), distribution volume ($V_D = K_1/k_3$), $k_1$ and $k_2$ for the FDG scenario, were compared across the range of 1C and 2C model fits obtained using AIF estimates from BCM, TE, CTE and PBPM for the $H_2O$- and FDG-PET cohorts. Delay was held constant for the purpose of this analysis, and the compartment models were optimized with respect to $(K1, k2, k3, V_B)$ (with $k_3 = k_4 = 0$ in the 1C model, and $k_4 = 0$ in the 2C model) via nonlinear estimation.

Figure 5.20 shows the distributions of percentage errors in estimating these parameters using varying AIF estimates. Results are visually clear in the $H_2O$ setting. For the FDG case, one-tailed Wilcoxon tests were carried out at the 5% significance level to assess bias from these distributions. For estimation of $K_1$, it was found that BCM was significantly more biased than PBPM ($p < 0.001$); no significant difference was found between TE and PBPM, and between CTE and PBPM. For estimation of $k_2$, it was found that BCM ($p < 0.001$) and TE ($p = 0.022$) were significantly more biased than PBPM; again no significant difference was found between CTE and PBPM. For estimation of $k_3$ (omitted

[2] (guided by the numerical analyses presented in supplementary materials)

from Fig. 6 for the sake of a simpler presentation), PBPM bias was significantly greater than BCM bias ($p < 0.005$) but TE bias significantly exceeded PBPM bias ($p < 0.001$); again no significant difference was found between CTE and PBPM. In summary, the PBPM model is a viable option for evaluation of physiological parameters. It outperformed all other models in both accuracy and precision in the $H_2O$ setting, and was either comparable to, or superior to performance of the other models in the FDG setting. These results illustrate its competitiveness and reliability for kinetic analysis across different tracers, against the most effective methods of reference.

## 5.6 Discussion

Kinetic modelling of dynamic PET imaging data relies on approximate knowledge of the Arterial Input Function (AIF), which is most accurately determined from direct arterial blood sampling. Less invasive AIF estimates are most commonly either image-derived input functions (IDIF) or population-based input functions (PBIF). The IDIF-based methodology consists of extracting the AIF from a region of interest (ROI) within a dynamic PET image that captures either a large blood vessel or the left cardiac ventricle. PBIF-based analysis consists in estimating a patient's AIF from scaling a population curve obtained from historical information on the patient's population. This approach is not subject to noisy PET information, but by construction of this scheme, the individual is assumed to have the same tracer injection protocol and physiological characteristics as the population, which is not always realistic.

Both strategies involve modelling of the AIF pattern, with the tri-exponential (TE) and convolved tri-exponential (CTE) models being two such methods of reference. These remain limited in their description of the injection profile, especially for PET tracers other than FDG. The population-based projection model (PBPM) approach proposed here combines strategies used in both IDIF and PBIF approaches in order to achieve flexible and reliable AIF estimation throughout the whole time course, by fitting a mixture of population-informed uptake patterns to individual patient imaging data. In this sense this methodology can be seen as the projection of individual patient PET tracer kinetics characteristics onto a basis of population uptake profiles. Unlike other modelling approaches using a boxcar function "on its own", PBPM incorporates a gamma distribution convolved with the boxcar function to achieve a more realistic representation

of signal arrival into plasma. Moreover, current PBIF methods require the injection protocol to be the same in all PET studies. Using a few population-based components, the proposed method can incorporate knowledge of the injection duration into the model fit, thus does not require the injection protocol to be the same in all PET studies.

A comparative analysis was carried out that included both TE and TCE, and a whole-body blood circulation model (BCM) as references for FDG-, $H_2O$- and FLT-PET datasets, as well as simulated datasets obtained from resampling of the clinical information. Results demonstrated that the proposed PBPM has overall higher accuracy, lower variability and greater adaptability to different tracers compared to the other three methods, and illustrated its consistency at varying noise levels. Application of the proposed approach to parametric imaging, using one- and two-compartment kinetic modelling scenarios, was also evaluated. In this experiment, the PBPM method yielded appropriate characterisation of flow, flux and distribution volume, and outperformed the other methods of reference for flow and distribution volume in particular, thus showing improved adaptivity to different tracers.

A natural end-goal is to apply AIF modelling to image-derived data, either because clinical sampling is not available or to facilitate non-invasive evaluation. As part of the technical contributions of this paper, regularization of the model should confer robustness against increased noise levels typically found in imaged blood-pool data. A region of interest from PET imaging of the left ventricle could be used in this sense, as the contrast of concentration of tracer from ventricles and their surrounding muscle is usually distinct. Follow-on work is planned around future access to datasets that combine sampling and imaging data to carry out such an evaluation. This will also yield the opportunity to evaluate the proposed PBPM method compared to IDIF techniques used commonly with major PET tracers.

Where only individual venous blood samples and no reliable arterial blood information are available, the proposed technique may still be considered, for example after conversion of the venous signals into arterial scales. Some venous input function (VIF) approaches were proposed that apply an arterio-venous transform scheme to estimate AIF, for example in 11C-labelled studies (Syvanen et al. 2006b).

The requirement for scale factor estimation, discussed in Section 5.2.4, impacts all modelling techniques, including the proposed PBPM strategy, but it is not

yet clear how. Analysing this impact will be the scope of follow-on work.

A critical minimum number of PET studies required to use the proposed PBPM technique with future studies remains to be determined and could vary with the PET radiotracer used. Numerical experiments demonstrated robustness of this model in this aspect, with stable model fit errors for even very few population studies.

This study has not discriminated the data in terms of healthy and cancer subjects, nor in terms of disease types. Although we do not anticipate significant differences in AIF profiles across such strata, using imaged data may introduce differences in PBPM estimates of AIF profiles. Further analyses would be required to explore this.

## 5.7 Conclusion

We proposed a statistical model of the arterial input function of a patient that leverages arterial uptake profile information at both the cohort and subject levels. Results from simulations demonstrated numerical stability and consistency of the approach at varying noise levels. Improvement in accuracy of the AIF representation over reference AIF models was assessed on three clinical cohorts, each imaged with one of three routinely used PET tracers (namely, FDG, $H_2O$ and FLT). Experiments further demonstrated that this representation of the AIF is viable for kinetic analysis of physiological parameters such as flow, flux and distribution volume from one- and two-compartment models. The proposed model was competitive for determination of kinetics from typical FDG template data, and outperformed other models when applied to $H_20$ settings. The proposed methodology can be incorporated in either population-based or image-derived input function estimation frameworks; the latter will be the scope of follow-on work assessing this model for non-invasive AIF estimation.

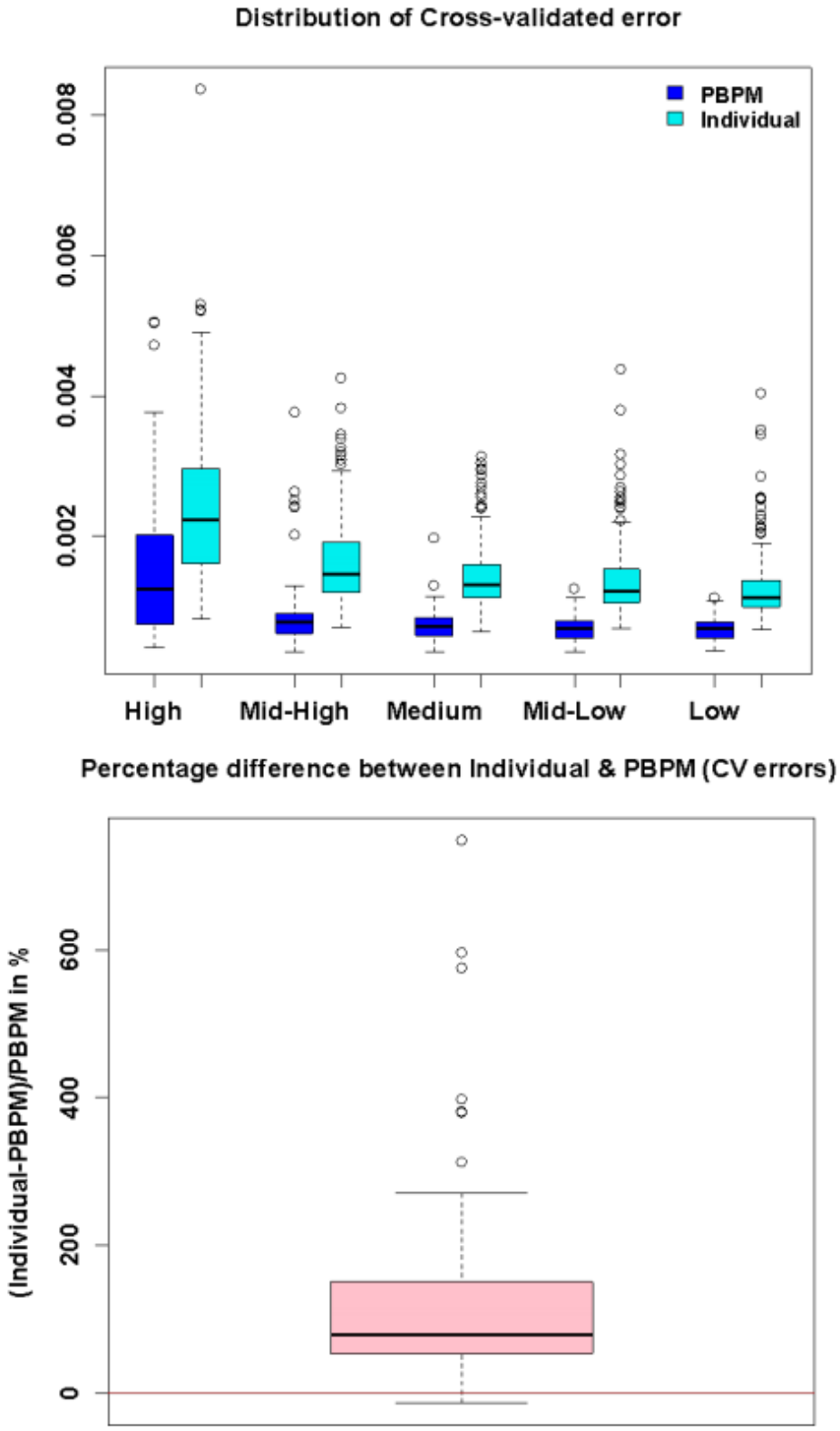


Figure 5.9: Top: distribution of PBPM and individual leave-one-out cross-validated fit errors (respectively darker and lighter colored) at varying noise levels. Bottom: percentage difference between 'individual' and PBPM at medium noise level.

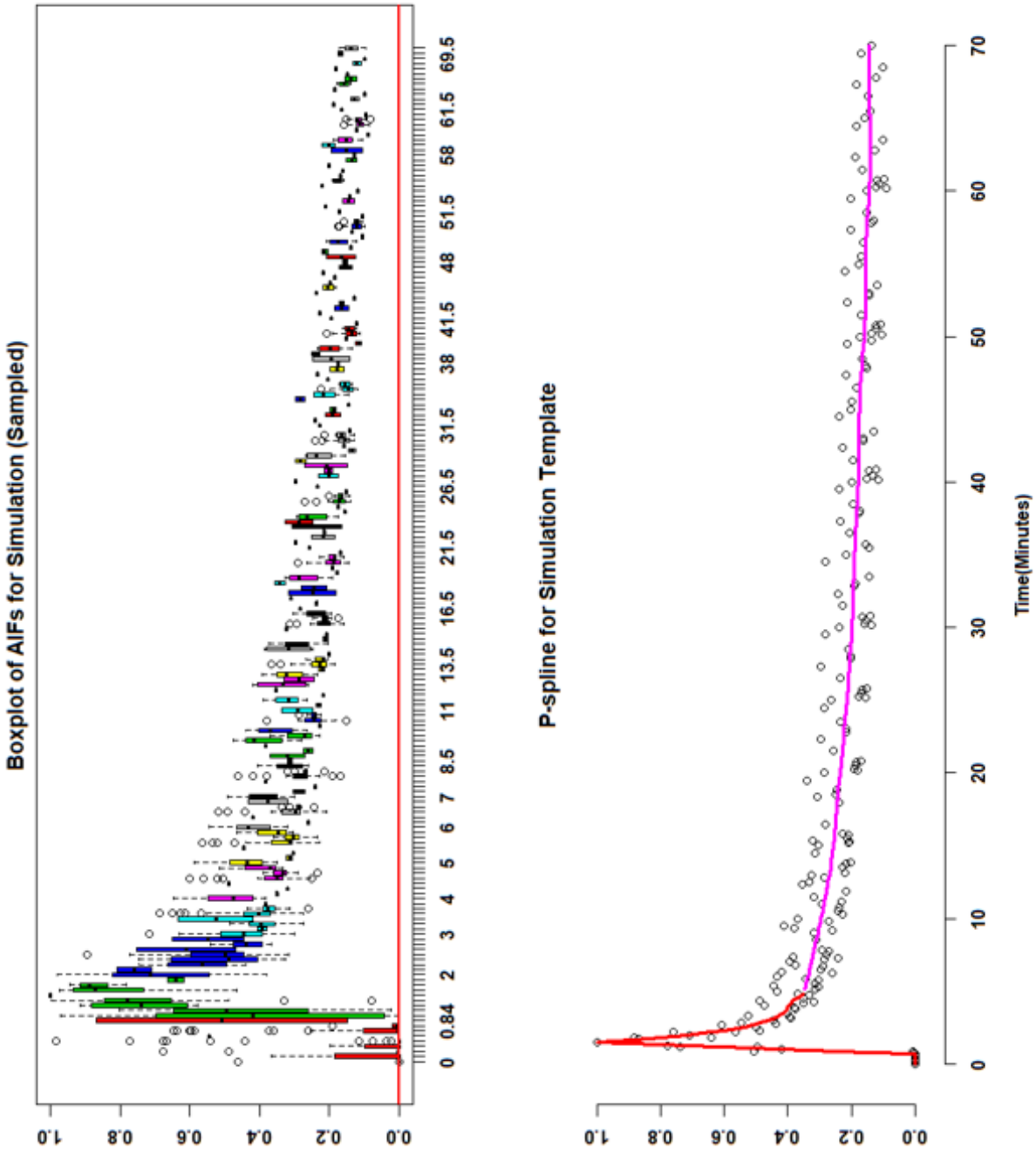


Figure 5.10: Top: Boxplot of 58 shifted arterially sampled AIFs. Bottom: Median of AIFs at each time point (empty circle) and P-spline smoothing of the medians with different values of smoothing parameter colored with red and violet blue.

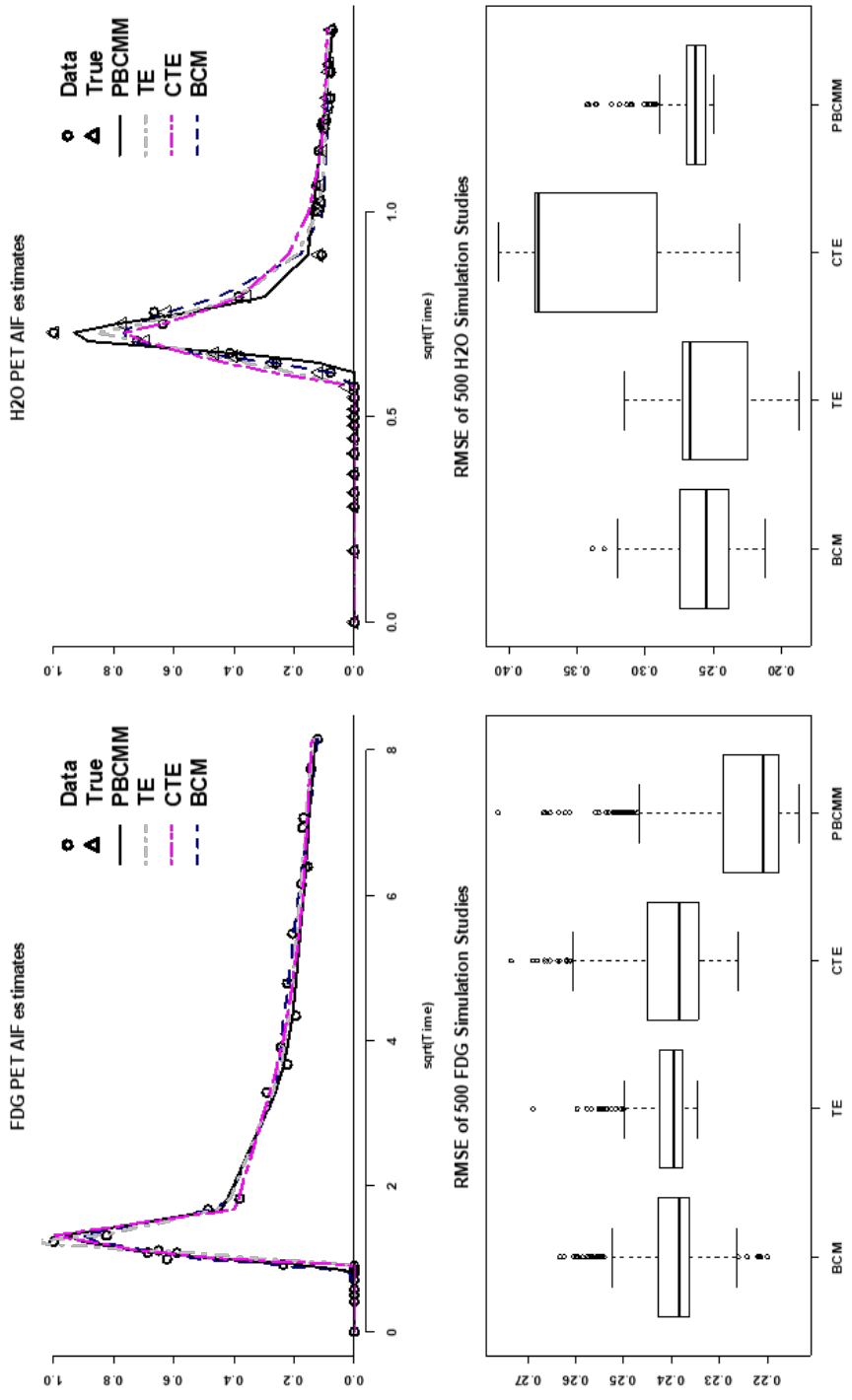


Figure 5.11: Performance of fit on 500 simulation FDG- and $H_2O$-PET studies using BCM, TE, CTE and PBPM.

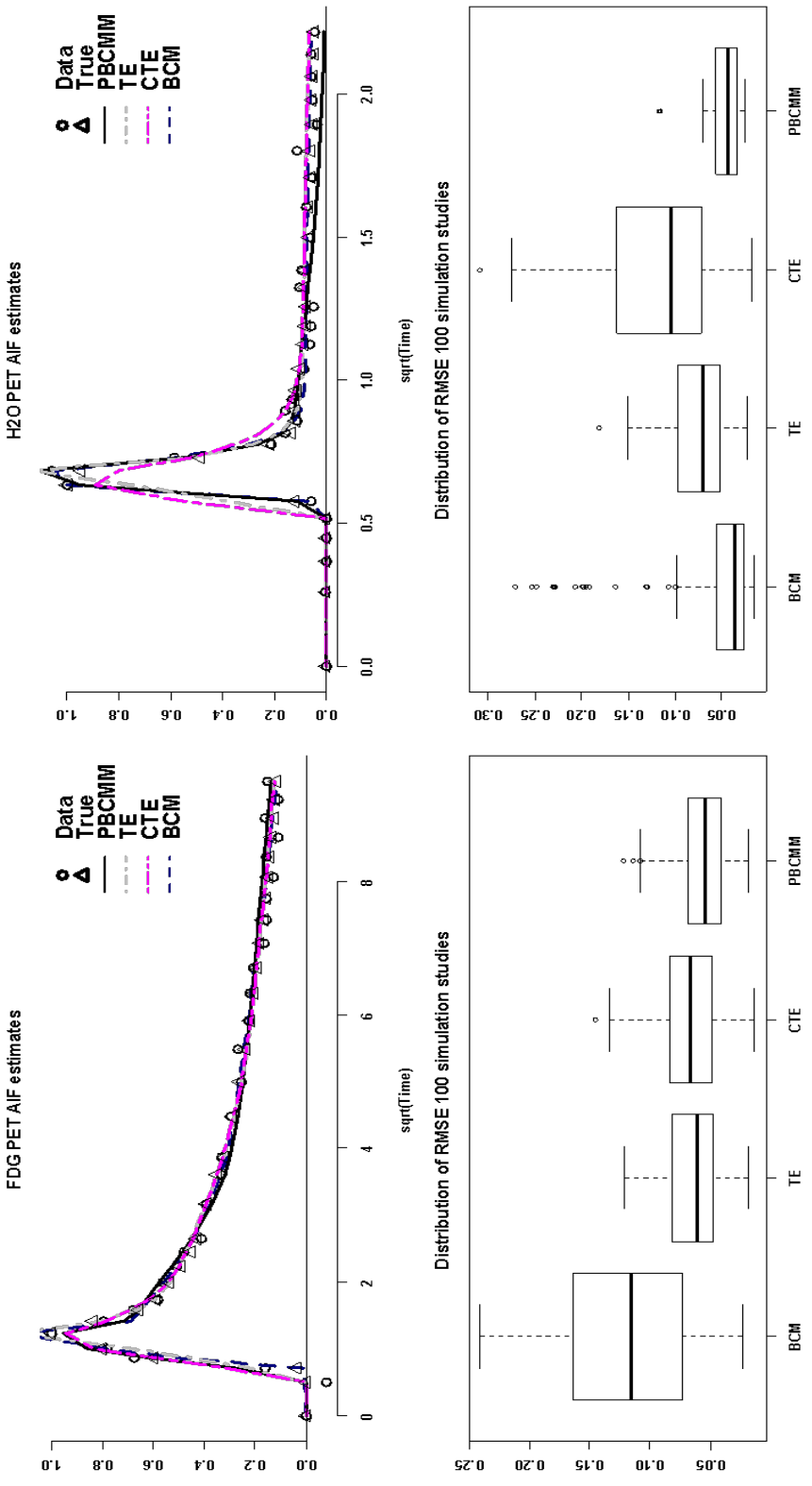


Figure 5.12: Model performance comparison for PBPM, TE, CTE and BCM on FDG (left) and $H_2O$ (right) PET simulation studies. Distributions of RMSE (5.10) for the two clinical cohorts (bottom) depict the relative fitting performance of the four models.

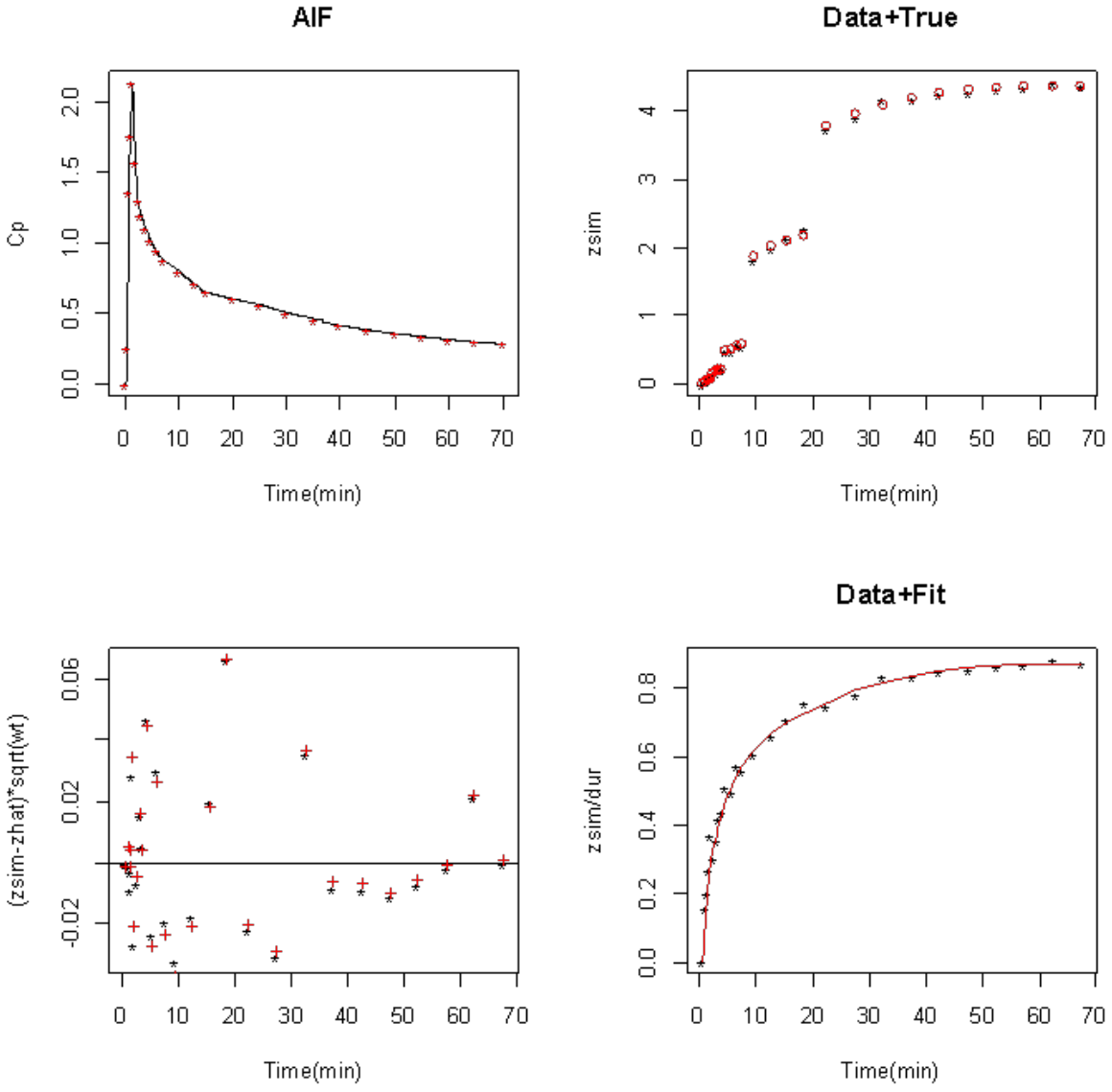


Figure 5.13: Top left: One example of clinical AIF; Top right: Simulated data and true data; Bottom left: Residuals of estimated curve to simulated one (black) and true one (red); Bottom right: Simulated data and fitted curve.

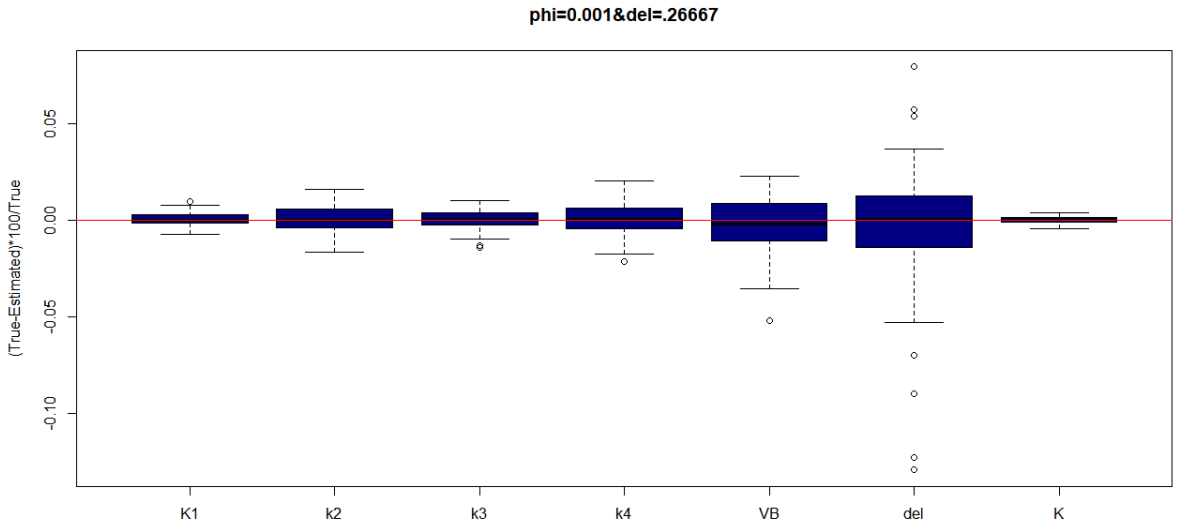


Figure 5.14: Top left: Example of a clinical AIF. Top right: Simulated data and true data. Bottom left: Residuals of estimated curve to simulated one (black) and true one (red). Bottom right: Simulated data and fitted curve.

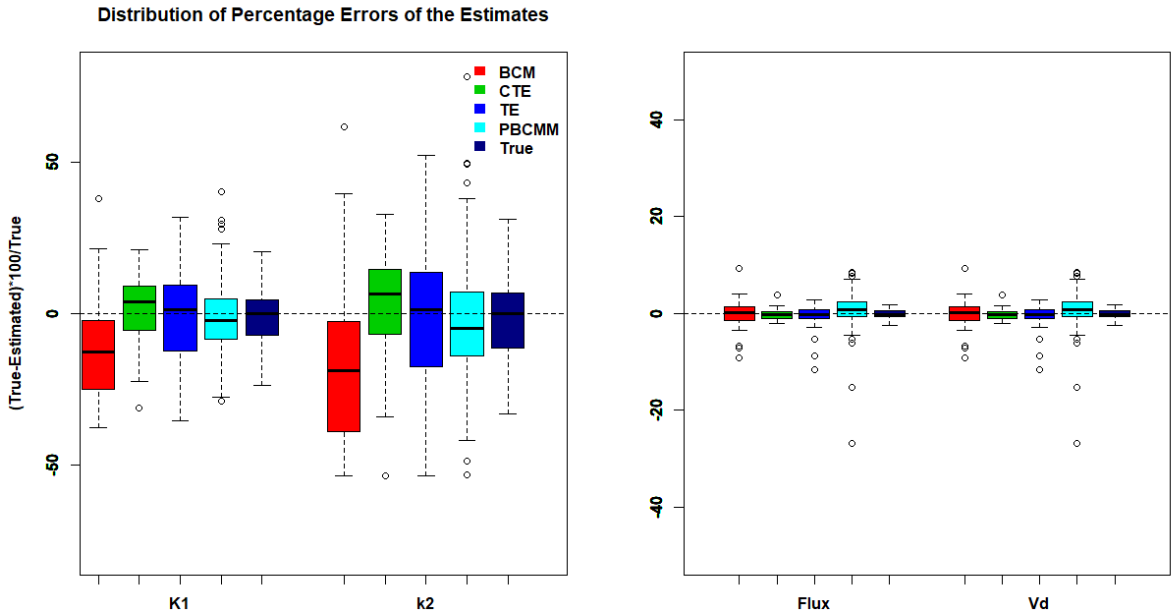


Figure 5.15: Distribution of percentage errors in estimating parameters using BCM, CTE, TE, PBPM estimated AIF and the true clinical AIF.

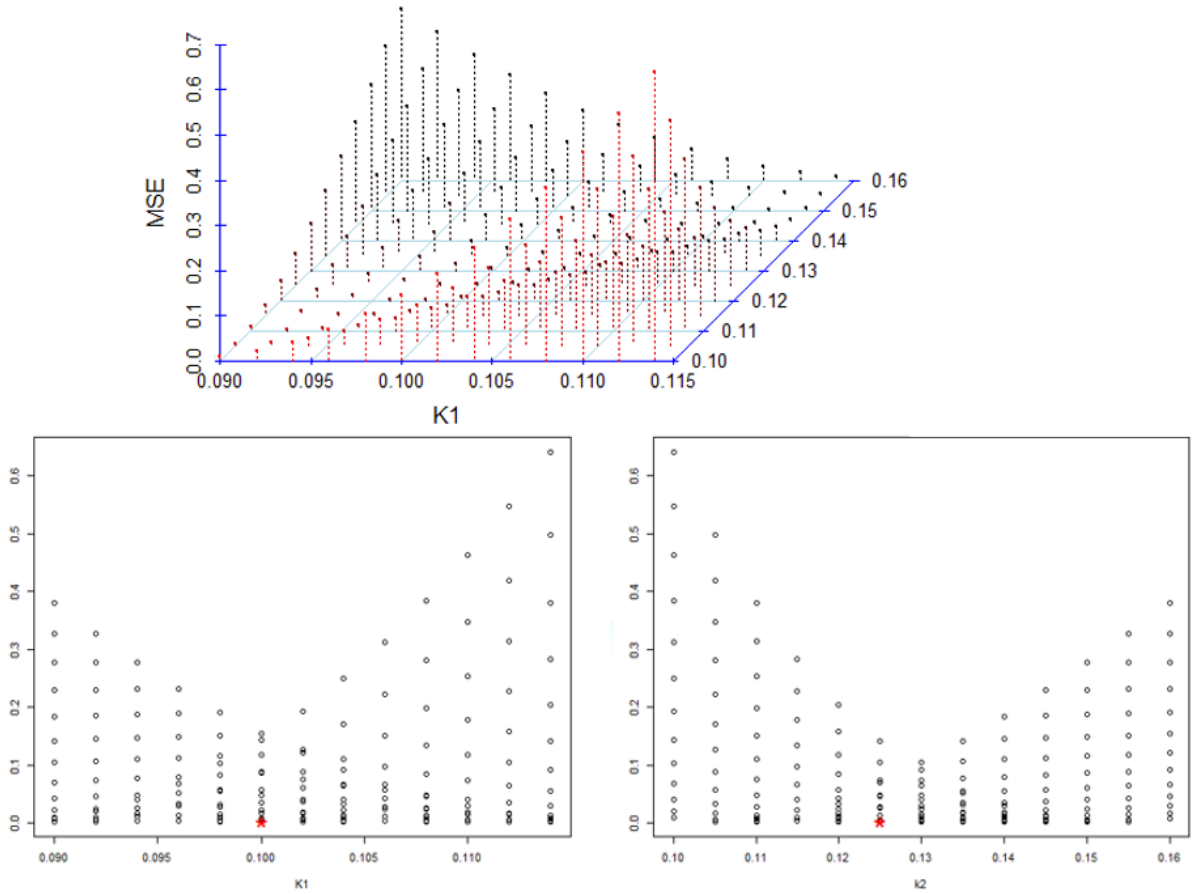


Figure 5.16: 3D (top) and 2D (bottom) scatter plot of the fit MSE for simulated data at noise level 0.04 against $K_1$ and $k_2$.

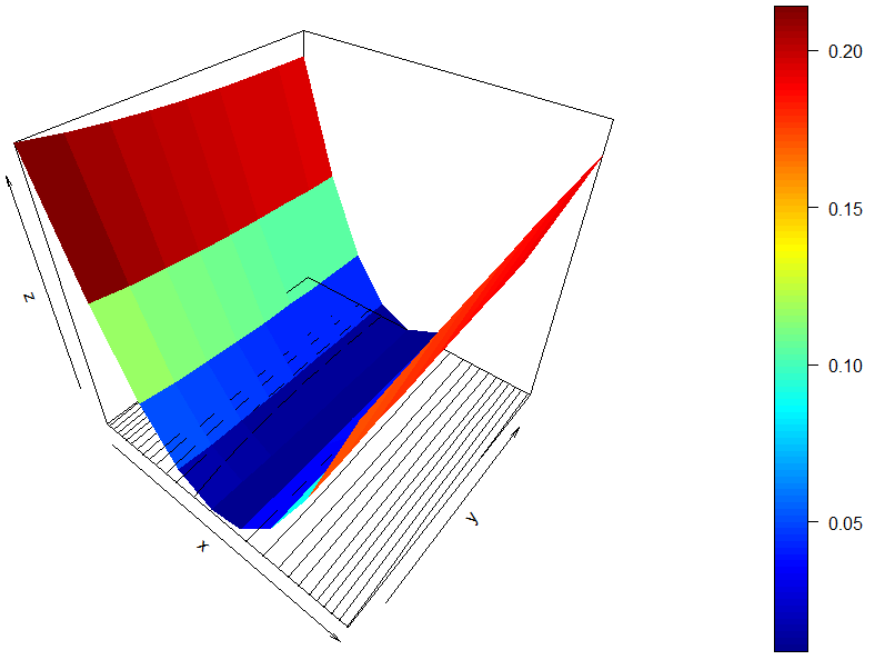


Figure 5.17: Surface plot of the criterion $(z)$ with respect to re-parameterized parameters $P_1$ $(x)$ and $P_2$ $(y)$.

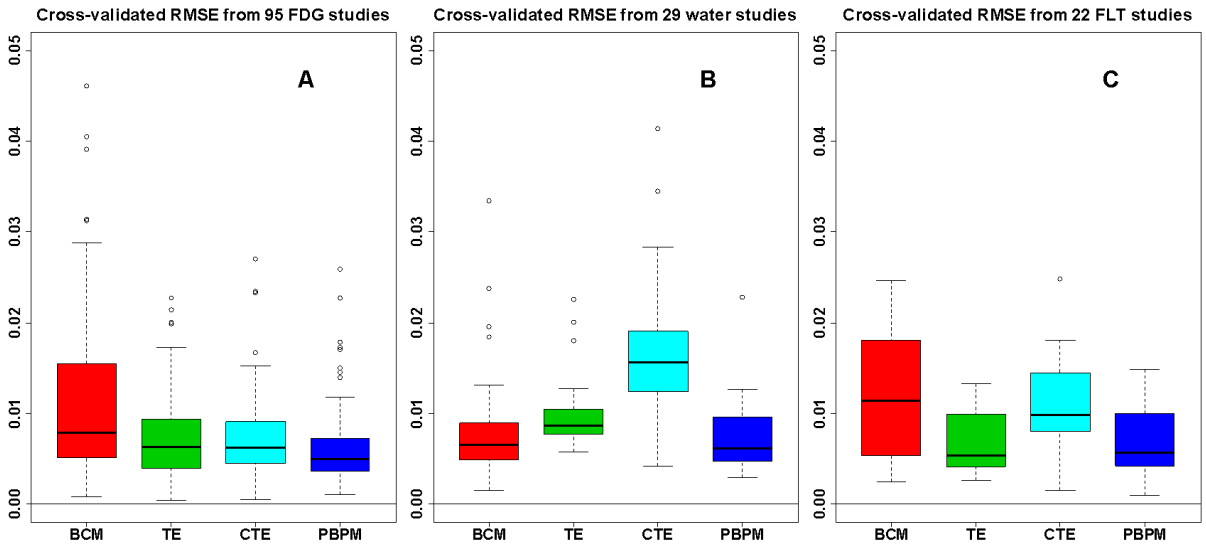


Figure 5.18: Model performance comparison for BCM, TE, CTE and PBPM on the FDG- (A), $H_2O$- (B) and FLT- (C) PET studies. Distributions of cross-validated errors (5.12) depict the relative fitting performance of the four models, and indicate that PBPM remains competitive for different tracers.

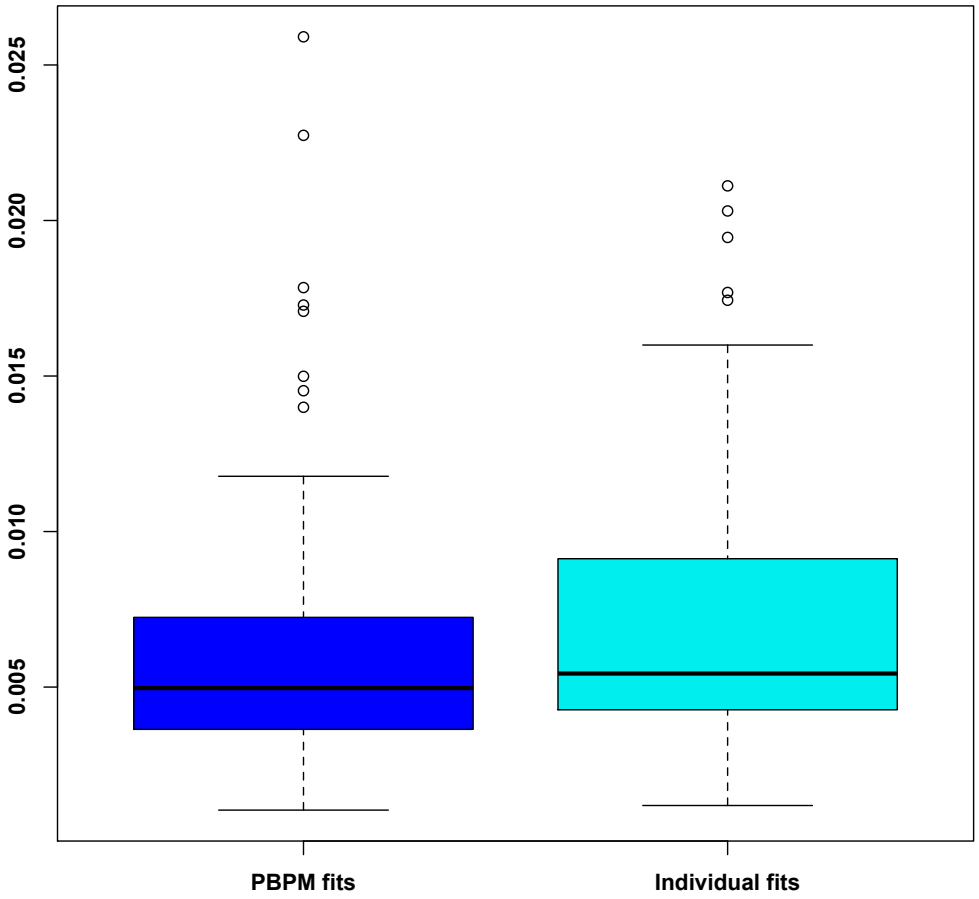


Figure 5.19: Comparison of cross-validated errors obtained when using a training population strategy to estimate the nonlinear parameters $\theta$ that determine the structure of the PBPM basis components (left), over a fully individual approach where the parametric vector $\theta$ is estimated directly from the same individual sampling data (right), showing a lower error tends to be achieved from a population-based strategy ($p < 0.0001$, one-sided paired Wilcoxon test).

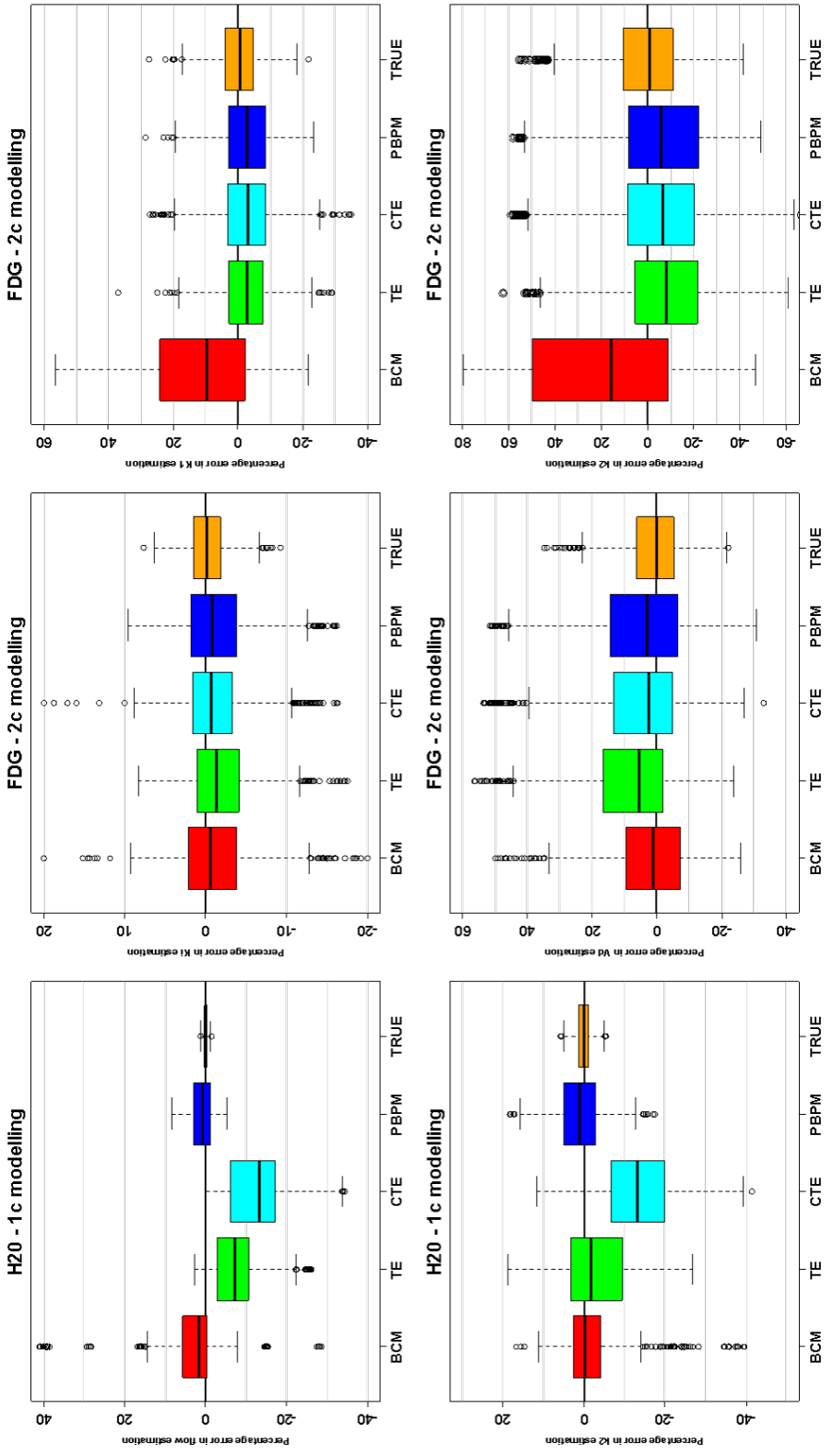


Figure 5.20: Distributions of percentage errors in estimates of flow $K_1$ (top left) and $k_2$ (bottom left) parameters from 1C modelling of simulated $H_2O$ uptake data, and flux $K_i$ (centre top), distribution volume $V_D$ (centre bottom), $K_1$ (top right), and $k_2$ (bottom right) parameters from 2C modelling of simulated FDG uptake data, using respectively BCM, TE, CTE, PBPM AIF estimates, or the true AIF used in simulating the template curves.

# Chapter 6

# Discussion and Conclusions

## 6.1 Summary of Contributions

Over the last few decades, a variety of medical imaging techniques have been developed and rolled out for clinical use. With the support of reconstructed images, one is able to observe and analyze what happens inside the patient non-invasively. CT and MRI are two common imaging techniques that provide anatomical information of the patient. Such images are used to visualize tissue, bone structure or blood circulation, to facilitate diagnosis and assessment.

Other modalities such as PET allow the capture of functional characteristics within the body. PET uses isotope labeled molecules as a tracer. Depending on the decay time of the radiotracer used, a study can last from a few minutes to over one hour. Analysis of this dynamic 3D data requires knowledge or estimation of the arterial input function (AIF) (Sokoloff et al. 1977, Patlak et al. 1983, Cunningham & Jones 1993). A traditional way of obtaining this AIF is direct sampling from the arterial or venous blood during the PET scan. Either can cause great discomfort to the patient. In recent decades, several alternatives have been developed. Some of them are introduced and discussed in Chapter 3. This PhD project was concerned with the task of exploring and developing novel statistical modelling methodologies to improve AIF estimation performance and generation across PET tracers.

A model previously proposed by our group named whole body blood circulation model (BCM) (Huang & O'Sullivan 2014, O'Sullivan et al. 2017) is described in Section 3.5. It provides a comprehensive and detailed picture of the whole

body blood circulation system, but it is computationally complex and time consuming, and prompted us to consider other strategies.

Chapter 4 introduces a first attempt at modelling AIFs. The tracer travel-rate projection model (TRPM) combines a concept from BCM with the idea of compartmental modelling (Kety & Schmidt 1948, Sokoloff et al. 1977), yielding increased accuracy. However, some limitations of the model are pointed out in Section 4.5, and addressed with a second proposal.

Chapter 5 develops a new model called the population-based projection model (PBPM) that extends the projection strategy used in TRPM to create a basis of travel profiles trained from independent cohort data. Simulation studies show that this new model is stable and at the same time flexible, simple but comprehensive. Firstly, PBPM significantly simplifies model computation. The nonlinear least squares process is bypassed and only linear coefficients are optimized in fitting individual curves, allowing for the optimization to be done in instant. The basis components represent traveling patterns of the tracer to reflect the functioning of various tissue types. The PBPM also allows for estimation of the scale factor from patient information, allowing for the true AIF to be recovered from the signal. This enables application of PBPM in future work on dynamic PET imaging. A comparative analysis was carried out that included both the tri-exponential model (TE) and convolved TE (CTE), and the BCM as references for FDG-, $H_2O$- and FLT-PET datasets, as well as simulated datasets obtained from resampling of the clinical information. Results demonstrated that the proposed PBPM has overall improved competitive accuracy and variability, and greater adaptability to different tracers compared to the other three methods, and illustrated its consistency at varying noise levels. Application of the proposed approach to parametric imaging, using one- and two-compartment kinetic modelling scenarios, was also evaluated. In this experiment, the PBPM method yielded appropriate characterisation of flow, flux and distribution volume, and outperformed the other methods of reference for flow and distribution volume in particular, thus showing improved adaptivity to different tracers.

## 6.2 Opportunities for Future Research

### 6.2.1 Application to Other Tracers

We have assessed the PBPM on three commonly used tracers. There are many popular compounds using other isotope labeled tracers. The PBPM construction should be adapted to these.

### 6.2.2 Estimating the AIF from Imaging Data

In this work, we used only blood sampling data. The PBPM approach can alternatively be applied to imaged regions of interest (ROI), $e.g.$ from a sphere with diameter of 6 mm at the center of the left ventricle (LV) (considered as a comparatively large arterial blood pool). As the preliminary demonstration, we drew such ROIs from breast cancer FDG-PET images, and used the time activity curves (TACs) for AIF extraction, yielding the results shown in Fig 6.1. PBPM performance could not be established since true AIF data were not available. In future work, the model may be applied to image data, using the LV ROI signal as the true AIF.

A scale factor should be incorporated as a later step in estimation of the AIF, but this scale factor is not available from the imaging data either, and arterial blood sampling is required to evaluate this quantity.

Images are used to derive the shape of AIFs from estimated LV curves. Manual ROI identification could be time consuming and subject to cross-user variability. The imaging data are from the LABCa studies where the LV ROI is obtainable. When the LV is not in the field of view, other blood pools may not easily be regionalized. The method was only applied to data from FDG and $H_2O$ studies for now, and further experimentation should be carried out on studies with other tracers. Figure 6.1 gives one example of manual LV ROI drawing and performance of PBPM fit on normalized imaging data from the same region. No obvious bias or misfitting can be visually detected. Further analysis could be done when both imaging data and arterial sample data become available.

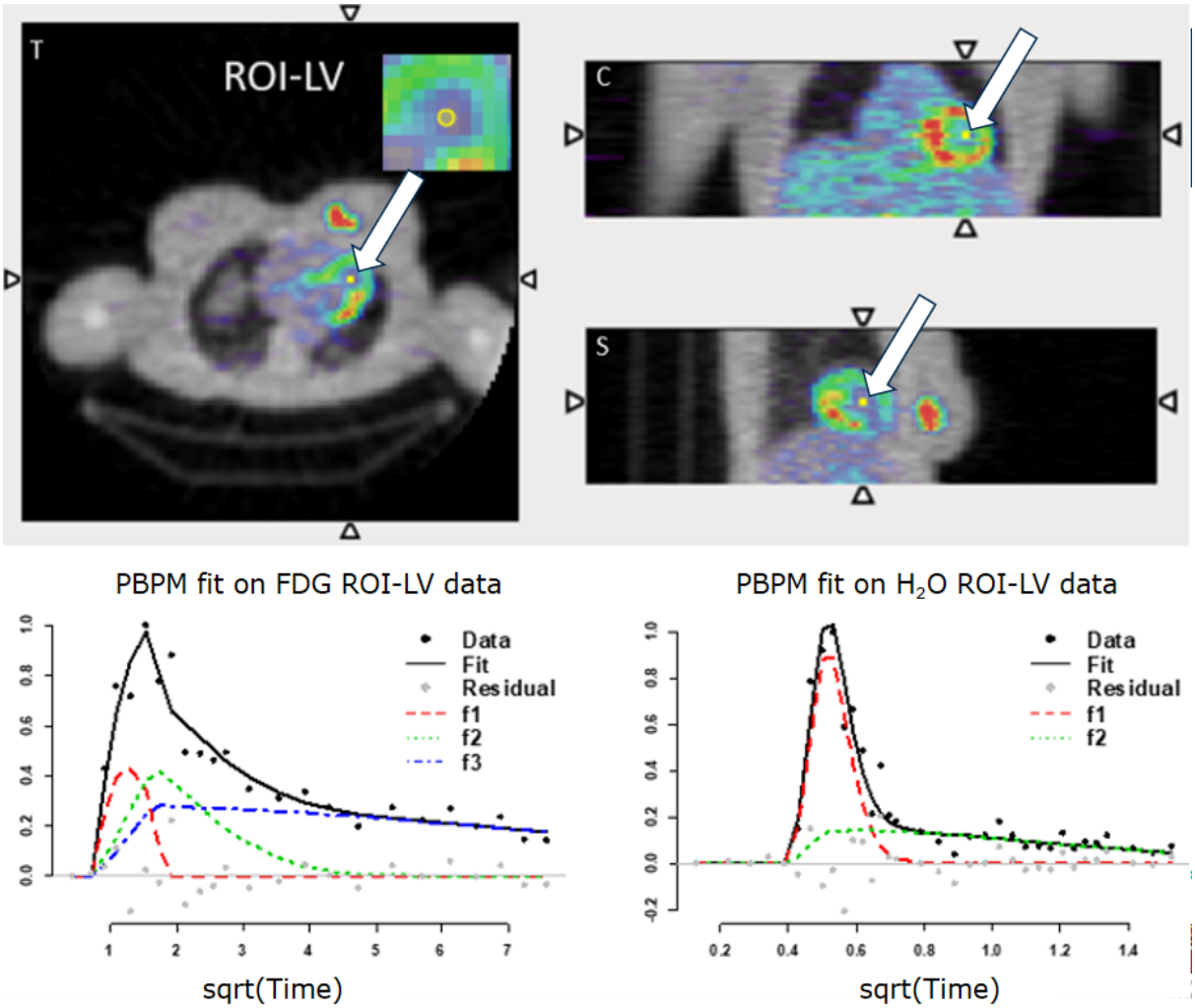


Figure 6.1: Example of ROI-LV drawing on PET imaging data of LABCa patients from University of Washington (top) (Mankoff et al. 2002, 2003, Tseng et al. 2004, Dunnwald et al. 2008, 2011, O'Sullivan et al. 2017). Imaging data are processed in AMIDE (Loening & Gambhir 2003). Example of PBPM fit on ROI-LV FDG data (bottom left) and $H_2O$ data (bottom right).

### 6.2.3 Reduced Scanning Times

As stated earlier and illustrated by Figure 5.9, the PBPM model provides an opportunity to reduce scanning time whilst achieving similar AIF prediction accuracy, which would be of particular interest for dynamic FDG-PET imaging. To explore this opportunity, the sampled AIFs were further fitted from the same clinical data but for a number of reduced scanning times. In current routine practice, the injection duration for FDG is usually less than 1 minute. This causes the injection profile to appear like the convolution of a narrower square function with a gamma distribution. In this dataset, some injections took up to

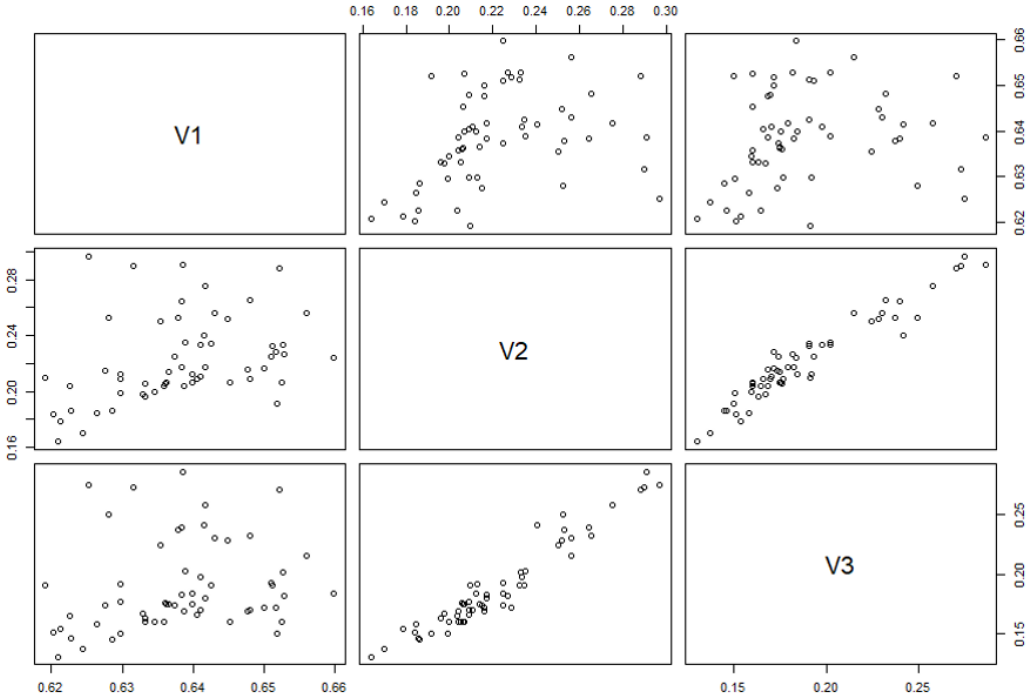


Figure 6.2: Paired scatter plot of estimated linear coefficients from PBPM applying to arterially direct sampled data.

2 minutes (33 cases) (Huang & O'Sullivan 2014). These particular studies were removed from the cohort in the interest of consistency, and only studies with a 1-minute (58 cases) injection duration were considered. Table 6.1 presents overall mean and standard error of estimation percentage errors for the AIF peak (defined as the 3-point average using the highest value and its two adjacent points), tail (defined in two different ways, as the 60-minute value and as the average of all signal values between 30 and 60 minutes), and mean transit time (MTT), defined as the integral of scaled AIF over the scanning time across all 58 FDG-PET studies and for scanning times $t$ (6.1). These percentage error statistics, which are also compared to those obtained from the commonly used TE model, suggest that one could estimate AIF peak, tail and MTT values at an acceptable loss of accuracy–even if reducing the scanning time from 62.5 down to 22.5 minutes. In contrast, estimation based on TE yields increasing estimation errors with reducing scanning times.

$$MTT(t) = \int_0^t C_P(s)ds \tag{6.1}$$

Figure 6.3 illustrates the overall PBPM RMSE distributions for varying scanning

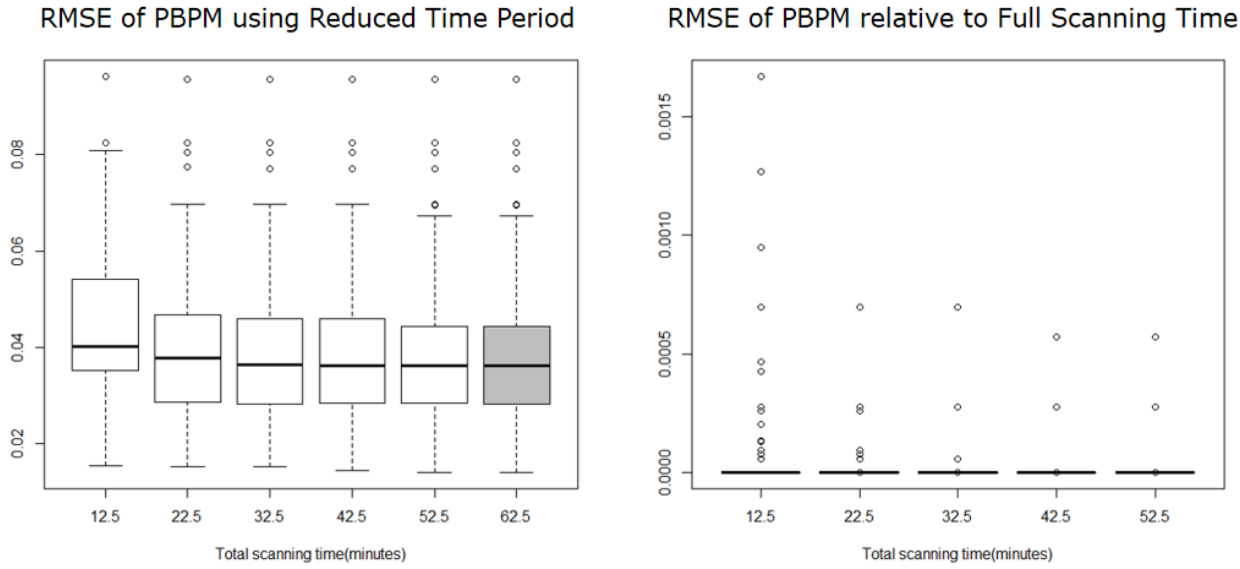


Figure 6.3: Distributions of PBPM fit errors (left), and of fit errors relative to the reference 62.5-minute fit (right), from the 58 FDG-PET SAIFs for varying scanning times.

times, using the full 62.5-minute scanning time as a reference for comparison (grey boxplot). It supports the results of Table 6.1 and shows that the overall distribution of PBPM fit errors does not change noticeably when scanning time is reduced from 62.5 minutes down to as low as 22.5 minutes.

Table 6.1: Mean and standard error of percentage errors ($i.e.$ $100 \times \frac{actual-predict}{actual}\%$) fitting 58 SAIFs using reduced scanning times.

| Scanning Time (mins) | Peak (3 pts average) | Tail (60) | Tail (30-60 average) | MTT (60) |
|---|---|---|---|---|
| up to 62.5 | $-0.27 \pm 0.56$ | $-7.33 \pm 0.93$ | $-0.92 \pm 0.49$ | $-0.61 \pm 0.33$ |
| TE | $0.03 \pm 0.88$ | $-4.84 \pm 0.55$ | $-1.53 \pm 0.26$ | $-0.52 \pm 0.09$ |
| up to 52.5 | $-0.24 \pm 0.56$ | $-8.40 \pm 1.04$ | $-1.86 \pm 0.56$ | $-1.28 \pm 0.36$ |
| TE | $0.03 \pm 0.88$ | $-6.59 \pm 0.74$ | $-2.64 \pm 0.31$ | $-1.17 \pm 0.14$ |
| up to 42.5 | $-0.15 \pm 0.56$ | $-9.07 \pm 1.15$ | $-2.44 \pm 0.67$ | $-1.65 \pm 0.43$ |
| TE | $0.03 \pm 0.88$ | $-9.90 \pm 0.98$ | $-4.80 \pm 0.41$ | $-2.42 \pm 0.21$ |
| up to 32.5 | $0.03 \pm 0.55$ | $-8.46 \pm 1.31$ | $-1.89 \pm 0.87$ | $-1.25 \pm 0.55$ |
| TE | $0.03 \pm 0.88$ | $-15.48 \pm 1.38$ | $-8.42 \pm 0.64$ | $-4.57 \pm 0.35$ |
| up to 22.5 | $0.07 \pm 0.55$ | $-5.66 \pm 1.59$ | $0.62 \pm 1.19$ | $0.42 \pm 0.76$ |
| TE | $0.02 \pm 0.88$ | $-21.15 \pm 2.32$ | $-12.34 \pm 1.50$ | $-6.91 \pm 0.86$ |
| up to 12.5 | $0.06 \pm 0.55$ | $3.03 \pm 3.26$ | $8.36 \pm 2.82$ | $5.54 \pm 1.88$ |
| TE | $0.01 \pm 0.88$ | $-26.25 \pm 5.19$ | $-15.38 \pm 3.64$ | $-8.79 \pm 2.19$ |

We have shown that this model can fit the AIF using only early data points. Components within our model are from a patient population. Only the linear

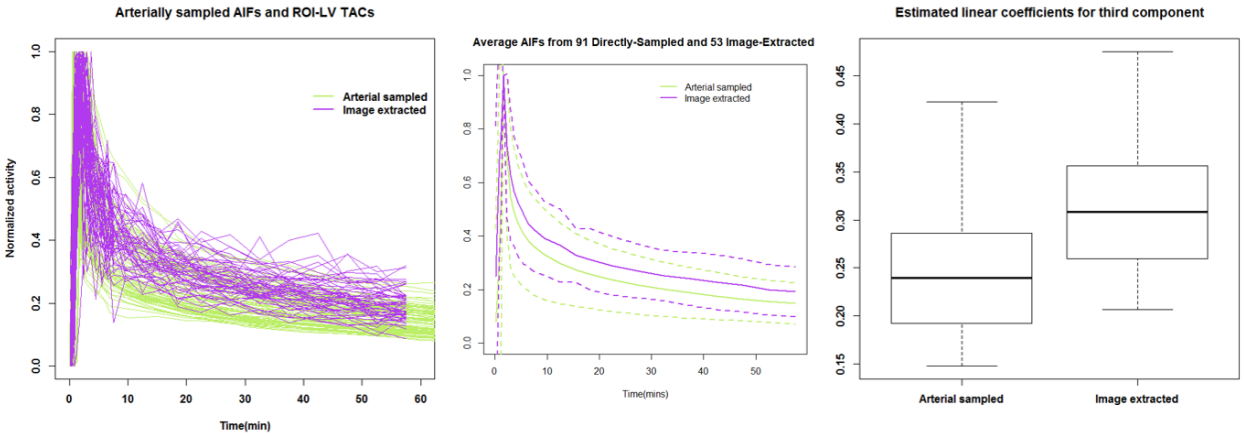


Figure 6.4: Left: 91 FDG-PET directly-sampled AIFs (Green) and 53 image-extracted ROI-LVs (Pruple); Mid: Mean and 95% confidence interval of the data; Right: Distribution of estimated linear coefficients for third components.

mixture parameters need to be defined in an application of PBPM. When scanning duration is reduced so much than the "late" basis components cannot be evaluated, it is still possible to estimate the proportion of this tail-end of the mixture using the other linear parameters. The reason why the PBPM can estimate the whole AIF curve from the early data points is that once the basis components are decided, the first and second linear parameters can be accurately estimated, since the components related to the first two linear parameters varies a lot at the beginning of the study, introducing a significant positive relationship between second and third linear parameters. Further assessment could be conducted on this aspect.

### 6.2.4 Assessment of Spillover in PET Imaging Data

Figure 6.4 (left) presents time courses of arterially sampled and image-extracted AIFs from our data. The distributions of these two groups of AIFs show that the median of the tails of image-derived AIFs is significantly greater than that of the sampled data. This is caused by the spillover effect inherent to PET imaging data. We could add a mathematical term to account for the effect to our model, so that the estimated AIF will be the sum of the original term and a new term called spillover, as shown in Fig 6.5. Future work on complete datasets including paired imaging and sampling data will be carried out to assess effectiveness of this correction approach.

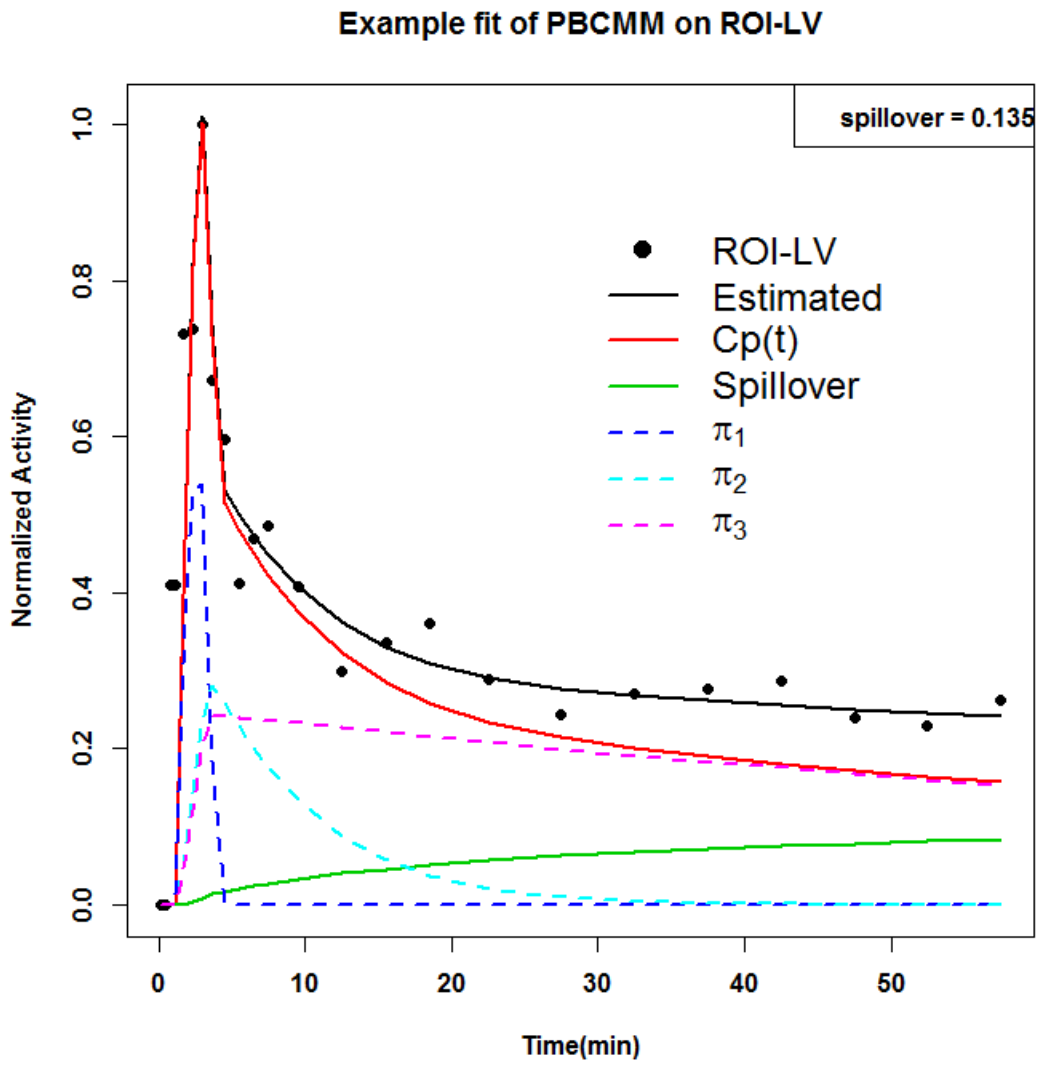


Figure 6.5: One example fit of the extended PBPM. Spillover is the estimated linear coefficient for the extended term.

### 6.2.5 Improvement of TRPM

The scope of this work was limited to the development of potential techniques, and the assessment and experimental validation of the PBPM, which we identified as the more promising model. Our initial attempt with the TRPM presented in Chapter 4 however holds potential for further improvement, which could be the subject of future work, at which point TRPM may also be evaluated.

### 6.2.6 Normalizing by Area Under the Curve

Added a new section 6.2.6 in the discussion section. An interesting conceptual alternative to the existing version of the PBPM that we will explore is to normalize the area under the curve of the signal to 1, instead of normalizing it to have its peak to 1. This would make the PBPM approach closer to a true mixture model and will be considered in follow-on work. We opted to normalize the peak to 1 because the peaks of the mixture components were also set to 1, $i.e.$ they are not PDF's either. This allowed us to preserve a simple evaluation of the true peak value (following subject-specific rescaling), which is correlated to the patient dose and also directly maps to key kinetic modelling parameters (as so does the peak-to-tail ratio). Irrespective of the normalization strategy used, the shape of the AIF estimate will be estimated similarly, and the final AIF curve estimate must be rescaled to the individual arterial signal scale, so both approaches should yield similar final estimates in the original signal domain. Normalizing to an AUC of 1 may however facilitate further uses of the PBPM since it would make interpretation of the mixing coefficients more practical. The current intended use of the PBPM does not include practical interpretation of these coefficients (the $\pi$'s in model (5.1)), as its output estimate is only anticipated to inform further kinetic modelling of the data.

Moreover, the typical constraint that $\sum_{j=1}^{J} \pi_j = 1$ would be required for such practical interpretation, but it is not a requirement in the current version of the PBPM since it is not *per se* a mixture model. Here it is slightly relaxed in order to address the possibility that the true (unmeasurable) unscaled peak value may be larger than the observed value (or, possibly but more rarely, lower than the observed and elevated due to additive noise). This principle remains true following scaling, and our relaxing the constraints on $\sum_j \pi_j$ allows to better adapt to that variability. Interpretation of these linear combination parameters remains loosely that of proportions.

## 6.3 Conclusion

Concerned with the question of estimating the arterial input function (AIF) of a patient, we initially developed a travel-rate projection model (TRPM), which highlighted opportunities for flexible and interpretable modelling of AIFs but with some limitations. This effort provided theoretical support that led us to

the population-based projection model (PBPM) model. This PBPM is the main contribution of this thesis. This approach consists of fitting a small number of basis functions from population data, to obtain typical early, intermediate and late uptake profiles. Individual subject AIF estimates are then obtained by projection of the observed blood signal onto this basis, in the form of a linear mixture of the population components. This method involves a relatively small number of model parameters and a simple fitting procedure. The method was assessed on arterial sampling data from $^{18}$F-FDG, $^{15}$O-$H_2O$ and $^{18}$F-FLT clinical studies and compared to reference techniques including tri-exponential models and a whole-body circulation model. Results demonstrated the reliability, flexibility, and potential benefit of this approach in estimating AIFs and various kinetic parameters for three of the most commonly used tracers in major applications of PET imaging.

# Appendix A

# List of Publications and Presentations by the Author

## A.1 Journal Paper

Z. Xiu, M. Muzi, J. Huang and E. Wolsztynski, "Patient-adaptive population-based modelling of arterial input function," IEEE Trans. Med. Imag., vol. 42, no. 1, pp. 132-147, Jan., 2023.

## A.2 Peer-reviewed Conferences

X. Meng, J. Huang, F. O'Sullivan and Z. Xiu, "Seeded MDS with a Large Number of Cases" Royal Statistics Society Annual Conference (RSS), Cardiff, UK, 3-6 Sept., 2018.

Z. Xiu, J. Huang, J. O'Sullivan, E. Wolsztynski, D. Mankoff and F. O'Sullivan, "Mixture Modelling for AIF Extraction from Dynamic PET Studies," Royal Statistics Society Annual Conference (RSS), Cardiff, UK, 3-6 Sept., 2018.

T. Mou, J. Huang, Z. Xiu and F. O'Sullivan, "Fitting Spatial Auto-Regression Models to 3-D PET Imaging Data," Royal Statistics Society Annual Conference (RSS), Glasgow, UK, 4-7 Sept. 2017.

Z. Xiu, J. Huang, J. O'Sullivan, E. Wolsztynski, D. Mankoff and F. O'Sullivan, "Calibrating a whole body circulation model for image-based AIF extraction

in the context of Blood Flow-Metabolism Mismatch Assessment in LABCa Patients," Royal Statistics Society Annual Conference (RSS), Manchester, UK, 5-8 Sept., 2016.

# Appendix B

# Assessment of Tracer Concentration at Injection

Here we consider assessment of the pattern of tracer concentration at injection, in the arm and right ventricle sites. In the PBPM model, we assume that the concentration of tracer from injection to the first arrival at the right ventricle shows a pattern of convolution between a gamma density function and a square wave rising over the injection duration. As introduced in Chapter 1, PET imaging reflects the concentration of tracer in the FOV of the human body over the scanning time. Before a PET scan, a dose of tracer will be injected into the vein at the wrist (for water and FDG injection) of the subject. At the very beginning, the venous blood carries the tracers to the right ventricle of the heart. After a beat of the heart, tracer molecules start traveling in the blood stream via arteries. Therefore, the shape of time course of concentration of tracer at injection and arm sites could described by a convolution between gamma and square wave. Also theoretically, the concentration of tracer at injection site should be slightly sharper than that at the arm site. The shape of the right ventricle time course should be like the time course at injection or arm site convolved with an exponential distribution. Here we use the dataset from University of Washington (See Section 4.4.1.2 for more details), drawing ROIs at injection, arm and right ventricle sites. For each site, tracer concentration within the ROI is extracted (see Figure B.1 for an example with an ROI in the arm).

50 FDG-PET studies (two were omitted due to operational difficulty) from University of Washington (Mankoff et al. 2003, Dunnwald et al. 2008, 2011, O'Sullivan et al. 2017) were used in this study. Figure B.2 presents the mean

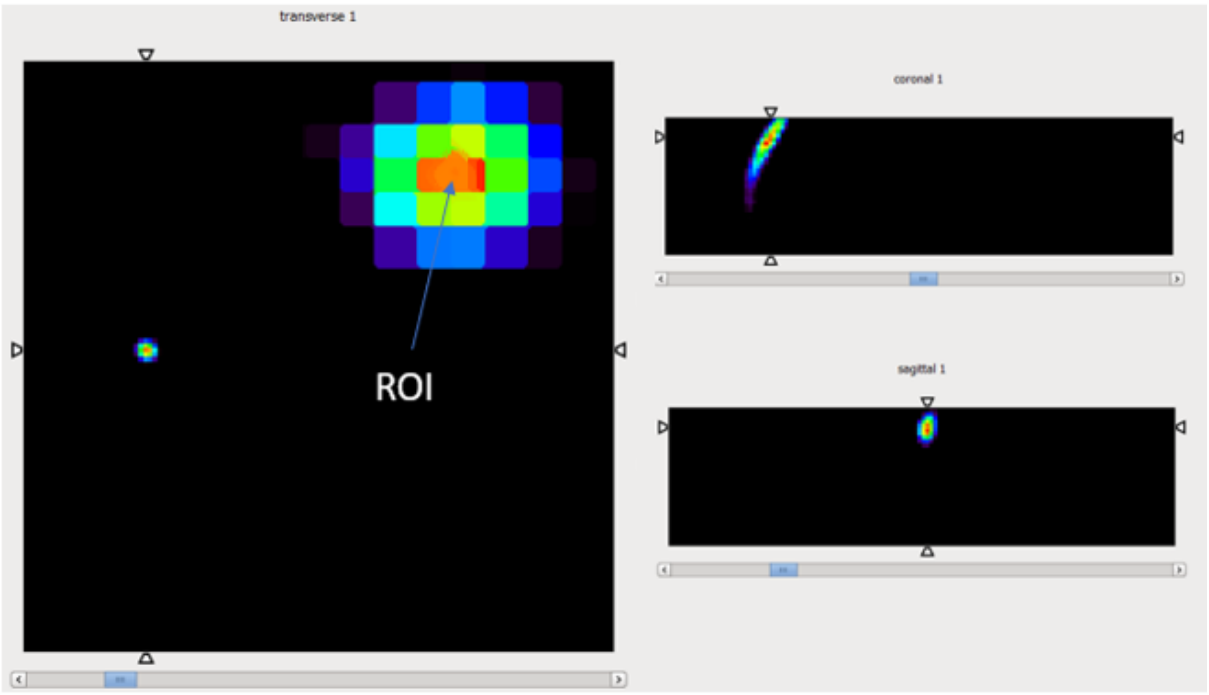


Figure B.1: Manually drawn ROI from PET imaging data from AMIDE (Loening & Gambhir 2003), located in the patient's arm.

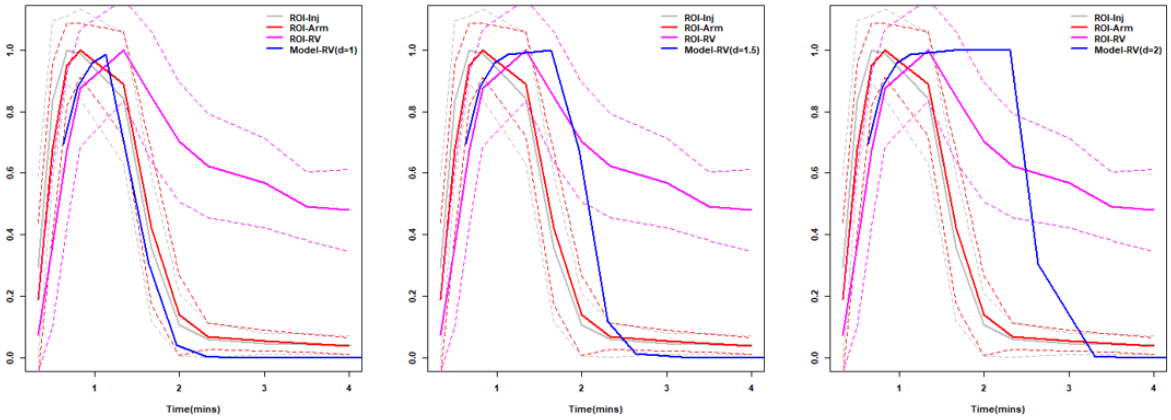


Figure B.2: Mean and 95% confidence interval of TACs from ROIs at the injection, arm and right ventricle for 50 FDG-PET studies and a convolution between gamma and square wave with different widths (blue).

and 95% confidence interval of TACs from ROIs at the injection, arm and right ventricle for 50 FDG-PET studies and a convolution between gamma and square wave with different widths (1, 1.5 and 2 minutes). The injection durations are 2 minutes for all 50 studies. From Figure B.2 left and middle (1 and 1.5 minutes, respectively) we can see the convolution provides a reasonable template overall. However, for a injection duration of 2 minutes, the convolution is too wide to be a representation of the time course of concentration at the arm site (or at first arrival of right ventricle). One reason would be that the operation of injection over the two minutes is not uniform, but a another gamma-like pattern. Since in the recent years, injection protocols usually involve automatic injection, and injection duration are usually around 60 to 90 seconds, the convolution approach seems appropriate.

Figure B.3 presents similar analyses for 51 $H_2O$-PET studies (one omitted due to operational difficulty) from the same dataset. Since the injection duration is short (bolus injection around 5 seconds), the variation in injection durations can be ignored. A convolution between a gamma function and a narrow square wave rising over the injection duration could fit the data well.

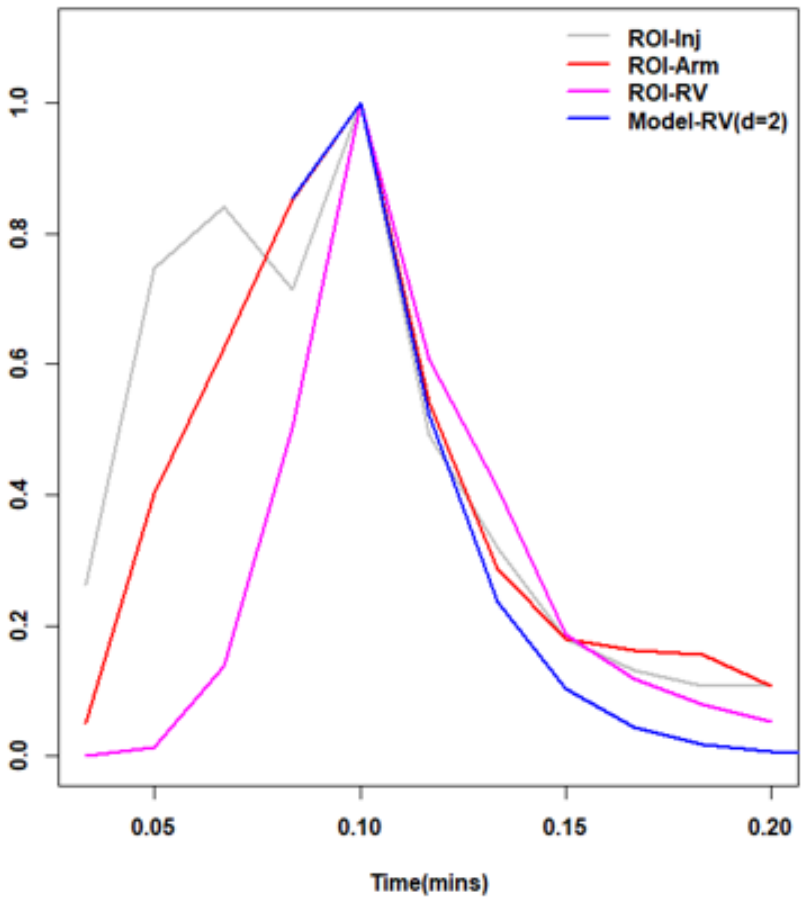


Figure B.3: Mean of TACs from ROIs at the injection, arm and right ventricle 51 $H_2O$-PET studies and a convolution between gamma and square wave with different widths (blue).

# Appendix C

# Convolution between Injection Function and Gamma Distribution

Consider the incomplete gamma function

$$P(a,x) = \frac{1}{\Gamma(\alpha)} \int_0^x t^{(a-1)} e^{-t} dt \tag{C.1}$$

defined by Abramowitz and Stegun ((Abramowitz & Stegun 1972)). Substituting $a = \alpha$ and $x = \beta t$ into C.1, we obtain

$$P(a,\beta t) = \frac{1}{\Gamma(\alpha)} \int_0^{\beta t} s^{(\alpha-1)} e^{-s} ds \tag{C.2}$$

Which we rearrange into

$$P(a,\beta t) = \int_0^t \frac{1}{\Gamma(\alpha)} \beta^\alpha x^{\alpha-1} e^{-\beta x} dx \tag{C.3}$$

Given the gamma probability density function (PDF)

$$g(x|\alpha,\beta) = \frac{1}{\Gamma(\alpha)} \beta^\alpha x^{\alpha-1} e^{-\beta x} \tag{C.4}$$

and the square wave function

$$I_d(x) = \begin{cases} 1 & \text{if } 0 < x < d \\ 0 & \text{otherwise} \end{cases} \tag{C.5}$$

their convolution where $t > d$ is given by

$$(I \circledast g)(t) = \int_0^{\inf} I_d(t-x)\frac{\beta^\alpha}{\Gamma(\alpha)}x^{\alpha-1}e^{-\beta x}dx \tag{C.6}$$

which we can rearrange into

$$(I \circledast g)(t) = \int_{t-d}^{t} \frac{\beta^\alpha}{\Gamma(\alpha)}x^{\alpha-1}e^{-\beta x}dx = P(\alpha,\beta t) - P(\alpha,\beta(t-d)) \tag{C.7}$$

Note that when $t - x > d$

$$(I \circledast g)(t) = 0 \tag{C.8}$$

and for $0 < t < d$

$$(I \circledast g)(t) = \int_0^{t} 1 \cdot \frac{\beta^\alpha}{\Gamma(\alpha)}x^{\alpha-1}e^{-\beta x}dx = P(\alpha,\beta t) \tag{C.9}$$

# Appendix D

# Historical Information from Arterially Sampled Data for TRPM

Here we report on analyses of performance of TRPM for arterially sampled data from 91 FDG and 39 water studies, described in Section 4.4.1.1. Since calibration of the TRPM differs for FDG and water studies, analyses for the two sets of data are presented separately.

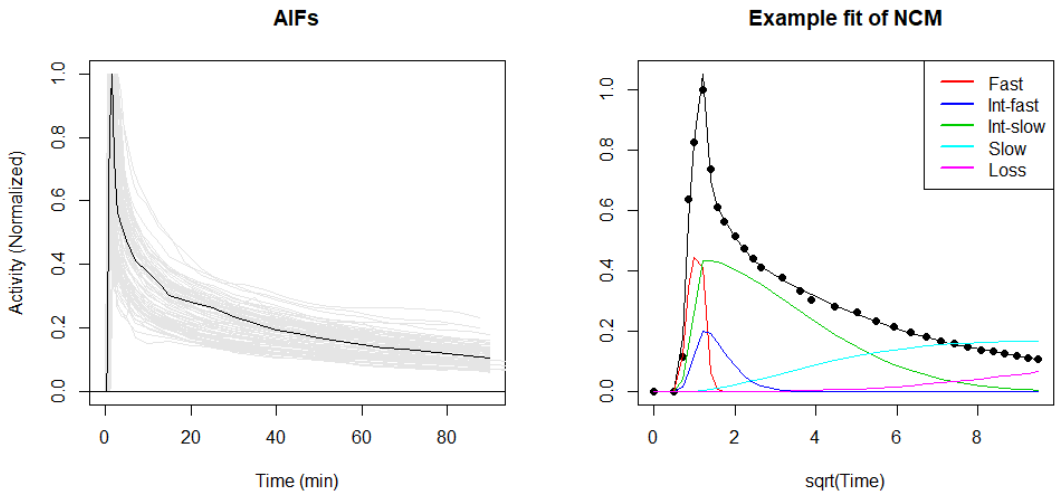


Figure D.1: Left: 91 arterially sampled FDG AIFs in grey dots, and one example in black; Right: TRPM fit on one example from that set. Black dots and line indicate sample and fit, respectively.

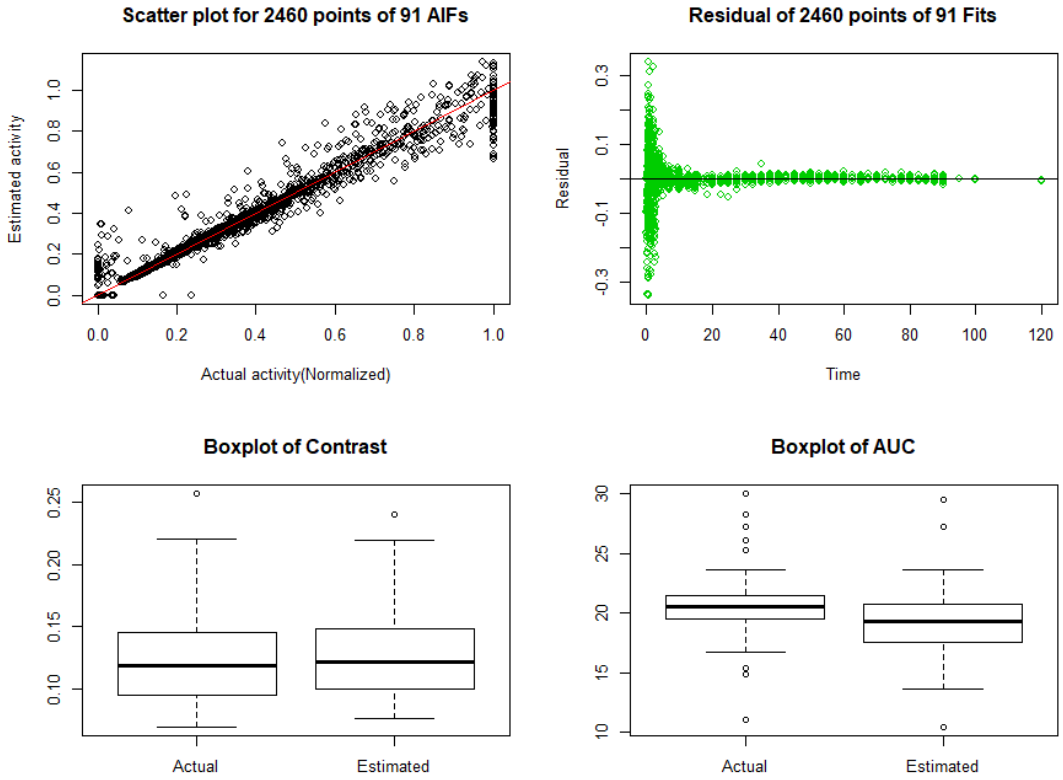


Figure D.2: Performance of TRPM without penalty on 91 arterially sampled AIFs from FDG studies.

## D.1 FDG Analysis

Arterially sampled data include 91 AIFs from FDG studies. Figure D.1 presents the AIFs and one example fit. The component curves shown with five colors are $\pi_j \cdot C_j(t)$s in Eq. (4.7). Then the summation of those five colorful curves is the predicted curve (the loss curve is negatively presented). The fitted curve passes through most of the data points.

Figure D.2 presents performance of TRPM without penalty on 91 directly sampled AIFs. From the top right plot, the absolute values of the residuals are greater at early time ($i.e.$ 0-4 minutes) than at late times. In FDG studies of the most variance in AIFs arises at the beginning of a AIFs study. The curve presents a steady decrease several minutes after injection. To reduce fit errors at early times, a possible solution is to add weights to each of the data points in terms of their variance in the optimization process. However, in our case, the absolute values of the residuals are reasonably small, and the information on one AIF carries depends not only on the curve value at each time, but also some

other meaningful values, $e.g.$ peak and tail values, and their contrast, AUC, $etc.$. Therefore, we can ignore the pattern of residual at this stage. Actually, various weight combinations have been applied during the study, but it seems difficult to reduce the difference of variance in predicting the curve at the beginning and end of the time course. The concentration of tracer is higher at the beginning than at later times though. The bottom of Figure D.2 shows that the contrast rate (value at tail over value at peak) and AUC (here we calculate the AUC after peak time) from the estimated curves are close to the actual ones. Taking Eq. (D.1), the mean (standard deviation) of percentage errors for 91 estimated contrasts and AUCs is 7.31(5.92) % and 8.36(5.51) %, respectively.

$$Percentage\ Error = \frac{|Actual - Estimated|}{Actual} \cdot 100\% \tag{D.1}$$

The estimated parameters are presented in Figure D.3. Mean and standard deviation for 91 estimates of $\theta = (\alpha, \beta, \lambda_f, \lambda_s)$ are 1.15(0.28), 4.08(2.07), 0.49(0.11) and 0.05(0.01), respectively. Estimated parameters may be saved for future use as historical information in the form of a Bayesian penalty in TRPM application.

## D.2 Water Analysis

For water studies, three components are used for TRPM. They are fast, intermediate and slow curves. The fast curve is the same as in the full model (see Eq. (4.2)). The intermediate curve has a similar formula as the inter-fast and inter-slow curves in the full model (see Eq 4.3 and Eq. (4.4)). Replacing the $\lambda_f$ in Eq 4.3 or $\lambda_s$ in Eq. (4.4) by $\lambda$, we get

$$C_{inter}(t) = \int_0^t e(t-s|\lambda)[g(\alpha,\beta) * I_d](s-\Delta)ds \tag{D.2}$$

Therefore, the slow curve is the integral of the intermediate curve:

$$C_{slow}(t) = \int_0^t \int_0^s e(s-u|\lambda)[g(\alpha,\beta) * I_d](u-\Delta)duds \tag{D.3}$$

Since only three components are used, the full model (see Eq. **??**) will be reduced to

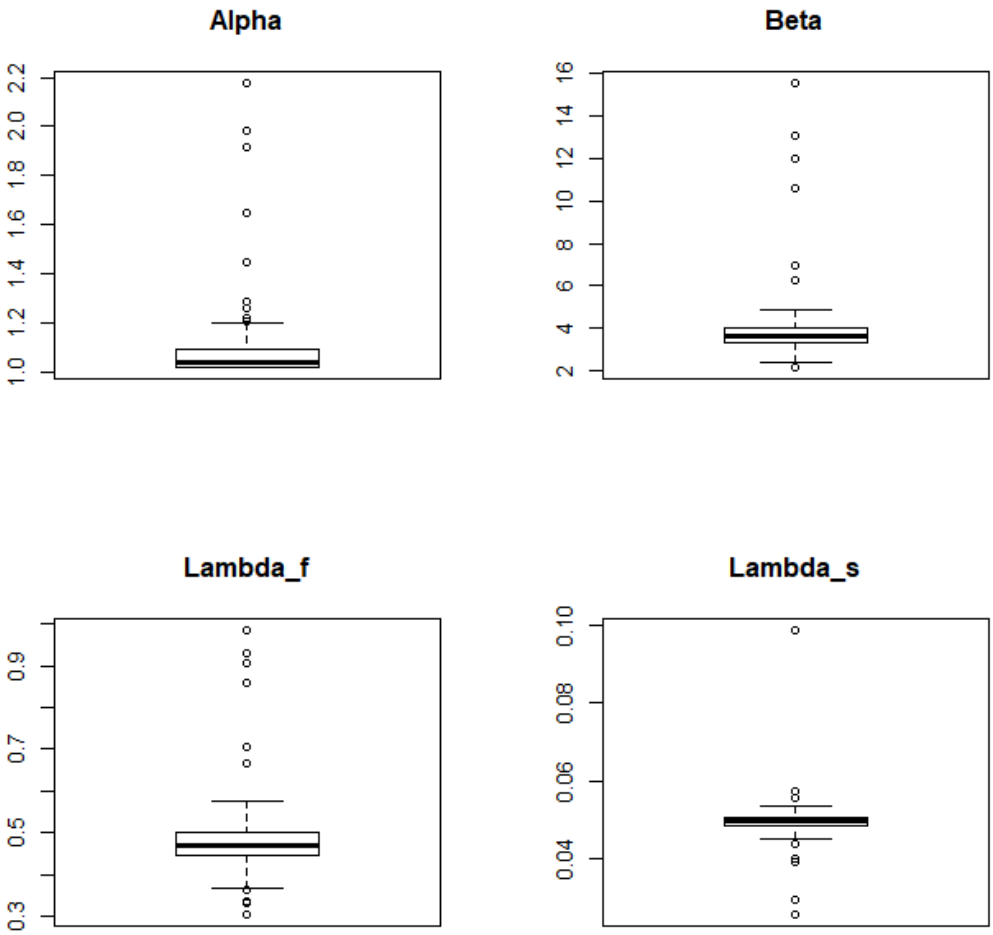


Figure D.3: Distribution of estimated parameters from 91 FDG studies.

$$ {}_nC_P(t) = \pi_1 \cdot C_{fast}(t) + \pi_2 \cdot C_{inter}(t) + \pi_3 \cdot C_{slow}(t) + error \tag{D.4}$$

Here we present one example fit in Figure D.4, showing a sharp elbow around one minute, which the model does not fit well. Also, the rate of continuing decrease in tracer concentration to the tail is steeper in the estimated curve than in the true data. Overall fitting performance for the 39 arterially sampled AIFs for water studies is however reasonable (see Figure D.5 for model fit residuals). The mean (standard deviation) of percentage error for contrast and AUC of 39 fits are 7.69(7.33) % and 19.02(15.52) %, respectively. Lack-of-fit around the elbow affects AUC dramatically, since calculation of the latter is sensitive to the shape of the curve after the peak. Fitting AIF in water studies is more

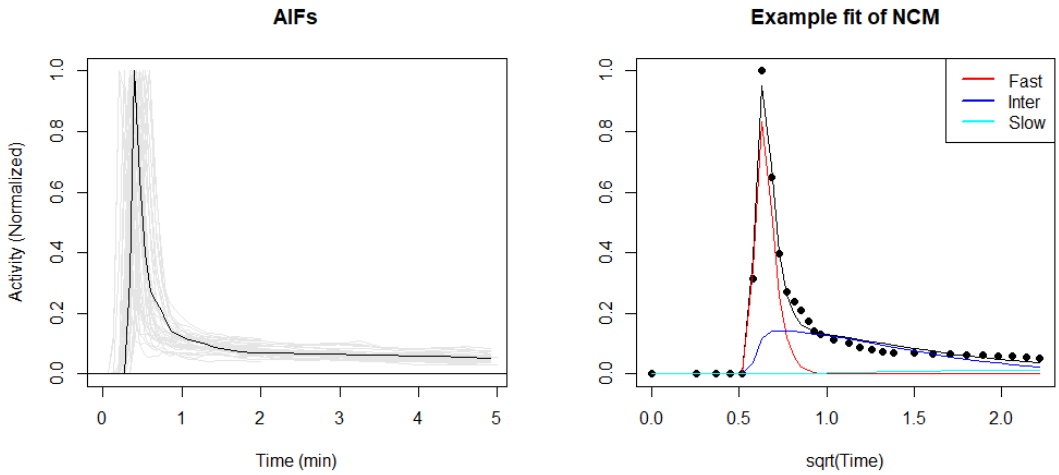


Figure D.4: Left: 39 arterially sampled AIFs from water studies in grey, and one example in black; Right: TRPM fit on one example from that set. Black dots and line indicate sample and fit, respectively.

challenging than for FDG studies. First, water studies are relatively short compared to FDG ones. The shape of a water AIF is also not steady. Therefore, the parameters in those AIFs tend to vary over a greater range, which hinders the optimization process. Second, water data is usually much noisier than FDG data. Although the data we analysed were smoothed, this affects performance from one case to another.

Distribution of estimates for parameters $\alpha$, $\beta$ and $\lambda$ are presented in Figure D.6. The mean (standard deviation) of 39 estimated $\alpha$'s, $\beta$'s and $\lambda$'s are 1.60(0.45), 18.50(7,91) and 0.71(0.32), respectively.

Overall and taking the above mentioned difficulties into account, the TRPM without penalty shows promising performance in fitting the two sets of arterially sampled AIFs from FDG and water studies. The range of errors is acceptable. Parameters estimated from such an experiment may be used as Bayesian penalty for future individual fitting. Likewise, initial values for parameters and boundaries from this experience may be applied in future analyses.

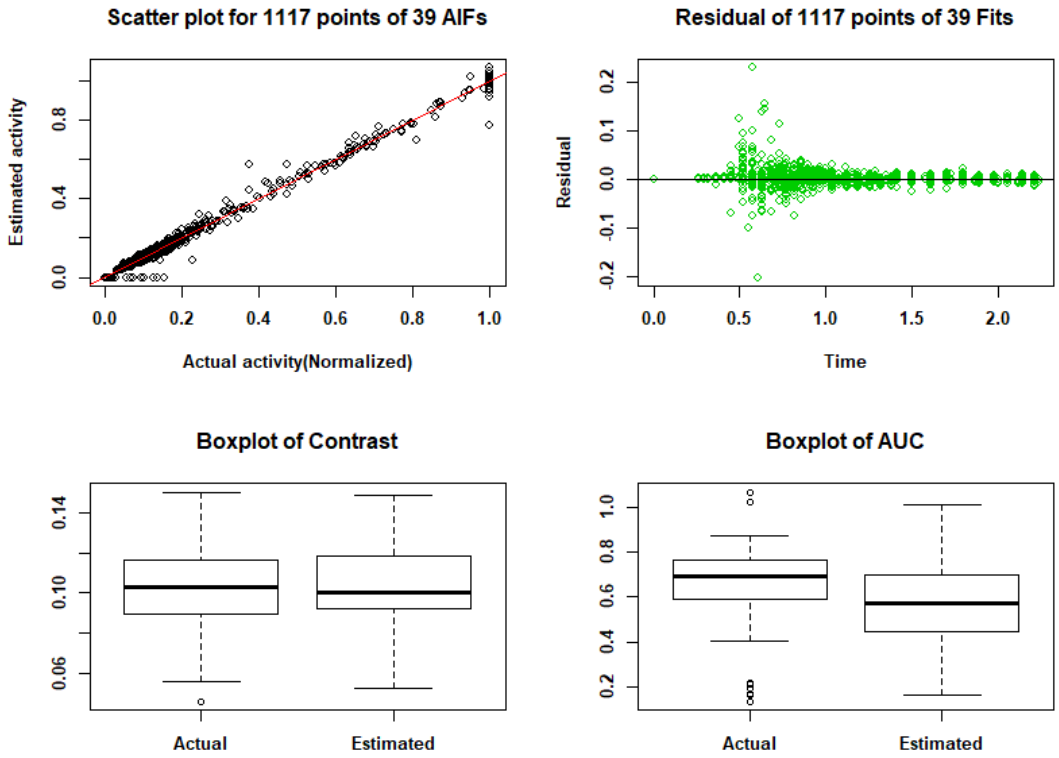


Figure D.5: Performance of TRPM without penalty on 39 Arterially sampled AIFs from water studies.

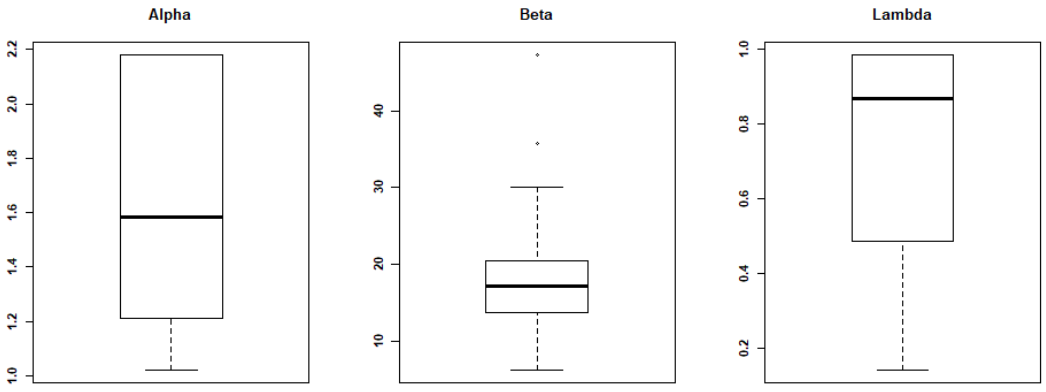


Figure D.6: Distribution of estimated parameters from 39 water population data.

## D.3 Principal Component Analysis of Parameter Estimates

PCA was applied to the estimated parameters from the above analysis. The number of individuals and parameters (in bracket) for FDG and water study were 91(4) and 39(3), respectively. Parameters were scaled so that the standard deviation for each parameter is 1. Figure D.7 shows the percentage of variance explained as a function of the number of components for both FDG and water studies. Over 95% and 80% of the variance was explained by the first two components for FDG and $H_2O$, respectively. Tables D.1 and D.2 present principal component loadings for FDG and water, respectively. In the two tables, all parameters are strongly weighted for the first two components, indicating that none of them may be ignored.

Table D.1: Principal component loadings for the FDG analysis.

| | PC1 | PC2 | PC3 | PC4 |
|---|---|---|---|---|
| $\alpha$ | -0.56 | 0.21 | 0.78 | 0.19 |
| $\beta$ | -0.58 | -0.04 | -0.21 | -0.79 |
| $\lambda_f$ | -0.57 | 0.11 | -0.58 | 0.57 |
| $\lambda_s$ | -0.16 | -0.97 | 0.12 | 0.14 |

Table D.2: Principal component loadings for the water analysis.

| | PC1 | PC2 | PC3 |
|---|---|---|---|
| $\alpha$ | 0.70 | 0.22 | 0.68 |
| $\beta$ | 0.71 | -0.11 | -0.69 |
| $\lambda$ | -0.08 | 0.97 | -0.23 |

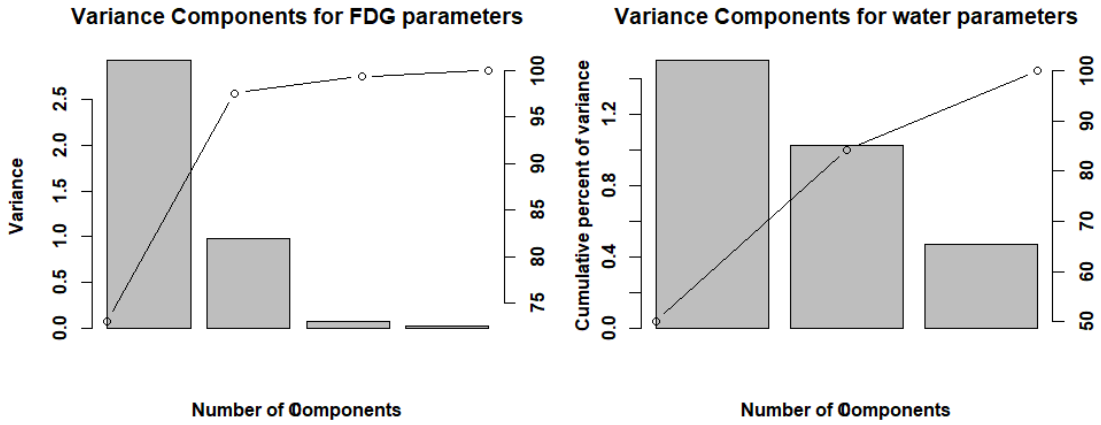


Figure D.7: Principal components of scaled TRPM parameter estimates from directly sampled AIFs from FDG (left) and water (right) studies and their cumulative proportion of variance.

# References


Abramowitz, M. & Stegun, I. A. (1972), 'Handbook of mathematical functions', p. 260.

Akerele, M. I., Zein, S. A., Pandya, S., Nikolopoulou, A. & Nehmeh, S. A. (2021), 'Population-based input function for tspo quantification and kinetic modeling with [11c]-dpa-713', EJNMMI physics **8**(1), 1–17.

Anderson, D. (1983), Compartmental Modeling and Tracer Kinetics, Springer-Verlag, Berlin.

Bailey, D. L., Karp, J. S. & Surti, S. (2005), Physics and Instrumentation in PET, Springer London, London, pp. 13–39.

Bailey, D. L., Townsend, D. W., Valk, P. E. & Maisey, M. N. (2005), Positron Emission Tomography Volume 3 || Image Reconstruction Algorithms in PET, Vol. 10.1007/b136169, pp. 63–91.

Bailey, D. L., Townsend, W, D., Valk, P. E. & Maisey, M. N. (2005), Positron Emission Tomography || Tracer Kinetic Modeling in PET, Vol. 10.1007/b136169, pp. 127–159.

Barber, D. C. (1980), 'The use of principal components in the quantitative analysis of gamma camera dynamic studies', Physics in Medicine and Biology **25**(2), 283–292.

Bentourkia, M. (2006), 'Kinetic modeling of PET-FDG in the brain without blood sampling', Computerized Medical Imaging and Graphics **30**(8), 447–451.

Bentourkia & M'hamed (2005), 'Kinetic modeling of pet data without blood sampling', IEEE Transactions on Nuclear Science **52**(3), 697–702.

Bertoldo, A., Rizzo, G. & Veronese, M. (2014a), 'Deriving physiological information from PET images: from SUV to compartmental modelling', Clinical and Translational Imaging **2**(3), 239–251.

Bertoldo, A., Rizzo, G. & Veronese, M. (2014b), 'Deriving physiological information from pet images: from suv to compartmental modelling', Clinical and Translational Imaging **2**(3), 239–251.

Bertran, M., Martinez, N., Carbajal, G., Fernandez, A. & Gomez, A. (2016), 'An open tool for input function estimation and quantification of dynamic PET FDG brain scans', International Journal of Computer Assisted Radiology and Surgery **11**(8), 1419–1430.

Boellaard, R. (2009), 'Standards for PET image acquisition and quantitative data analysis', Journal of Nuclear Medicine **50**(Suppl 1), 11S–20S.

Boellaard, R., Krak, N. C., Hoekstra, O. S. & Lammertsma, A. A. (2004), 'Effects of noise, image resolution, and ROI definition on the accuracy of standard uptake values: a simulation study', J. Nucl. Med. **45**(9), 1519–1527.

Bois, D. D. & Bois, E. D. (1916), 'A formula to estimate the approximate surface area if height and weight be known', Arch. Intern. Med.(Chic) **17**(6 2), 863–871.

Bottou, L. & Bengio, Y. (1995), Convergence properties of the k-means algorithms, in G. Tesauro, D. S. Touretzky & T. K. Leen, eds, 'Advances in Neural Information Processing Systems 7', MIT Press, pp. 585–592.
**URL:** *http://papers.nips.cc/paper/989-convergence-properties-of-the-k-means-algorithms.pdf*

Brock, C. S., Young, H., Osman, S., Luthra, S. K., Jones, T. & Price, P. M. (2005), 'Glucose metabolism in brain tumours can be estimated using [18f]2-fluorodeoxyglucose positron emission tomography and a population-derived input function scaled using a single arterialised venous blood sample.', International Journal of Oncology **26**(5), 1377.

Brooks, D., Black, P., Arcangeli, M., Aoki, T. & Wilmore, D. (1989), 'The heated dorsal hand vein: an alternative arterial sampling site', Journal of Parenteral and Enteral Nutrition **13**(1), 102–105.

Carson, R. E., Breier, A., de Bartolomeis Andrea, Saunders, R. C., Su, T. P., Schmall, B., Der, M. G., Pickar, D. & Eckelman, W. C. (1997), 'Quantification of amphetamine-induced changes in [11C] raclopride binding with continuous infusion', Journal of Cerebral Blood Flow and Metabolism **17**(4), 437–447.

Carson, R. E., Channing, M. A., Blasberg, R. G., Dunn, B. B., Cohen, R. M., Rice,

K. C. & Herscovitch, P. (1993), 'Comparison of bolus and infusion methods for receptor quantitation: Application to [18F]cyclofoxy and positron emission tomography', Journal of Cerebral Blood Flow and Metabolism **13**(1), 24–42.

Cawley, G. (2006), [IEEE the 2006 IEEE international joint conference on neural network proceedings - Vancouver, BC, Canada (2006.07.16-2006.07.21)] the 2006 IEEE international joint conference on neural network proceedings - leave-one-out cross-validation based model selection criteria for weighted LS-SVMs, number 0, pp. 1661–1668.

Chen, K., Bandy, D., Reiman, E., Huang, S.-C., Lawson, M., Feng, D., Yun, L.-S. & Palant (1998), 'A noninvasive quantitation of the cerebral metabolic rate for glucose using positron emission tomography $^{18}$F-fluorodeoxyglucose, the patlak method, and an imaged-derived input function', **18**, 716–723.

Chen, K., Chen, X., Renaut, R., Alexander, G. E., Bandy, D., Guo, H. & Reiman, E. M. (2007), 'Characterization of the image-derived carotid artery input function using independent component analysis for the quantitation of [18F] fluorodeoxyglucose positron emission tomography images', Physics in Medicine and Biology **52**(23), 7055–7071.

Choi, Y., Hawkins, R., Huang, S., Gambhir, S., Brunken, R., Phelps, M. & Schelbert, H. (1991), 'Parametric images of myocardial metabolic rate of glucose generated from dynamic cardiac PET and 2-[18F]fluoro-2-deoxy-d-glucose studies.', J. Nucl. Med. .

Clark, V. & Kruse, J. (1992), 'Arterial catheterization', Crit. Care Clin. **8**, 687–697.

Copeland, K., Kenney, F. & KS, N. (1992), 'Heated dorsal hand vein sampling for metabolic studies: a reappraisal', Am. J. Physiol. .

Croteau, E., Lavalle, E., Labbe, S. M., Hubert, L., Pifferi, F., Rousseau, J. A., Cunnane, S. C., Carpentier, A. C., Lecomte, R. & Bnard, F. (2010), 'Image-derived input function in dynamic human PET/CT: methodology and validation with 11C-acetate and 18F-fluorothioheptadecanoic acid in muscle and 18F-fluorodeoxyglucose in brain', Eur. J. Nucl. Med. Mol. Imag. **37**(8), 1539–1550.

Cunningham, V. J. & Jones, T. (1993), 'Spectral analysis of dynamic PET studies', Journal of Cerebral Blood Flow and Metabolism **13**(1), 15–23.

Dimitrakopoulou-Strauss, A., Pan, L. & Sachpekidis, C. (2021), 'Kinetic model-

ing and parametric imaging with dynamic PET for oncological applications: General considerations, current clinical applications, and future perspectives', European Journal of Nuclear Medicine and Molecular Imaging **48**, 21–39.

Dunnwald, L., Doot, R., Specht., J. & et al (2011), 'Pet tumor metabolism in locally advanced breast cancer patients undergoing neoadjuvant chemotherapy: value of static vs kinetic measures of fluorodeoxyglucose uptake', Clinical Cancer Research .
**URL:** *http://clincancerres.aacrjournals.org/content/early/2011/03/01/1078-0432.CCR-10-2649*

Dunnwald, L., Gralow, J., Ellis, G. & et al (2008), 'Tumor metabolism and blood flow changes by positron emission tomography: relation to survival in patients treated with neoadjuvant chemotherapy for locally advanced breast cancer', **26**(27), 4449–4457.

Eberl, S., Anayat, A. R., Fulton, R. R., Hooper, P. K. & Fulham, M. J. (1997), 'Evaluation of two population-based input functions for quantitative neurological FDG PET studies', European Journal of Nuclear Medicine and Molecular Imaging **24**(3), 299–304.

Endres, C. J. & Carson, R. E. (1998), 'Assessment of dynamic neurotransmitter changes with bolus or infusion delivery of neuroreceptor ligands', Journal of Cerebral Blood Flow and Metabolism **18**.

Eyal, S., Ke, A., Muzi, M., Link, J. M., Mankoff, D. A., Collier, A. C. & Unadkat, J. D. (2010), 'Regional p-glycoprotein activity and inhibition at the human blood-brain barrier as imaged by positron emission tomography', **87**(5), 579–585.

Farde, L., Eriksson, L., Blomquist, G. & Halldin, C. (1989), 'Kinetic analysis of central [11C]raclopride binding to D2-dopamine receptors studied by PET-a comparison to the equilibrium analysis', Journal of Cerebral Blood Flow and Metabolism **9**, 696–708.

Feng, D., Ho, D., Chen, K., Wu, L.-C., Wang, J.-K., Liu, R.-S. & Yeh, S.-H. (1995), 'An evaluation of the algorithms for determining local cerebral metabolic rates of glucose using positron emission tomography dynamic data', IEEE transactions on medical imaging **14**(4), 697–710.

Feng, D., Huang, S. C. & Wang, X. (1993), 'Models for computer simulation

studies of input functions for tracer kinetic modeling with positron emission tomography', Int. J. Biomed. Comput. **32**(2), 95–110.

Feng, D., Wong, K.-P., Wu, C.-M. & Siu, W.-C. (1997), 'A technique for extracting physiological parameters and the required input function simultaneously from PET image measurements: theory and simulation study', IEEE Transactions on Information Technology in Biomedicine **1**(4), 243–254.

Frackowiak, R. S. J., Lenzi, G.-L., Jones, T. & Heather, J. D. (1980), 'Quantitative measurement of regional cerebral blood flow and oxygen metabolism in man using 15O and positron emission tomography', Journal of Computer Assisted Tomography **4**(6), 727–736.

Fung, E. K. & Carson, R. E. (2013), 'Cerebral blood flow with [15O] water pet studies using an imaged-derived input function and MR-defined carotid centerlines', Phys. Med. Biol. **58**(6), 1903–1923.

Golub, G. H., Heath, M. & Wahba, G. (1979), 'Generalized cross-validation as a method for choosing a good ridge parameter', Technometrics **21**(2), 215–223.

Graham, M. & Lewellen, B. (1993), 'High-speed automated discrete blood sampling for positron emission tomography', J. Nucl. Med. .

Graham, M. M., Muzi, M., Spence, A. M., O'Sullivan, F., Lewellen, T. K., Link, J. M. & Krohn, K. A. (2002), 'The fluorodeoxyglucose lumped constant in normal human brain', **43**, 1157–1166.

Guo, H., Renaut, R. A. & Chen, K. (2007), 'An input function estimation method for FDG-PET human brain studies', Nuclear Medicine and Biology **34**(5), 0–492.

Hamberg, L., Hunter, G., Alpert, N., Choi, N., Babich, J. & Fischman, A. (1994), 'The dose uptake ratio as an index of glucose metabolism: useful parameter or oversimplification?', J. Nucl. Med. **35**(8), 1308–1312.

Hartley, H. O. (1961), 'The modified Gauss-Newton method for the fitting of non-linear regression functions by least squares', Technometrics **3**(2), 269–280.

Hawe, D., Fernández, F. R. H., O'Suilleabháin, L., Huang, J., Wolsztynski, E. & O'Sullivan, F. (2012), 'Kinetic analysis of dynamic positron emission tomogra-

phy data using open-source image processing and statistical inference tools', Wiley Interdisciplinary Reviews: Computational Statistics **4**(3), 316–322.

Herscovitch, P., Markham, J. & Raichle, M. E. (1983), 'Brain blood flow measured with intravenous H2(15)O. i. theory and error analysis', **24**(9), 782–789.

Holt, A., Pasca, E., Heijmink, S. W., Teertstra, J., Muller, S. H. & van der Heide, U. A. (2012), The impact of overall injection time on the arterial input function and pharmaco-kinetic analysis using the tofts model in dce-mri for prostate cancer patients, in 'Proc. Intl. Soc. Mag. Reson. Med', Vol. 20, p. 238.

Houston, A. S. (1984), 'The effect of apex-finding errors on factor images obtained from factor analysis and oblique transformation (nuclear medicine)', Phys. Med. Biol. **29**(9), 1109–1116.

Huang, J. & O'Sullivan, F. (2014), 'An analysis of whole body tracer kinetics in dynamic pet studies with application to image-based blood input function extraction', IEEE Trans. Med. Imag. **33**(5), 1093–1108.

Huang, S. C. & Phelps, M. E. (1986), Principles of tracer kinetic modeling in positron emission tomography and autoradiography, in M. Phelps, J. Mazziotta & H. Schelbert, eds, 'Positron Emission Tomography and Autoradiography: Principles and Applications for the Brain and Heart', New York: Raven Press, pp. 287–346.

Hyvarinen, A. & Oja, E. (1997), 'A fast fixed-point algorithm for independent component analysis', Neural Computation **9**(7), 1483 – 1492.

Ito, H., Hietala, J., Blomqvist, G., Halldin, C. & Farde, L. (1998), 'Comparison of the transient equilibrium and continuous infusion method for quantitative PET analysis of [11C]raclopride binding', Journal of Cerebral Blood Flow and Metabolism **18**, 941–950.

Joseph A. Thie, K. F. H. & Smith, G. T. (2000), 'The diagnostic utility of the lognormal behavior of PET standardized uptake values in tumors', J. Nucl. Med. **41**(10), 1664–1672.

JROGEL (2012), Positron Emission Tomograph.
**URL:** *https://quantumtunnel.wordpress.com/2012/12/15/positron-emission-tomography-sci-advent-day-14/*

Kao, P.-F., Kim, S., Jr., H. N. W., Lever, J. R., Ravert, H. T. & Dannals,

R. F. (1996), 'Assessing neuroreceptor occupancy by continuous infusion of carbon-11 labeled radioligands', European Journal of Nuclear Medicine and Molecular Imaging **23**(2), 141–144.

Kato, A., Menon, D., Diksic, M. & Yamamoto, Y. L. (1984), 'Influence of the input function on the calculation of the local cerebral metabolic rate for glucose in the deoxyglucose method', Journal of Cerebral Blood Flow and Metabolism **4**(1), 41–46.

Kety, S. S. & Schmidt, C. F. (1948), 'The nitrous oxide method for the quantitative determination of cerebral blood flow in man: Theory, procedure and normal values', J. Clin. Invest. **27**(4), 476–483.

Kim, J., Herrero, P., Sharp, T., Laforest, R., Rowland, D. J., Tai, Y. C., Lewis, J. S. & Welch, M. J. (2006), 'Minimally invasive method of determining blood input function from PET images in rodents', J. Nucl. Med. **47**(2), 330–336.

Kimura, Y., Naganawa, M., Shidahara, M., Ikoma, Y. & Watabe, H. (2007), 'Pet kinetic analysis —pitfalls and a solution for the logan plot', Annals of Nuclear Medicine **21**(1), 1–8.

Koon-Pong Wong; Feng, D.; Meikle, S. F. M. (2001), 'Simultaneous estimation of physiological parameters and the input function - in vivo PET data', IEEE Transactions on Information Technology in Biomedicine **5**(1), 67–76.

Laforest, R., Sharp, T. L., Engelbach, J. A., Fetting, N. M., Herrero, P., Kim, J., Lewis, J. S., Rowland, D. J., Tai, Y. C. & Welch, M. J. (2005), 'Measurement of input functions in rodents: Challenges and solutions', Nucl. Med. Biol. **32**(7), 679–685.

Laruelle, M. (2000), 'Imaging synaptic neurotransmission with in vivo binding competition techniques: A critical review', Journal of Cerebral Blood Flow and Metabolism **20**(3), 423–451.

Lassen, N. A. (1992), 'Neuroreceptor quantitation in vivo by the steady-state principle using constant infusion or bolus injection of radioactive tracers', Journal of Cerebral Blood Flow and Metabolism **12**(5), 709–716.

Lawson, C. L. & Hanson, R. J. (1974), Solving Least Squares Problems, Prentice-Hall, Englewood Cliff, New Jersey.

Levenberg, K. (1944), 'A method for the solution of certain non-linear problems in least squares', Quarterly of Applied Mathematics **2**(2), 164–168.

Liptrot, M., Adams, K. H., Martiny, L., Pinborg, L. H., Lonsdale, M. N., Olsen, N. V., Holm, S., Svarer, C. & Knudsen, G. M. (2004), 'Cluster analysis in kinetic modelling of the brain: a noninvasive alternative to arterial sampling', NeuroImage **21**(2), 483–493.

Loening, A. M. & Gambhir, S. S. (2003), 'AMIDE: A free software tool for multimodality medical image analysis', **2**(3), 131–137.

Logan, J., Fowler, J. S., Volkow, N. D., Ding, Y. S., Wang, G.-J. & Alexoff, D. L. (2001), 'A strategy for removing the bias in the graphical analysis method', Journal of Cerebral Blood Flow and Metabolism **21**(3), 307–320.
**URL:** *https://doi.org/10.1097/00004647-200103000-00014*

Logan, J., Fowler, J. S., Volkow, N. D., Wolf, A. P., Dewey, S. L., Schlyer, D. J., MacGregor, R. R., Hitzemann, R., Bendriem, B. & Gatley, S. J. (1990), 'Graphical analysis of reversible radioligand binding from time-activity measurements applied to [N-11C-methyl]-(-)-cocaine PET studies in human subjects', Journal of Cerebral Blood Flow and Metabolism **10**(5), 740–747.

Maisey, M. N. (2005), Positron Emission Tomography in Clinical Medicine, Springer London, London, pp. 1–12.

Mankoff, D., Dunnwald, L., Gralow, J. & et al (2002), 'Blood flow and metabolism in locally advanced breast cancer: Relationship to response to therapy', **43**(4), 500–509.

Mankoff, D., Dunnwald, L., Gralow, J. & et al (2003), 'Changes in blood flow and metabolism in locally advanced breast cancer with neoadjuvant chemotherapy', **44**(11), 1806–1814.

March, G. M., Elfatori, S. & Beaulé, P. E. (2013), 'Clinical experience with tranexamic acid during primary total hip arthroplasty', Hip International **23**(1), 72–79.

Mintun, M. A., Raichle, M. E., Kilbourn, M. R., Wooten, G. F. & Welch, M. J. (1984), 'A quantitative model for the in vivo assessment of drug binding sites with positron emission tomography', Annals of Neurology **15**(3), 217–227.

Morris, E. D., Endres, C. J., Schmidt, K. C., Christian, B. T., Muzic, R. F. & Fisher, R. E. (2004), 'Kinetic modeling in positron emission tomography', Emission tomography: The fundamentals of PET and SPECT **46**(1), 499–540.

Muzi, M., Mankoff, D. A., Link, J. M., Shoner, S., Collier, A. C., Sasongko, L. &

Unadkat, J. D. (2009), 'Imaging of cyclosporine inhibition of P-glycoprotein activity using 11C-verapamil in the brain: Studies of heathy humans', **50**(8), 1267–1275.

Muzi, M., Spence, A. M., O'Sullivan, F., Mankoff, D. A., Wells, J. M., Grierson, J. R., Link, J. M. & Krohn, K. A. (2006), 'Kinetic analysis of 3'-deoxy-3'-18F-fluorothymidine in patients with gliomas', Journal of Nuclear Medicine **47**(10), 1612–1621.

Nadler, S. B., Hidalgo, J. U. & Blochc, T. (1962), 'Prediction of blood volume in normal human adults', Surgery **51**(2), 224–232.

Naganawa, M., Kimura, Y., Ishii, K., Oda, K., Ishiwata, K. & Matani, A. (2005), 'Extraction of a plasma time-activity curve from dynamic brain PET images based on independent component analysis', IEEE Transactions on Biomedical Engineering **52**(2), 201–210.

National Institute of Mental Health team, N. I. (2018), CNS Radiotracer Table. [Online; accessed 14-November-2018].

Ogden, R. T., Zanderigo, F., Choy, S., Mann, J. J. & Parsey, R. V. (2010), 'Simultaneous estimation of input functions: an empirical study', Journal of Cerebral Blood Flow & Metabolism **30**(4), 816–826.

Olshen, A. B. & O'Sullivan, F. (1997), 'Camouflaged deconvolution with application to blood curve modeling in FDG PET studies', Journal of the American Statistical Association **92**(440), 1293–1303.

original by Berwin A. Turlach; R port by Andreas Weingessel; Fortran contributions from Cleve Moler dpodi/LINPACK), S. (2019), quadprog: Functions to solve Quadratic Programming Problems. R package version 1.5-8.
**URL:** *https://CRAN.R-project.org/package=quadprog*

O'Sullivan, F. (1993), 'Imaging radiotracer model parameters in PET: a mixture analysis approach', IEEE Transactions on Medical Imaging **12**(3), 399–412.

O'Sullivan, F. (2005), 'Locally constrained mixture representation of dynamic imaging data from PET and MR studies', Biostatistics **7**(2), 318–338.

O'Sullivan, F., Kirrane, J., Muzi, M., O'Sullivan, J. N., Spence, A. M., Mankoff, D. A. & Krohn, K. A. (2009), 'Kinetic quantitation of cerebral PET-FDG studies without concurrent blood sampling: statistical recovery of the arterial input function', IEEE transactions on medical imaging **29**(3), 610–624.

O'Sullivan, F., Kirrane, J., Muzi, M., O'Sullivan, J. N., Spence, A. M., Mankoff, D. A. & Krohn, K. A. (2010), 'Kinetic quantitation of cerebral PET-FDG studies without concurrent blood sampling: Statistical recovery of the arterial input function', IEEE Transactions on Medical Imaging **29**(3), 610–624.

O'Sullivan, F., Muzi, M., Mankoff, D. A., Eary, J. F., Spence, A. M. & Krohn, K. A. (2014), 'Voxel-level mapping of tracer kinetics in PET studies: A statistical approach emphasizing tissue life tables', The Annals of Applied Statistics **8**(2), 1065–1094.

O'Sullivan, F., Muzi, M., Spence, A. M., Mankoff, D. M., O'Sullivan, J. N., Fitzgerald, N., Newman, G. S. & Krohn, K. A. (2009), 'Nonparametric residue analysis of dynamic PET data with application to cerebral FDG studies in normals', J. Am. Stat. Assoc. **104**, 556–571.

O'Sullivan, F., O'Sullivan, J., Huang, J., Doot, R., Muzi, M., E.Schubert, Peterson, L., Dunnwald, L. & Mankoff, D. (2017), 'Assessment of a statistical AIF extraction method for dynamic PET studies with $^{15}$O water and $^{18}$F fluorodeoxyglucose in locally advanced breast cancer patients', **5**(1).

O'Sullivan, F. & Wahba, G. (1985), 'A cross validated bayesian retrieval algorithm for nonlinear remote sensing experiments', J. Comput. Phys. **59**, 441–455.

Parsey, R. V., Slifstein, M., Hwang, D.-R., Abi-Dargham, A., Simpson, N., Mawlawi, O., Guo, N.-N., Heertum, R. V., Mann, J. J. & Laruelle, M. (2000), 'Validation and reproducibility of measurement of 5-HT1A receptor parameters with [carbony1-11C]WAY-100635 in humans:comparison of arterial and reference tissue input functions', J. Cereb. Blood Flow Metab. **20**(7), 1111–1133.

Patlak, C. S., Blasberg, R. G. & Fenstermacher, J. D. (1983), 'Graphical evaluation of blood-to-brain transfer constants from multiple-time uptake data', Journal of Cerebral Blood Flow and Metabolism **3**(1), 1–7.

Phelps, M. E., Huang, S. C., Hoffman, E. J., Selin, C., Sokoloff, L. & Kuhl, D. E. (1979), 'Tomographic measurement of local cerebral glucose metabolic rate in humans with (F-18)2-fluoro-2-deoxy-D-glucose: Validation of method', Annals of Neurology **6**(5), 371–388.

Philipp, T. M., Circiumaru, V., Cardi, C. A., Thomas, D. A., Bal, H. & Acton,

P. D. (2006), 'Simplified quantification of small animal [18F]FDG PET studies using a standard arterial input function', **33**(8), 948–954.

Poulin, E., Lebel, R., Croteau, E., Blanchette, M., Tremblay, L., Lecomte, R., Bentourkia, M. & Lepage, M. (2013), 'Conversion of arterial input functions for dual pharmacokinetic modeling using gd-dtpa/mri and 18f-fdg/pet', Magnetic Resonance in Medicine **69**(3), 781–792.

R Core Team (2016), R: A Language and Environment for Statistical Computing, R Foundation for Statistical Computing, Vienna, Austria.
**URL:** *https://www.R-project.org/*

Raichle, M. E., Martin, W. R., Herscovitch, P., Mintun, M. A. & Markham, J. (1983), 'Brain blood flow measured with intravenous H2(15)O. ii. implementation and validation', **24**(9), 790–798.

Rissanen, E., Tuisku, J., Luoto, P., Arponen, E., Johansson, J., Oikonen, V., Parkkola, R., Airas, L. & Rinne, J. O. (2015), 'Automated reference region extraction and population-based input function for brain [(11)c]tmsx pet image analyses', Journal of Cerebral Blood Flow and Metabolism **35**(1), 157–65.

Sabbatini, R. M.E. (1997), 'The cyclotron and PET', http://www.cerebromente.org.br/n01/pet/petcyclo.htm. [Online; accessed 16-November-2018].

Sanabria-Bohórquez, S. M., Maes, A., Dupont, P., Bormans, G., de Groot, T., Coimbra, A., Eng, W., Laethem, T., Lepeleire, I. D., Gambale, J., Vega, J. M. & Burns, H. (2003), 'Image-derived input function for [11C]flumazenil kinetic analysis in human brain', Molecular Imaging and Biology **5**(2), 0–78.

Sari, H., Erlandsson, K., Barnes, A., Atkinson, D., Arridge, S., Ourselin, S. & Hutton, B. (2014), Modelling the impact of injection time on the bolus shapes in pet-mri aif conversion, in 'EJNMMI physics', Vol. 1, SpringerOpen, pp. 1–3.

Sari, H., Erlandsson, K., Law, I., Larsson, H., Ourselin, S., Arridge, S., Atkinson, D., & Hutton, B. (2017), 'Estimation of an image derived input function with mr-defined carotid arteries in FDG-PET human studies using a novel partial volume correction method', **37**(4), 1398–1409.

Shiozaki, T., Sadato, N., Senda, M., Ishii, K., Tsuchida, T., Yonekura, Y., Fukuda, H. & Konishi, J. (2000), 'Noninvasive estimation of FDG input function for quantification of cerebral metabolic rate of glucose: Optimization and multicenter evaluation', Nuclear Medicine Communications **41**(10), 1612–1618.

Sokoloff, L., Reivich, M., Kennedy, C., DesRosier, M. H., Patlak, C. S., Pettigrew, K. D., Sakurada, O. & Shinohara, M. (1977), 'The [14C]deoxyglucose method for the measurement of local cerebral glucose utilization: theory, procedure, and normal values in the conscious and anesthetized albino rat', **28**, 897–916.

Spence, A. M., Muzi, M., Graham, M. M., O'Sullivan, F., Krohn, K. A., Link, J. M., Lewellen, T. K., Lewellen, B., Freeman, S. D., Berger, M. S. & Ojemannn, G. A. (1998), 'Glucose metabolism in human malignant gliomas measured quantitatively with PET, l-[C-ll]Glucose and FDG: Analysis of the FDG lumped constant', J. Nucl. Med. **39**, 440–448.

Syvanen, S., Blomquist, G., Appel, L., Hammarlund-Udenaes, M., Langstrom, B. & Bergstrom, M. (2006a), 'Predicting brain concentrations of drug using positron emission tomography and venous input: modeling of arterial-venous concentration differences', European Journal of Clinical Pharmacology **62**(10), 839–848.

Syvanen, S., Blomquist, G., Appel, L., Hammarlund-Udenaes, M., Langstrom, B. & Bergstrom, M. (2006b), 'Predicting brain concentrations of drug using positron emission tomography and venous input: modeling of arterial-venous concentration differences', European Journal of Clinical Pharmacology **62**(10), 839–848.

Takikawa, S., Dhawan, V., Robeson, W., Spetsieris, P., Chaly, T., Dahl, R., Margouleff, D. & Eidelberg, D. (1993), 'Noninvasive quantitative FDG/PET studies using an estimated input function derived from a population arterial blood curve', **188**, 131–186.

Thie, J. A. (2004), 'Understanding the standardized uptake value, its methods, and implications for usage', J. Nucl. Med. **45**(9), 1431–1434.

Tomasi, G., Bertoldo, A., Bishu, S., Unterman, A., Smith, C. B. & Schmidt, K. C. (2009), 'Voxel-based estimation of kinetic model parameters of the L-[1-11C]leucine PET method for determination of regional rates of cerebral protein synthesis: validation and comparison with region-of-interest-based methods', Journal of Cerebral Blood Flow and Metabolism **29**(7), 1317–1331.

Tonietto, M., Rizzo, G., Veronese, M. & Bertoldo, A. (2015), Modelling arterial input functions in positron emission tomography dynamic studies, in 'Pro-

ceedings of the Annual International Conference of the IEEE Engineering in Medicine and Biology Society (EMBC '15)'.

Tonietto, M., Zanderigo, F., Bertoldo, A., Devanand, D. P. & Stankoff, B. (2019), Multicenter validation of population-based input function with non-linear mixed effect modeling for voxel-wise quantification of [18 f]FDG metabolic rate, in '2019 IEEE 16th International Symposium on Biomedical Imaging (ISBI)'.

Tseng, J., Dunnwald, L., Gralow, J. & et al (2004), '$^{18}$F-FDG kinetics in locally advanced breast cancer: Correlation with tumor blood flow and changes in response to neoadjuvant chemotherapy', **45**(11), 1829–1837.

Turku BioImaging team (2018), 'PET imaging', http://www.bioimaging.fi/methods/pet-mri/. [Online; accessed 15-November-2018].

van der Weerdt, A. P., Klein, L. J., Visser, C. A., Visser, F. C. & Lammertsma, A. A. (2002), 'Use of arterialised venous instead of arterial blood for measurement of myocardial glucose metabolism during euglycaemic-hyperinsulinaemic clamping', European Journal of Nuclear Medicine and Molecular Imaging **29**(5), 663–669.

Veronese, M., Rizzo, G., Bertoldo, A., & Turkheimer, F. E. (2016), 'Spectral analysis of dynamic PET studies: A review of 20 years of method developments and applications', Computational and Mathematical Methods in Medicine **2016**(8), 1–15.
**URL:** *https://doi.org/10.1155/2016/7187541*

Vriens, D., de Geus-Oei, L.-F., Oyen, W. J. & Visser, E. P. (2009), 'A curve-fitting approach to estimate the arterial plasma input function for the assessment of glucose metabolic rate and response to treatment', Journal of Nuclear Medicine **50**(12), 1933–1939.

Watabe, W., Channing, M. A., Riddell, C., Jousse, F., Libutti, S. K., Carrasquillo, J. A., Bacharach, S. L. & Carson, R. E. (2001), 'Noninvasive estimation of the aorta input function for measurement of tumor blood flow with [/sup 15/o] water', IEEE transactions on medical imaging **20**(3), 164–174.

Wikipedia contributors (2018a), 'Carl David Anderson — Wikipedia, the free encyclopedia', https://en.wikipedia.org/w/index.php?title=Carl_David_Anderson&oldid=863065013. [Online; accessed 15-November-2018].

Wikipedia contributors (2018b), 'Gamma distribution — Wikipedia, the free encyclopedia', https://en.wikipedia.org/w/index.php?title=Gamma_distribution&oldid=870977901. [Online; accessed 21-December-2018].

Wikipedia contributors (2018c), 'Henri Becquerel — Wikipedia, the free encyclopedia', https://en.wikipedia.org/w/index.php?title=Henri_Becquerel&oldid=866969827. [Online; accessed 15-November-2018].

Wikipedia contributors (2018d), 'Logit — Wikipedia, the free encyclopedia', https://en.wikipedia.org/w/index.php?title=Logit&oldid=866450157. [Online; accessed 14-December-2018].

Wikipedia contributors (2018e), 'Marie Curie — Wikipedia, the free encyclopedia', https://en.wikipedia.org/w/index.php?title=Marie_Curie&oldid=867436756. [Online; accessed 15-November-2018].

Wikipedia contributors (2018f), 'Paul Dirac — Wikipedia, the free encyclopedia', https://en.wikipedia.org/w/index.php?title=Paul_Dirac&oldid=867870234. [Online; accessed 15-November-2018].

Wong, K.-P., Feng, D., Meikle, S. & Fulham, M. (2002), 'Segmentation of dynamic PET images using cluster analysis', IEEE Transactions on Nuclear Science **49**(1), 200–207.

Wu, H., Hoh, C., Choi, Y., Schelbert, H., Hawkins, R., Phelps, M. & Huang, S. (1995), 'Factor analysis for extraction of blood time-activity curves in dynamic FDG-PET studies', J. Nucl. Med. .

Xiu, Z., Huang, J., Muzi, M. & Wolsztynski, E. (2022), Patient-adaptive Population-based Modeling of Arterial Input Functions.
**URL:** *https://www.techrxiv.org/articles/preprint/Patient-adaptive_Population-based_Modeling_of_Arterial_Input_Functions/20456802*

Xiu, Z., Huang, J., O'Sullivan, J., Wolsztynski, E., Dave, M. & O'Sullivan, F. (2016), Calibrating a whole body circulation model for image-based AIF extraction in the context of Blood Flow-Metabolism Mismatch Assessment in LABCa Patients, Royal Statistics Society Annual Conference (RSS), Manchester, UK.

Xiu, Z., Huang, J., O'Sullivan, J., Wolsztynski, E., Mankoff, D. & O'Sullivan, F. (2018), 'Mixture modelling for aif extraction from dynamic pet studies', Royal Statistics Society Annual Conference (RSS), Glasgow, UK .

Xiu, Z., Huang, J. & Wolsztynski, E. (2020), pbcmm.
**URL:** *https://github.com/ryanxiu/pbcmm.git*

Yetik, I. & Qi, J. (2006), [IEEE 3rd IEEE international symposium on biomedical imaging: Macro to nano, 2006. - Arlington, Virginia, USA (april 6, 2006)] 3rd IEEE international symposium on biomedical imaging: Macro to nano, 2006. - direct estimation of kinetic parameters from the sinogram with an unknown blood function, pp. 295–298.

Zaidi, H. (2006), Quantitative Analysis in Nuclear Medicine Imaging, Springer, New York.

Zanderigo, F., Ogden, R. T. & Parsey, R. V. (2013), 'Reference region approaches in PET: a comparative study on multiple radioligands', **33**(6), 888–897.

Zanderigo, F., Ogden, R. T. & Parsey, R. V. (2014), 'Noninvasive blood-free full quantification of positron emission tomography radioligand binding', J. Cereb. Blood Flow Metab. **35**(1), 148–156.

Zanotti-Fregonara, P., Chen, K., Liow, J.-S., Fujita, M. & Innis, R. B. (2011), 'Image-derived input function for brain PET studies: Many challenges and few opportunities', J. Cereb. Blood Flow Metab. **31**, 1986–1998.

Zanotti-Fregonara, P., Hines, C. S., Zoghbi, S. S., Liow, J.-S., Zhang, Y., Pike, V. W., Drevets, W. C., Mallinger, A. G., Jr., C. A. Z., Fujita, M. & Innis, R. B. (2012), 'Population-based input function and image-derived input function for [$^{11}$C](R)-rolipram PET imaging: Methodology, validation and application to the study of major depressive disorder', NeuroImage **63**(3).

Zanotti-Fregonara, P., Liow, J., Comtat, C., Zoghbi, S., Zhang, Y., Pike, V., Fujita, M. & Innis, R. (2012), 'Image-derived input function in PET brain studies: blood-based methods are resistant to motion artifacts', Nucl. Med. Commun. **33**(9), 982–989.

Zasadny, K. R. & Wahl, R. L. (1993), 'Standardized uptake values of normal tissues at PET with 2-[fluorine-18]-fluoro-2-deoxy-dglucose: variations with body weight and a method for correction', Radiology **189**(3), 847–850.

Zeng, G. L., Kadrmas, D. J. & Gullberg, G. T. (2012), 'Fourier domain closed-form formulas for estimation of kinetic parameters in reversible multi-compartment models', BioMedical Engineering OnLine **11**(1).

Zhou, S., Chen, K., Reiman, E. M., Li, D.-m. & Shan, B. (2012), 'A method for

generating image-derived input function in quantitative 18F-FDG PET study based on the monotonicity of the input and output function curve', Nuclear Medicine Communications **33**(4), 362–370.